Chemical Probe Development for Bromodomain and PHD Finger-containing Transcription Factor (BPTF) Reader Domains as Anti-Cancer Therapy

A DISSERTATION
SUBMITTED TO THE FACULTY OF THE
UNIVERSITY OF MINNESOTA

BY

Caroline R. Buchholz

IN PARTIAL FULFILLMENT OF THE REQUIREMENTS
FOR THE DEGREE OF
DOCTOR OF PHILOSOPHY

ADVISOR

Dr. William C.K. Pomerantz

June 2023

Acknowledgements

I would like to first acknowledge my gratitude for my advisor, Dr. William Pomerantz, for his encouragement and sharing his enthusiasm for science. Thank you for caring for your students as not only scientists but people. I could not imagine my journey any other way.

Thank you to Dr. Huda Zahid, my mentor, for the unwavering leadership and wisdom. I feel lucky to have gotten to work at the bench alongside you. To Dr. Jorden Johnson for passing along her knowledge, to Dr. Prakriti Kalra and Dr. Noelle Olson for answering all of my questions. Many thanks to all of the Pomerantz lab members whether it be support in my research or the mental breaks doing puzzles and drinking hot cocoa.

I am so grateful for all my friends who have been my support system. Huda Zahid for all the adventures, Chun-Ju Tsou for all of the hobbies we attempted, and Prakriti Kalra for a shared appreciation of oatmeal chocolate chip bars. My cohort, who have become lifelong friends: Thank you to Jessica Fuller my other half in grad school, Nicole Bentz for the constant support with a dose of chaos, Brandi McKnight for always telling it how it is. To Erika Suessmith, Jamie Pryhuber, and Colette Manley who got me through college. To Soniya Coutinho for the movie nights and baking. To Brian Khong for starch madness, Survivor nights, and unconditional support.

Most importantly to my family, especially, my parents, Susan and Joe Buchholz, who have always been there for me and supported my love of learning and science. Thank you!

Abstract

Epigenetics is the study of mechanisms that result in differential gene expression without changes to the underlying DNA. In cancer, there is a dysregulation in gene expression, which can be driven by epigenetic proteins. One such protein implicated in numerous cancers is BPTF (bromodomain and PHD finger-containing transcription factor), an epigenetic protein whose main function is the recognition of post-translationally modified histones within chromatin and is the largest subunit of the nucleosome remodeling factor complex. BPTF binds chromatin via interactions with acetylated histone H4, (H4K16ac), through a structural motif called a bromodomain and trimethylated histone H3, (H3K4me$_3$), via its C-terminal PHD finger to facilitate chromatin remodeling. BPTF's oncogenic function is in part associated with increased chromatin accessibility and a direct protein-protein interaction with the oncoprotein c-MYC. Together, this makes BPTF a promising anti-cancer drug target. Therefore, the design of chemical probes for both reader domains (bromodomain and PHD finger) would be advantageous to better understand disease function.

The first part of this thesis will detail structure-based design of BPTF bromodomain inhibitors. In Chapter 2, I describe the development of **BZ1**, the most potent reported BPTF bromodomain inhibitor (K_d = 6.3 nM) at the time. Design was aided by SAR around a pyridazinone scaffold and co-crystal structures, where we identified an acidic triad as a targetable feature for potency and selectivity gains in future inhibitor development. We were able to show that these tool compounds synergistically sensitized chemotherapeutics in a triple negative breast cancer cell line via on-target activity. While **BZ1** has >350-fold selectivity over BET bromodomains, top-off targets included the bromodomains of BRD9 and CECR2. In Chapter 3, I describe efforts targeting a structured water in the BPTF binding site to improve selectivity. I

optimized competitive assays for rapid off-target quantification, that led to second generation inhibitor, **BZ2**, which has improved selectivity over BRD9 and CECR2. Furthermore, we began to use the BZ scaffold to identify cell lines sensitive to BPTF inhibition and develop heterobifunctional molecules.

The second part of this thesis will describe a screening effort that led to the discovery of the first reported chemical matter for the BPTF PHD finger. In Chapter 4, I describe a fragment-based screen using ^{1}H CPMG NMR, which had a 5.7% hit rate against BPTF PHD. Eight hits were validated in a secondary direct binding assay, and further identified to compete with the histone peptide. Two scaffolds, pyrrolidine- and pyridazine-containing fragments respectively, were prioritized by SAR by catalog. Molecular docking and HSQC NMR began to elucidate binding interactions. In Chapter 5, I continued developing assays to investigate ligand-protein binding interactions, as well as preliminary selectivity tests against a related PHD finger, KDM5A PHD3. Additionally, SAR around one of the hit scaffolds revealed potential directions for future inhibitor design. In the future, these approaches will allow for understanding of the PHD fingers biological role in disease, as well as dual domain inhibition.

Finally, Appendices A-B describe support to collaborative projects in a structural biology capacity. For our BRD4 project, another bromodomain we study in the Pomerantz lab, I solved a co-ligand crystal structure to aid in BRD4 inhibitor design (PDB: 7MLS). For an alpha synuclein project in the Sachs lab that was investigating the effects of pH in ^{1}H,^{15}N-HSQC NMR spectroscopy, I assigned resonances and generated chemical shift plots to determine what resonances were significantly perturbed by pH.

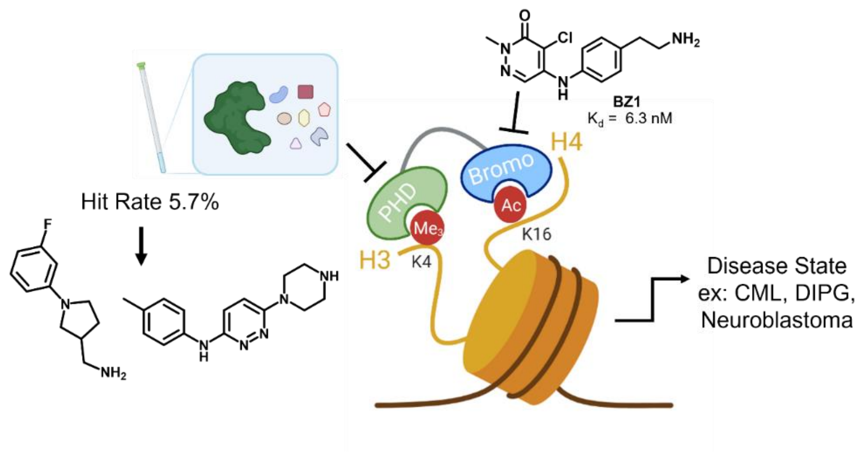
Hit Rate 5.7%
F
N
NH$_2$
N
H
N
N
N
NH
O
N
N
Cl
N
H
NH$_2$
BZ1
K$_d$ = 6.3 nM
PHD
Me$_3$
Bromo
Ac
H3
K4
H4
K16
Disease State
ex: CML, DIPG,
Neuroblastoma

Table of Contents

Contents

List of Tables

List of Figures

List of Schemes

List of Abbreviations

5FW	5-Fluorotryptophan
3FY	3-Fluorotyrosine
4PL	4-Paramter Logistic
aSyn	α-synuclein
ADME	Absorption Distribution Metabolism and Excretion
AlphaScreen	Amplified Luminescence Proximity Homogenous Assay
AML	Acute Myeloid Leukemia
AQ	Acquisition Time
BAZ2A/B	Bromodomain Adjacent to Zinc Finger Domain 2A/2B
BET	Bromodomain and Extra Terminal Domain
Boc	*tert*-butyloxycarbonyl
BPTF	Bromodomain and Plant Homeodomain (PHD) Transcription Factor
BRD	Bromodomain
BRD4	Bromodomain-containing protein 4
BRD7	Bromodomain-containing protein 7
BRD9	Bromodomain-containing protein 9
BSA	Bovine Serum Albumin
BURBOP	Broadband Universal Rotation by Optimized Pulses
CA	Carbonic Anhydrase 1
CECR2	Cat Eye Syndrome Critical Region protein 2
CHAPS	3-[(3-cholamidopropyl)dimethylammonio]-1-propanesulfonate
CML	Chronic Myeloid Leukemia

COSY	Correlated Spectroscopy
CPMG	Carr Purcell Meiboom Gill
CS	Consensus Site
CSA	Chemical Shift Anisotropy
CSAR	Chemical Shift Anisotropy Ranking
CSP	Chemical Shift Perturbation
c-MYC	Avian myelocytomatosis virus oncogene cellular homolog
DCM	Dichloromethane
DDT	DNA-binding Homeobox and Different Transcription Factors
DIEA	*N*,*N*-Diisopropylethylamine
DMF	*N*,*N*-Dimethylformamide
DMSO	Dimethyl sulfoxide
DNA	Deoxyribonucleic acid
DSF	Differential Scanning Fluorimetry
DTT	Dithiothreitol
EC_{50}	Half Maximal Effective Concentration
E. coli	*Escherichia coli*
EDG	Electron Donating Group
EDTA	Ethylenediaminetetraacetic acid
ESI-MS	Electrospray Ionization-Mass Spectrometry
ESI-TOF	Electrospray Ionization-Mass Time of Flight
EWG	Electron Withdrawing Group
FALZ	Fetal Alzheimer Antigen

FAXS	Fluorine direct binding CSA and Exchange for Screening
FBDD	Fragment-Based Drug Discovery
FBS	Fetal Bovine Serum
FDA	Food and Drug Administration
Fmoc	9-Fluorenylmethyloxycarbonyl
FPLC	Fast Protein Liquid Chromatography
FRAP	Fluorescence Recovery After Photobleaching
GCN5	General Control Nonderepressible 5
HATs	Histone Acetyltransferases
HDACs	Histone Deacetylases
HEPES	4-(2-hydroxyethyl)-1-piperazineethanesulfonic acid
HOX	Homeobox Genes
HRMS	High Resolution Mass Spectrometry
HSQC	Heteronuclear Single Quantum Coherence
IC50	Half Maximal Inhibitory Concentration
ILOE	Interligand Nuclear Overhauser Effect
ING2	Inhibitor of Growth Family Member 2
IP	Immunoprecipitation
IR	Imatinib Resistant
ISWI	Imitation Switch/Sucrose Non-Fermentable
ITC	Isothermal Titration Calorimetry
Kac	Acetyl Lysine
KAT2B	Lysine Acetyltransferase 2B

K_d	Dissociation Constant
KD	Knockdown
KDM5A	Lysine (K)-Specific Demethylase 5A (JARID1A)
K_i	Inhibition Constant
Kme	Methyl Lysine
KO	Knockout
LB	Luria Broth
LC-MS	Liquid Chromatography-Mass Spectrometry
LE	Ligand Efficiency
LEF	Local Environment of Fluorine
MALDI	Matrix-Assisted Laser Desorption Ionization
MD	Molecular Dynamics
MTS	3-(4,5-dimethylthiazol-2-yl)-5-(3-carboxymethoxyphenyl)-2-(4-sulfophenyl)-2H-tetrazolium
NADP/H	Nicotinamide Adenine Dinucleotide Phosphate
NCI60	NCI-60 Human Tumor Cell Lines Screen
n-FABS	*n*-Fluorine Atoms for Biochemical Screening
NIH	National Institute of Health
NMR	Nuclear Magnetic Resonance
NOE	Nuclear Overhauser Effect
NOESY	Nuclear Overhauser Effect Spectroscopy
NS	Number of Scans
NURF	Nucleosome Remodeling Factor

NUP98	Nucleoporin 98
PAINS	Pan-Assay Interference Compounds
PCAF	p300/CBP-Associated Factor
PDB	Protein Data Bank
PEG	Polyethylene Glycol
PHD	Plant Homeodomain
PHF23	PHD Finger Protein 23a
PMSF	Phenylmethylsulfonyl fluoride
PRE	Paramagnetic Relaxation Enhancement
PrOF NMR	Protein-Observed Fluorine NMR
PTMs	Post-translational modifications
RbAP46/48	Retinoblastomabinding protein p46/48
RNA	Ribonucleic acid
RP-HPLC	Reversed-Phase High Performance Liquid Chromatography
rt	room temperature
RT-qPCR	Reverse Transcription Quantitative Real-Time PCR
SAR	Structure-Activity Relationship
SDM	Site Directed Mutagenesis
SDS-PAGE	sodium dodecyl sulfate–polyacrylamide gel electrophoresis
SGC	Structural Genomics Consortium
shRNA	Short Hairpin RNA
SNF2L	Transcription regulatory protein SNF2
SPR	Surface Plasmon Resonance

SWI/SNF	SWItch/Sucrose Non-Fermentable
SynTF	Synthetic Transcription Factor
TFA	Trifluoroacetic acid
TKI	Tyrosine Kinase Inhibitors
TIPS	Triisopropylsilane
TR-FRET	Time-Resolved Fluorescence Energy Transfer
TROSY	Transverse Relaxation-Optimized Spectroscopy
Tris	Tris(hydroxymethyl)aminomethane
UV-Vis	Ultraviolet-Visible Spectroscopy
VDW	van der Waals
WPF	Tryptophan Proline Phenylalanine
WT	Wild type

1) Introduction

Part of this introduction (Section 1.6) is reproduced from ref[1]: Buchholz, C.R.; Pomerantz, W.C.K. ^{19}F NMR viewed through two different lenses: ligand-observed and protein-observed ^{19}F NMR applications for fragment-based drug discovery. *RSC Chem. Bio.* **2021**, *2*, 1312–1330.

1.1 Epigenetics and Transcriptional Regulation

Changes in phenotype without changes to genotype are governed by epigenetic processes. These changes occur through heritable but reversible modifications to DNA and chromatin. DNA can be methylated, and chromatin can be modified on histones, which are the proteins that DNA is wrapped around to form nucleosomes and further packaged into chromatin.[2] These modifications lead to differential activation and repression of genes ultimately affecting cellular differentiation in healthy cells.[3] However, alterations in these modifications can lead to disease (**Figure 1.1**).[4,5]

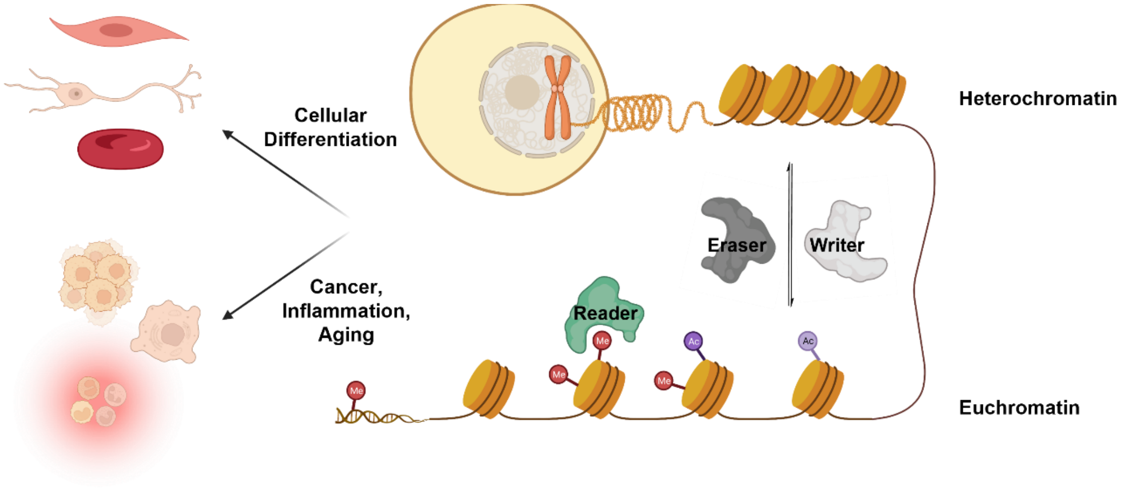

Figure 1.1: Epigenetic Proteins Role in Transcriptional Regulation

The histone code is the pattern of histone tail modifications and the epigenetic effector proteins that interact with them which dictates modulation of gene expression, or transcriptional regulation. These patterns govern the equilibrium between the state of euchromatin, which is open or transcriptionally active chromatin, and heterochromatin, which is closed or transcriptionally silenced.[6] The epigenetic proteins involved in these processes belong to three classes: writer proteins, which enzymatically add post-translational modifications (PTMs) to histone tails, eraser proteins which enzymatically remove histone PTMs, and reader proteins which recognize histone PTMs and can recruit other transcription factors (**Figure 1.1**).[7] Chemical epigenetics explores the chemical mechanisms involved in epigenetics and targets epigenetic effector proteins for the treatment of disease.[8]

1.2 BPTF: Emerging Role in Disease

Bromodomain PHD Finger Transcription Factor (BPTF) is an epigenetic protein whose main function is the recognition of post-translationally modified histones within chromatin and is the largest subunit of the nucleosome remodeling factor complex (NURF). In addition to BPTF the NURF complex is composed of SNF2L, an ISWI ATPase remodeler, and RBAp46/48, WD-40 repeat histone mediators.[9,10] Upon recruitment to histones, NURF can mediate sliding of nucleosomes and alter DNA accessibility, leading to the regulation of hundreds of genes (**Figure 1.2A**).[11,12] BPTF itself has been shown to regulate cell proliferation and Smad transcription factor signaling pathways in early tissue development of mice.[13]

BPTF binds chromatin via interactions with acetylated histone H4, (H4K16ac), through an epigenetic reader domain called a bromodomain and methylated histone H3, (H3K4me2/3), via its C-terminal PHD finger to facilitate chromatin remodeling (**Figure 1.2A**).[14,15] It has been demonstrated this is a multivalent recognition event, the PHD finger binding to H3K4me2/3 helps gives the bromodomain selectivity for H4K16ac over other acetylated lysines. Additionally, these two PTMs are known to reside within the same nucleosome in humans.[15] In the nucleosome context, PTM crosstalk further regulates if these particular PTMs are accessible to BPTF.[16,17] In addition to the reader domains, full length BPTF contains a N-terminal PHD finger of unknown function, a DDT DNA-binding homeobox, and a glutamine rich acidic region (PolyQ) (**Figure 1.2B**).[18]

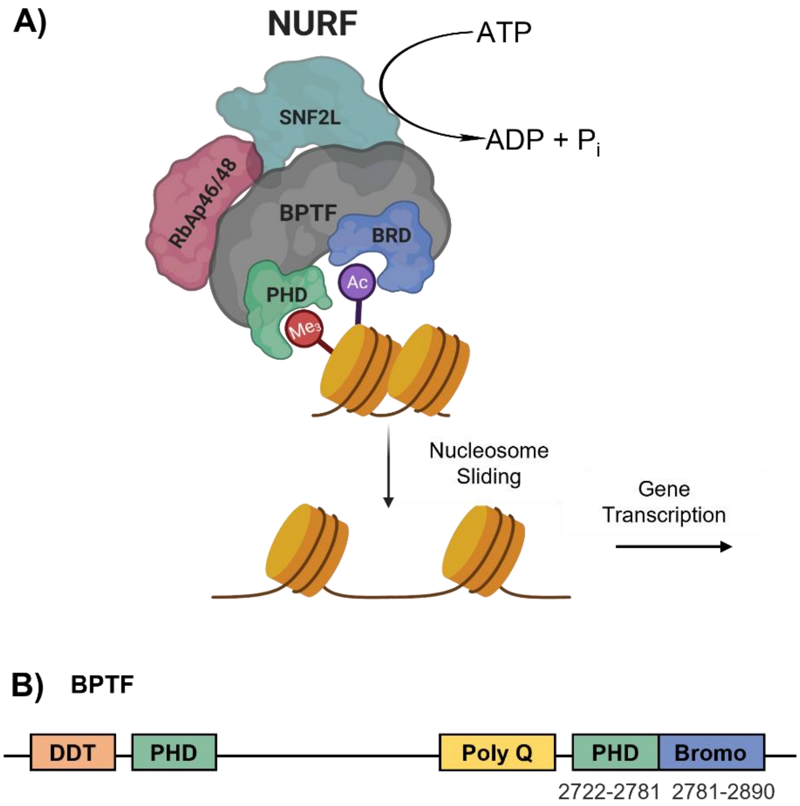

Figure 1.2: NURF Complex and BPTF Role in Biology

A) NURF complex, depicting BPTF bound to PTMs by the bromodomain (BRD) and PHD finger, and chromosomal sliding. B) Domain diagram of full length BPTF.

BPTF became a protein of interest in the cancer research field after a translocation in the *BPTF* gene, located on chromosome 17q, was associated with pre-malignant phenotypes and frequently amplified in neuroblastoma.[19] Since then BPTF has been implicated in glioma,[20,21] melanoma,[22] breast cancer,[23] non-small-cell lung cancer,[24] colorectal cancer,[25] bladder cancer,[26] hepatocellular carcinomas,[27,28] and renal carcinoma.[29] Additionally, BPTF's oncogenic function has been shown to be in part associated with increased chromatin accessibility, aberrant gene regulation, and a direct protein-protein interaction with the oncoprotein c-MYC.[23,30–32] Together, this makes BPTF a promising anti-cancer drug target.

1.3 Epigenetic Reader Domains: Bromodomains

Bromodomains are a class of epigenetic reader proteins that recognize N-acetylated lysines on histone tails, and were first identified as transcriptional activators in 1992 from the *brahma* gene in *Drosophila*.[33] There are 61 bromodomains found in 46 proteins that are structurally organized into eight families.[34] The BPTF bromodomain is a part of the Family I bromodomains (**Figure 1.3A**).

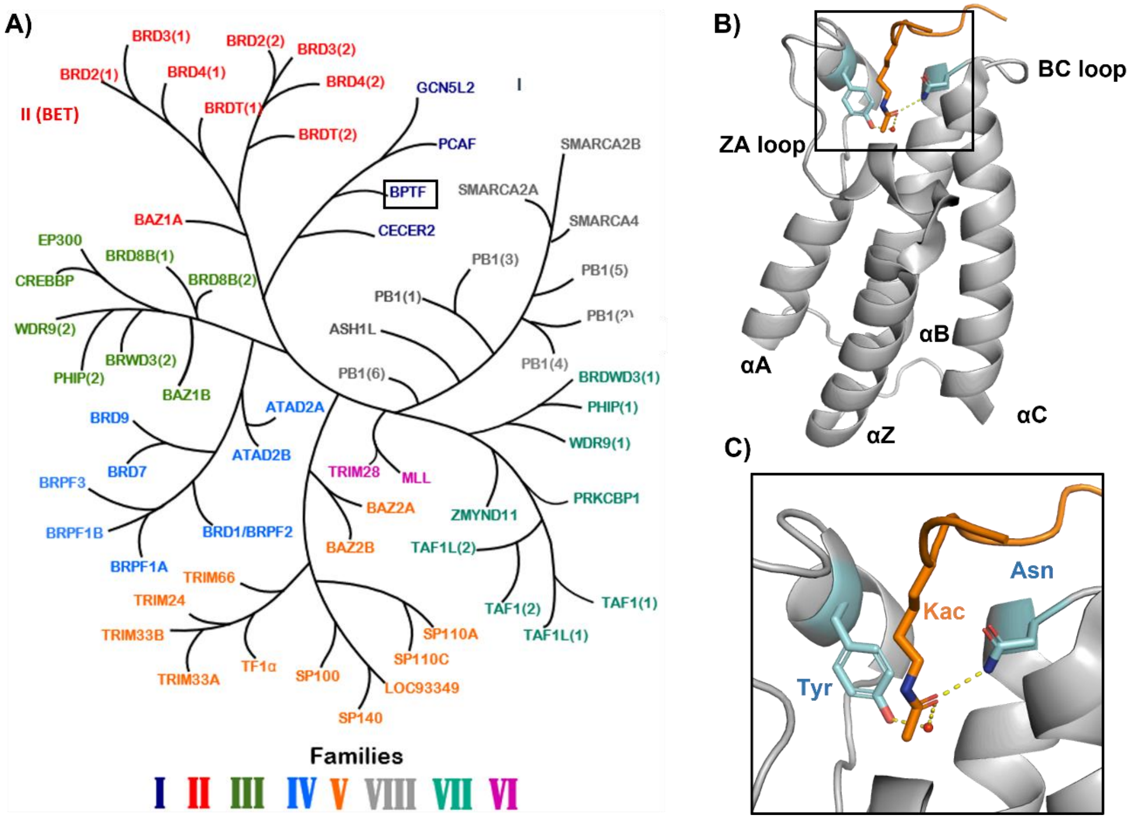

Figure 1.3: Bromodomain Families and Structure

A) Phylogenetic tree of the human bromodomain family. (Figure adapted with permission from ref. 35 Copyright 2019 Springer Nature). B,C) BPTF bromodomain (grey) bound to H4K16ac (orange) showing key hydrogen bond interactions with Asn and Tyr (blue) and conserved water (red sphere, PDB: 3QZS).

Bromodomains are typically ~110 residues and are composed of four α-helical bundles (αA, αB, αC, and αZ) and 2 structural loops (ZA and BC).[36] The first co-crystal structures showed the acetylated lysine binding site to be a hydrophobic pocket between the ZA and BC loops (**Figure 1.3B**).[37,38] Within the binding pocket, an asparagine residue makes key hydrogen bonding interactions through its amide nitrogen with the carbonyl of the acetylated lysine, as well as a water-mediated tyrosine bond to the same carbonyl (**Figure 1.3C**). The asparagine residue is highly conserved across bromodomains and a key recognition element for acetylated histone tails. Additionally, five structural waters are conserved across bromodomains, which are important when considering the druggability and inhibitor development for each respective bromodomain.[35,39] The BPTF bromodomain co-crystallized with H4K16ac has these canonical interactions in form I (**Figure 1.3B,C**), and in this binding mode can make bivalent interactions where the PHD finger binds simultaneously to H3K4me3.[15]

1.3.1 Bromodomains Implicated in Disease

In diseases states, such as cancer, inflammation, and viral replication, bromodomain-containing proteins have been identified as having aberrant function.[40] BET (bromodomain and extra terminal), or Family II bromodomains for example, which are essential for transcriptional regulation in healthy cells, are implicated in the pathogenesis of NUT midline carcinoma and play a central role in acute myeloid leukemia (AML).[41]

The growing interest in bromodomains role in disease led to the first bromodomain inhibitor, NP1, which targeted PCAF. NP1 was discovered through a $^{1}H,^{15}N$ HSQC NMR screen (IC_{50} = 1.37 μM), and further optimized analogs were used to show anti-HIV activity in cells.[42,43] The major breakthrough in the field came with the reports in 2010 for the first submicromolar bromodomain inhibitors, which targeted BET bromodomains. I-BET (now IBET762), which has a K_d of 50-60 nM for BET bromodomains, became the first bromodomain inhibitor to enter clinical trials, where it was used for NUT-midline carcinoma treatment.[35,44] Additionally, it was shown to downregulate inflammatory genes.[44] (+)-JQ1, which has a K_d of 20-190 nM for BET bromodomains, was used a tool compound to show reduction of c-Myc transcription in AML, and later entered clinical trials for treating solid tumors.[45] Since then, over half of all bromodomains have reported inhibitors and BET inhibitors continue to be used in clinical trials.

1.3.2 BPTF Bromodomain Inhibitor Development

The role of BPTF in disease and the success of previous bromodomain inhibitors demonstrates the importance of developing BPTF bromodomain inhibitors (**Figure 1.4**). The first reported selective inhibitor for the BPTF bromodomain was AU1 (K_d = 2.8 µM), which came out of a PrOF NMR screen conducted by Urick et al.[46] AU1 was used as a tool compound in preliminary studies, where AU1 treatment in Eph4 cells decreased cellular proliferation and c-Myc DNA occupancy.[23] In follow up SAR studies, the *S*-enantiomer was determined to be active but there were no significant increases in potency or selectivity. In addition low ligand efficiency, off-target kinase activity and stability issues limited further studies.[47]

Since then, progress in the BPTF inhibitor development field has led to nanomolar inhibitors. Commercial probes TP-238 (K_d = 120 nM),[48] a CECR2/BPTF chemical probe reported by Takeda and the Structural Genomics Consortium (SGC), and NVS-BPTF-1 (K_d = 71 nM),[49] a BPTF chemical probe reported by Novartis and the SGC, have low nanomolar K_ds for BPTF. However, TP-238 is 12-fold more selective for CECR2 and NVS-BPTF-1 has comparable affinity for similar bromodomains as well as solubility and ADME issues that prevent *in vivo* applications. DC-Bpi-11, which was designed by TP-238 deconstruction, was also reported as a potent BPTF bromodomain inhibitor (K_d = 21 nM) but lacked selectivity data for relevant bromodomains.[50] A follow up report reported the DC scaffold as potent CECR2 inhibitors, and reported DC-Bpi-11 as 8-fold selective for CECR2 over BPTF.[51] Additionally, low micromolar inhibitors, 5 (IC_{50} = 36 µM),[52,53] a tetrahydroquinoline scaffold, and GSK4027 (K_d = 1.7 µM),[54] a pyridazinone scaffold were reported in literature. No further work has been reported exploring tetrahydroquinolines, but GSK4027 has been used to design low nanomolar inhibitors for BPTF bromodomains using the first small-molecule BPTF crystal structures.[52]

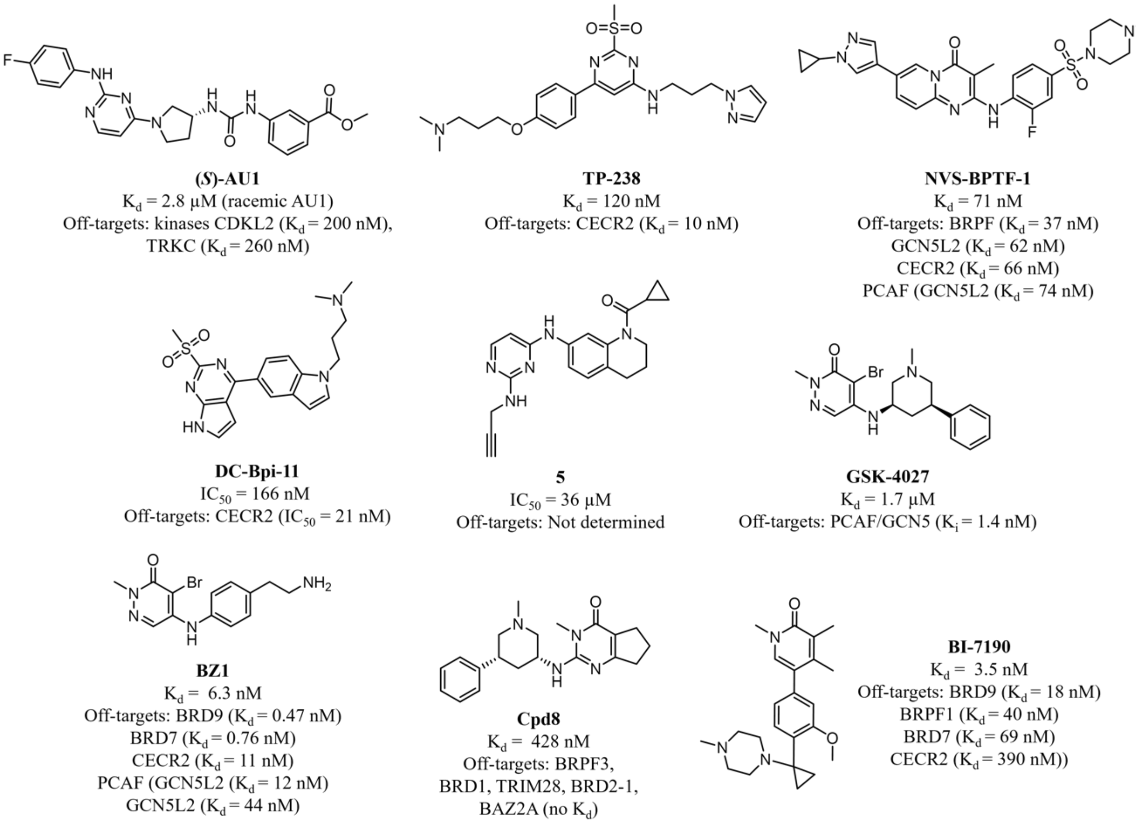

Figure 1.4: Reported BPTF Bromodomain Inhibitors with *In Vitro* Affinity and Off-Targets

BZ1, optimized by structure-based design from the pyridazinone core of GSK4027, is the second most potent reported BPTF inhibitor (K_d = 6.3 nM).[55] Even with off-target binding observed for BRD9/BRD7 and other Family I bromodomains, the design rules established by SAR have allowed for more selective inhibitors (Chapters 2,3). Around the same time a DSF screen against BPTF identified a compound, Cpd1, which had the same phenyl piperidine core as GSK4027. Subsequent optimization around this core resulted in the BPTF inhibitor Cpd8 (K_d = 428 nM).[56]

Most recently, the most potent BPTF inhibitor BI-7190 (K_d = 3.5 nM) was reported.[57] The BI probes were originally designed for BRD9, but some analogs were found to have greater off-target activity for BPTF. Lead compound BI-7190's selectivity for BPTF over BRD9/7 and CECR2 was attributed to conformational rigidity and complementary electrostatic interactions. While *in vitro* studies confirmed potency and selectivity for BPTF, BI-7190 had minimal effects in cell toxicity and modulating transcription in the studied cancer cell lines.[57] Overall, reported BPTF bromodomain inhibitors have been optimized to be potent and selective chemical probes, but it still remains to be determined if bromodomain inhibition alone is sufficient for inhibition of BPTF function in cells.

1.4 Epigenetic Reader Domains: PHD Fingers

PHD fingers are one of many classes of methyl-lysine readers that recognize methylation marks with high sequence specificity. The first PHD finger was identified in 1993 in the protein HAT3.1 as a novel metal binding homeodomain that interacted with DNA in *Arabidopsis*, thus the name Plant Homeo Domain (PHD) finger.[58] Since then over 291 PHD fingers have been identified in humans, making them one of the largest class of epigenetic reader proteins.[59] While most methyl-lysine readers recognize PTMs through an aromatic cage, PHD fingers specifically have a conserved zinc binding motif and are 50-80 residues long with two anti-parallel β-sheets.[60] Their biological role was identified in 2006 when the PHD fingers of BPTF and ING2 were found to recognize trimethylation at lysine 4 on histone 3 (H3K4me3). Wysocka et al. wanted to identify proteins that bound to H3K4me3 and pulled out the PHD finger of BPTF from HEK293 cell lysates. They further showed BPTF is essential for *HOX* gene expression.[14] Around the same time the Gozani lab was investigating what the PHD finger of ING2 bound to, and through pulldown identified histone H3. Additionally, they found that its specific interaction with H3K4me3 modulated gene repression in response to DNA damage.[61] In general the interactions between PHD fingers and histone H3 modulate essential biological functions, including nucleosome remodeling and gene regulation.[62]

Ligand recognition depends on which methylation state each individual PHD finger recognizes. PHD fingers that recognize H3K4me3 use van der Walls and cation-π interactions in an aromatic cage to stabilize the trimethyl ammonium group. The aromatic cage is made up of two to four aromatic and hydrophobic residues, with a conserved tryptophan. In some cases, the PHD finger has a R2 pocket adjacent to the aromatic cage, separated by the conserved tryptophan. This pocket forms salt bridges or hydrogen bonds through Asp, Glu, or Gln to the guanidium group of H3R2. On the other hand, PHD fingers that recognize H3K4me0 have acidic and hydrophobic residues that form hydrogen bonds and electrostatic interactions with the lysine amine. In both cases, the histone tail adopts an anti-parallel β-strand to interact with the β-sheets in the PHD finger.[60] Overall PHD fingers are known to have high specificity for each respective histone H3 PTM.

The BPTF PHD finger recognizes H3K4me3 marks (K_d = 2.7 μM) with high specificity. The molecular basis for this read-out relies on its aromatic cage, R2 pocket, and histone backbone interactions (**Figure 1.5**). The first six histone H3 residues (ARTKme3QT) form an antiparallel β-sheet with K21-D27 in BPTF, where three direct hydrogen bonds to the histone backbone are made. Additionally, the amino terminus of histone H3 is anchored through direct hydrogen bonds with the backbone carbonyls of I48 and D49 in BPTF. The aromatic cage of BPTF is made up of three tyrosines (Y10, Y17, and Y23) and tryptophan (W32), which form canonical van der Walls and cation-π interactions with K4me3 (**Figure 1.5C**). W32 is situated in between the aromatic cage and the R2 surface channel, which gives selectivity for K4 over K9 and K27. The R2 pocket is made of G25 which makes direct and water-mediated hydrogen bonds with the guanidium group and D27 which makes electrostatic interactions.[63] In the context of full-length BPTF, the PHD finger is connected to the bromodomain by an alpha helical linker.[15]

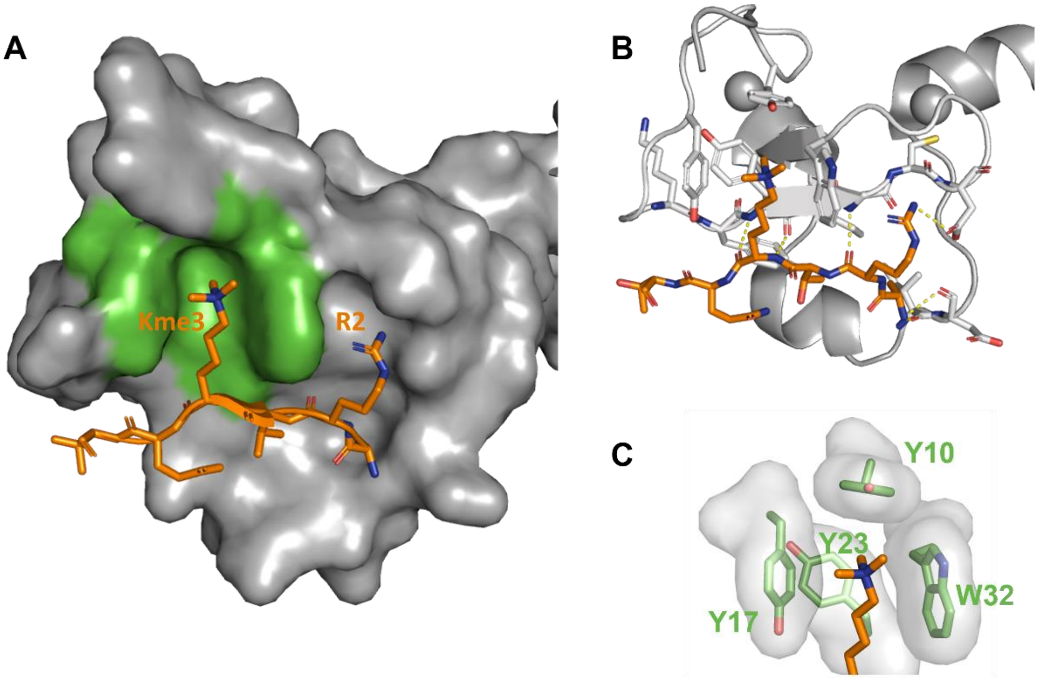

Figure 1.5: Structure of BPTF PHD Bound to H3K4me3.

A) Crystal structure of BPTF PHD (gray surface) bound to H3K4me3 (orange), with aromatic cage highlighted in green. B) Hydrogen bonds between BPTF PHD (gray) and histone H3 (orange). C) Aromatic cage of BPTF PHD. PDB: 2F6J.

1.4.1 PHD Fingers Implicated in Disease

Mutations and translocations to *PHD* genes can lead to disease state. For example, the PHD fingers of RAG2 and AIRE have been implicated in immunodeficiency, those of NSD1, ATRX, CBP, and PHF6 are implicated in neurological disorders, and the PHD fingers of ING1, KDM5A, PHF23, BPTF, Pygo, NSD1/3, NSD2, MML, and PFH1 are all implicated in cancer.[64] A specific example of histone methylation misinterpreted during oncogenesis is in AML. Translocation of nucleoporin-98 (NUP98) is a common chromosomal abnormality in AML, and three of its identified fusion partners are PHD-finger containing proteins (KDM5A, PHF23, BPTF)[65–68]. Mechanistically, it has been shown that the PHD finger is critical in driving leukemogenesis in these fusions. Furthermore, blocking the interactions with histone H3 by both small molecule inhibition and systematic mutations results in cell death.[69] These implications highlight a potential role for PHD finger inhibitors in regulating disease.

1.4.2 Current Chemical Probes for PHD Fingers

Targeting PHD fingers in disease has been highly sought, however they are considered difficult targets due to their shallow binding pockets.[70] Currently only three published studies have targeted PHD fingers with small molecules. (**Figure 1.6**). The PHD3 of KDM5A (also referred to as JARID1A), which recognizes H3K4me3, was screened against using the NIH Clinical Collection and a HaloTag assay platform. Four FDA drugs (amiodarone, disulfiram, phenothiazine, and tegaserod) were identified. Disulfiram was found to be eject the structural zinc ions from the PHD finger, and therefore is probably a non-specific covalent inhibitor. Amiodarone's metabolites (di-*N*-desethylamiodarone) and synthesized analogs (WAG-003 and WAG-005) were tested and found to be more potent than the parent drug. The scaffold was predicted to bind in the R2 pocket, but little supporting evidence was obtained.[71] A follow-up study further optimized amiodarone into compound 1a, but of moderate affinity (IC_{50} = 166 μM) and promiscuous binding.[72] Even with these limitations, Amiodarone, in addition to Disulfiram, have been used to inhibit histone 3 interactions in NUP98 fusions with the PHF32 PHD finger with modest and robust cell growth inhibition respectively. Additionally, Disulfiram was shown to interact with KDM5A and BPTF PHD fingers *in vitro*.[69] The PHD finger of Pygo, which recognizes H3K4me3, was screened against using the Maybridge fragment library and an NMR-based assay platform. Aminobenzothiazole containing fragments were identified to bind to a distal site, adjacent to a PPI site with the protein BCL9. Additionally, benzimidazole containing fragments (CF16 and CF18) were identified to bind in the aromatic cage by HSQC NMR (K_d = 7.3 and 14.7 mM respectively) and CF16 competed off the native histone H3 tail.[73] Most recently, the PHD fingers of BAZ2A and BAZ2B, which recognize H3K4me0, were targeted by *in silico* analysis, followed by biophysical validation. One of the hits, Fr19, was co-crystallized with BAZ2A PHD, in the first example of a PHD finger crystallized with a fragment. From this structural data, two optimized fragments (Fr21, Fr23) were designed and Fr23 displaced off the native histone H3 tail with an IC_{50} of 100 μM for BAZ2A and 200 μM for BAZ2B.[74] The chemical matter described here are all starting points for PHD finger inhibitor development, and require future design and optimization to develop chemical probes.

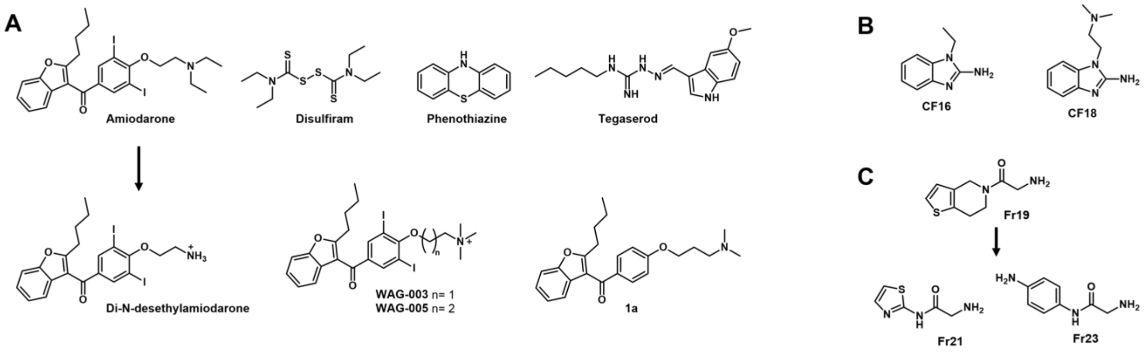

Figure 1.6: Existing Small Molecule Chemical Matter for PHD Fingers.
Small molecule inhibitors for A) KDM5A PHD3, B) Pygo PHD, and C) BAZ2A and BAZ2B PHD.

Beyond small molecule inhibition, other approaches include cyclic peptides and macrocyclic compounds have been used (**Figure 1.7**). Taking inspiration from peptidomimetic inhibitors designed for the related methyl-lysine readers, chromodomains, the Fujimori lab developed a covalent cyclic peptide that targets KDM5A PHD3. A truncated peptide scan identified ARTKme3QT as a starting point to cover a large surface area in the shallow binding pocket. Macrocyclization by tethering K4 and T6 allowed for structural rigidification that afforded enhanced cell permeability and proteolytic stability. Installing a lysine-reactive electrophilic warhead (phenylsulfonylfluoride) on Q5 could provide selectivity, as the targeted K1620 on KDM5A seems to be non-conserved across PHD fingers. Cyclicpeptides C-33, D-34, and D-35 bound to KDM5A PHD3 with a K_i of 500 nM, 510 nM, and 380 nM respectively, and labeled KDM5A within six hours of incubation. C-33 was used to show capture of KDM5A in HEK293T cells. These cyclopeptide will be valuable tools for future PHD finger inhibitor development. In a similar approach, another macrocycle, calixarenes were used to directly bind methylated histones and cage them to block PHD finger binding. The four phenol repeats in calix[4]arenes mimic the aromatic cage found in PHD fingers. Compounds 29-31 were selective for H3K4me3 over H3K9me3. Tested calix[4]arenes were active against a range of PHD fingers, including ING2, KDM5A, and MLL1 *in vitro*. Furthermore, 29 disrupted MLL localization at H3K4me3 rich regions *in vivo*.[75] These supramolecular cages could be used in the future as general tools for H3K4me3 inhibition. Overall, there is a general need for more PHD inhibitors.

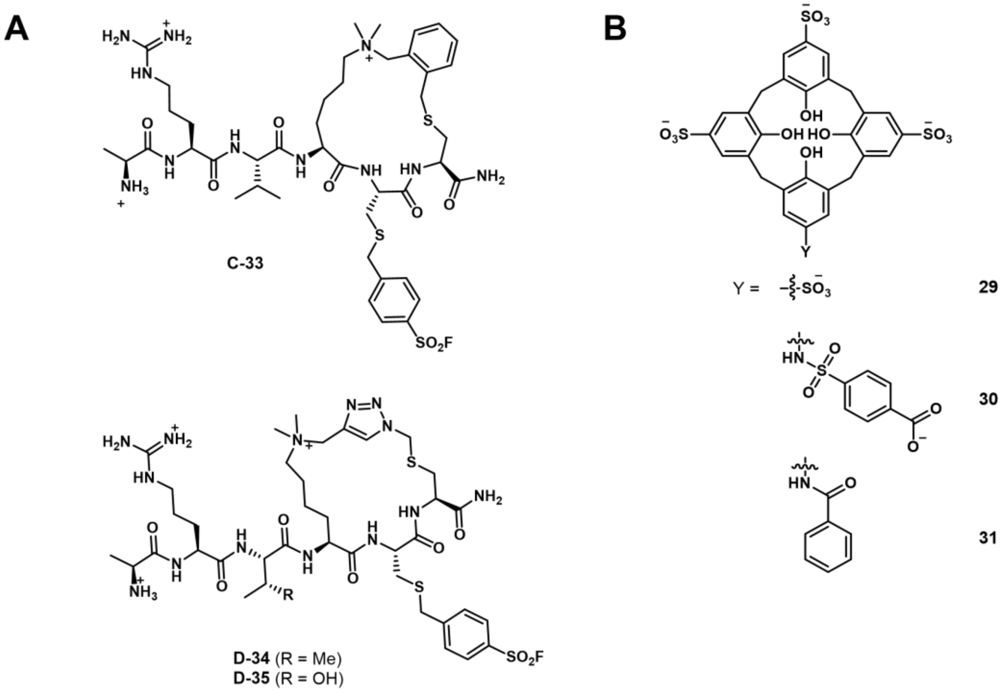

Figure 1.7: Macrocycles that Inhibit PHD Finger-H3K4me3 Interactions.

A) Covalent cyclic peptides that target KDM5A PHD3 and B) calix[4]arenes that target H3K4me3.

1.5 Biophysical Tools for Reader Domain Inhibitor Development

The discovery of chemical probes for epigenetic reader proteins has been aided by the application of biophysical tools. The following sections describes the application of NMR and AlphaScreen experiments in quantifying binding interactions and aiding structural biology.

1.5.1 Competitive Inhibition Technique: AlphaScreen

AlphaScreen is a competition-based assay which can be used in initial screening or quantification. The assay uses a bead-based platform to measure IC_{50}. A donor bead is coated in streptavidin and an appropriate biotinylated histone tail peptide is used to bind to the bead. An acceptor bead is coated in nickel (nickel nitrilotriacetic acid) which can associate with a His-tagged target protein. Upon complex formation between the reader domain and histone tail, the beads are brought in close proximity. After irradiation at 680 nm the donor bead produces singlet oxygen, which reacts with the acceptor bead and excites it to emit at 550 nm (**Figure 1.8**). This is a distance dependent effect, the short lifetime of singlet oxygen in solution limits the distance between beads to 200 nm for signal. If competitive inhibitor is added and disrupts the complex, there is a loss in signal as the beads are no longer in close proximity. Upon titration of ligand, an IC_{50} can be measured.[76]

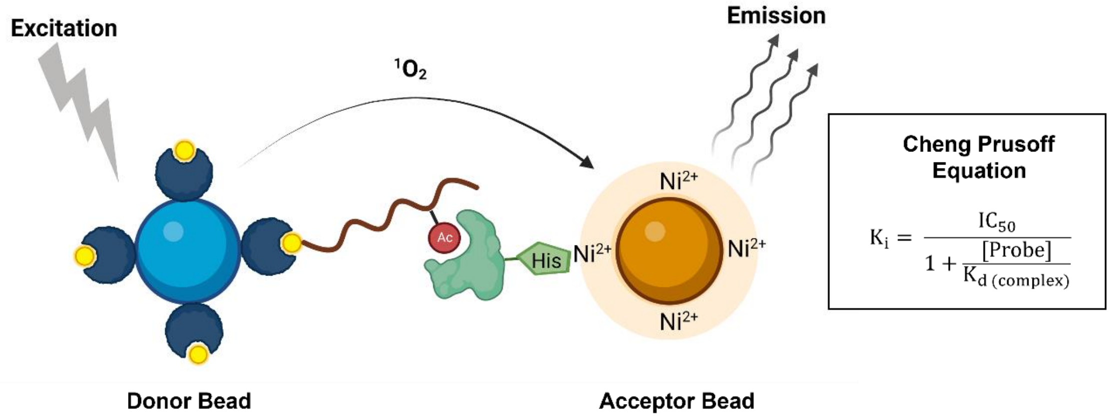

Figure 1.8: Complex Formation in AlphaScreen Assay.

The IC_{50} of small molecules can approximate the K_i due to the multivalent bead platform. The beads used are multivalent giving an avidity effect, where low nanomolar amount of biotinylated peptide probe and His-tagged protein can give sufficient signal. When [probe] is much lower than the K_d of the probe for the protein, which in this case the typical K_d of histone tail peptides for reader domains is in the micromolar range, the ratio in the Cheng Prusoff equation approaches zero.[35] Therefore, IC_{50} can approximate K_i (**Figure 1.8**).

When setting up an AlphaScreen assay for a target protein, the protein and probe concentration must be carefully considered. In addition to balancing the Cheng Prusoff ([probe]<<complex K_d), there needs to be sufficient concentrations to get signal but not past the hook point where there is oversaturation of beads and signal decrease (**Figure 1.9**).[77] AlphaScreen has been developed for many bromodomains, as well as PHD fingers, for inhibitor development projects.

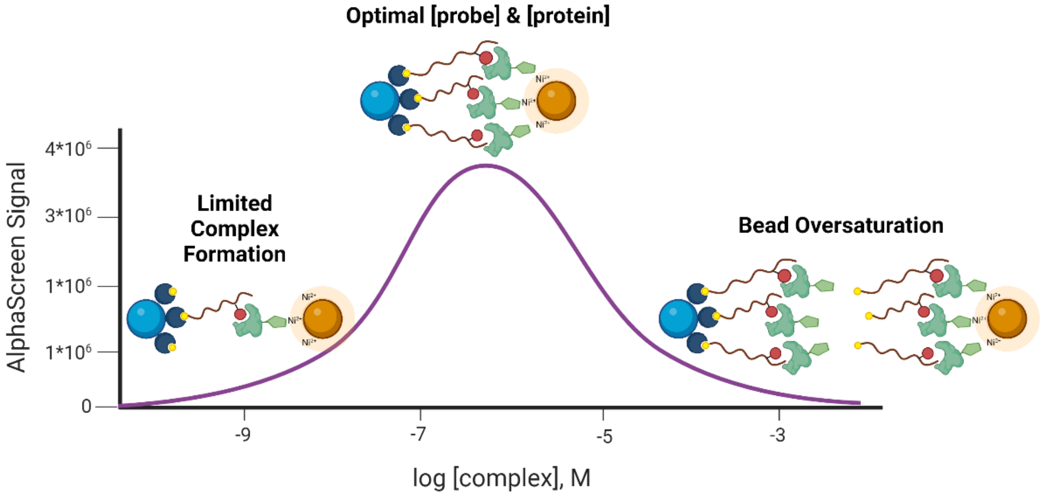

Figure 1.9: Hook Effect in AlphaScreen Assay.

1.5.2 NMR Techniques: HSQC NMR

NMR methods have been useful in the context of initial screening methods for chemical matter against target proteins, like epigenetic reader proteins. Additionally, they can be used to elucidate binding information. $^{1}H,^{15}N$ HSQC NMR is a 2D protein-observed NMR technique that can give structural binding information. A well dispersed spectrum of ^{15}N-labeled protein will have distinct resonances for each backbone secondary amide, as well as sidechain amines in Asn, Gln, Arg, and Trp. Upon addition of ligand, obtained spectra can be used to identify key residues involved in protein-ligand binding interactions if resonances are assigned. Even if resonances are not assigned, chemical shift perturbations (CSPs) upon titration of ligand can be used for K_d calculations.[78] In an example case study with the bromodomain of BRD4, significant CSPs upon titration of ligand can be seen (**Figure 1.10**).[79]

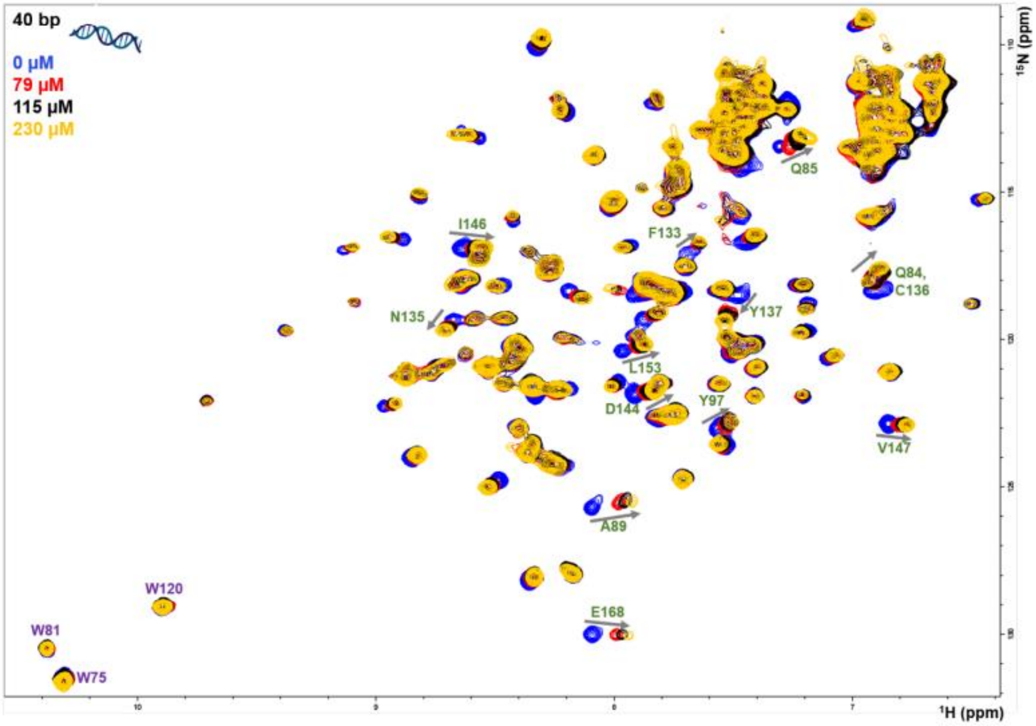

Figure 1.10: HQSC Spectra of BRD4 Bromodomain Upon Titration of Ligand. (from ref **79**)

Other NMR techniques, like ligand-observed CPMG NMR and protein-observed ^{19}F (PrOF) NMR experiments will be discussed in the following section in the context of FBDD.

1.6 ^{19}F NMR in Fragment-Based Drug Discovery

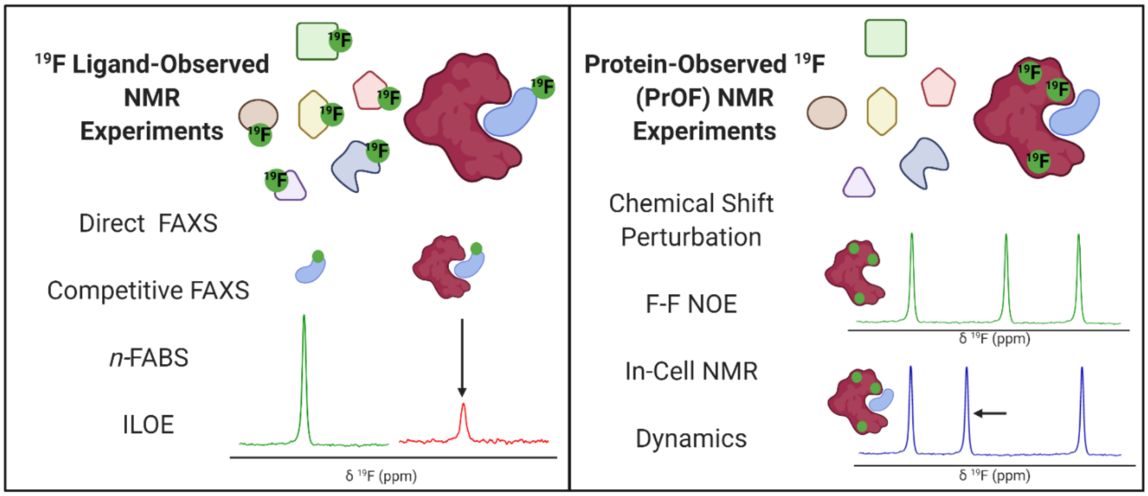

^{19}F NMR has emerged as a powerful tool in drug discovery, particularly in fragment-based screens. The favorable magnetic resonance properties of the fluorine-19 nucleus, the general absence of fluorine in biological settings, and its ready incorporation into both small molecules and biopolymers, has enabled multiple applications of ^{19}F NMR using labeled small molecules and proteins in biophysical, biochemical, and cellular experiments. This review will cover developments in ligand-observed and protein-observed ^{19}F NMR experiments tailored towards drug discovery with a focus on fragment screening. We also cover the key advances that have furthered the field in recent years, including quantitative, structural, and in-cell methodologies. Several case studies are described for each application to highlight areas for innovation and to further catalyze new NMR developments for using this versatile nucleus.

1.6.1 The Influence of Fluorine at the Chemistry and Biology Interface

Innovations in using organofluorine compounds at the chemistry and biology interface have continued to emerge over the last 80 years. Developments in biomedicine, including early work on anesthetics,[80] PET imaging,[81] magnetic resonance imaging,[82] nuclear magnetic resonance spectroscopy (NMR),[83] blood substitutes,[82] herbicides,[84] and FDA approved drugs,[84] support the broad utility of an atom that lacks sufficient endogenous levels in biological systems. With the highest electronegativity of all atoms, fluorine forms the strongest chemical bonds with carbon (e.g., 131 kcal/mol C-F bond dissociation energy for CF_4).[85] Given the significant bond strength from fluorination, and low susceptibility to oxidation, carbon-fluorine bonds impart metabolic stability to biomedicines. However, early evidence of significant toxicity with low molecular weight fluorinated anesthetics, demonstrated that organofluorine compounds were not as physiologically inert as previously thought.[80] We now know that in addition to providing a protective role for new medicines, organofluorine functional groups can engage in a variety of noncovalent interactions, including dipolar interactions and sometimes weak hydrogen bonds, as well as significantly altering the physicochemical properties of fluorinated molecules.[86–88]

In 2007 a comprehensive analysis by Müller et al. showed that ~20% of all pharmaceuticals contained at least one fluorine atom.[84] Although this statistic is often cited, this percentage has risen in recent years. While 29% in 2011,[89] percentages of fluorinated small molecule drugs increased to 47% in 2018,[90] 41% in 2019,[91] and 33% in 2020.[92‡] This rise can in part be attributed to both an increased knowledge of new strategies for using fluorine in biomedicine,[93] new biomedical applications for organofluorine molecules,[82] and a significant increase in synthetic methods for fluorination.[94]

Given that NMR has played a prominent role in the early stages of drug discovery, and the increased number of fluorinated small molecule drugs cited above, ^{19}F NMR has emerged as an important tool for drug development. ^{19}F NMR of small molecules (ligand-observed ^{19}F NMR) preceded target-based biomolecular ^{19}F NMR and as such is more developed.[83,95–97] However, NMR applications of fluorinated proteins (protein-observed ^{19}F NMR) is gaining increasing attention.[83,98–100] Here we provide an update on new applications in ligand-observed and protein-observed fluorine NMR in drug discovery, with a particular focus on the emerging applications in fragment-based drug discovery (FBDD).

1.6.2 A Brief Timeline for ^{19}F NMR Development

^{19}F is a spin ½ nucleus and a 100% abundant isotope with a gyromagnetic ratio close to ^{1}H NMR leading to an 83% similar signal sensitivity. Given these favorable magnetic resonance properties, ^{19}F NMR studies of fluorinated molecules have provided foundational knowledge of magnetic resonance properties since the early stages of NMR research. Dickinson in 1950, provided some of the first characterization of chemical shifts using solutions of inorganic and organofluorine compounds (**Figure 1.11**).[101] Using a series of fluorinated molecules, Gutkowsky and Hoffman also provided early analyses of magnetic nuclear shielding and coupling for deducing effects on charge distribution and molecular structure.[102] In the context of biomolecular ^{19}F NMR, fluorinated phenylalanine derivatives were first used to study protein-ligand interactions with chymotrypsin in 1967.[103]

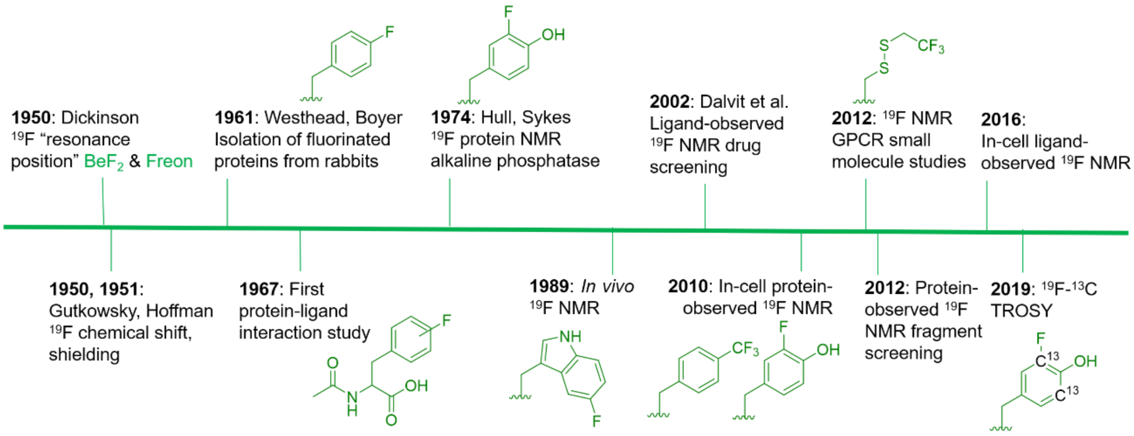

Figure 1.11: An abbreviated timeline of 19F NMR development with select examples. Fluorinated molecules shown in green. Side chains from left to right are: 4-fluorophenylalanine (4FF), 3-fluorotyrosine (3FY), 5-fluorotryptophan (5FW), trifluoromethyl-L-phenylalanine (tfmF), 3FY, 2,2,2-trifluoroethanethiol (TET), and 13C-labeled 3FY.

Access to fluorinated proteins for protein-observed ^{19}F NMR was facilitated by prior studies interested in the plasticity of the biosynthetic machinery for tolerating unnatural amino acids. Fluorinated phenylalanine and tyrosine were first studied for their effects on bacteria and demonstrated a growth inhibition effect,[104] which was overcome through sustained culturing.[105] Boyer and Westhead subsequently showed 4-fluorophenylalanine could be incorporated into proteins when fed to rabbits, and the isolated proteins retained enzymatic activity.[106] Ultimately, Hull and Sykes characterized the first fluorinated protein by ^{19}F NMR, 84 kDa alkaline phosphatase in 1974, which was produced in *E. coli* via metabolic labeling with 3-fluorotyrosine.[107]

The first applications for drug screening were pioneered by Dalvit and co-workers who have since developed a suite of techniques for screening fluorinated ligands against proteins.[108–110] The absence of fluorine in naturally occurring biomolecules, and the high sensitivity of the fluorine nucleus for detecting binding interactions, has led to significant interest in this approach over the last two decades in both academia and the pharmaceutical industry. The impact of this approach can be seen through the development of new pulse sequences, improved NMR probe designs, and commercial access to fluorinated small molecule libraries.

Protein-observed fluorine NMR while originally increasing the size of proteins that could be readily studied by biomolecular NMR, was largely limited to the study of protein folding and molecular recognition of native substrates.[111] Concerns over the significant chemical shift anisotropy (CSA) leading to significantly broader resonances than fluorinated small molecules was one potential limitation for applying this approach to small molecule screening.[109,112] Despite this concern, the first analysis of small molecule agonists and antagonists with the β-adrenergic receptor was reported by Wüthrich and co-workers in 2012.[113] The same year, the fluorinated KIX domain of coactivator CBP, was used in a preliminary demonstration of small molecule screening to discover inhibitors of protein-protein interactions.[114] The significant CSA challenge is beginning to be addressed through ^{19}F-^{13}C transverse relaxation-optimized spectroscopy (TROSY)-based NMR methods.[115] Improved cryo-probe designs for increasing both the size-range of fluorinated proteins, the sensitivity of the NMR experiment, and the lack of a biological background also offer exciting opportunities for in-cell NMR.[116,117]

To date, both ligand-observed and protein-observed ^{19}F NMR methods have become increasingly adopted in drug discovery applications with many opportunities for innovation. The next section will highlight some general principles to be considered for ^{19}F NMR followed by specific discussions of ^{19}F NMR in drug discovery.

1.6.3 Spectral Behavior of the ^{19}F Nucleus for ^{19}F NMR

One significant advantage of ^{19}F NMR over ^{1}H NMR methods when used for small molecule discovery is its hyperreponsiveness to changes in chemical environment. While the traditional range of chemical shifts for ^{1}H NMR spans ~ 14 ppm, the fluorine chemical shift range has been reported to be up to 800 ppm wide.[118] For fluorinated side chains found in proteins, this range approaches 170 ppm.[99] This range is comparable to the ~200 ppm range of chemical shifts for drug-like motifs.[119] In the context of different chemical environments being produced upon small molecule binding, Urick et al. found ^{19}F resonances from a fluorinated tryptophan to be ~6-20 times more responsive than ^{1}H resonances on the same amino acid.[120] Even solvent isotopes effects on the chemical shift from H_2O and D_2O can be observed for ^{19}F resonances, leading to chemical shift differences up to 0.25 ppm.[121] The solvent isotope experiment has been used as a sensitive method for characterizing solvent exposure of fluorinated protein side-chains.[122]

The chemical shift sensitivity difference between ^{19}F NMR over ^{1}H NMR can be attributed to differential contributions to the nuclear shielding parameters. The nuclear shielding parameter is composed of both diamagnetic and paramagnetic shielding contributions.

Diamagnetic shielding is based on ground state contributions of the electrons in the presence of an external field, whereas the paramagnetic term is based on coupling of ground and excited state orbitals and is thus dependent on their energy difference.[123] In the case of ^{1}H chemical shifts, diamagnetic shielding is typically the main contribution dominated by electrons in the 1s orbital. However for ^{19}F NMR, either term can dominate due to low lying orbitals from fluorine's lone pair electrons.

Despite the large chemical shift window for ^{19}F NMR, significant progress has been made in quantum chemical method developments for accurate prediction of fluorine chemical shifts. This is particularly relevant for fluorinated small molecules which can be calculated using relatively low level theoretical methods as these molecules possess fewer atoms and dynamic conformations than fluorinated biopolymers.[124] In the case of fluorinated proteins, Oldfield and co-workers were the first to successfully report accurate prediction of the fluorine chemical shifts of a 5-fluorotryptophan-labled *E.coli* galactose binding protein which contains five tryptophans with fluorine resonances spanning ~ 10 ppm.[125] They concluded that that weak and long-range electronic interactions were the dominant contribution to the chemical shift dispersion versus van Der Waals effects. Conversely, Lau and Gerig's analysis of a more dynamic protein, dihydrofolate reductase, was unable to effectively account for all aspects of nuclear shielding contributions and dynamic motions to accurately predict chemical shifts.[126] More recent efforts using quantum chemical methods by Isley et al. studying 3-fluorotyrosine-labeled BRD4, highlight the importance of accounting for explicit solvation of the fluorinated amino acids which can significantly affect chemical shift predictions leading in some cases to significant error.[127] Accurate prediction of fluorine chemical shifts in proteins still remains a significant challenge.

In the context of ligand binding experiments, chemical shift perturbations can be used for sensitive quantitative affinity measurements; however, the limit of detection is based on both the rate of chemical exchange, as well as the relationship between the absolute affinity and the amount of receptor being used in the experiment. These experiments are discussed in subsequent sections.

1.6.4 Chemical Shift Anisotropy Effects on ^{19}F NMR Spectra

Transverse (T_2) relaxation mechanisms significantly affect the observed line widths in ^{19}F NMR spectra and are particularly sensitive to both the magnetic field strength and the size of the fluorinated molecule under study. For most organofluorine compounds, the predominant contributions to T_2 relaxation are dipole-dipole interactions and CSA. For large fluorinated biomolecules, CSA-mediated relaxation is typically the dominant mechanism at high field strengths. **Equation 1** shows the T_2 dependence on the square of the magnetic field strength (ω_F), the shielding anisotropy of the nucleus ($\sigma_\parallel$- $\sigma_\perp$), and the rotational correlation time (τ_C) for the protein under study.[128]

$$\frac{1}{T_2} = \frac{2}{15}(\sigma_\parallel - \sigma_\perp)^2 \omega_F{}^2 \tau_c (\frac{2}{3} + \frac{1}{2(1+\omega_F{}^2 \tau_c{}^2)}) \qquad (1)$$

At 235 MHz Hull and Sykes showed approximately 50% of the line width of 3-fluorotyrosine-labeled alkaline phosphatase was caused by CSA, cancelling out the signal to noise and resolution gains from acquiring a spectrum at a 2.5 times higher magnetic field strength.[112]

To address the challenge of the large CSA effect, F-C TROSY methods have been developed for aryl ^{19}F-^{13}C bonds, using conditions where the dipole-dipole interactions and CSA cancel.[115] This has led to the characterization of proteins as large as 180 kDa, and has more recently been applied to ^{13}C-labeled fluorouracil in RNA including ligand binding studies.[129] Conversely CF_3-TROSY may be limited to lower field strengths where the CSA effects are negligible. At high field strengths, TROSY effects were not observed due to the high CSA of the CF_3 group.[130] Given the significant effects on NMR spectra, the CSA effect and the magnetic field strength for acquiring the spectra, should be a significant consideration when choosing a ^{19}F NMR experiment in particular for large biomolecules.

1.6.5 ^{19}F NMR Applications in Fragment-Based Drug Discovery

The following sections will elaborate on the use of ^{19}F NMR in the field of FBDD. The start of NMR research in this field began with the contributions from Abbott labs describing an SAR by NMR approach in 1996 using protein-observed methods.[131] ^{19}F NMR would subsequently be used as a complementary tool in 2002 focusing on ligand-observed NMR.[132] The successful outcome of FBDD programs is supported by four FDA-approved drugs, with one originating from NMR screening (**Figure 1.12**).[133–136] FBDD, offers a powerful solution to the chemical space challenge surrounding drug-like molecules of an approximate molecular weight up to 500 g/mol, which is estimated to be ~10^{63}.[137] FBDD approaches reduce this chemical space via screening low molecular weight molecules typically less than 300 g/mol to more effectively sample the chemical space necessary to bind a given target. This reduces the library sizes that need to be screened from tens of thousands of molecules to more manageable sizes typically ranging from 500 to 2000 compounds. The challenge associated with screening fragments is their low affinity for their target, typically in the micromolar to millimolar affinity range. As such, NMR is well-positioned as a sensitive biophysical technique to both detect and quantify these interactions. In the sections below, we will first discuss ligand-observed ^{19}F NMR methods followed by a discussion of newer ligand discovery applications of protein-observed ^{19}F NMR. For earlier examples, readers are referred to several prior reviews on this subject.[98,138,139]

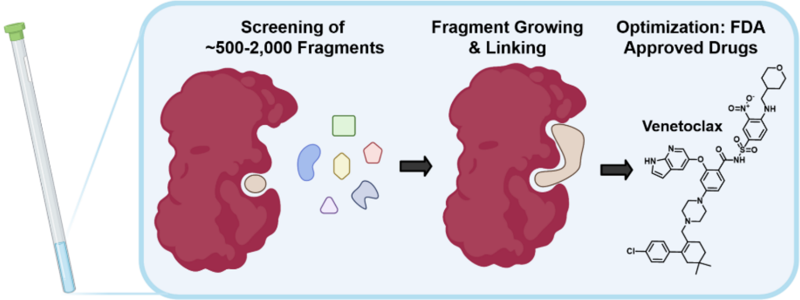

Figure 1.12: NMR in Fragment-Based Drug Discovery.

1.6.6 Ligand-Observed ^{19}F NMR

A key application of ligand-observed ^{19}F NMR for small molecule screening takes advantage of the NMR properties of the biomolecular target that can be transferred to a small molecule in chemical exchange with the bound and unbound states. Based on the most commonly used approaches, ligand-observed ^{19}F NMR experiments can be broadly broken down into fluorine direct binding chemical shift anisotropy and exchange for screening (FAXS) experiments, competitive inhibition FAXS, and *n*-fluorine atoms for biochemical screening (n-FABS), which is more specifically substrate/cofactor-based (**Figure 1.13**). FAXS can be further categorized by the NMR parameter detected, but most commonly uses transverse relaxation filters. Other NMR experiments that have been described monitor changes in chemical shift perturbation and transferred or direct NOEs.[140] These experiments have been prominently used for FBDD, and as such are extensively reviewed.[83,95–97] In recent years several enabling methodologies have been developed that further the field, including creation of unique fluorinated fragment libraries,[141] broadband protocols for expanded mixtures,[142] quantitative methodology for measuring dissociation constants,[143,144] multi-dimensional NMR experiments (e.g., COSY,[145] ILOE[140]), and screening protocols with both cellular lysates and intact cells.[146,147] Many of these advances will be highlighted here.

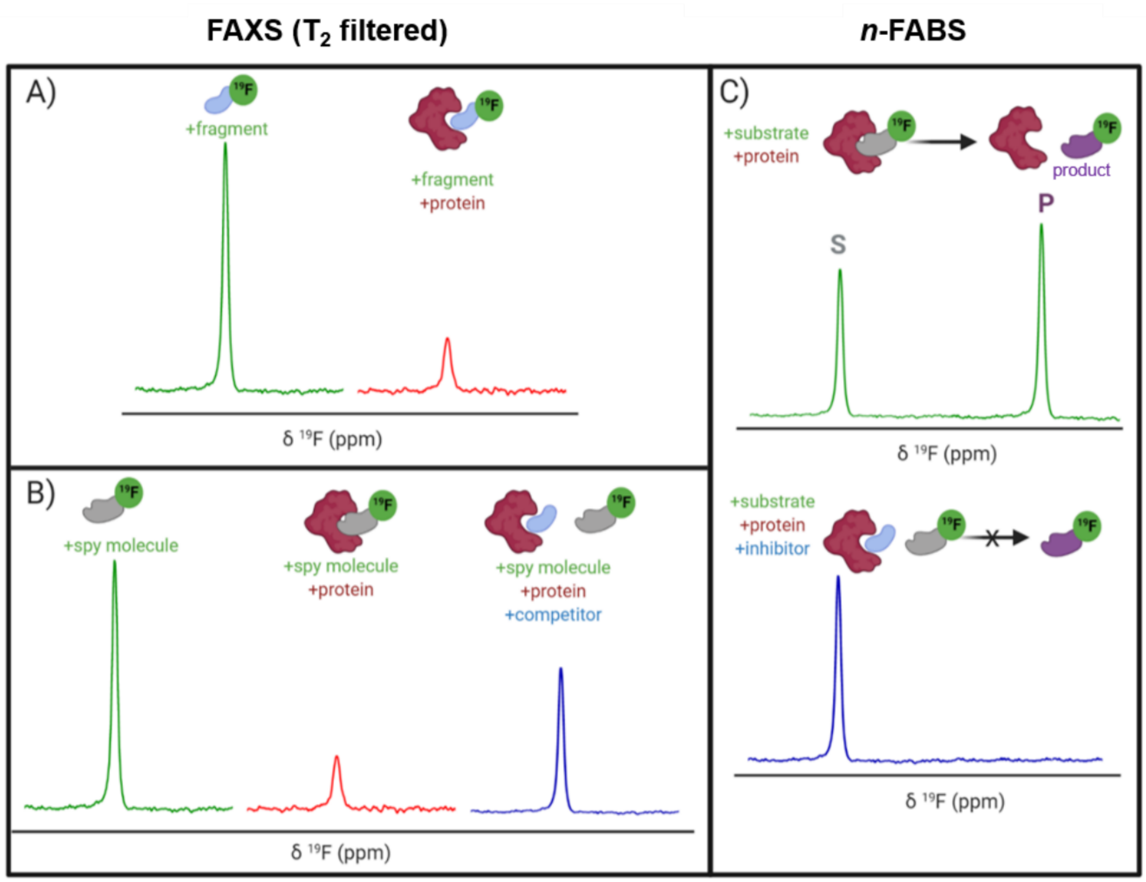

Figure 1.13: Idealized ^{19}F NMR Spectra for Ligand-Observed Fragment Screening. A) direct binding FAXS and B) competitive inhibition FAXS using a CPMG pulse sequence, and C) n-FABS.

1.6.6.1 The T_2 Filter Experiment

T_2 relaxation filter experiments, like those used in FAXS, use a Carr-Purcell-Meiboom-Gill (CPMG) pulse sequence to detect ligand binding. In a CPMG pulse sequence a hard 90° excitation pulse is followed by a series of 180° refocusing pulses that create an echo.[148,149] This echo decays exponentially as a function of T_2 relaxation. When a ligand binds to a protein, the protein transfers its shorter T_2, which is inversely related to molecular weight and magnetic field strength, and the echo diminishes faster in comparison to the free ligand. Such a T_2-based filter experiment leads to an observed difference in resonance intensity of the free ligand in solution, and indicates ligand binding. The large ^{19}F CSA is particularly well-suited for T_2 relaxation experiments. CSA is the main mechanism of T_2 relaxation under high fields (>300 MHz)[150] that are used today which can lead to large effects in signal perturbation from binding. A main limitation of CPMG experiments is the lack of a strong response for inhibitors binding in slow chemical exchange, a characteristic of high affinity interactions (i.e., $K_d < 1\ \mu M$). When screening low molecular weight fragments, this is usually less of a concern due to their typical weaker affinity and thus fast chemical exchange binding characteristics.

1.6.6.2 FAXS in Fragment Screening

FAXS was first introduced by Dalvit et al. as a competitive binding assay for which a known fluorinated weak affinity binder, known as a spy molecule, is displaced by a competitive ligand.[110] The binding event is monitored using a T_2 filter-based CPMG pulse sequence. To identify a suitable spy molecule generally a library of fluorinated molecules is screened against the target or a known ligand for the target is fluorinated. An appropriate spy molecule will have a significant drop in signal when a CPMG pulse is applied and protein is added which will create a large signal window for displacement by a competitive molecule. As a rule of thumb, a pK_d of 3.0–5.5 can lead to fast enough exchange kinetics to observe displacement over a wide affinity range while possessing sufficient affinity to form a protein complex with a significant population to detect changes in relaxation.[151] The spy molecule can then be used to screen for new competitive inhibitors, both qualitatively through rank ordering inhibitors based on a return in resonance intensity, or quantitatively through inhibitor titrations. The latter experiments lead to the inhibition dissociation constant, K_i, if the spy molecule's affinity (K_d) has been previously determined using **Equation 2** where F is the displacement value of the spy molecule upon addition of a competitive inhibitor.[109]

$$\mathrm{K_I} = \frac{(100-F)[I]\mathrm{K_D}}{F([\mathrm{L_T}+\mathrm{K_D})} \qquad (2)$$

An attractive feature of this approach is that while spy molecules are weak affinity binders, they can be used to determine the K_i of high affinity ligands.[151] This method is also suitable for fragment-based screening because of its ability to detect low affinity molecules while at low ligand concentrations which avoids solubility issues from screening ligands at high concentrations, typical in many biophysical fragment screening methods. This approach is also relatively high throughput due to the low amounts of protein required along with rapid affinity ranking and mixture screening. An advantage of the competitive mode is that a fluorinated library is not needed; however if fragment mixtures are used, hit mixtures will need to be deconvoluted.

A recent application of competitive FAXS in fragment-based drug discovery was a screen against sepiapterin reductase, a target in chronic pain.[152] This assay was chosen because the competitive mode allowed the researchers to focus their screen on a substrate binding pocket, and detection of the ^{19}F signal allowed for the use of large amounts of cosubstrate, NADP/NADPH. N-acetylserotonin, a known binder ($K_d \sim 5\ \mu M$) was fluorinated with a CF_3 moiety, to serve as the spy molecule. A return of signal intensity was readily observed upon spy molecule displacement by a known inhibitor used as their control. A 4,750-member library containing a diverse array of planar, sp^3-enriched, and polar fragments was screened in mixtures of 12 using a CPMG pulse sequence. Out of 26 primary hits, 21 were confirmed in an enzymatic inhibition assay. Crystal structures and structure-based design led to a promising inhibitor with double-digit nanomolar potency, good ligand efficiency (LE, 0.53), and favourable absorption, distribution, metabolism, and excretion properties for further lead optimization.

FAXS screening using a fluorinated fragment library in the direct binding format can be another way to generate spy molecules without the need for subsequent chemical modifications of the hits. Furthermore, the direct mode can be used to screen for fluorinated inhibitor motifs since ^{19}F is prevalent in drugs and can be an important functional group for non-covalent interactions.[153] One emerging application for fragment-based ^{19}F NMR screening is directed at nucleic acid drug targets. The first instance of ^{19}F NMR fragment-based screening of a nucleic acid target was against telomeric repeat containing RNA (TERRA), an anti-cancer drug target because of the dependence on TERRA to form telomere heterochromatin in cancer.[154] Known ligands of the G-quadruplexes that form TERRA *in vivo* were polyaromatic, making them poor candidates for drug discovery. To discover diverse, more drug-like chemical matter, a 355-member fluorinated fragment library with fragments containing either a CF_3 or CF moiety was screened by FAXS in mixtures of eight. ^{19}F NMR spectra were recorded, 1D-spectra with and without a CPMG T_2 filter, for the fragment cocktails alone and in a mixture with $TERRA_{16}$. A decrease in signal intensity and line broadening upon addition of $TERRA_{16}$ in the T_2 filtered spectrum was seen for 20 molecules (5.6% hit rate). Follow-up on seven of their hits demonstrated selectivity against tRNA and duplex DNA, indicating the sensitivity of this method for finding selective binders of noncoding RNA.

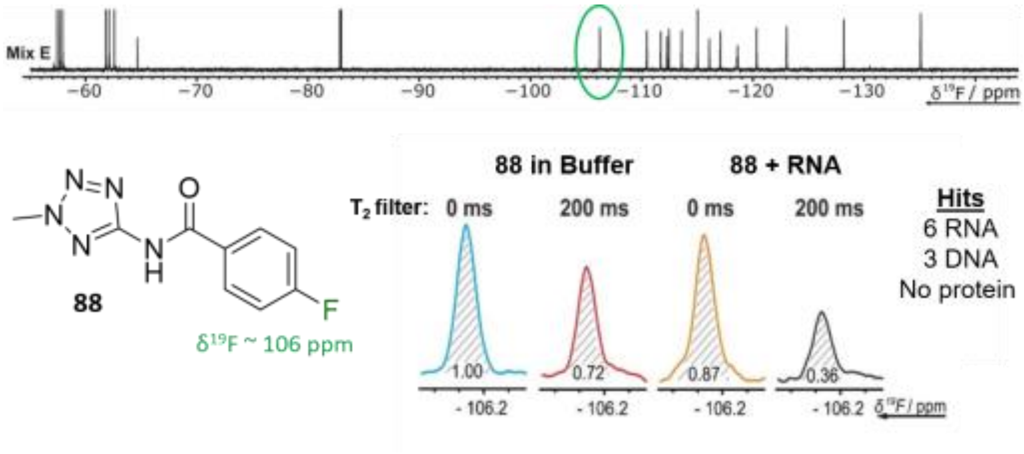

Figure 1.14: FAXS Screening Against Nucleic Acid Targets.

Example fragment **88** from fragment mixture E and the ^{19}F resonance in the T2 filtered experiment with an RNA target **88** was a hit for 9 of the 24 targets screened against. (adapted from ref. [155] with permission from Wiley-VCH, copyright 2020).

FAXS screening has been further expanded to additional nucleic acid targets and takes advantage of the speed of the NMR experiments and the large mixture sizes that can be resolved. Enabled by the throughput of the NMR experiment, Binas et al. screened a fluorinated library against fourteen RNA targets while counter-screening against five DNA and five protein targets.[155] 101 fluorinated fragments were screened against each target in five mixtures (20-21 fragments each) with and without a T_2 filter **(Figure 1.14**). Out of the 74 fragments that were classified as hits, proteins had the highest hit rate at 16-55 hits for each, excluding a phosphatase that has a known low druggability. RNA had the next highest hit rate, in particular riboswitch RNAs had 7-26 hits each. DNA had the lowest hit rates with the duplex only having one hit, and G-quadruplexes having 12-20 hits. There was some overlap in hits for each class of biomolecules (13 fragments hit all 3 classes), but there were also distinct hits for each class.

1.6.6.3 *n*-FABS in Fragment Screening

n-FABS is an activity-based method where a substrate or cofactor of an enzymatic reaction is labeled with *n* fluorine atoms. In the original study, a CF_3 moiety was appended onto the respective peptide substrate of the target proteins, AKT1 and trypsin, and the conversion of the enzymatically modified substrates to their respective products were detected by ^{19}F NMR.[108] This approach was advantageous for measuring IC_{50} values as one can detect both substrate and product. Additionally, the low nM amount of protein required makes it a useful method for rapid, high-throughput screening of fragments. Higher *n* values allow for even greater sensitivity.[156] The primary drawback is the additional deconvolution experiments for mixtures that show activity, which uses additional reagents and time.

A recent example of *n*-FABS applied to fragment screening is against uridine nucleoside ribohydrolase (UNH), a target in *Trichomonas vaginalis* infection. Shea et al. had previously developed a ^{19}F NMR activity-based assay following the conversion of 5-fluorouridine to 5-

fluorouracil, a substrate and product that are already fluorinated, and screened the NIH clinical compound collection.[157] After following up on several hits and concluding the target, UNH, was druggable, a fragment screen using a 2,000 member library in mixtures of six fragments was employed to identify diverse chemical scaffolds that would be suitable for drug discovery efforts.[158] Mixtures with at least 75% inhibition were deconvoluted and 97 hits were identified (4.9%). 18 compounds had an IC_{50} under 20 μM, several of which had a LE above 0.5, which is ideal for elaboration.[159] In particular, a 3-hydroxypyrrolidine was further investigated as a fragment scaffold that could be expanded due to its potency, LE, and vectors for SAR exploration.[158]

1.6.6.4 Fluorinated Fragment Libraries & Efficient Screening of Chemical Space

An essential component for ^{19}F NMR fragment-based screening is the development of fluorinated fragment libraries, whether this be for spy molecule generation or direct screening. As this field has evolved, in-house collections, commercial libraries, and diversity-oriented synthesis methods have been developed. Single fluorinated motifs (CF, CF_2, CF_3), or motifs that can be decoupled are ideal when they result in isolated singlet ^{19}F resonances,[119] but polyfluorinated fragments are also used.[156,160–163] Another consideration is the fraction of sp^3 carbons (Fsp^3) of the fragments. As inspiration, bioactive natural products tend to have more 3D-character. Recently a focus on 3D fragments and their importance has been studied and has resulted in the creation of Fsp^3-rich libraries.[164,165] Applying this to fluorinated fragments specifically, a recent report showed a diversity-oriented synthesis approach to create a more diverse fluorinated fragment library, the 3F library.[141] 115 fragments were synthesized from nine core scaffolds and exhibited higher Fsp^3 character and natural-product likeness, as well as ideal physicochemical properties, in comparison to two commercial libraries. To demonstrate the usability of this library a direct FAXS screen against four protein targets was employed. 105 of the fragments passed quality control and were screened in mixtures of 17-24 fragments with a T_2 filter. Hit rates from 3-11% were obtained validating the utility of this diverse library in fluorinated fragment screening.

To efficiently screen chemical space, it is necessary to balance screening a large number of fragments while also minimizing experiment time and reagents. One newly developed solution is to maximize the chemical shift range of detection to not only allow simultaneous screening of diverse fluorine motifs, but also to screen larger mixtures.[142] The span of ^{19}F drug-like motifs covers from -20 to -240 ppm.[119] Current CPMG pulse sequences, the most commonly used ^{19}F NMR experiment used in ligand-observed screening, consist of a hard 90° excitation pulse followed by 180° refocusing pulses. These limit the usable bandwidth to ±15 kHz to maintain 50% of the full signal integral. This means that mixtures have to be designed so that fragments only cover a small chemical shift range and several experiments must be performed to cover the whole range of drug-like motifs. Adiabatic 180° refocusing pulses, in the place of hard pulses, have previously been used to combat this issue, but only extend to ±30 kHz to maintain 50% of the full signal integral. To achieve a goal of at least ±60 kHz, which would cover most of the drug-like motif range, broadband universal rotation by optimized pulses (BURBOP), which are designed for nuclei with large chemical shift ranges, were developed into 90° and 180° pulses that are compatible with CPMG (**Figure 1.15A**).[142] Experimentally, it was shown to achieve on average 82% signal integral over 120 kHz. As an initial test, 35 compounds that spanned a chemical shift range of 183 ppm were sampled in a single 1D ^{19}F CPMG experiment. In comparison, using hard pulses took four experiments and an adiabatic 180° pulse took two experiments to cover the whole range.

Demonstrating BURBOP applicability in screening, a new library, LEF4000, which is an expansion of the local environment of fluorine (LEF) library that focused on augmenting diversity based on the existing 2D fingerprint of fluorinated fragment library members, was screened against a bacterial enzyme target, CoaD.[142] A hit rate of 6%, with hits encompassing the entire drug-like motif chemical shift range, demonstrated the importance of broadband methods such as this one that would allow efficient enrichment of existing fluorinated fragment libraries. To test the applicability of "supermixtures," 152 compounds were combined and screened at once (**Figure 1.15B**). The resulting signal reduction of hits were comparable to the spectra seen in the original screen with smaller mixtures, suggesting competition at the same binding site had little impact on hit detection, and demonstrating the utility of larger mixtures in screening.

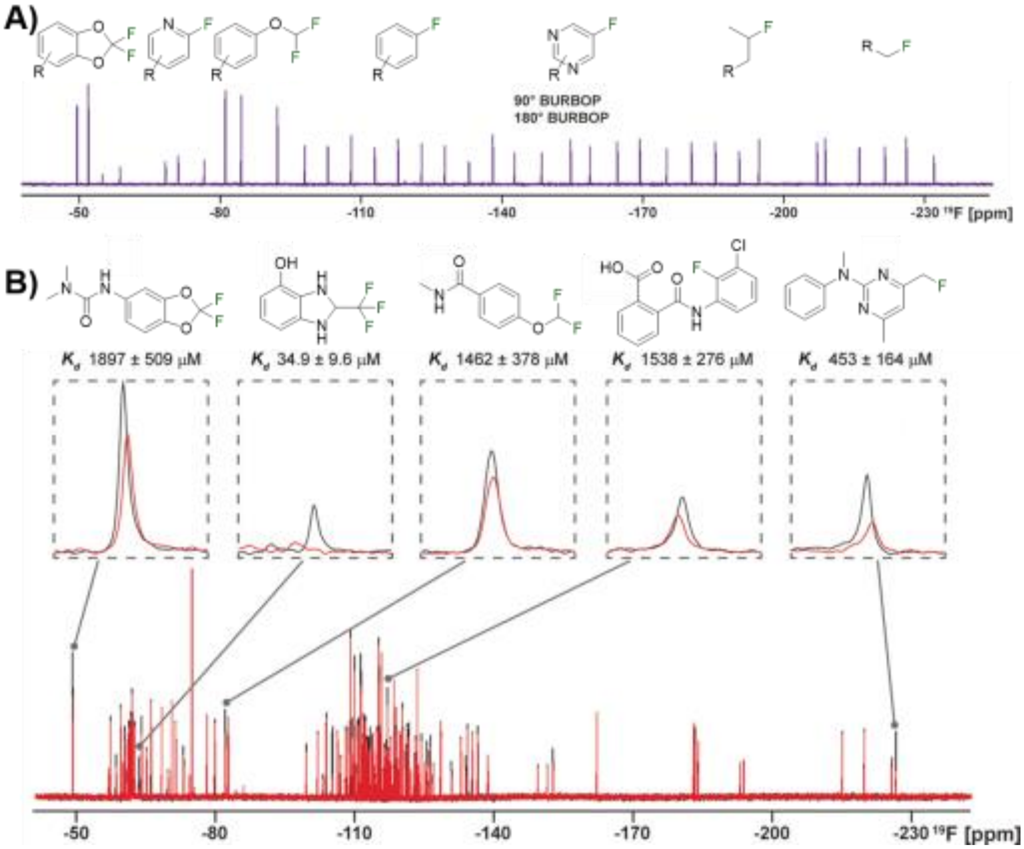

Figure 1.15: BURBOP Pulse in Practice.

A) 19F fragment mixture with diverse motifs covered by a BURBOP pulse in the resulting ^{19}F CPMG experiment (adapted from ref. [166] with permission from Wiley-VCH, copyright 2020). **B)** Representative screening hits from a supermixture of 152 fragments in absence (black) and presence (red) of the protein target CoaD (adapted from ref. [166] with permission from Wiley-VCH, copyright 2020).

1.6.6.5 Quantification of Protein Ligand Interactions by ^{19}F NMR

Once a library has been screened, the next step is to prioritize fragment hits for follow up studies; quantification methods are critical for this. Biophysical methods beyond NMR commonly used in drug discovery do not work as well with fragment screening because of low fragment affinities and solubility issues. For NMR methods, as described previously, using a spy molecule in a competitive FAXS experiment can lead to K_i determination. However, establishing a spy molecule that is suitable can sometimes be difficult and the K_d cannot be derived readily from direct FAXS experiments when measuring T_2 filter, STD, or waterLOGSY effects because the response is not proportional to affinity.[120,167] For T_2 filter experiments this is because in the intermediate to fast exchange regime that fragments exist in, the observed relaxation rate ($R_{2,obs}$) is the weighted average of the relaxation rate in the free ($R_{2,f}$) and bound state ($R_{2,b}$) plus a term that accounts for line broadening, the exchange term (R_{ex}). Both $R_{2,b}$, which dipolar relaxation (R_{DD}) and CSA relaxation (R_{CSA}) contribute to, and R_{ex} are unknown values limiting one's ability to extract a K_d. Additionally, both terms vary widely making relative ranking of ligand binders challenging.

$$\mathrm{R_{2,obs} = p_f R_{2,f} + p_b(R_{DD} + R_{CSA}) + R_{ex}} \quad (3)$$

To address this challenge, a new NMR methodology, chemical shift anisotropy ranking (CSAR), removes all other sources of relaxation so that only CSA relaxation is contributing to the relaxation rate, which can accurately be summed using chemical shielding tensor calculations to determine a fraction bound, and from there a K_d.[143] This is achieved by a spin lock frequency (10 MHz) in a high field (e.g., 16.4 T) to eliminate the exchange term. In the elaborated methodology two different magnetic fields strengths are used to subtract out the dipolar relaxation contribution leaving only CSA, but in the simplified FastCSAR the dipolar relaxation is treated as constant between the free and bound state. Trypsin was used as a model protein to rank known ligands using CSAR and FastCSAR, and compared to the spy method to show the validity of this approach. There are limitations to this approach, including calculating chemical shielding tensors. Broader use beyond trypsin awaits further validation. However, FastCSAR has the advantage of ranking hits from one ligand concentration in comparison to a titration.

Another reported quantification method using direct FAXS relies on a ligand titration to quantify K_d.[144] This methodology only works for molecules with low binding affinities and conditions where the total ligand concentration is approximately equal to the concentration of free ligand, i.e. using low protein concentration. To demonstrate with direct FAXS using a T_2 filter, HSP90 was screened at 0.8 µM with three ligands at varying concentrations up to 160 µM to derive a K_d by plotting transverse relaxation rate with and without protein $((R_2)_{+E+L} - (R_2)_{-E+L_0})$ as a function of ligand concentration (**Equation 4**). A similar quantification can be done based on longitudinal relaxation rates (R_1).

$$((R_2)_{+E+L} - (R_2)_{-E+L_0}) \\ = ((R_2)_{+E+L_0} - (R_2)_{-E+L_0})(\frac{K_D+[L_0]}{K_D+[L]}) \quad (4)$$

The utility of this approach is in the precise affinity ranking of hits from FBDD campaigns to select candidates for follow-up.

1.6.6.6 ^{19}F NOE for Fragment Linking

Fragment expansion is an important principle behind FBDD. Theoretically the binding energy of each fragment is additive when appropriately linked, and the entropic cost from binding two fragments is reduced creating a strong binder compared to the weak binding fragments on their own. However, this linkage is not trivial and can take trial and error to see improvements in affinity. A ^{19}F NMR fragment-based screening approach against BACE-1, a drug target implicated in Alzheimer's disease, used ^{19}F-^{19}F intermolecular NOE to assist efficient linkage.[140]

First, a constructed fluorinated fragment library was screened and had a hit rate of 0.5%, which is comparable to traditional fragment screens against BACE-1.[168,169] Hits were characterized and quantified by a differential chemical shift perturbation method, which was validated by parallel SPR K_d determinations. To pursue fragment linking, hits or seed fragments, were combined with other fluorinated fragments in ^{19}F-^{19}F NOESY experiments.[140] The presence of ^{19}F-^{19}F NOEs indicated that fragments were binding simultaneously and were close in space (within ~5 Å) and could potentially be linked. In a proof of concept, two protonated forms of fluorinated fragments were joined to form a compound with 100-fold potency increase relative to the original hit.[170] This method is analogous to interligand NOE (ILOE) in ^{1}H NMR. In later BACE-1 studies, a ^{19}F NMR fragment screening campaign for a second site was completed followed by ^{1}H-^{1}H ILOE NMR experiments and molecular modeling to extend a lead compound into an additional pocket yielding a highly potent and selective inhibitor.[171]

1.6.6.7 In-Cell NMR Screening by *n*-FABS

Fragment-based screening largely take place with isolated biomolecule targets. However, testing ligands closer to their true physicological conditions is desirable. New methodologies that permit screening in lysates and in living cells is valuable; the biorthogonality of ^{19}F is well-suited for this this type of screen. A new application using *n*-FABS has achieved this.[97] In short, fatty acid amide hydrolase (FAAH), a target in pain and inflammation, was suitable for *n*-FABS screening because the lower enzyme quantities required could potentially overcome the challenges associated with screening against membrane-bound proteins like FAAH. A truncated form of FAAH fused to MBP that retained enzymatic activity but did not aggregate was screened using a fluorinated natural substrate analog, ARN1203 (**Figure 1.16A**). Using an in-house generated library, 115 fluorinated fragments in mixtures of five were screened which led to a hit rate of 16.5%.[172] This system was then taken to cell lysates using HEK293 cells that overexpressed human FAAH (hFAAH). Recombinant hFAAH expresses in low yield so screening in cell extracts is desirable. To validate the established *1*-FABS assay using ARN1203 in lysates, a known inhibitor was used to quench the reaction. The determined IC_{50} for hFAAF lysate and the previously isolated MBP-rFAAH were compared for two known potent inhibitiors and two of the weaker binding fragments hits and found to be comparable.[147] Following this success, the *1*-FABS assay was taken into transfected HEK293 cells. Control experiments with ^{19}F NMR spectra of cell lysate and supernatant showed that ARN1203 could get into cells, and that the product was be found in the transfected but not control cells (**Figure 1.16B**).[146] The same potent inhibitors were used and shown to have comparable inhibition as in the cell lysate and fragments were used to show a dose-response demonstrating the sensitivity of the assay in cells.

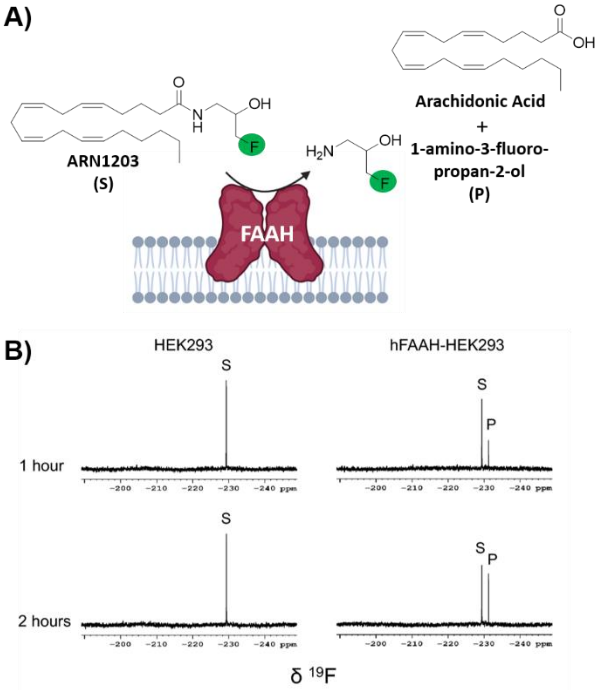

Figure 1.16: *n*-FABS in Cells.

A) *n*-FABS assay setup for FAAH where a fluorinated natural substrate analog, ARN1203, is cleaved in the presence of hFAAH to a traceable fluorinated product **B)** ^{19}F NMR spectra of intact HEK293 cells (control) and intact transfected HEK293 cells with ARN1203 (adapted from ref. [97] with permission from Springer, copyright 2020).

1.6.7 Protein-Observed ^{19}F NMR

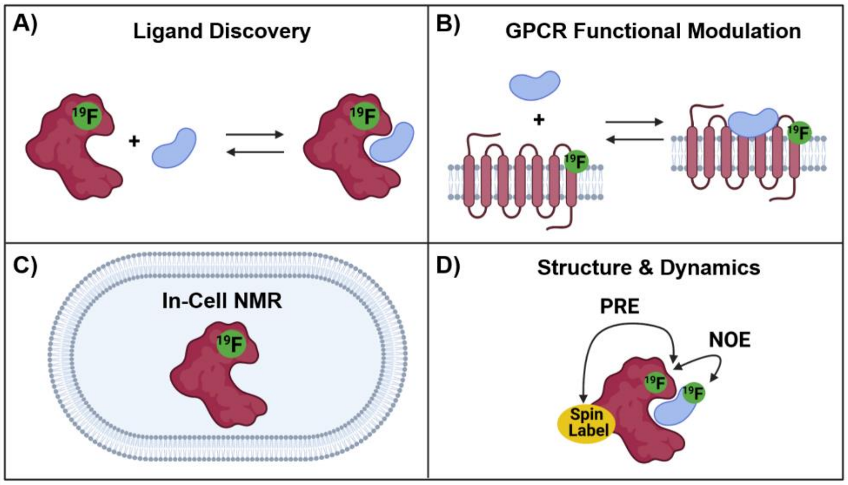

Figure 1.17: Protein-Observed ^{19}F NMR Studies

A) Ligand discovery with soluble proteins **B)** GPCR functional modulation with agonists and antagonists, **C)** in-cell NMR and **D)** structural and dynamics using NOE and PRE NMR.

The development of protein-observed ^{19}F (PrOF) NMR applications for ligand screening was initially slower to develop than ligand-observed methods, but has since benefitted from the introduction of more sensitive cryoprobes to facilitate ligand screening. PrOF NMR takes advantage of perturbations in ^{19}F-labelled protein resonances induced upon ligand binding. Proteins have been labelled with ^{19}F to study protein folding and function by NMR since the seminal reports by Hull and Sykes in 1974.[107,138] However, it is only in the past decade that PrOF NMR methods have been applied to small molecule discovery and screening efforts. A strength of PrOF NMR in studying protein-ligand interactions, particularly in the area of FBDD, is the rapid determination of a K_d for weak binding ligands while providing structural information regarding the ligand binding site and allosteric effects. Methods for incorporating fluorine into proteins have been previously reviewed,[173,174] but include amber suppression,[175,176] post-translational bioconjugation with reactive fluorinated molecules,[177,178] enzymatic labeling,[179] and metabolic labeling.[173] Given the relatively conservative replacement of a hydrogen to fluorine atom, many different fluorinated amino acids are recognized by the natural biosynthetic machinery. This has led to metabolic labeling to be the most commonly used form of protein labeling, with over 21 different amino acids being reported in the literature.[99] As PrOF NMR has become more widely adopted, proteins as large as 180 kDa have been studied by this approach, and have included both soluble and membrane-bound proteins, as well as multidomain proteins (**Figure 1.17**). The following sections will discuss several of the main approaches that PrOF NMR has been used for in FBDD as well as more detailed case studies.

1.6.7.1 The Chemical Shift Perturbation Experiment

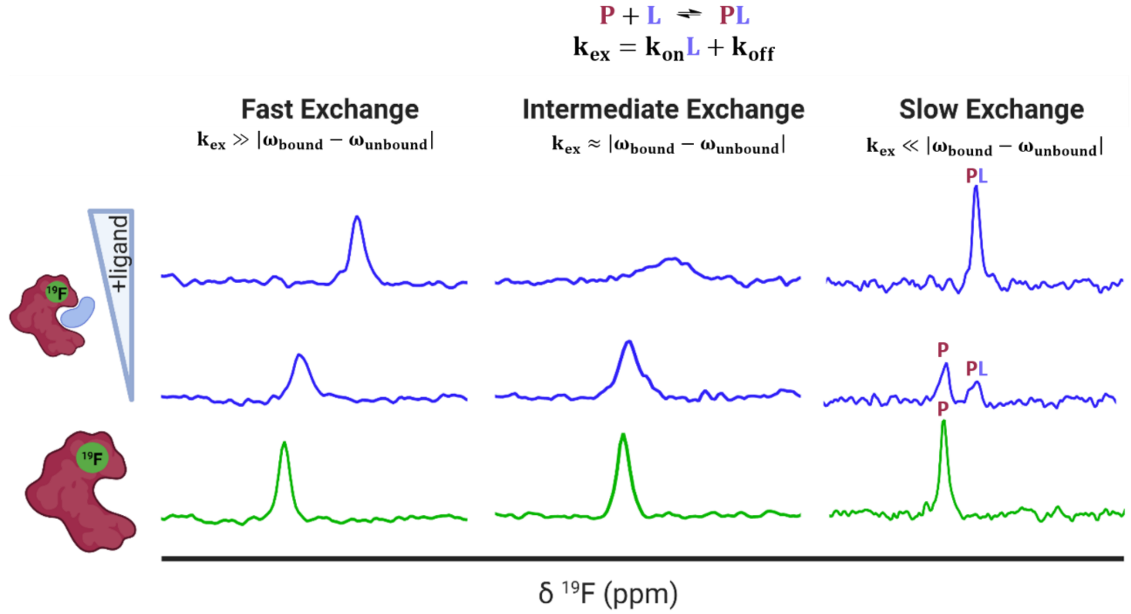

Figure 1.18: Idealized Spectra of Protein-Observed ^{19}F NMR.
Ligands in fast chemical exchange (left), intermediate exchange (middle), and slow exchange indicating the distinct states of free (P) and bound (PL) protein (right).

The predominant method for characterizing protein-ligand interactions via PrOF NMR is through a chemical shift perturbation experiment. In such an experiment, the observed resonances are affected differentially depending on the chemical exchange rate which is dictated by the on and off-rates for complex formation and dissociation and the resonance frequency of the bound and unbound states (Figure 1.18). For fragment screening, these small molecule interactions tend to be weak (K_d = mid micromolar to millimolar). Under these conditions a single resonance is observed for the binding interaction, where the chemical shift is the weighted average of the bound and unbound states. Upon ligand titration, the observed change in chemical shift can be fitted to a non-linear regression curve to calculate K_d using **Equation 5**.

$$\Delta\delta = \Delta\delta_{max} * \frac{(K_d+L+P)-\sqrt{(K_d+L+P)^2-4PL}}{2P} \qquad (5)$$

Either a resonance broadening or complete resolution into two distinct resonances indict intermediate and slow exchange binders respectively, and are typically characteristic of higher affinity interactions with slow off-rates.[180] However this is not always the case, where even weak ligands can exhibit slow chemical exchange binding.[181] In chemical shift perturbation experiments, nonspecific effects such as protein aggregation or denaturation can be readily detected which are indicated by a global decrease in resonance intensity or coalescence of protein resonances which helps to identify potential false positives hits in screens.[120]

1.6.7.2 Conformational Studies/Agonist & Antagonist Binding Case Studies with GPCRs

Prior to PrOF NMR fragment-based screening efforts, PrOF NMR was used to study known ligand-protein interactions. One significant example is the study of G protein-coupled receptor (GPCR) signaling using ^{19}F NMR. GPCRs make up a large portion of drug targets in FDA approved drugs, but the mechanisms underlying the differing degrees of signaling, or biased signaling, are complex. To study the conformational states of the GPCR β_2-adrenergic receptor (β_2AR) upon agonist binding by ^{19}F NMR, Liu et al. labeled three cysteines on three distinct helices of the intracellular region of β_2AR with 2,2,2-trifluoroethanethiol (TET).[113] Cysteine labeling is generally conducted with CF_3-based tags because the fast internal rotation gives rise to sharp resonances. Cys265 and Cys327 were selected because they are located on helices VI and

VII respectively which upon activation are known to change conformations. Cys 265 and Cys327 each had two components to their respective ^{19}F signal indicating an equilibrium between two different conformations, an inactive and active state. Upon agonist binding which activate G-protein signaling, there was a larger shift towards the active state in helix VI (Cys265) than in helix VII (Cys327). The reverse was observed upon binding of β-arrestin biased ligands, which primarily shifted the equilibrium of helix VII (Cys327) towards an active conformational state. Additionally, the efficacy of partial and full agonists could be distinguished by the relative ratio of the inactive and active resonance, demonstrating PrOF NMR to be a valuable tool in GPCR functional studies. A similar study by Kim et al. labeled β_2AR with a trifluoromethyl tag (-$COCF_3$) to study the equilibria of GPCR functional states.[182] In the apo state, the ^{19}F spectra revealed three states ($S_{1\text{-}3}$), and upon addition of inverse, partial, and full agonists they were assigned by analyzing the population of each state to two distinct inactive conformers (S_1 and S_2) and an intermediate active state (S_3). When a G-protein mimic was added along with agonist, a fourth state (S_{4a}) that was fully active was observed. These studies highlight the sensitivity of PrOF NMR for mapping out binding interactions and conformational landscapes on a therapeutically important class of proteins. PrOF NMR has continued to be used to further characterize the conformational states and allosteric regulation of β_2AR and the adenosine A_{2A} receptor (A_{2A}R).[183–187] In addition, cysteine labelling ^{19}F NMR approaches have also been used to study the dynamics of soluble proteins.[188,189]

1.6.7.3 Ligand Discovery for the KIX Domain: A Case Study for Fragment Screening

Although prior studies had used fluorinated proteins to characterize both native and synthetic small molecules, the first use of PrOF NMR as a tool for small-molecule discovery was reported by Pomerantz et al. targeting the KIX domain of the coactivator CBP/p300 using a pilot screen of 50 fragments.[114] Prior NMR work by Wright and Dyson has provided a detailed picture of the molecular mechanisms involving transcriptional activation domains (e.g. Myb, CREB, and MLL) binding to two distinct binding sites on this small protein domain.[190,191] A key insight for this screen focused on the general enrichment of aromatic amino acids at protein-protein interaction interfaces.[192,193] In the case of KIX, six of the seven aromatic amino acids participated in direct binding interactions and/or being involved in allosteric regulation. PrOF NMR using KIX metabolically labeled with 3-fluorotyrosine (3FY) at five positions covering both binding sites was thus chosen for screening against the KIX domain.

PrOF NMR was attempted to potentially overcome challenges associated with discovering new ligands for dynamic interfaces as previous KIX screening efforts had resulted in only a few inhibitors.[194] Using fluorine-labeled KIX, the authors characterized the binding and affinity via chemical shift perturbation of a known inhibitor of the KIX-CREB protein-protein interaction, Napthol-ASE-phosphate,[194] and fragment molecules 1-10, from a previous tethering fragment screen for the MLL binding site.[195] Following the success of detecting weak binding ligands, a pilot study of 50 fragments were screened against 3FY-KIX in mixtures of 10 leading to the identification of 1G7, a pyrrole-substituted benzoic acid.[114]

To assess KIX's druggability, the first complete small-molecule screen using PrOF NMR was completed against KIX with an expanded 508 member fragment library by Gee et al.[196] The whole screen was completed in 510 minutes in 85 mixtures (5-6 fragments each) at 40 µM 3FY KIX (20 mg total), demonstrating the rapid nature of PrOF NMR screening as well as the low amount of protein required. Most fragment hits affected the resonance in the MLL binding site (Y631) significantly more than those in the CREB binding site (Y649, Y650, Y658). Further SAR studies identified aryl and phenylacetic acid pharmacophores for the MLL binding site hits, which may mimic hotspot residues in the sequence DIMDFVL found in the KIX-binding MLL peptide. Subsequent studies using more elaborated fragments and a dually labeled KIX protein with 3FY and 4-fluorophenylalanine (4FF) at F612, further elucidated the binding site to be near, but distinct from the MLL binding site.[197] This result was important as it indicated that the KIX domain could be targeted without competing against endogenous transcription factor interactions.

1.6.7.4 Ligand Discovery for the SPSB2 and AMA proteins: Case Studies for Characterizing Binding Site Interactions

Another early example of PrOF NMR was described by the Norton lab focusing on the SPRY domain-containing SOCS box protein 2 (SPSB2), a target implicated in infectious diseases for its role in recruiting an E3 ligase to inducible nitrous oxide synthase (iNOS) for degradation.[198] In this case, PrOF NMR was used as a secondary validation assay. A 5-fluorotryptophan (5FW) construct of SPSB2 was metabolically labeled at six Trp sites, of which W207's resonance was most perturbed upon binding of the N-terminal peptide of iNOS (**Figure 1.19A**). The key peptide residues interacting with the SPRY domain of SPSB2 are DINNN, the indole of W207 is nearby the backbone of an Asn residue of DINNN and solvent exposed under apo conditions explaining why a significant change in chemical shift was observed upon ligand addition. To test the sensitivity for detecting ligand interactions, analogs of hits from a fragment screen (STD and CPMG) were shown to perturb W207 demonstrating their binding in the iNOS binding site. A nonspecific binder known to bind outside the iNOS pocket perturbed resonances that were not W207. An SPBS2 inhibitor was subsequently designed using a stabilized, cyclic peptide analog of DINNN (CP0).[199] Affinity and kinetics were assessed using SPR and ITC, while PrOF NMR was utilized to confirm that the cyclic peptide bound to the iNOS binding site by perturbation of W207, albeit with ~0.5 ppm less of a shift in comparison to the linear peptide, indicating a slightly altered binding interaction. Similar studies were done with more stable cyclic analogs, a cystathionine analog and a lactam-bridge analog that were more resistant to REDOX, and perturbed W207 in a similar pattern to CP0.[200]

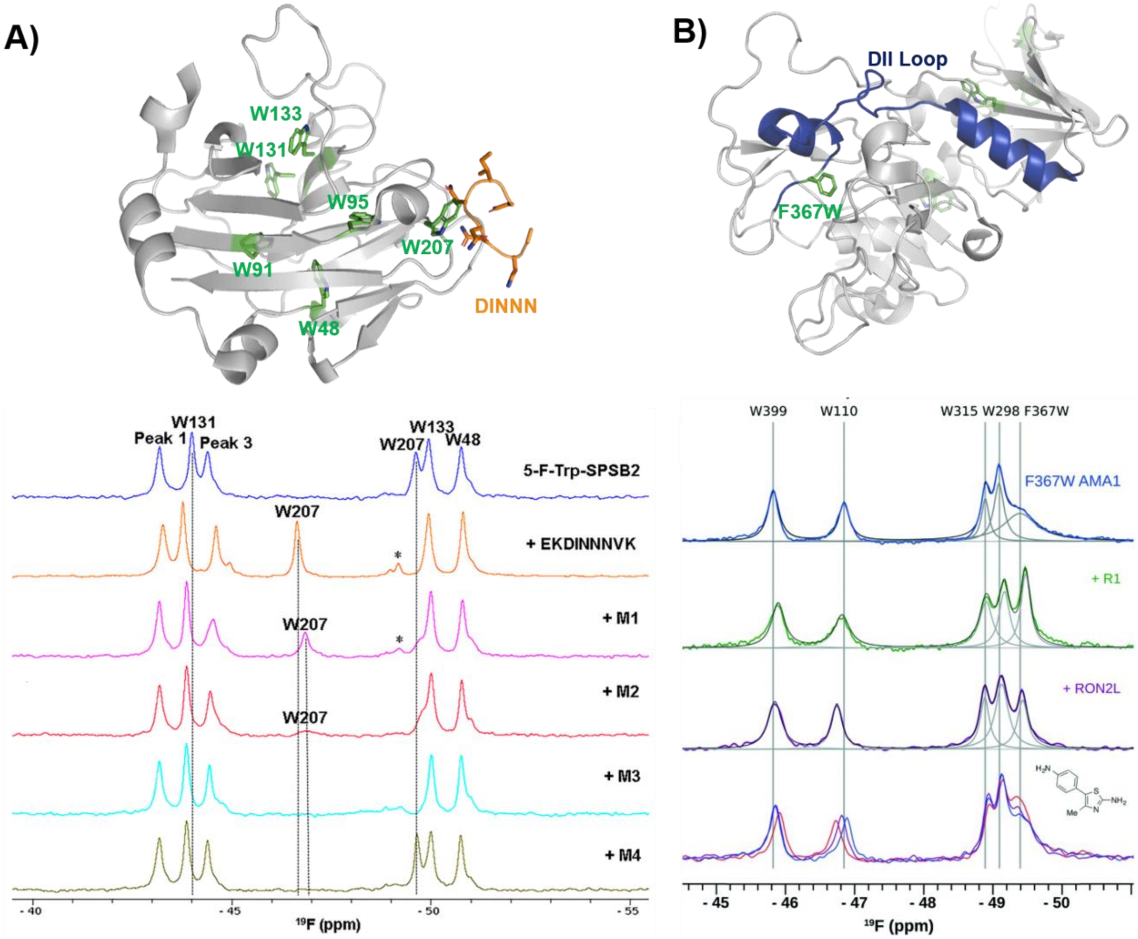

Figure 1.19: PrOF NMR Spectra of SPSB2 and AMA1 with Ligands

A) SPSB2 (grey) bound to DINNN (orange) with tryptophan residues in green (PDB: 3EMW, top); 19F NMR spectra of 5FW-SPSB2 alone, bound to a DINNN peptide, and bound to peptidomimetics M1, M2, M3, M4 (bottom, adapted from ref. [100] with permission from MDPI, copyright 2016) **B)** AMA1 in apo form (grey) highlighting the DII loop in blue and tryptophan residues in green, both mutated and native (PDB: 2Z8V, top); 19F NMR spectra of F367W 5FW-AMA1 alone, bound to peptides R1 and RON2L, and bound to a series of aminothiazole fragments (0,1,3 μM, bottom, adapted from ref. [201] with permission from Royal Society of Chemistry, copyright 2016).

In subsequent studies using PrOF NMR with a new smaller, more drug-like cyclic pentapeptide, as well as peptidomimetics (M1-M4), the dynamics of binding interactions with SPBS2 were assessed.[202,203] From these binding studies, it was observed in several cases that W207's resonance sharpened in intensity which suggested binding in the iNOS pocket differing in the effect to other ligands, which broaden W207 further suggesting more than one bound conformation (**Figure 1.19A**). To further probe the importance of each residue in the N-termini of iNOS in its interaction with the SPRY domain of SPBS2, PrOF NMR was once again used.[204] Different extents of broadening were observed in W207, and longer N-termini peptides tended to have higher affinity coupled with less broadening suggesting transient interactions that contribute to a single binding pose.

Similarly, PrOF NMR has been applied to study conformational changes induced upon ligand binding. AMA1, which is found on the surface of parasites, is a target in malarial diseases and disruption of an AMA1-RON2 complex is inhibitory. The domain II (DII) loop of AMA1 is known to be displaced by peptide binders (RON2L and R1); to track loop dynamics upon ligand interaction Ge et al. labelled the DII loop with 5FW (F367W, **Figure 1.19B**).[201,205] Using their fluorinated protein construct, fragments from previous screening efforts were characterized to determine where they bound. One fragment series saw a concentration-dependent sharpening of the F367W resonance with lower magnitude than that of the peptides, suggesting these fragments displace the DII loop but have a lower affinity interaction, while the other two fragment series did not affect F367W's resonance, indicating that they bind in a distinct site that does not induce a change in the DII loop.

1.6.7.5 Screening to Lead Molecules Using Bromodomains as a Case Study

The utility of PrOF NMR screening in drug discovery has been demonstrated ranging from fragment screening to later stage lead molecule development in targeting the bromodomains of epigenetic regulatory proteins. Bromodomains participate in PPIs with acetylated lysines on histone tails and over half of all 61 bromodomains are enriched with at least four aromatic amino acids in the histone binding site, which can be fluorine labeled.[206] Furthermore, fluorinated bromodomain constructs have been shown to be sensitive NMR probes for both native ligand and small molecule interactions and have been used to characterize the bromodomains of CBP, CECR2, BPTF, BRD4, BRDT, BRD2, *Pf*GCN5, and PCAF (**Figure 1.20A,B**).[46,114,206–210] In a cross-validation study of PrOF NMR, a 930 member fragment library was screened against the first bromodomain of 5FW-labeled BRD4 (BRD4 D1) in mixtures of five using both PrOF NMR and ligand-observed ^{1}H CPMG NMR (with and without competitor validation).[120] Comparing the individual fragments, there was 85% overlap in hit detection when using competitors. PrOF NMR could detect false positives in several cases where a single molecule was found to be the cause of signal reduction in their respective mixtures, possibly through inducing protein aggregation. Both the speed of the PrOF NMR assay and the ability to rank order compounds via K_d were seen as advantages of PrOF NMR, whereas the removal of a time intensive deconvolution step, lower protein concentration, and use of unlabeled protein are advantages for ^{1}H CPMG NMR.

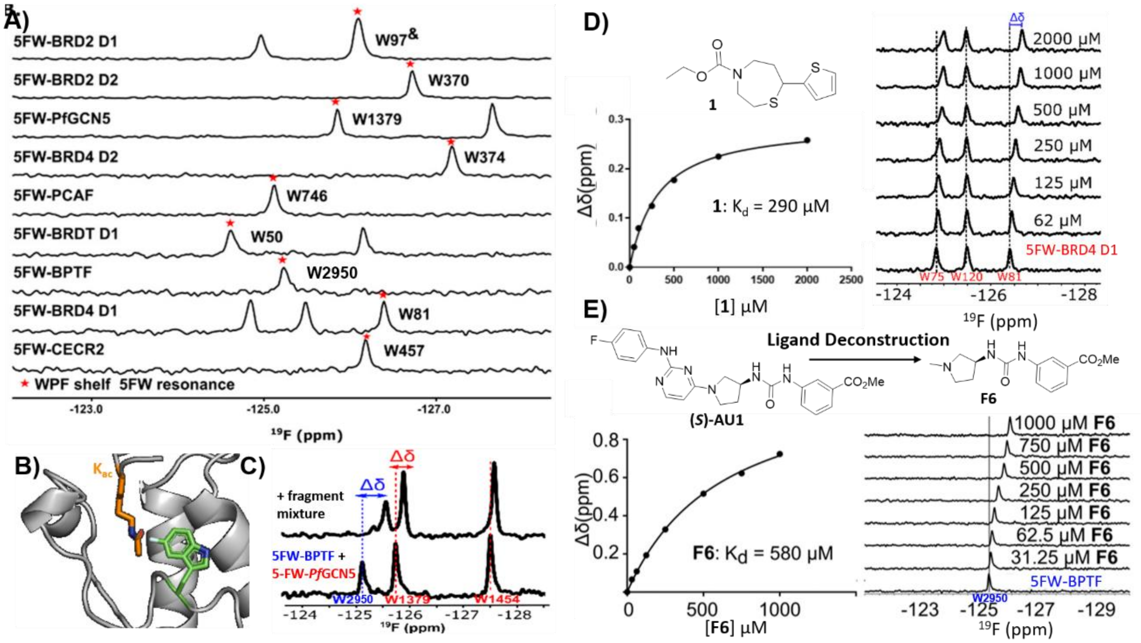

Figure 1.20: PrOF NMR Spectra of Bromodomains with Ligands

A) PrOF NMR spectra of various 5FW-labeled bromodomains. The tryptophan reporter residue located in the WPF shelf denoted by asterisk. (adapted from ref. 53 with permission from MDPI, copyright 2020). **B)** The tryptophan reporter residue (5FW) in bromodomains is adjacent to the acetyl lysine (K_{ac}) binding site.

(PDB:3QZS, pending) **C)** PrOF NMR titration of a fragment mixture that has hits for both 5FW-BPTF and 5FW *Pf*GCN5 in a dual protein mixture (adapted from ref. 53 with permission from MDPI, copyright 2020). **D)** PrOF NMR titration with fragment hit **1** with 5FW-BRD4 D1 and K_d determination from W81. (adapted from ref. 53 with permission from American Chemical Society, copyright 2019). **E)** PrOF NMR titration with deconstructed fragment **F6** (from parent molecule **(*S*)-AU1**) with 5FW-BPTFand K_d determination from W2950. (adapted from ref. 47 with permission from Royal Society of Chemistry, copyright 2019).

To investigate potential advantages for screening 3D fragments, which have recently come into focus as a way to potentially enhance library diversity,[164,165] a 467 member 3D-enriched fragment library was screened against 5FW-BRD4 D1 in the same workflow using PrOF and ^{1}H CPMG NMR for a direct comparison.[53] The overall hit rate was lower in comparison to the traditional library screen described above, which is often a concern due to the increased complexity of more 3D fragments. Nonetheless, novel hits were discovered with high affinity and selectivity towards BRD4 D1 over structurally similar bromodomains from the same family (bromodomain and extra-terminal (BET) family). Structure-activity relationship studies were conducted on a highly 3D 1,4-acylthiazepane scaffold leading to a ligand efficient (0.41), 20 μM binder (**Figure 1.20D**). 1,4-acylthiazepanes were later shown to have ~10-fold higher affinity for the second bromodomain of BET proteins, using fluorine-labeled constructs containing the two tandem bromodomains of BRD4 and BRDT.[208]

Bromodomain selectivity is challenging because of their relatively conserved acetyl lysine binding sites. Screening of protein mixtures is one method to enable selectivity information upfront. In PrOF NMR, the simplicity and large chemical shift dispersion of ^{19}F resonances allows ease of screening in mixtures. 5FW-BRD4 D1, which was used in previous screening efforts, and another bromodomain, 5FW-BPTF, have three resonances (W75, W81, W120) and one resonance (W2950) respectively that are sufficiently resolved. As a proof of concept, known inhibitors, including kinase inhibitors selective for BRD4-D1 over BPTF, were shown to selectively perturb W81 (the main reporter resonance in BRD4 D1 located near the binding site) and not W2950 in a mixture.[206] Urick et al. proceeded to screen a 229 small molecule library (published kinase inhibitor set (PKIS I and II)) against 5FW-BRD4 D1 and 5FW-BPTF simultaneously which led to new selective leads for each protein.[46]

Examining the hits for BRD4 D1, SB-284851-BT, a 1,4,5- trisubstituted-imidazole, was identified as one of the strongest binders.[46] When further characterizing selectivity of 1,4,5-trisubstituted-imidazoles across BET family bromodomains, Divakaran et al. found a preference for binding to the first bromodomains (D1s), with a >55 fold selectivity for BRD4 D1 compared to BRD4 D2 for compound **V**.[211] Cui et al. used this knowledge to design an improved inhibitor, **5**, with submicromolar affinity and 9-33 fold selectivity for BRD4 D1 over the remaining BET bromodomains.[212] The selectivity for BRD4-D1 was further confirmed using the fluorine-labeled BRD4 tandem domain construct.[208]

Of the small molecule hits for BPTF from the dual screen with BRD4 D1, the tightest binders were molecules with arylurea motifs.[46] AU1 was selected for follow-up, which in its racemic form had a K_d of 2.8 μM by ITC, and by PrOF NMR titrations it was determined that (*S*)-AU1 was the active enantiomer perturbing the reporter resonance, W2950, in the acetyl lysine binding pocket.[46,47] Furthermore, Kirberger et al. used PrOF NMR to guide SAR efforts to improve the solubility and stability concerns, as well as ligand deconstruction to determine the contribution of each fragment to guide potency gains (**Figure 1.20E**).[47] Unfortunately there were no significant improvements made in regard to these efforts, but these experiments demonstrate the utility of PrOF NMR in hit optimization. Examining bromodomain selectivity by PrOF NMR, AU1 was shown to be the first selective inhibitor of BPTF with selectivity over BRD4 D1 and moderate selectivity over a highly homologous bromodomain, PCAF. Recently a combined workflow which consists of PrOF NMR fragment screening followed by hit mixture deconvolution by ^{1}H CPMG NMR against two bromodomains (BPTF and *Pf*GCN5) simultaneously has been reported, which cuts down on time and resources needed for FBDD (**Figure 1.20C**).[209]This work on selective bromodomain inhibitor development aided by PrOF NMR highlights ^{19}F NMR as a useful tool from screening through chemical probe development.

1.6.7.6 Quantification of Weaker Interactions in Intermediate and Slow Exchange

The sensitivity of PrOF NMR is suited for quantifying weak interactions like fragments and peptides, and benefits from increased resolution versus ^{1}H,^{15}N-HSQC NMR;[213] however, ligand binding that is in intermediate chemical exchange can be challenging to quantify. To address this challenge, Stadmiller et al. demonstrated the use of ^{19}F NMR lineshape analysis to quantify both binding constants and kinetic rates of association of protein-ligand interactions.[214] The stabilized T22G drosophila drk N-terminal SH3 domain was metabolically labelled with 5FW at W36, located near the binding interface, and the results of 1D ^{19}F lineshape analysis were compared to the more well-established 2D ^{1}H,^{15}N-HSQC NMR. Four reported peptide binders, derived from the SH3-SOS interactions, were evaluated. The peptides exhibited interactions on the intermediate or milliseconds (ms) timescale (exchange rate ~0.01–100 ms) with SH3, which is appropriate for lineshape broadening analysis. Experimentally derived parameters K_d, k_{on}, and k_{off} were nearly equivalent for all peptides by 1D ^{19}F NMR compared to 2D ^{1}H,^{15}N-HSQC NMR. ^{19}F NMR was used here as a faster method, with a five minute acquisition time in comparison to 20 min for 2D HSQC NMR experiments, which along with ease of analysis makes it a useful tool in probing weak ligand interactions.

In some instances weaker binders can exhibit slow exchange. In this case, the integration of the peak intensity of the bound and unbound states can be used to derive a K_d when the K_d is near or above the protein concentration avoiding stoichiometric binding. Such a case was observed for the carbohydrate binding protein LecA studied by Shanina et al. for lectin inhibitor development.[181] LecA was metabolically labelled with 5FW at all four native tryptophan residues, of which W42 and W33 are near the binding site of the natural carbohydrate ligand, D-galactose. 5FW-LecA was titrated with known weak binder, N-acetyl D-galactosamine. Despite weak affinity, two distinct W42 resonances were detected as ligand was added, indicating slow chemical exchange. The K_d was calculated from the change in peak intensity of the W42 resonance over ligand concentration and found to be 780 μM. As tryptophans are frequently found in carbohydrate binding sites,[215] a similar PrOF NMR approach could be applied to lectin drug-discovery campaigns.

1.6.7.7 ^{19}F NOE and PRE Experiments for Characterizing Biopolymer Structure and Dynamics

^{19}F NMR can be exploited to obtain structural information of protein-ligand complexes, in particular through extracting interatomic distances. In the case of ^{19}F-^{19}F NOEs where a protein and ligand are both fluorine-labeled, short range information can be obtained. In the first such intermolecular application with small molecules and proteins, Bcl-xL, a popular anticancer target, was metabolically labelled with 4FF at ten residues.[216] Addition of a known inhibitor with three fluorine resonances led to observable crosspeaks in the resulting NOESY spectrum (**Figure 1.21A**). This result indicated strong intermolecular NOEs between the ligand and protein consistent with known structural information. Prior work assessing intramolecular interactions has been performed on rhodopsin,[217] SH3 domains,[218] and a fatty acid binding protein.[219,220] More recently intramolecular NOEs were observed between two pentafluorosulfonyl-substituted phenylalanines In a folded protein.[221]

^{19}F paramagnetic relaxation enhancement (PRE) experiments complement NOE experiments with longer range information. The Gronenborn lab has showed this technique to give structural information over distances of 12-24 Å, which is comparable to ^{1}H PRE (13-25

Å).[222] This was shown in a case study with lectin cyanovirin-N (CV-N), which was labeled with the commonly used spin label MTSL, introduced by mutated cysteines in a linker region, and differentially fluorine-labeled amino acids, at either W49 or F4, F54, and F80. (**Figure 1.21B**). These type of long distance studies can help elucidate 3D structure when traditional structure studies are not tractable, particularly useful for studies of large, globular proteins, membrane proteins, or fragment-protein complexes which may be more difficult to crystallize. PRE measurements have also been used to show dynamic conformational effects within Myc upon Myc-Max heterodimer formation and interactions with DNA.[223]

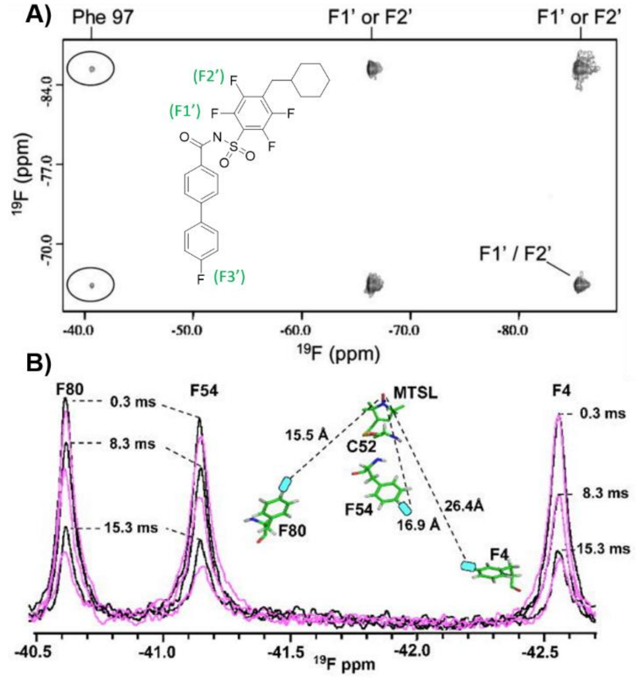

Figure 1.21: ^{19}F NOE and PRE Experiments.

A) ^{19}F-^{19}F NOESY spectra of 4FF-Bcl-xL with a fluorinated ligand, protein-ligand complex crosspeaks circled (adapted from ref. [216] with permission from Springer, copyright 2006). **B)** ^{19}F NMR spectra of 4FF-MTSL labeled CV-N reduced (black) and oxidized (magenta) at differing relaxation delays (adapted from ref. [222] with permission from Wiley-VCH, copyright 2016).

1.6.7.8 In-cell ^{19}F NMR

The absence of ^{19}F in biological systems makes the transition to in-cell studies a natural advancement, as it avoids spectral background signals. Early studies were completed in the yeast *S. cerevisiae* by inducible expression of target proteins and labeling with 5FW to measure protein mobility in cells.[224–227] The scope of methodology has since been expanded to other systems beyond yeast. An early example in *E. coli* monitored protein conformational changes upon ligand binding to enzymes by site-specific incorporation of trifluoromethyl-L-phenylalanine (tfmF) at TAG nonsense codons.[176] Seminal contributions in the field by Pielak and co-workers identified methodology to overcome signal broadening of globular proteins in cells. Experiments with ^{15}N-labelled and 3FY-labelled globular proteins, like GFP, failed to detect signal due to the high viscosity of cells and nonspecific interactions.[116] Alternatively ^{19}F NMR spectra for α-synuclein, a disordered protein, both in vitro and in cells indicated that the internal motion of disordered proteins could retain resolved ^{19}F resonances.[228] The use of tfmF, which has a CF_3 group that has its own internal fast bond rotation, also resulted in observable in-cell NMR resonances in two tested globular proteins (GFP and HDH).[116] In a systematic evaluation of labeling methods for in-cell NMR, it was recommended to first use ^{19}F- or ^{15}N- labeling, highlighting the power of ^{19}F for in cell NMR. The major limitation that still exists is with proteins that interact strongly with other biomolecules in cells, causing signal broadening and making detection difficult.[229] Despite this, in-cell ^{19}F NMR has continued to be used in several applications including protein stability,[230] protein mobility,[231] and thermodynamic analyses.[232] Additionally, novel models systems have been investigated as more robust and less crowded systems for in-cell ^{19}F NMR.[233]

1.6.8 Outlook and ^{19}Future Directions

Looking towards the future, we anticipate a sustained increase in innovative new methods for characterizing protein-ligand interactions via both ligand-observed and protein-observed ^{19}F

NMR. Now that significant signal enhancements can be achieved due to the availability of high sensitivity ^{19}F NMR cryoprobes, the repertoire of experiments continue to increase, including techniques such as dynamic nuclear polarization.[234] These experiments significantly augment the structural and quantitative binding information that can be achieved for FBDD. Such advances also continue to fuel innovation in chemical synthesis, as more fluorinated small molecule libraries are available and new synthetic strategies are being developed. In the case of ligand-observed NMR screening, the library sizes for screening has significantly increased and now benefit from improved pulse sequences allowing for larger mixture sizes and higher throughput. We anticipate these methods to continue to be applied to more challenging drug targets such as RNA. ^{19}F-^{19}F ILOE NMR experiments discussed above can also help researchers address the challenges of fragment linking, even in the absence of crystal structures. New innovations in both ^{19}F-^{19}F and ^{1}H-^{19}F NOE experiments are also anticipated in the future to guide inhibitor development.

In our last perspective, we noted the significant challenge of ^{19}F CSA as a limitation for protein-observed ^{19}F NMR.[98] However since that time, Aryl ^{19}F-^{13}C TROSY methods have been reported for biopolymers,[115] and have now been applied to ligand binding.[129] However only a limited set of fluorinated amino acids and nucleic acids have been used, in part due to the requirement of specific ^{13}C and ^{19}F labeling. Improved access to these building blocks may augment the types of biopolymers which can be studied by this approach. Finally, quantifying the dynamics associated with ligand binding in addition to the thermodynamic binding affinity is another source of continued development in ^{19}F NMR. We envision broader adoption of these methods by the research community. While lineshape analysis and PRE measurements were described above, quantitative measurements of slow time scales for binding interactions can also be measured via CPMG-based relaxation dispersion ^{19}F NMR and newer innovations with off and on resonance R1ρ experiments.[235] The latter allows for faster dynamics to be assessed while longer time scale protein-ligand interactions can be probed with chemical exchange saturation transfer (CEST) ^{19}F NMR.[236,237] The experiments covered here and those currently being developed will continue to provide a wealth of information for capturing dynamic biomolecular interactions, fueling new advances in drug discovery.

1.7 Preface to this Thesis

The following thesis describes my work on developing chemical probes for epigenetic reader domains of BPTF through screening and structure-based design. Chapter 2 is published work in the *Journal of Medicinal Chemistry* describing rational design of BPTF bromodomain inhibitors around a pyridazinone scaffold and design rules for future inhibitor development. Chapter 3 expands on the lead compound from the previous chapter, **BZ1**, and its application in cell toxicity studies, heterobifunctional molecules, and further selectivity gains. Chapter 4 describes a fragment-based screen against the BPTF PHD finger and the identification of hit scaffolds for further lead development, which is in preparation for publication. Chapter 5 is unpublished work that further explores BPTF PHD hit scaffolds through preliminary SAR, studying binding interactions, and examining selectivity. Finally, the appendices detail two published collaborative projects using structural biology to assist BRD4 bromodomain inhibitor development in the Pomerantz Lab and alpha-synuclein pH effects in collaboration with the Sachs lab in the Department of Biomedical Engineering.

1.8 Acknowledgements

Figures 1.1, 1.2, 1.8, 1.9 1.12, 1.13, 1.16a, 1.17, 1.18 created using BioRender.

2) New Design Rules for Developing Potent, Cell-Active Inhibitors of the Nucleosome Remodeling Factor (NURF) via BPTF Bromodomain Inhibition

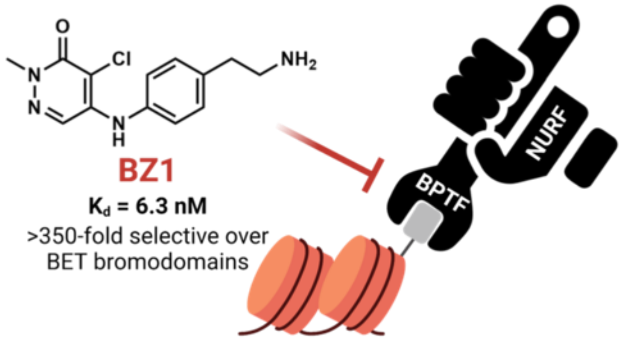

Reprinted with permission from ref.[55] Zahid, H.;* Buchholz, C. R.;* Singh, M.; Ciccone, M. F.; Chan, A.; Nithianantham, S.; Shi, K.; Aihara, H.; Fischer, M.; Schönbrunn, E.; dos Santos, C. O.; Landry, J. W.; Pomerantz, W. C. K. New Design Rules for Developing Potent Cell-Active Inhibitors of the Nucleosome Remodeling Factor (NURF) via BPTF Bromodomain Inhibition. *J. Med. Chem.* **2021**, *64* (18), 13902–13917. Copyright (2021) American Chemical Society.

Contribution of Authors: H.Z. and C.R.B. synthesized the compounds and performed NMR experiments; H.Z. performed AlphaScreen assays; M.S. and M.F.C. performed cellular experiments; H.Z., C.R.B., A.C., S.N. and K.S. performed crystallography; E.S., H.A., C.O.D.S., M.F., J.W.L. and W.C.K.P. oversaw the experiments and interpretation of data; H.Z., C.R.B. and W.C.K.P. wrote the manuscript. All authors have given approval to the final version of the manuscript. *These authors contributed equally.

Motivation: The goal of the work described in this chapter is to build on previous BPTF bromodomain inhibitor development described in Chapter 1 (Section 1.3). We sought to use established biophysical assays and x-ray crystallography to further elaborate the pyridazinone scaffold into a more potent BPTF bromodomain inhibitor. We have also begun to study the effect of these inhibitors on cancer cell toxicity and BPTF target genes discussed in sections 2.2.6 and 2.2.7. The cellular activity is further elaborated upon in Chapter 3.

2.1 Introduction

Epigenetic processes involve heritable changes in gene expression without altering the underlying DNA sequence.[238] Gene accessibility leading to these changes occurs through mechanisms such as DNA methylation, covalent modifications of histones, chromatin remodeling, and exchange of histones.[239] In the case of chromatin remodeling, ATP-dependent processes are catalyzed by multidomain protein complexes which include SWI/SNF, ISWI, CHD and INO80.[240] Of these, SWI/SNF has been extensively studied and is implicated in ~20% of human cancers.[241] The mammalian SWI/SNF complexes, BAF and PBAF, have emerged as attractive epigenetic therapeutic targets, for which chemical inhibitors and catalytically degrading molecules of complex members BRD7 and BRD9 have been developed.[242,243] In contrast, the ISWI family is less well-studied for its potential role as a therapeutic target. Nucleosome Remodeling Factor (NURF) is one member of the ISWI family, consisting of an ATPase domain SNF2L, a WD-repeat protein RbAP46/48, and a chromatin-binding protein, BPTF (**Figure 2.1A**).[244] Chemical probe development for these complex members remains at an early stage.[245]

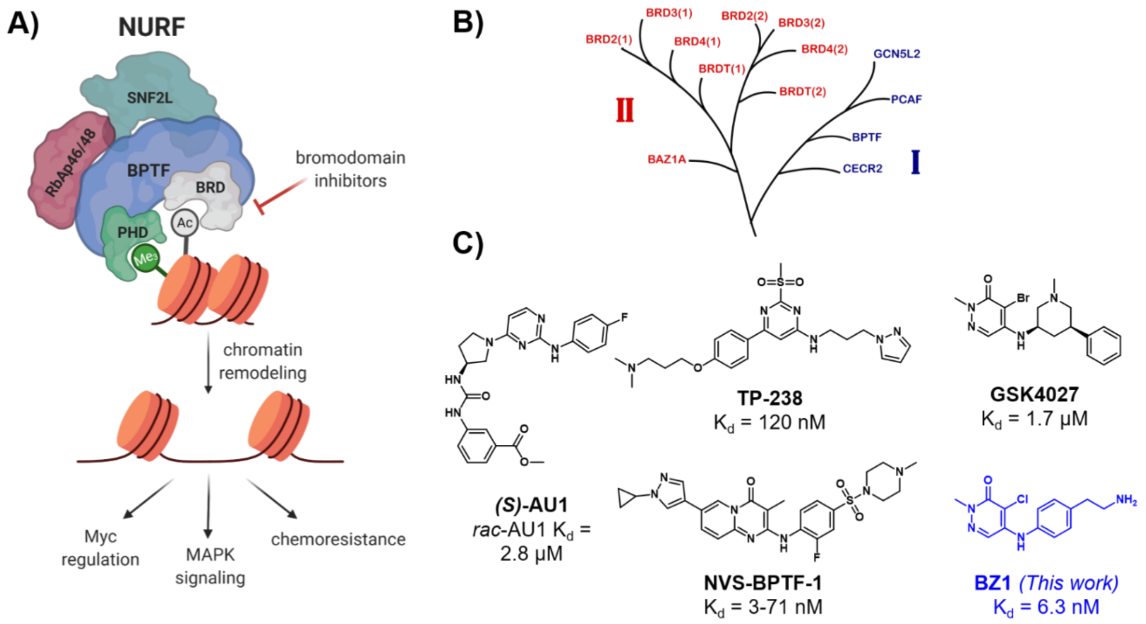

Figure 2.1: BPTF Interactions with Chromatin, Downstream Signaling, and Reported Small-Molecule Inhibitors.

A) BPTF interacts with chromatin through the bromodomain (BRD) and PHD domain, directing the chromatin remodeling complex NURF to genes, leading to downstream phenotypic effects such as Myc regulation, MAPK signaling and resistance to chemotherapeutics. B) Part of the bromodomain phylogenetic tree, showing class I and class II (BET) bromodomains (adapted with permission from Pomerantz et al.[246]). C) Reported BPTF bromodomain inhibitors with in vitro affinities.

BPTF (Bromodomain PHD Finger Transcription Factor) is the largest subunit of NURF and is considered essential for its function.[247] BPTF contains a bromodomain, two PHD fingers, a DNA-association domain, three nuclear receptor binding motifs, and a glutamine-rich domain.[248] Both the bromodomain and C-terminal PHD domain are structurally well-characterized and are responsible for binding to acetylated and methylated histones respectively.[249] While BPTF is known to be essential in normal cellular processes such as embryonic development,[250] T-cell homeostasis[251] and differentiation of mammary epithelial cells,[252] the oncogenic effects of BPTF have been recently well-documented. BPTF is overexpressed in melanoma, where it impacts MAPK signaling, and is regulated by the melanocyte-inducing transcription factor, MITF.[253,254]

High BPTF levels correlate with c-Myc expression in various cancers, regulation of Myc signaling, and Myc protein-protein intractions.[255,256] Additional oncogenic roles for BPTF have been found in breast cancer,[252] non-small-cell lung cancer,[24] colorectal cancer,[257] and high-grade gliomas.[20,21]

BPTF also confers chemoresistance to cancer cells; overexpression of BPTF promotes resistance to BRAF inhibitors in melanoma[253] and knockdown of BPTF sensitizes hepatocellular carcinoma cells to chemotherapeutic drugs.[258] The implication of BPTF in cancer and its key role as a NURF subunit makes it a potential new therapeutic target for small-molecule inhibitor development. One attractive targeting element is the bromodomain, which is computationally predicted to be highly druggable.[259] However, the role of the bromodomain in many of these disease states needs to be established.

While inhibitor development for class II bromodomain and extraterminal domain (BET) family proteins (**Figure 2.1B**) have resulted in translation of numerous inhibitors into the clinic,[260] non-BET class I bromodomains such as BPTF have received less attention.[261] To address this need, we reported AU1 as the first small-molecule inhibitor of the BPTF bromodomain (K_d = 2.8 μM, **Figure 2.1C**).[262] Importantly this molecule was selective over the BET protein BRD4, given the strong phenotype of BRD4 in regulating cell cycle, proliferation, and inflammatory pathways.[263] AU1 has since been used in mouse mammary epithelial cells showing decreased proliferation, cell cycle arrest, and reduced c-Myc-DNA occupancy;[252] however in other cell lines, off-target activity was identified.[264] Most recently, AU1 showed enhancement of anti-cancer activity when used in combination with the chemotherapeutic drug doxorubicin in vitro and in vivo in 4T1 breast cancer models.[265] Mechanistic studies showed these processes to be autophagy-dependent and AU1 effects on topo2-isomerase-DNA crosslinks and DNA damage recapitulated the effects from BPTF knockdown experiments. However, the off-target kinase activity of AU1, its poor physicochemical properties, and low ligand efficiency, posed significant challenges to inhibitor development and highlighted the need for new and more potent BPTF inhibitors. Recently, several inhibitors were disclosed online by the structural genomics consortium; TP-238, a dual CECR2/BPTF chemical probe (12-fold higher affinity for CECR2 over BPTF)[266] and NVS-BPTF-1, a potent BPTF inhibitor in vitro but with poor solubility and ADME properties (**Figure 2.1C**).[267,268] Encouragingly, TP-238 administration to cells was shown to reduce BPTF chromatin binding, supporting the importance of bromodomain inhibition.[266] However, detailed reports and their characterization have yet to be described in the primary literature. Given the emerging role of BPTF in cancer, there is a significant need for improved potent and selective inhibitors.

Here we describe the development of BPTF bromodomain inhibitor **BZ1** with nanomolar affinity (K_d = 6.3 nM) and > 350-fold selectivity over BET bromodomains. This inhibitor and analogues are obtained via a facile synthesis route with no more than 2-3 synthetic steps. The high affinity, aqueous solubility, and physicochemical properties of these inhibitors enabled us to obtain several cocrystal structures with BPTF for rationalizing our structure-activity-relationship data and to identify an acidic triad as a targetable feature of the binding site for future inhibitor development. Finally, we use the 4T1 breast cancer cell chemotherapeutic synergy model previously validated for BPTF on-target engagement,[265] to show that our scaffolds are both generally well-tolerated by cells, and enhance doxorubicin cytotoxic effects to wild type breast cancer cells but not identical cells with BPTF knockdown, demonstrating specificity in their biological activity. The improved biochemical properties and cellular activity of **BZ1** makes it a lead scaffold to further efforts in selective BPTF inhibitor discovery for developing new BPTF-specific chemical tools. Future work will focus on engineering selectivity for BPTF over other class I bromodomains and the BRD7/9 off-targets of this scaffold.

2.2 Results and Discussion

As a first step towards BPTF inhibitor development, we recently cross-validated several biophysical assays for BPTF ligand screening including a competitive inhibition AlphaScreen assay using an acetylated histone peptide and SPR binding experiments. We used several compounds reported in the literature or online, including TP-238 and GSK4027, a PCAF/GCN5L2 inhibitor[269] with off-target affinity for BPTF (K_d = 1.7 µM, **Figure 2.1C**). Using these inhibitors and new fragment compounds from our lab, we reported a number of small-molecule cocrystal structures with the BPTF bromodomain.[270] From these studies, we chose GSK4027 for further analysis to establish design rules for inhibitor development.

From our cocrystal structure of GSK4027 with the BPTF bromodomain (**Figure 2.2**), the carbonyl group acted as the acetyl lysine histone mimic, forming a hydrogen bond with N3007, and the bromine atom pointed into the binding pocket. The pyridazinone core formed π-stacking interactions with the gatekeeper residue F3013 (not shown here, see **Figure 2.7**). The WPF shelf was engaged by hydrogen bonding to the P2951 backbone and W2950 by an edge-to-face interaction with the pendant phenyl ring, as previously shown with PCAF/GCN5L2.[271] In - addition, we identified the acidic patch residues D2957 and D2960 as key targets for inhibitor design (**Figure 2.2 inset**). We also showed that TP-238 could engage these side chains supporting this approach.[270] Among class I bromodomains, BPTF is the only member with two acidic groups at this site so we hypothesized that interactions with these side chains could improve both affinity and potentially selectivity for BPTF. We anticipated that these interactions would provide multiple sites to fine-tune the potency and selectivity of our inhibitors.

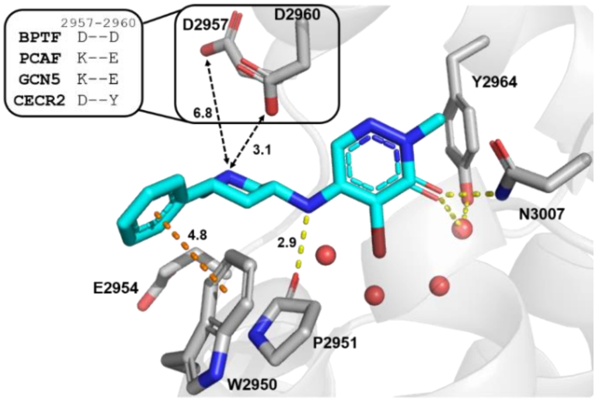

Figure 2.2: Co-crystal structure of GSK4027 (cyan) with BPTF bromodomain (gray, PDB: 7K6R). Four conserved structured waters are shown as red spheres. Hydrogen bonds are shown as yellow dashed lines and aromatic interaction as orange dashed line. The distances (Å) between key residues are indicated. Inset: Residues in other class I bromodomains (PCAF, GCN5 and CECR2) corresponding to D2957 and D2960 in BPTF.

We first tested 4,5-dichloropyridazinone, as a parent fragment of GSK4027 representing the acetylated lysine pharmacophore for the BPTF bromodomain. We used protein-observed fluorine (PrOF) NMR as a sensitive biophysical assay to quantify weak interactions with BPTF, using a fluorine-labeled tryptophan at W2950.[272] In this experiment, the protein resonance showed a significant dose-dependent shift and broadening below 100 µM of the compound (Figure 2.3). A dose-dependent chemical shift perturbation at low concentrations was consistent with significant affinity of this pharmacophore for BPTF.

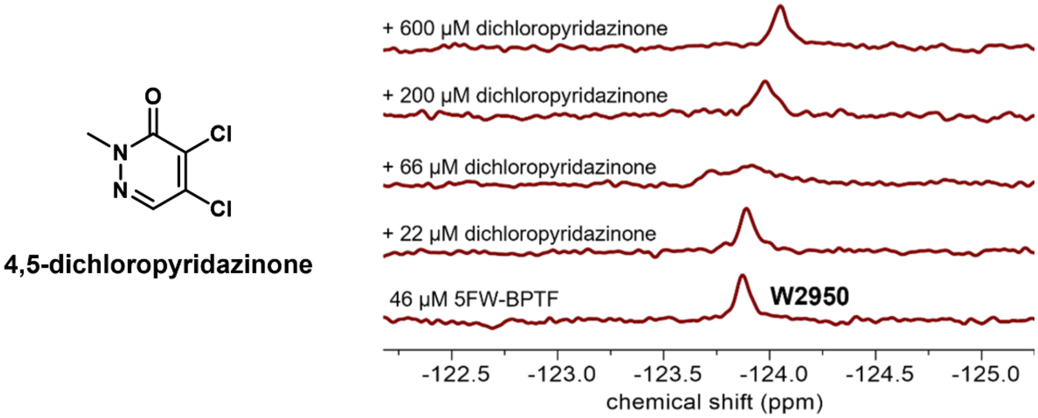

Figure 2.3: PrOF NMR titration of 4,5-dichloropyridazinone with 5FW-BPTF.

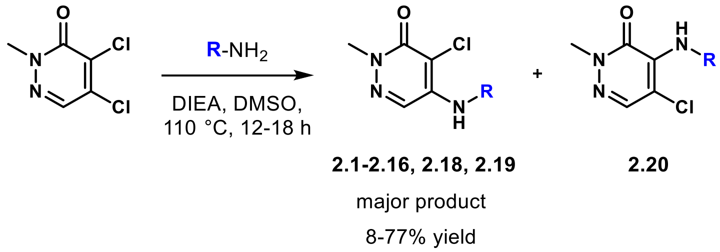

Scheme 2.1: Nucleophilic aromatic substitution with 4,5-dichloropyridazinone and primary amines

Encouraged by the apparent potency of the starting fragment and the relatively facile synthesis towards elaborated compounds (**Scheme 2.1**), we generated a library of pyridazinone-containing aliphatic amines similar to GSK4027 (**Table 2.1**) and tested them with BPTF using PrOF NMR and the competitive inhibition AlphaScreen assay described in Chapter 1.[270]

2.2.1 Aliphatic Pyridazinone Series

The initial synthesis started with a nucleophilic aromatic substitution reaction with various aliphatic amines, generating the desired compounds **2.1-2.5** as the major isomers (**Table 2.1**). Our initial characterization of the affinity of **2.1-2.3** was recently reported.[270] The IC_{50} values ranged from 7.7-31 μM. Although we were unable to significantly increase the affinity of these analogues, we were encouraged by their ligand efficiency (0.38-0.49), which were a significant improvement over AU1 (0.22) and in agreement with the benchmarked value of ~0.3 for suitable drug candidates.[273] To gain structural insight, we acquired cocrystal structures of compounds **2.1-2.4** with BPTF (**Figure 2.4**). These structures supported the importance of the exocyclic amine in maintaining the hydrogen bonding interaction with the backbone carbonyl of P2951, similar to GSK4027. However, the ring size and position of the endocyclic amine group did not significantly impact the affinity of the compounds and accessibility to the acidic D2957 and D2960 side chains. Interestingly, these crystal structure revealed a water-mediated hydrogen bond with E2954, an interaction not previously explored in BPTF inhibitor design.

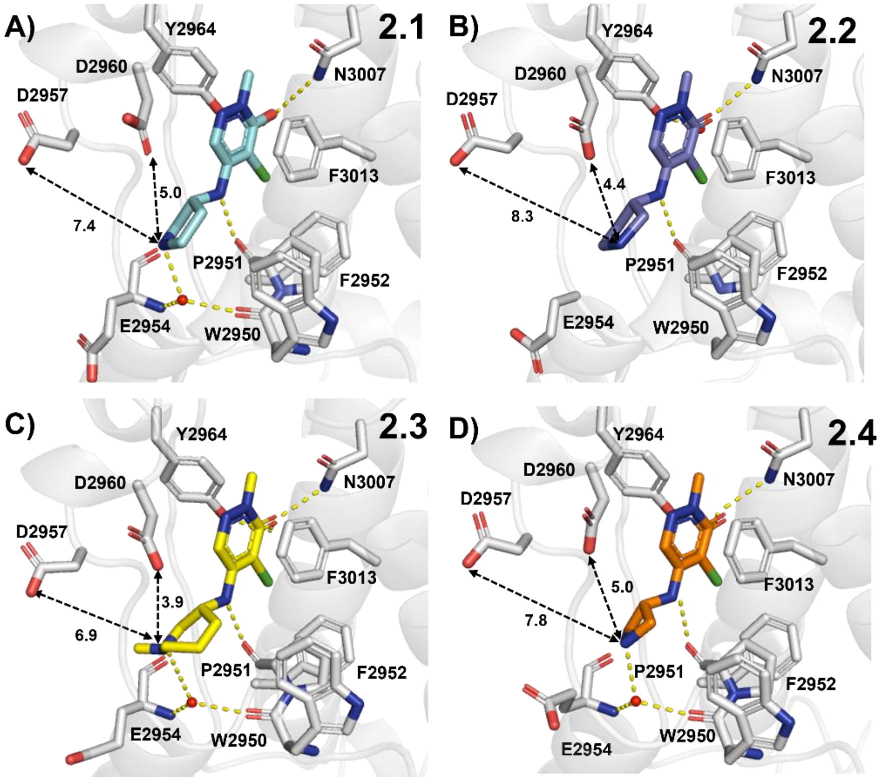

Figure 2.4: BPTF bromodomain (gray) cocrystal structures with Compounds 2.1-2.4

A) **2.1** (PDB: 7LPK, 1.39 Å resolution), B) **2.2** (PDB: 7LRK, 1.44 Å resolution), C) **2.3** (PDB: 7LPO, 1.66 Å resolution), and D) **2.4** (PDB: 7LRO, 1.45 Å resolution). Hydrogen bonds are shown as yellow dashed lines. The distances (Å) between key residues are indicated. Three of the conserved structured waters are excluded for clarity.

Table 2.1: SAR with aliphatic pyridazinones and BPTF.

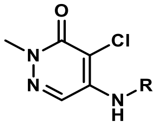

2.1-2.5

	R	BPTF AlphaScreen IC_{50} (μM)	L.E.
GSK 4027	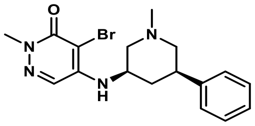	1.5 ± 0.2[270]	0.35

2.1	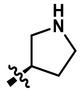	10 ± 2[270]	0.45
2.2	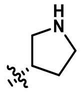	31[270]	0.41
2.3	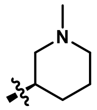	19[270]	0.38
2.4	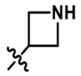	8.7	0.49
2.5	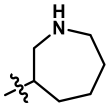	7.7	0.41

AlphaScreen values were an average of two technical replicates with N = 1, except for GSK4027 and **2.1** which were averages of six and three experimental replicates, respectively. Binding isotherms shown in Error! Reference source not found..

2.2.2 Aromatic Amine Substituted Pyridazinones

Based on our hypothesis that the N-H interaction with P2951 was critical for the affinity of our pyridazinone inhibitors, we proposed that the more acidic anilinic N-H could be a stronger H-bond donor compared to aliphatic amines.[274] Therefore, in our second series of inhibitors, we investigated aromatic amine-substituted pyridazinones (**Table 2.2**). The aniline-substituted compound **2.6** (previously reported as a PCAF and BRD9 inhibitor with affinities of 10 μM and 2.5 μM respectivley[275]) demonstrated a 10-fold improvement in affinity and higher ligand efficiency (L.E.) compared to our previous aliphatic amine analogues.

Table 2.2: Aniline-substituted pyridazinones and substituent effects for binding to BPTF.

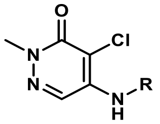

	R	BPTF AlphaScreen IC_{50} (μM)	L.E.

2.6	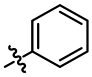	0.95	0.51
2.7	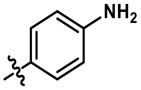	3.2	0.44
2.8	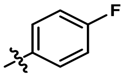	0.70	0.49
2.9	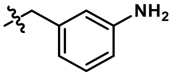	11	0.40

AlphaScreen values were an average of two technical replicates, N = 1. Binding isotherms shown in Error! Reference source not found..

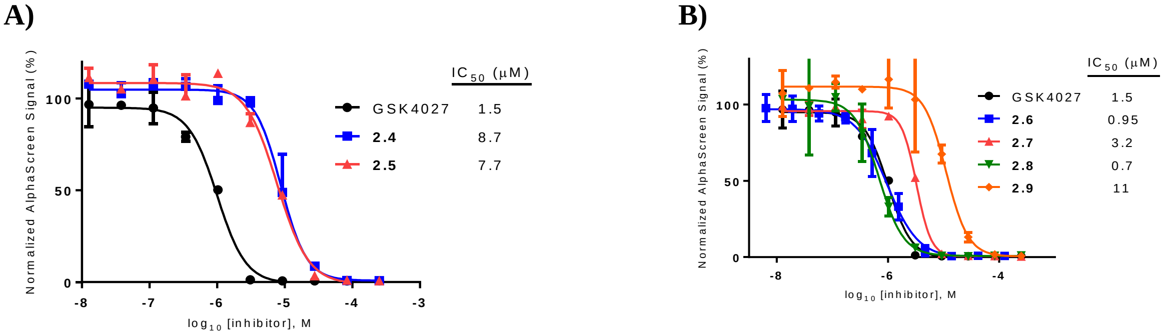

Figure 2.5: AlphaScreen of BPTF with compounds from A) Table 2.1 and B) Table 2.2.

We compared the effects of electron-donating and -withdrawing substituents on the aromatic ring and found that the *para*-fluoro group (**2.8**) led to an improved affinity compared to a *para*-amino group (**2.7**). This observation was consistent with the importance of the hydrogen-bonding interaction with the P2951 backbone, which would be assisted by an electron-withdrawing group on the ring and the more acidic character of the conjugate acid of the anilinic NH. In agreement with this data, compound **2.9**, containing a benzylic amine group attached to the pyridazinone core, was also a weaker binder of BPTF compared to **2.6** and **2.7**. Interestingly, an analogue of **2.9** was also recently identified as the starting fragment for BRD9 inhibitors, with $\mathrm{pIC_{50}} = 5.7$ and 6-fold selectivity over PCAF.[276]

2.2.3 Aromatic Pyridazinones: Effect of Basic Group Substitution

In a further round of SAR, based on our acidic patch hypothesis, we investigated different amine substitutions on the aromatic ring for engaging D2957 and D2960 (**Table 2.3**). Encouragingly, extending the NH_2 group or an *N*,*N*-dimethyl group by just one methylene (from compound **2.7** to **2.10** or **2.11**) resulted in a ~10-fold improvement in potency, with IC_{50} values of 0.29 μM and 0.31 μM, and ligand efficiencies of 0.50 and 0.44 respectively for compounds **2.10** and **2.11**. We attributed this gain in affinity to a potential electrostatic interaction between the amine group and the aspartate side chains of BPTF. Such an interaction was also consistent with the loss in affinity observed when the amine was removed (**2.14**) or the positive charge neutralized via acetylation (**2.17**).

Table 2.3: SAR with aromatic pyridazinones with different basic groups substitutions for binding to BPTF.

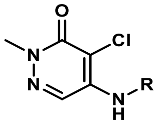

	R	BPTF AlphaScreen IC_{50} (μM)	L.E.
2.10	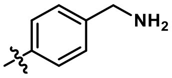	0.29 ± 0.08	0.50
2.11	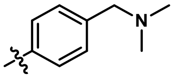	0.31	0.44
2.12	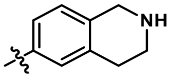	0.25	0.45
2.13	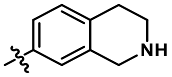	0.37	0.44
2.14	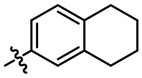	3.9	0.37
2.15	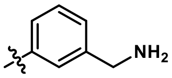	0.80	0.46

2.16	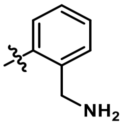	0.22	0.50
2.17	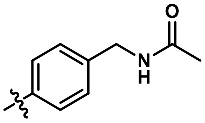	0.97	0.39

AlphaScreen values were an average of two technical replicates with N = 1, except for **2.10** where it was an average of three experimental replicates. Binding isotherms shown in **Figure 2.6.**

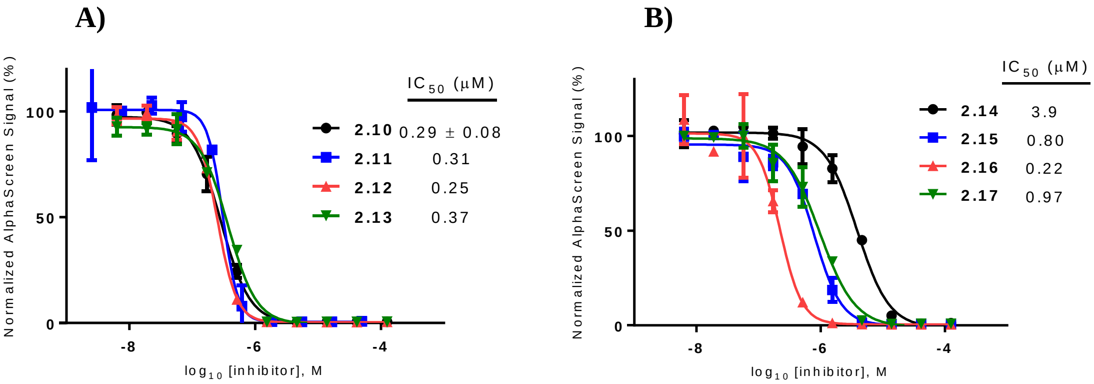

Figure 2.6: AlphaScreen titration of BPTF with compounds from Table 2.3.

We further looked at the effect of the position of the amine group, expecting to see significant differences based on which orientation of the group was more favorable for engaging D2957 and D2960. Surprisingly, the regioisomers **2.12** and **2.13** displayed similar affinities, which were comparable to **2.10**. In this series, **2.15**, where the amine was no longer restricted in a ring, was a weaker binder compared to **2.13**. While compound **2.16** showed a high affinity, it was obtained in the lowest synthetic yield and was also previously reported to have affinity for an off-target bromodomain, BRD9.[269]

We turned to X-ray crystallography to obtain structural information that could account for the similar affinities of our amine analogues **2.10-2.13** (**Figure 2.7**). Similar to our aliphatic amines, all cocrystal structures displayed the canonical hydrogen bonding with N3007 and water-mediated hydrogen bonding with Y2964 and a key hydrogen bond with P2951. The phenyl groups were 3.8-5.0 Å from W2950, which could contribute to the higher potency of our aromatic series over the aliphatics, forming a CH-π interaction. The amine group on compound **2.10** was 2.9 Å away from D2960, which could explain the improved affinity over compounds **2.7**, **2.14**, and **2.17**. While compound **2.12** retained these interactions, to our surprise, the different orientation of the basic group in compound **2.13** led to an interaction with E2954. Therefore, we attribute the improved affinities of our aromatic pyridazinone series compared to the aliphatics, to an additional aromatic interaction with the WPF shelf, strengthened H-bonding interactions with P2951, and differential engagement of side chains in a potential acidic triad (D2960, D2957 and E2954), depending upon the relative orientations of the amine moieties.

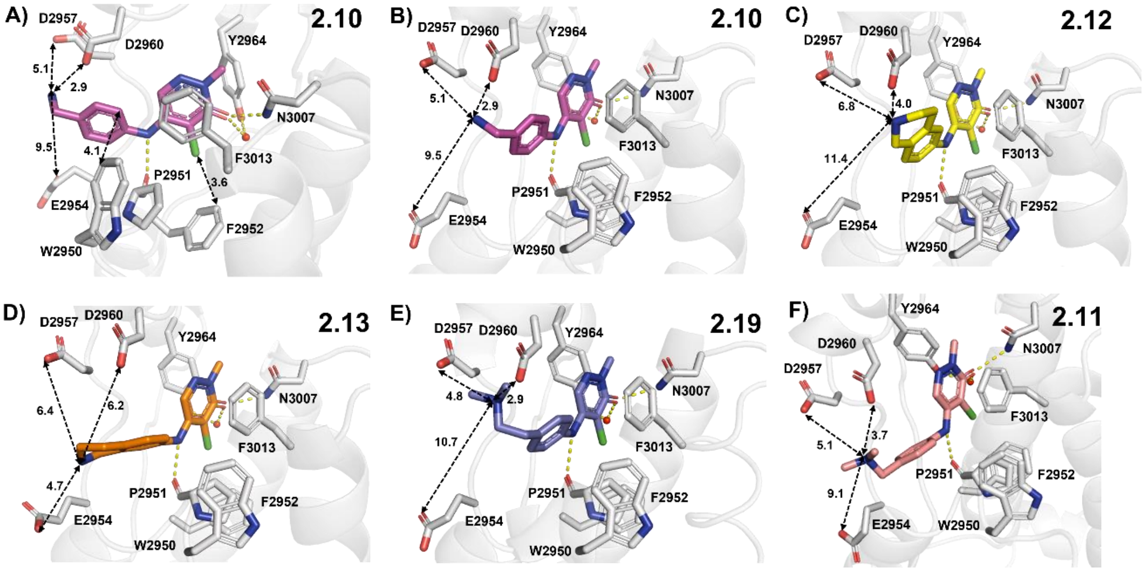

Figure 2.7: Co-crystal structures of BPTF bromodomain (gray) with compounds 2.10-2.13 and 2.19. A,B) **2.10** (magenta, PDB: 7RWP, 1.73 Å resolution), C) **2.12** (yellow, PDB: 7RWQ, 1.90 Å resolution), D) **2.13** (orange, PDB: 7RWO, 1.58 Å resolution), E) **2.19** (blue, PDB ID: 7M2E, 1.75 Å resolution) and F) **2.11** (PDB: 7RWN, 1.39 Å resolution). Hydrogen bonds are shown as yellow dashed lines. The distances (Å) between key residues are indicated. Three of the conserved structured waters are excluded for clarity.

Based on this structural analysis, we proposed that extending the amine group could lead to a further improvement in potency as D2957 was 5.1-6.8 Å away from the basic group on our compounds. In support of this, compound **2.18**, with just an additional methylene, showed a 4-

fold improvement in affinity over **2.10**, with an AlphaScreen IC_{50} of 67 nM and ligand efficiency 0.51 (Error! Reference source not found.). The *N*,*N*-dimethyl analogue, **2.19**, was slightly less potent, but may improve cellular permeability due to fewer hydrogen bond donors.[277] To test the importance of the H-bond with P2951, we also isolated the 4-position regioisomer **2.20**. Supporting this interaction, we measured a significantly reduced potency (IC_{50} = 10 μM). For future cellular studies, **2.20** can serve as an important negative control compound (140-fold weaker affinity than **2.18**).

Table 2.4: Aromatic pyridazinones with extended basic group.

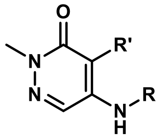

2.18, 2.19, 2.21, 2.22

	R	R'	BPTF Alpha Screen IC_{50} (μM)	L.E.
2.18 (BZ1)	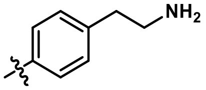	Cl	0.067 ± 0.01	0.51
2.19	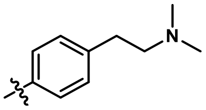	Cl	0.17	0.44
2.20	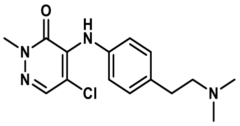	Cl	10	0.32
2.21	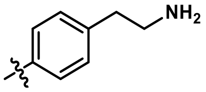	Br	0.036 ± 0.008	0.53
2.22	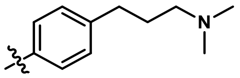	Cl	0.056 ± 0.01	0.45

AlphaScreen values were an average of two technical replicates, with N = 1 except for **2.18** (**BZ1**) which was an average of seven experimental replicates and **2.21**-**22** which were averages of three experimental replicates. Binding isotherms shown in **Figure 2.8**.

To validate our designs, we obtained a cocrystal structure of BPTF with **2.19**, a close analogue of our lead inhibitor **2.18** (**Figure 2.7E**). In this case, the amino group was now within 5 Å of D2957 and D2960, supporting the enhanced affinity for engaging either acidic group via electrostatic interactions.

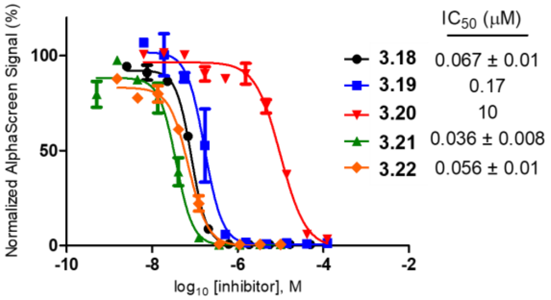

Figure 2.8: AlphaScreen titration of BPTF with compounds from Table 2.4.

2.2.4 Selectivity Profile of Compound 2.18 (BZ1) with Bromodomain Families

We next conducted a preliminary assessment of the selectivity of compound **2.18**, referred to as **BZ1** here onwards, using our PrOF NMR assay (**Figure 2.9B-D**). The tryptophan residue in the WPF shelf of three class I bromodomains, BPTF, PCAF, CECR2 and one class II bromodomain, BRD4(1) were fluorine-labelled (**Figure 2.9A**) and the chemical shift perturbation on titrating in **BZ1** was observed. For both BPTF and PCAF, a slow exchange regime stoichiometric titration was observed, with the bound and unbound resonances resolved at sub-stoichiometric concentrations of **BZ1**. CECR2 showed intermediate chemical exchange, indicating that **BZ1** was a weaker binder for CECR2 compared to BPTF and PCAF in this assay. Importantly, BRD4(1) demonstrated fast-intermediate exchange, showing qualitatively that **BZ1** was the weakest inhibitor for BET bromodomains under study here. We further used our AlphaScreen assay to quantify the affinity for BRD4(1) as a representative member of the BET family (**Figure 2.9E**). In this experiment, **BZ1** was found to be 400-fold selective for BPTF over BRD4(1), consistent with the PrOF NMR results. Selectivity over the BET family is important for non-BET chemical probes because BET inhibition shows a strong cellular phenotype which can mask any BPTF-dependent effects. In both BPTF and PCAF, an acidic residue is present in the acidic dyad, whereas in CECR2 and BRD4(1) the 3D equivalent is a tyrosine or leucine, respectively, and may account for some of the apparent selectivity differences (**Figure 2.2** and **Figure 2.9C**). Moreover, our PrOF NMR data also demonstrated that **BZ1** with a clogP = 1.6 can be titrated at high micromolar concentrations at 1% DMSO and shows dose dependence, indicating good solubility. The solubilities of **BZ1, 2.19,** and **2.20** were further confirmed up to 100 μM at 0.1% DMSO using UV-Vis spectroscopy (**Figure 2.19).**

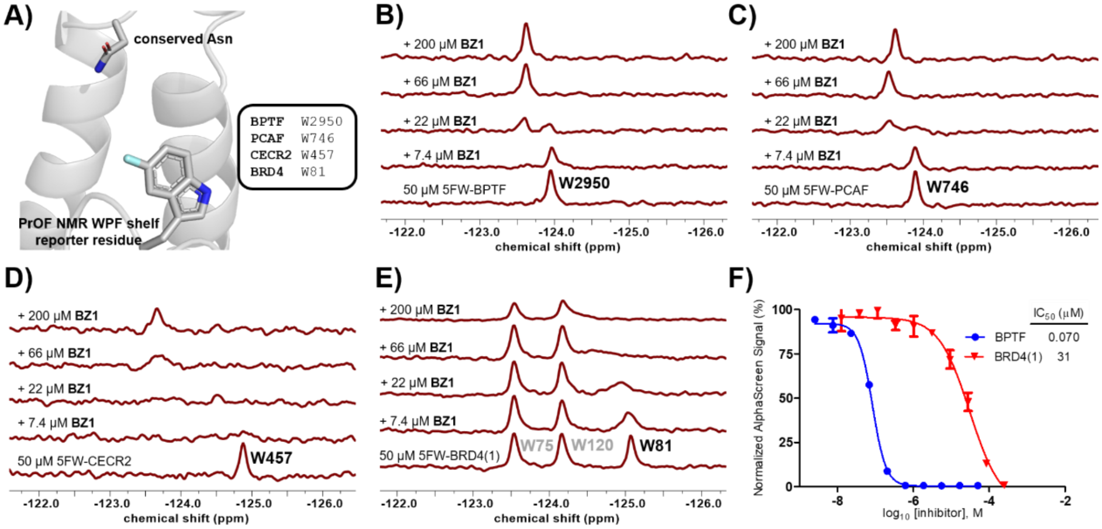

Figure 2.9: Selectivity analyses of BZ1 with representative bromodomains.

A) The tryptophan residues in the binding sites of BPTF (PDB ID: 7JT4), PCAF, CECR2 and BRD4(1) were fluorine-labeled to act as reporters for PrOF NMR. **BZ1** was titrated with 50 μM of 5-fluorotryptophan (5FW)-labeled proteins. Slow chemical exchange regimes were observed with B) 5FW-BPTF and C) 5FW-PCAF, indicating the high affinity of **BZ1** for these proteins. Intermediate exchange with D) 5FW-CECR2 and E) 5FW-BRD4(1) indicated **BZ1** was a weaker binder. F) Affinity values of **BZ1** for BPTF (blue) and BRD4(1) (red) were quantified using AlphaScreen competition experiments.

Based on the preliminary assessment of BPTF selectivity and affinity of **BZ1** by PrOF NMR and AlphaScreen competition assays, we next characterized our ligand using a commercial BROMOscan assay. Using this assay, the K_d of **BZ1** for BPTF was determined to be 6.3 nM (**Figure 2.10B**). Given the low concentration of ligand and protein used, AlphaScreen can be used to estimate K_i values as was previously the case for characterizing BRD4-ligand interactions,[278] however our assay for BPTF may slightly underestimate the affinity. Given the high affinity of **BZ1**, we measured its selectivity against a panel of 32 representative bromodomains with a one-point measurement in the same assay format (**Table 2.7**). We screened at 140 nM, approximately twenty times above the K_d of **BZ1** for BPTF (**Figure 2.10A**). Encouragingly, consistent with our PrOF NMR and AlphaScreen results, the BET family proteins, were weakly inhibited with the highest estimated affinity for BRD4(1) (71% inhibition). For Class I, bromodomains, BPTF and PCAF were significantly inhibited as expected (100% inhibition), with lower levels of inhibition for CECR2 and GCN5L2. Although, BRD7 and BRD9 lack acidic residues corresponding to the acidic triad (**Figure 2.10C**), they were also strongly inhibited (99%). Recently reported pyridazinone-based inhibitors also bind to these proteins[276] and BRD9 was reported as the closest off-target for TP-238.[266] These studies supported good on-target BPTF inhibition, and identified several off-targets bromodomains for a more quantitative selectivity analysis.

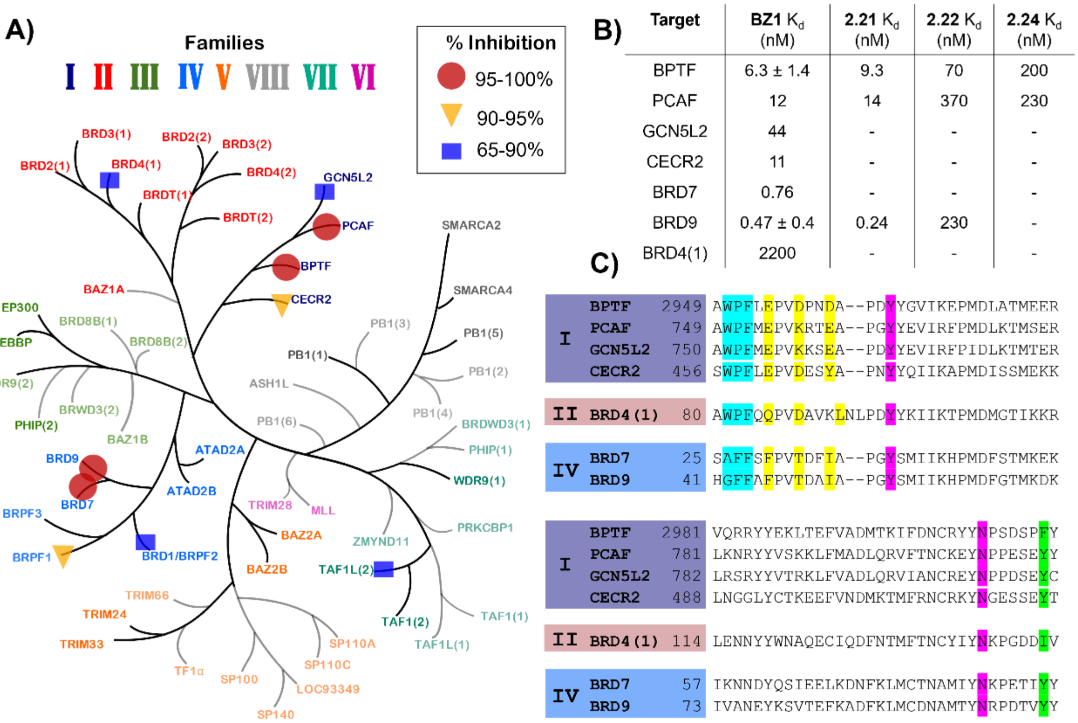

Target	BZ1 K_d (nM)	2.21 K_d (nM)	2.22 K_d (nM)	2.24 K_d (nM)
BPTF	6.3 ± 1.4	9.3	70	200
PCAF	12	14	370	230
GCN5L2	44	-	-	-
CECR2	11	-	-	-
BRD7	0.76	-	-	-
BRD9	0.47 ± 0.4	0.24	230	-
BRD4(1)	2200	-	-	-

```
I   BPTF    2949 AWPFLEPVDPNDA--PDYYGVIKEPMDLATMEER
    PCAF     749 AWPFMEPVKRTEA--PGYYEVIRFPMDLKTMSER
    GCN5L2   750 AWPFMEPVKKSEA--PDYYEVIRFPIDLKTMTER
    CECR2    456 SWPFLEPVDESYA--PNYYQIIKAPMDISSMEKK

II  BRD4(1)   80 AWPFQQPVDAVKLNLPDYYKIIKTPMDMGTIKKR

IV  BRD7      25 SAFFSFPVTDFIA--PGYSMIIKHPMDFSTMKEK
    BRD9      41 HGFFAFPVTDAIA--PGYSMIIKHPMDFGTMKDK

I   BPTF    2981 VQRRYYEKLTEFVADMTKIFDNCRYYNPSDSPFY
    PCAF     781 LKNRYYVSKKLFMADLQRVFTNCKEYNPPESEYY
    GCN5L2   782 LRSRYYVTRKLFVADLQRVIANCREYNPPDSEYC
    CECR2    488 LNGGLYCTKEEFVNDMKTMFRNCRKYNGESSEYT

II  BRD4(1)  114 LENNYYWNAQECIQDFNTMFTNCYIYNKPGDDIV

IV  BRD7      57 IKNNDYQSTEELKDNFKLMCTNAMIYNKPETIYY
    BRD9      73 IVANEYKSVTEFKADFKLMCDNAMTYNRPDTVYY
```

Figure 2.10: Selectivity analysis of BZ1 and analogs via BROMOscan.

A) Single-point measurement of 140 nM **BZ1** against a representative panel of 32 bromodomains via BROMOscan. Percent inhibition ranges are shown by: circles 95-100%, triangles 90-95% and squares 65-90%. (Adapted with permission from Pomerantz et al.)[246]. B) K_d values for **BZ1** with BPTF and off-target class I (PCAF, GCN5L2, CECR2,) and class IV (BRD7, BRD9) bromodomains and BRD4(1) as the highest off-target from the BET family and K_d values for compound **2.21, 2.22** and **2.24** with BPTF, PCAF and BRD9. Values are averages of two technical replicates, N = 1, except **BZ1** with BPTF and BRD9, which are averages of two experimental replicates. C) Sequence alignment of selected bromodomains highlighting WPF shelf motif (cyan), 3D equivalents of acidic triad (yellow), K_{ac} mimetic H-bonding groups (magenta), and the gatekeeper residue (green).

Given that these measurements were only estimates of affinity, we carried out a full titration for five additional bromodomains (**Figure 2.10B** and **Figure 2.20**). In this case, we obtained a 350-fold selectivity over BRD4(1). However, our selectivity over class I bromodomains, PCAF, CECR2, and GCN5L2 was reduced. Surprisingly, the affinity for BRD7 and 9 was stronger than expected (K_d = 0.76 and 0.47 nM respectively) and represents an important off-targets for future inhibitor designs. During the course of preparing this manuscript, a new BPTF inhibitor (Cpd8) was reported with an affinity of 428 nM (Section 1.3).[279] However selectivity studies against BRD9 and class I bromodomains were not conducted in this study to allow comparisons. Currently the ability to potently inhibit both the SWI/SNF and NURF nucleosome remodeling complexes have yet to be explored and may provide a novel mechanism for therapeutic applications.

As an initial evaluation of two additional analogs to improve activity, we synthesized and tested **2.21** and **2.22**. **2.21** is an analogue of **BZ1** which replaces the chloro group with a bromine atom, analogous to GSK4027. **2.22** is an analog of **2.19** which extends the amino group by one additional methylene to further engage D2957. In the case of **2.21,** there was a small but significant improvement in affinity by AlphaScreen relative to **BZ1** and a 3-fold increase in potency of **2.22** relative to **2.19** (**Table 2.4**). We further measured their affinity and selectivity by BROMOscan. While the K_d of **2.22** was weaker (K_d = 70 nM), both BRD9 affinity and PCAF affinity were weakened more significantly and now result in a modest selectivity over BRD9 and further selectivity over PCAF. These results support our design strategy for targeting the two acidic residues of BPTF to enhance the selectivity of our inhibitor series.

2.2.5 Exploring the SAR at the Pyridazinone N-CH_3

As a second attempt to improve selectivity and/or affinity, in our final SAR series, we investigated the N-CH_3 position on the pyridazinone core. Using the cocrystal structure reported for NVS-BPTF-1,[267] we hypothesized that the cyclopropyl-substituted pyrazole ring may contribute to the affinity and selectivity for BPTF. In our scaffold, the analogous position would be the R' substituent in **Table 2.5**. We observed that small alkyl groups and a propargyl group were tolerated at that position, albeit with no improvement in affinity. However, all the analogues retained their selectivity over BRD4(1).

Table 2.5: Aromatic pyridazinones with 2-position N-alkyl substituents.

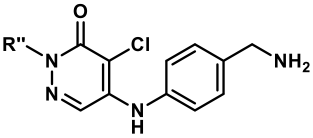

	R’’	BPTF AlphaScreen IC50 (μM)	BRD4(1) AlphaScreen IC50 (μM)
2.10	CH_3	0.29	42
2.23		0.55	35
2.24	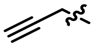	0.38	71
2.25	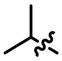	0.79	NB

AlphaScreen values were an average of two technical replicates with N =1. NB indicates that the compound was non-binding up to 250 μM. Binding isotherms shown in **Figure 2.11.**

We further characterized the affinity of **2.24** with BPTF and BRD4(1) using BROMOscan, obtaining K_d values of 200 nM and 230 nM respectively (**Figure 2.10B** and **Figure 2.23**). Although we were not able to improve selectivity over the closely-related bromodomain of PCAF, the alkyne group can serve as a useful click-chemistry handle for further modifications of the pyridazinone scaffold.

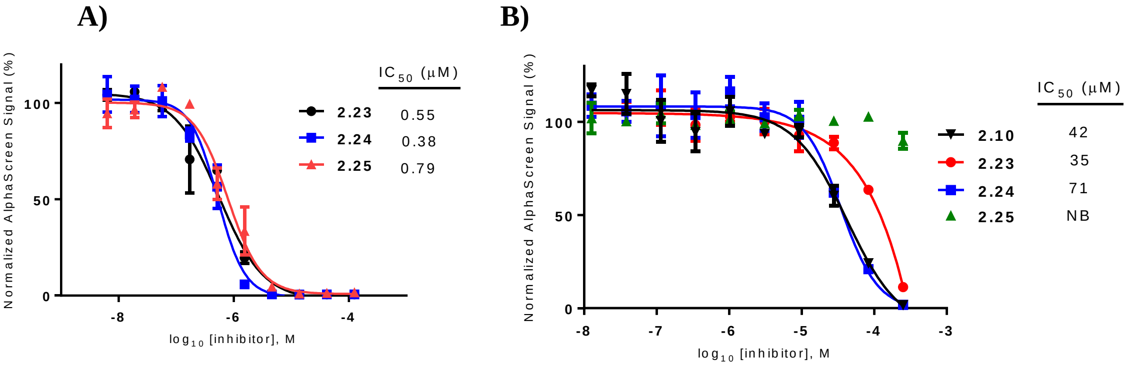

Figure 2.11: AlphaScreen titration of A) BPTF and B) BRD4 D1 with compounds from Table 2.5.

2.2.6 Enhancing Toxicity of Chemotherapeutics in a Model Breast Cancer Cell Line

With potent inhibitors in hand, we sought to conduct an initial assessment of cellular activity prior to further selectivity optimization. BPTF has been implicated in resistance to chemotherapeutics for treating hepatocellular carcinoma,[258] and BRAF inhibitors for melanoma therapy.[253] We recently identified BPTF suppression of Topoisomerase 2 poisons, including doxorubicin and etoposide, whose cytotoxic activity was enhanced with BPTF knockdown or bromodomain inhibition with AU1.[265] While knockdown of BPTF in 4T1 mouse breast cancer cells[280] does not exhibit toxicity on its own,[281] AU1 treatment exhibited toxicity at higher concentrations consistent with an off-target effect. We first tested several of our pyridazinones and found them to be well-tolerated by the 4T1 cells up to mid-micromolar concentrations, with the exception of **BZ1** which started to exhibit some toxicity at 8 μM (% survival = 56 and 89% in two separate experiments) **(Figure 2.13A** and **Figure 2.12**). **BZ1, 2.19** and a regioisomer control, **2.20**,[282] were further used for combination treatment with doxorubicin at concentrations lacking significant toxicity with inhibitor alone (**Figure 2.13A,B**).

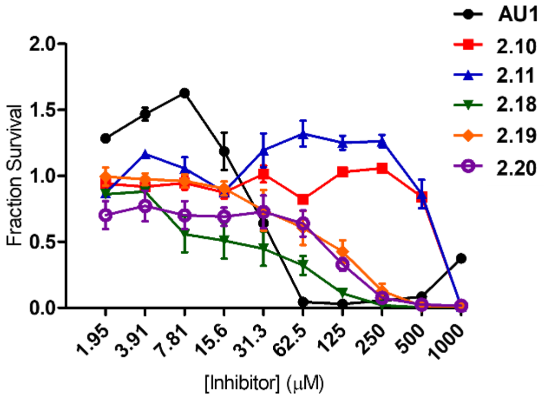

Figure 2.12: MTS assay with AU1 and pyridazinone inhibitors 2.10-2.11, 2.18-2.20.

Encouragingly, **BZ1** and **2.19** sensitized 4T1 cells to doxorubicin, exhibiting sensitization similar to BPTF shRNA knockdown levels, while **2.20** did not. A separate dose dependence experiment showed **BZ1** maintained strong biological effects down to 2.5 μM while **2.19** was 2-4-fold less effective (**Figure 2.14)**. This result was consistent with the weaker affinity of **2.19** towards the BPTF bromodomain. It is unclear if the lack of an effect at concentrations closer to the inhibitors' biochemical potencies are due to a lack of cellular uptake, or if alternate mechanisms are also important such as engagement of additional BPTF domains with chromatin.

As a control for off-target effects in our doxorubicin-sensitization studies, no further toxicity was observed when BPTF knockdown cells were treated with BPTF pyridazinone inhibitors and doxorubicin at these concentrations despite the high BRD9 affinity (**Figure 2.13C,D**). Additional toxicity was observed for AU1 at the highest concentrations tested. Together, these results are consistent with an on-target BPTF bromodomain inhibition effect of a new inhibitor class.

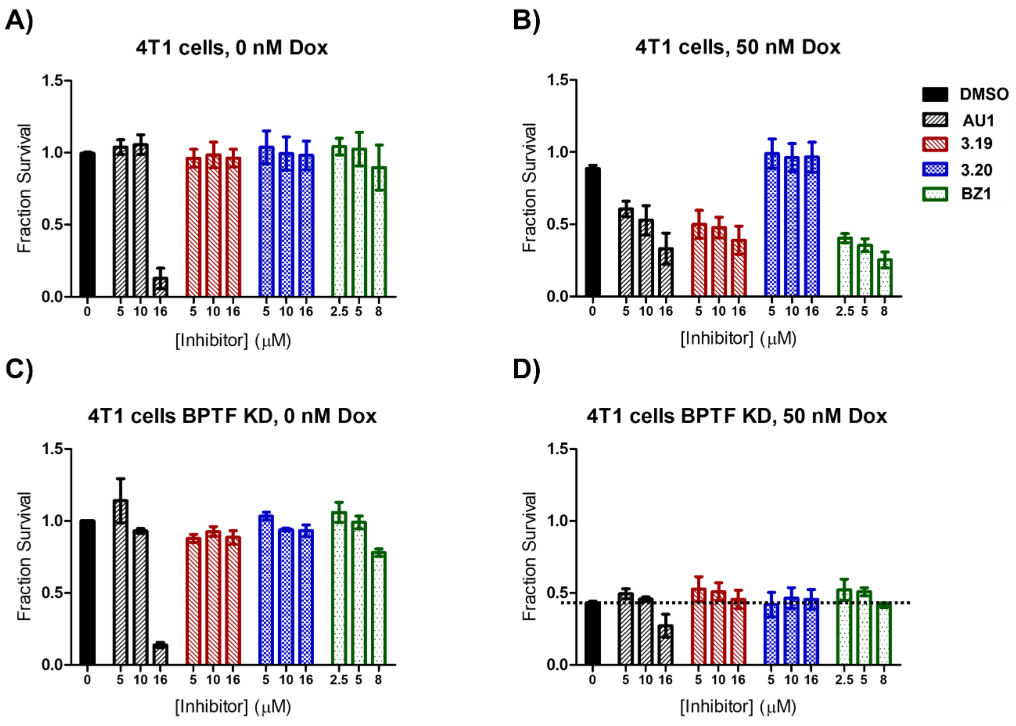

Figure 2.13: AU1, 2.19 and BZ1 synergize with chemotherapy doxorubicin in 4T1 breast cancer cells. Compound **2.20** was used as a negative control. 4T1 cells were tested A) without doxorubicin B) in the presence of 50 nM doxorubicin. As a control for off-target effects, shRNA-mediated BPTF knockdown

(KD) cells were treated with BPTF inhibitors with and without doxorubicin in C) and D) respectively. Fraction survival values are averages of three experimental replicates, except DMSO controls which are averages of nine experimental replicates.

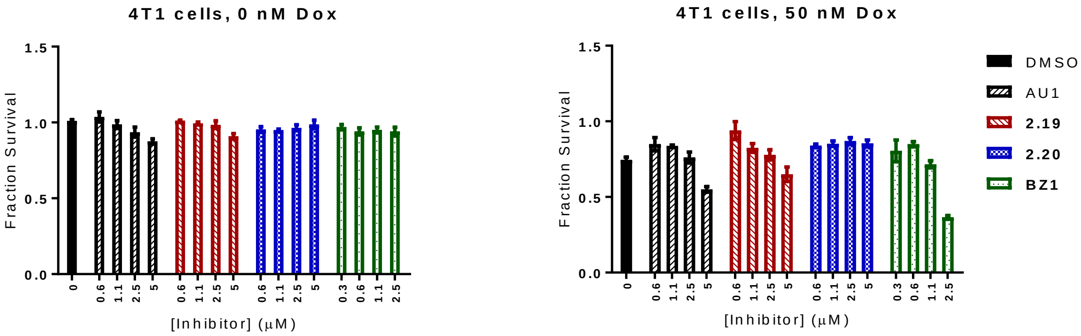

Figure 2.14: 4T1 cells tested with compounds at lower concentrations than Figure 2.13. 4T1 cells were tested with AU1 and pyridazinone inhibitors **2.19**, **2.20** and **BZ1** at lower concentrations than in Error! Reference source not found.**A**) without doxorubicin B) in the presence of 50 nM d oxorubicin. Fraction survival values are averages of three experimental replicates, except DMSO controls which are averages of nine experimental replicates.

2.2.7 Pyridazinones Effect on BPTF Target Genes

As a final evaluation of BPTF-dependent cellular effects, we tested the effects of **2.19** on several potential BPTF target genes. **2.19** was chosen due to its low level of toxicity in 4T1 cells, and its regioisomer control **2.20**. We also tested AU1 as a second control for BPTF inhibition. Given the lack of BPTF inhibitors, few-BPTF dependent genes have been validated for bromodomain inhibition and prior work has shown BPTF bromodomain inhibitors do not replicate all genes affected by BPTF depletion.[268]

We previously showed BPTF inhibition was associated with alteration to lineage commitment and stem cell maintenance. Loss of BPTF expression in a mixed population of Krt5-expressing mammary stem cells induced differentiation, a process that was accompanied by changes to chromatin accessibility and altered gene expression activation.[252] We thus decided to investigate the effects of our BPTF inhibitors in mammary luminal cells. We used the murine

Eph4 cell line, an immortalized, normal-like system previously shown to activate molecular process of luminal cell differentiation,[283,284] and were responsive to AU1 treatment.[252] Here, Eph4 cells were treated with AU1 (5 μM), **2.19** (5 μM), and its regioisomer control **2.20** (5 μM), followed by either apoptosis analysis or RNA extraction (**Figure 2.15**). The mRNA levels of the three genes were analyzed via RT-qPCR based on our prior analysis of BPTF knockout studies in mammary epithelial luminal cells which included two highly upregulated genes, Stratifin (*Sfn*), a regulator of mitotic translation, and Small proline rich protein 1A (*Sprr1a*), which is involved in keratinocyte differentiation. We also analyzed *Myc* levels given prior reports on BPTF regulation,[21] although our prior knockout data did not show a statistically significant effect (**Table 2.6).**

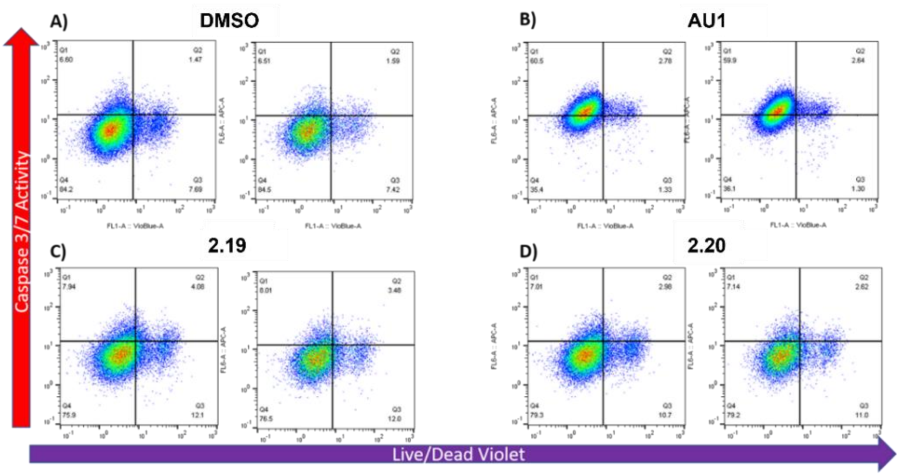

Figure 2.15: Caspase activation and viability analysis of Eph4 cells treated with 5 μM compound or DMSO.

Table 2.6: RNA-seq data from prior BPTF KO studies.[252]

Gene	fold-change	p-value
Sfn	11.5	1.42E-05
Sprr1a	7.59	0.000138
Myc	2.26	0.0938

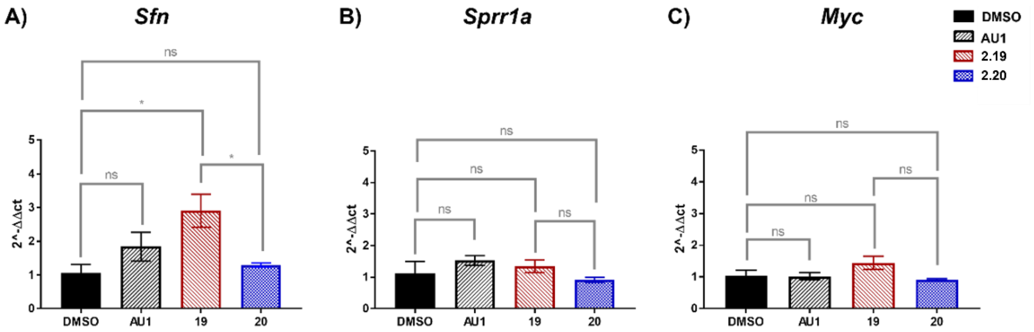

Figure 2.16: RT-qPCR Analysis of BPTF Regulated Genes.

A) S*fn*: DMSO vs AU1: p= 0.5994, **2.19** vs **2.20**: p= 0.0263*, DMSO vs **2.19**: p=0.0388*, DMSO vs **2.20**: p= 0.9798 B) S*prr1a*: DMSO vs AU1: p= 0.515 NS, **2.19** vs **2.20**: p= 0.3264 NS, DMSO vs **2.19**: p= 0.8727 NS, DMS0 vs **2.20**: p=0.9037 NS C) *Myc*: DMSO vs AU1: p>0.9999 NS, **2.19** vs **2.20**: p= 0.0568, DMSO vs **2.19**: p= 0.3265 NS, DMSO vs **2.20**: p=0.9557 NS.

We found that compound **2.19** treatment led to minimal toxicity against Eph4 cells and induced a statistically significant increase in *Sfn* which was not significantly affected by **2.20** (**Figure 2.16A**). AU1 upregulated *Sfn* but did not reach a high enough level of statistical significance. Conversely, *Sprr1a* was not significantly affected by any treatment (**Figure 2.16B**). This result suggests potential differential effects between bromodomain inhibition and whole protein knockout. *Myc* levels were also unaffected relative to DMSO treatment ((**Figure 2.16C**). Unaffected *Myc* levels are consistent with a lack of caspase activation by **2.19** (**Figure 2.15**). From this preliminary analysis, we show that compound **2.19** treatment can induce cellular effects in at least one gene associated with BPTF knockout studies, and warrants further investigation. A limitation of the analysis is the comparison to BPTF knockout cells from a mixed population, and a need for analysis with more selective bromodomain inhibitors which is the focus of future work.

2.3 Conclusions

We describe the development of new BPTF inhibitors based on a pyridazinone scaffold with our lead molecule **BZ1** having a high affinity for BPTF (K_d = 6.3 nM) and >350-fold selectivity over the BET family, making it the most potent inhibitor for the BPTF bromodomain in the published literature. We use the cocrystal structures of our analogues to establish a framework of structure-based design that can aid future efforts in rational development of chemical probes and to engineer selectivity over off-target bromodomains (**Figure 2.17**). Molecule **2.22** is one such example for reducing affinity towards BRD7/9. As not all bromodomain inhibitors exhibit cellular effects, here we use breast cancer cell lines to show that our inhibitors have on-target activity for BPTF and sensitize to the chemotherapy drug doxorubicin. Their activity is significantly improved relative to AU1, which is less effective with a sharp toxicity profile starting above 16 μM. The high potency, solubility and ligand efficiency (0.51) of **BZ1** makes it a suitable lead for further medicinal chemistry optimization and the development of new chemical biology tools.

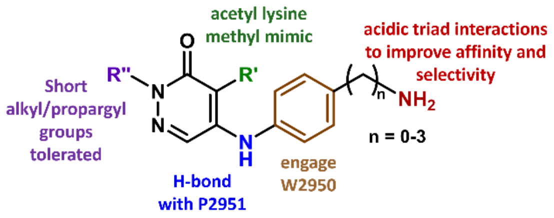

Figure 2.17: Design rules established from pyridazinone SAR studies.

2.4 Experimental Section

Materials and Methods. All commercially available reagents were used without further purification. Flash column chromatography was performed on a Teledyne-Isco Rf-plus CombiFlash instrument with RediSep columns. NMR spectra were collected on a Bruker Avance III AX-400 or a Bruker Avance III HD-500 equipped with a Prodigy TCI cryoprobe. Chemical shifts (δ) were reported in parts per million (ppm) and referenced to residual solvent signals for Chloroform-*d* (^{1}H 7.26 ppm), Dimethyl Sulfoxide-*d*$_6$ (^{1}H 2.50 ppm, ^{13}C 39.5 ppm) and Methanol-d$_4$ (^{1}H 3.31 ppm, ^{13}C 49.0 ppm). Coupling constants (J) are in Hz. Splitting patterns were reported as s (singlet), d (doublet), t (triplet), q (quartet) and m (multiplet). High resolution ESI-MS spectra were recorded on a Thermo Fischer Orbitrap Velos equipped with an autosampler. Where stated, compounds were purified by reverse-phase high-performance liquid chromatography (RP-HPLC) on a C-18 column using 0.1% TFA water and CH_3CN as solvents and TFA salts were quantified using the procedure described by Carlson et. al.[285]

Purity Analysis. All compounds tested in cells were ≥95% pure by RP-HPLC. Compounds **2.18-2.20** were run on a RP-HPLC with a C-18 column over a gradient of 0-10% ACN in 0.1% TFA H_2O over 60 min. Spectral traces are shown in **Figure 2.18**.

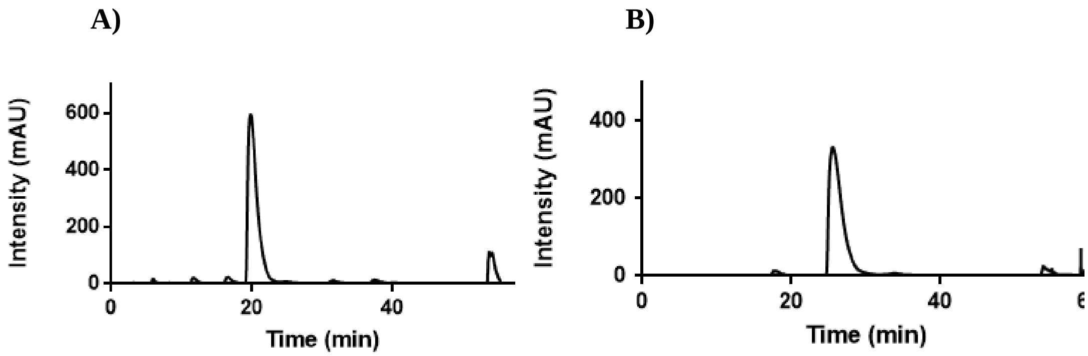

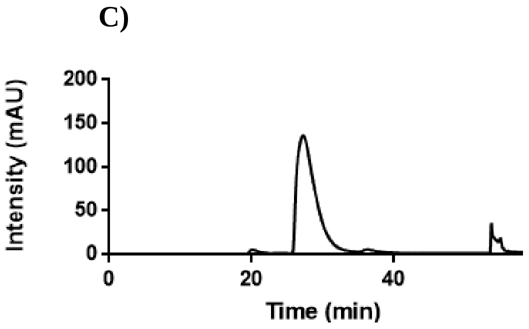

Compound	% Purity
2.18	95
2.19	97
2.20	97

Figure 2.18: Analytical HPLC traces of compounds 2.18-2.20.

HPLC spectra at 272 nm of A) **2.18**, B) **2.19**, and C) **2.20** over a gradient of 0-10% ACN in H_2O with a calculated % purity from 0-50 min (excluding the solvent front).

General procedure A for the synthesis of compounds 2.1-2.16, 2.18-2.25. Step 1: The nucleophilic aromatic substitution procedure was adapted from Humphreys et al.[286]

4,5-dichloro-2-methylpyridazin-3(2*H*)-one (1.0 eq.) was stirred in DMSO (1 mL) at room temperature, followed by addition of the primary amine (1.2 eq) and *N,N*-Diisopropylethylamine (2.0 eq.). The reaction mixture was heated in a sealed tube at 120 °C for 18 h. Following completion of the reaction, the reaction mixture was extracted into ethyl acetate, washed with saturated sodium bicarbonate solution (3×20 mL) and finally with brine (20 mL). The organic layer was dried over magnesium sulfate, filtered, concentrated in vacuo and purified by flash column chromatography (CombiFlash Rf system: 4 g silica, hexanes/ethyl acetate, 0-100% ethyl acetate, 30 minutes unless stated otherwise). The 4- and 5-positional isomers were obtained, with the 5-positional isomer as the more polar fraction. Step 2: The product from Step 1 was stirred in DCM (1 mL) at RT, followed by addition of trifluoroacetic acid (5.0 eq.) and stirred at RT for an additional 2 h. Step 3: The DCM was removed under vacuum and the product was isolated either as a TFA salt or a free base compound. To obtain the TFA salt, cold diethyl ether was added dropwise to precipitate out the product and the diethyl ether was removed in vacuo. For the free amine compounds, the mixture from Step 2 was extracted into DCM and treated with 1 M NaOH to attain a pH > 10. The DCM layer was dried with magnesium sulfate, filtered and the DCM was removed in vacuo to obtain the product.

General procedure B for the synthesis of compounds 2.26-2.28. 4,5-dichloropyridazin-3(2*H*)-one (1.0 eq.) was stirred in DMF (5 mL) followed by addition of sodium hydride (1.1 eq) and the alkyl bromide (1.4 eq.). The reaction mixture was stirred at room temperature for 12 h. Following completion of the reaction, the reaction mixture was extracted into ethyl acetate, washed with distilled water and finally with brine. The organic layer was dried over magnesium sulfate, filtered, concentrated in vacuo and purified by flash column chromatography (CombiFlash Rf system: 24 g silica, hexanes/ethyl acetate, 0-100% ethyl acetate, 20 minutes).

GSK4027 was purchased from Cayman Chemicals. The synthesis and characterization of compounds **2.1-2.3** were described previously.[270]

5-(azetidin-3-ylamino)-4-chloro-2-methylpyridazin-3(2*H*)-one (2.4). Following the general procedure A, (4,5-dichloro-2-methylpyridazin-3(2*H*)-one (150 mg, 0.838 mmol, 1.0 eq.), *tert*-butyl 3-aminoazetidine-1-carboxylate (173 mg, 1.01 mmol, 1.2 eq.), *N,N*-Diisopropylethylamine (292 μL, 1.68 mmol, 2.0 eq.)), product **2.4** was obtained as a brown solid (211 mg, 77% yield over two steps). ^{1}H NMR (400 MHz, DMSO-d_6) δ 8.78 (d, J = 68.6 Hz, 2H), 7.76 (s, 1H), 7.16 (d, J = 7.3 Hz, 1H), 4.76 (h, J = 7.5 Hz, 1H), 4.28 – 4.19 (m, 2H), 4.18 – 4.08 (m, 2H), 3.60 (s, 3H). ^{13}C NMR (126 MHz, DMSO-d_6) δ 158.5 (q, J = 34.9 Hz), 156.8, 143.2, 126.6, 116.1 (q, J = 293.4 Hz), 106.4, 52.6, 44.1 (one resonance obscured by solvent). HRMS (ESI-TOF) calculated for $C_8H_{12}ClN_4O^+$ [M+H]$^+$: 215.0694, observed 215.0686.

5-(azepan-3-ylamino)-4-chloro-2-methylpyridazin-3(2*H*)-one (2.5). Following the general procedure A, (4,5-dichloro-2-methylpyridazin-3(2*H*)-one (114 mg, 0.636 mmol, 1.0 eq.), *tert*-butyl 3-aminoazepane-1-carboxylate (150 mg, 0.699 mmol, 1.1 eq.), *N,N*-Diisopropylethylamine (222 μL, 1.27 mmol, 2.0 eq.)), product **2.5** was obtained as a brown oil (49 mg, 21% yield over two steps). ^{1}H NMR (500 MHz, DMSO-d_6) δ 9.05 (s, 2H), 7.93 (s, 1H), 6.35 (d, J = 9.2 Hz, 1H), 4.27 – 4.14 (m, 1H), 3.60 (s, 3H), 3.27 – 3.09 (m, 4H), 2.06 – 1.94 (m, 1H), 1.91 – 1.83 (m, 1H), 1.82 – 1.71 (m, 3H), 1.62 – 1.47 (m, 1H). ^{13}C NMR (126 MHz, DMSO-d_6) δ 158.5, 156.8, 143.2, 126.5, 105.7, 49.4, 49.4, 46.4, 33.2, 24.8, 22.1 (one resonance obscured by solvent). HRMS (ESI-TOF) calculated for $C_{11}H_{18}ClN_4O^+$ [M+H]$^+$: 257.1164, observed 257.1154.

4-chloro-2-methyl-5-(phenylamino)pyridazin-3(2*H*)-one (2.6). Following step 1 of the general procedure A, (4,5-dichloro-2-methylpyridazin-3(2*H*)-one (634 mg, 3.54 mmol, 1.1 eq.), aniline (300 mg, 3.22 mmol, 1.0 eq.), *N,N*-Diisopropylethylamine (1.12 mL, 6.44 mmol, 2.0 eq.)), product **2.6** was obtained as a yellow solid (73 mg, 10% yield over two steps). ^{1}H NMR (500 MHz, DMSO-*d*$_6$) δ 8.73 (s, 1H), 7.64 (d, *J* = 1.7 Hz, 1H), 7.39 (d, *J* = 7.7 Hz, 2H), 7.25 (d, *J* = 7.9 Hz, 2H), 7.20 (t, *J* = 7.4 Hz, 1H), 3.61 (s, 3H). ^{13}C NMR (126 MHz, DMSO-*d*$_6$) δ 157.5, 142.8, 139.0, 129.9, 128.1, 125.4, 124.0, 109.0 (one resonance obscured by solvent). HRMS (ESI-TOF) calculated for $C_{11}H_{11}ClN_3O^+$ [M+H]$^+$: 236.0585, observed 236.0575.

5-((4-aminophenyl)amino)-4-chloro-2-methylpyridazin-3(2*H*)-one (2.7). Following the general procedure A, (4,5-dichloro-2-methylpyridazin-3(2*H*)-one (300 mg, 1.68 mmol, 1.0 eq.), *tert*-butyl (4-aminophenyl)carbamate (419 mg, 2.01 mmol, 1.2 eq.), *N,N*-Diisopropylethylamine (584 µL, 3.35 mmol, 2.0 eq.)), product **2.7** was obtained as a brown solid (49 mg, 8% yield over two steps). ^{1}H NMR (500 MHz, Methanol-*d*$_4$) δ 7.49 (s, 1H), 7.00 (d, *J* = 8.6 Hz, 2H), 6.77 (d, *J* = 8.6 Hz, 2H), 4.59 (s, 1H), 3.70 (s, 3H). ^{13}C NMR (126 MHz, Methanol-*d*$_4$) δ 160.1, 148.3, 146.2, 129.2, 128.8, 128.3, 117.0, 107.4, 40.5. HRMS (ESI-TOF) calculated for $C_{11}H_{12}ClN_4O^+$ [M+H]$^+$: 251.0694, observed 251.0683.

4-chloro-5-((4-fluorophenyl)amino)-2-methylpyridazin-3(2*H*)-one (2.8). Following step 1 of the general procedure A, (4,5-dichloro-2-methylpyridazin-3(2*H*)-one (532 mg, 2.97 mmol, 1.1 eq.), 4-fluoroaniline (300 mg, 2.70 mmol, 1.0 eq.), *N,N*-Diisopropylethylamine (940 µL, 5.40 mmol, 2.0 eq.)), product **2.8** was obtained as a white solid (52 mg, 8% yield over two steps). ^{1}H NMR (500 MHz, DMSO-*d*$_6$) δ 8.69 (s, 1H), 7.57 (s, 1H), 7.34 – 7.18 (m, 4H), 3.60 (s, 3H). ^{13}C NMR (126 MHz, DMSO-*d*$_6$) δ ^{13}C NMR (126 MHz, DMSO-*d*$_6$) δ 159.5 (d, *J* = 242.0 Hz), 157.0, 142.6, 134.8, 134.7, 127.4, 126.2 (d, *J* = 8.5 Hz), 116.1 (d, *J* = 22.6 Hz), 108.0 (one resonance obscured by solvent). HRMS (ESI-TOF) calculated for $C_{11}H_{10}ClFN_3O^+$ [M+H]$^+$: 254.0491, observed 254.0477.

5-((3-aminobenzyl)amino)-4-chloro-2-methylpyridazin-3(2*H*)-one (2.9). Following the general procedure A, (4,5-dichloro-2-methylpyridazin-3(2*H*)-one (150 mg, 0.838 mmol, 1.0

eq.), *tert*-butyl (3-(aminomethyl)phenyl)carbamate (224 mg, 1.01 mmol, 1.2 eq.), *N,N*-Diisopropylethylamine (292 µL, 1.68 mmol, 2.0 eq.)), product **2.9** was obtained as a brown solid (50 mg, 23% yield over two steps). ^{1}H NMR (500 MHz, DMSO-*d*$_6$) δ 7.61 (s, 1H), 7.22 (t, *J* = 6.5 Hz, 1H), 6.96 (t, *J* = 7.7 Hz, 1H), 6.45 (d, *J* = 1.9 Hz, 1H), 6.42 (dt, *J* = 7.9, 1.9 Hz, 2H), 5.08 (s, 2H), 4.41 (d, *J* = 6.5 Hz, 2H), 3.54 (s, 3H). ^{13}C NMR (126 MHz, DMSO-*d*$_6$) δ 156.8, 149.0, 144.7, 139.6, 129.1, 126.5, 113.9, 112.7, 111.6, 104.8, 45.3 (one resonance obscured by solvent). HRMS (ESI-TOF) calculated for $C_{12}H_{14}ClN_4O^+$ $[M+H]^+$: 265.0851, observed 265.0842.

5-((4-(aminomethyl)phenyl)amino)-4-chloro-2-methylpyridazin-3(2*H*)-one (2.10). Following the general procedure A, (4,5-dichloro-2-methylpyridazin-3(2*H*)-one (250 mg, 1.39 mmol, 1.0 eq.), *tert*-butyl (4-aminobenzyl)carbamate (279 mg, 1.26 mmol, 0.9 eq.), *N,N*-Diisopropylethylamine (487 µL, 2.79 mmol, 2.0 eq.)), product **2.10** was obtained as a brown solid (65 mg, 14% yield over two steps). ^{1}H NMR (500 MHz, DMSO-*d*$_6$) δ 8.84 (s, 1H), 8.13 (s, 3H), 7.63 (s, 1H), 7.46 (d, *J* = 8.2 Hz, 2H), 7.29 (d, *J* = 8.5 Hz, 2H), 4.03 (q, *J* = 5.6 Hz, 2H), 3.62 (s, 3H). ^{13}C NMR (126 MHz, DMSO-*d*$_6$) δ 157.1, 142.1, 138.9, 130.2, 130.1, 127.8, 123.1, 109.3, 41.85 (one resonance obscured by solvent). HRMS (ESI-TOF) calculated for $C_{12}H_{14}ClN_4O^+$ $[M+H]^+$: 265.0851, observed 265.0839.

4-chloro-5-((4-((dimethylamino)methyl)phenyl)amino)-2-methylpyridazin-3(2*H*)-one (2.11). Following step 1 of the general procedure A, 4,5-dichloro-2-methylpyridazin-3(2*H*)-one (328 mg, 1.83 mmol, 1.1 eq.), 4-((dimethylamino)methyl)aniline (245 µL, 1.66 mmol, 1.0 eq.), *N,N*-Diisopropylethylamine (579 µL, 3.32 mmol, 2.0 eq.) and purification by flash column chromatography (CombiFlash Rf system: 4 g silica, DCM/methanol, 0-20% methanol, 20 minutes), product **2.11** was obtained as a brown solid (46 mg, 9% yield). ^{1}H NMR (500 MHz, Chloroform-*d*) δ 7.66 (s, 1H), 7.36 (d, *J* = 7.9 Hz, 2H), 7.15 (d, *J* = 7.9 Hz, 2H), 6.39 (s, 1H), 3.76 (s, 3H), 3.43 (s, 2H), 2.26 (s, 6H) (NH not observed). ^{13}C NMR (126 MHz, DMSO-*d*$_6$) δ

157.0, 142.4, 137.2, 135.7, 129.7, 127.6, 123.5, 108.2, 62.8, 44.9. HRMS (ESI-TOF) calculated for $C_{14}H_{18}ClN_4O^+$ $[M+H]^+$: 293.1164, observed 293.1150.

4-chloro-2-methyl-5-((1,2,3,4-tetrahydroisoquinolin-6-yl)amino)pyridazin-3(2*H*)-one (2.12). Following the general procedure A, (4,5-dichloro-2-methylpyridazin-3(2*H*)-one (198 mg, 1.11 mmol, 1.1 eq.), *tert*-butyl 6-amino-3,4-dihydroisoquinoline-2(1*H*)-carboxylate (250 mg, 1.01 mmol, 1.0 eq.), *N,N*-Diisopropylethylamine (351 μL, 2.01 mmol, 2.0 eq.)), product **2.12** was obtained as a yellow solid (51 mg, 17% yield over two steps). ^{1}H NMR (500 MHz, DMSO-d_6) δ 8.62 (s, 1H), 7.60 (s, 1H), 7.05 (d, *J* = 8.2 Hz, 1H), 6.99 (dd, *J* = 8.3, 2.2 Hz, 1H), 6.96 (s, 1H), 3.85 (s, 2H), 3.60 (s, 3H), 2.96 (t, *J* = 5.7 Hz, 2H), 2.69 (t, *J* = 6.0 Hz, 2H). ^{13}C NMR (126 MHz, DMSO-d_6) δ 157.0, 142.6, 136.0 (two resonances partially overlapping), 132.8, 127.5, 127.1, 124.2, 121.4, 107.8, 47.1, 42.8, 28.4. HRMS (ESI-TOF) calculated for $C_{14}H_{16}ClN_4O^+$ $[M+H]^+$: 291.1007, observed 291.0996.

4-chloro-2-methyl-5-((1,2,3,4-tetrahydroisoquinolin-7-yl)amino)pyridazin-3(2*H*)-one (2.13). Following the general procedure A, (4,5-dichloro-2-methylpyridazin-3(2*H*)-one (198 mg, 1.11 mmol, 1.1 eq.), *tert*-butyl 7-amino-3,4-dihydroisoquinoline-2(1*H*)-carboxylate (250 mg, 1.01 mmol, 1.0 eq.), *N,N*-Diisopropylethylamine (351 μL, 2.01 mmol, 2.0 eq.)), product **2.13** was obtained as a yellow solid (29 mg, 10% yield over two steps). ^{1}H NMR (500 MHz, DMSO-d_6) δ 8.61 (s, 1H), 7.59 (s, 1H), 7.09 (d, *J* = 8.1 Hz, 1H), 6.99 (dd, *J* = 8.1, 2.2 Hz, 1H), 6.90 (d, *J* = 2.3 Hz, 1H), 3.83 (s, 2H), 3.60 (s, 3H), 2.95 (t, *J* = 5.9 Hz, 2H), 2.67 (t, *J* = 5.9 Hz, 2H) (NH not observed). ^{13}C NMR (126 MHz, DMSO-d_6) δ 157.0, 142.6, 136.9, 135.7, 131.9, 129.9, 127.5, 121.7, 121.5, 107.8, 47.3, 43.0, 27.9. HRMS (ESI-TOF) calculated for $C_{14}H_{16}ClN_4O^+$ $[M+H]^+$: 291.1007, observed 291.0995.

4-chloro-2-methyl-5-((5,6,7,8-tetrahydronaphthalen-2-yl)amino)pyridazin-3(2*H*)-one (2.14). Following step 1 of the general procedure A, (4,5-dichloro-2-methylpyridazin-3(2*H*)-one (334 mg, 1.87 mmol, 1.1 eq.), 5,6,7,8-tetrahydronaphthalen-2-amine (250 mg, 1.70 mmol, 1.0 eq.), *N,N*-Diisopropylethylamine (592 µL, 3.40 mmol, 2.0 eq.)), product **2.14** was obtained as a yellow solid (175 mg, 36% yield over two steps). ^{1}H NMR (500 MHz, DMSO-d_6) δ 8.57 (s, 1H), 7.59 (s, 1H), 7.06 (d, *J* = 8.1 Hz, 1H), 6.97 – 6.92 (m, 2H), 3.59 (s, 3H), 2.70 (t, *J* = 4.8, 2.4 Hz, 4H), 1.72 (t, *J* = 3.3 Hz, 4H). ^{13}C NMR (126 MHz, DMSO) δ 157.5, 143.1, 138.2, 136.1, 134.2, 130.2, 127.9, 124.7, 121.8, 108.1, 29.2, 28.8, 23.2, 23.0 (one resonance obscured by solvent). HRMS (ESI-TOF) calculated for $C_{15}H_{17}ClN_3O^+$ [M+H]$^+$: 290.1055, observed 290.1038.

5-((3-(aminomethyl)phenyl)amino)-4-chloro-2-methylpyridazin-3(2*H*)-one (2.15). Following the general procedure A, (4,5-dichloro-2-methylpyridazin-3(2*H*)-one (250 mg, 1.39 mmol, 1.0 eq.), *tert*-butyl (3-aminobenzyl)carbamate (279 mg, 1.26 mmol, 0.9 eq.), *N,N*-Diisopropylethylamine (487 µL, 2.79 mmol, 2.0 eq.)), a portion of the crude product (71 mg, crude 15% yield) was then purified by reverse-phase HPLC (5-40% CH_3CN gradient over 30 minutes) to obtain product **2.15** as a brown solid. ^{1}H NMR (500 MHz, DMSO-d_6) δ 8.84 (s, 1H), 8.14 (s, 3H), 7.75 (s, 1H), 7.44 (m, 1H), 7.31 (m, 1H), 7.25 (m, 2H), 4.03 (q, *J* = 5.7 Hz, 2H), 3.63 (s, 3H). ^{13}C NMR (126 MHz, DMSO-d_6) δ 157.0, 142.0, 138.9, 135.2, 129.8, 127.8, 125.1, 123.4, 123.0, 109.3, 42.1 (one resonance obscured by solvent). HRMS (ESI-TOF) calculated for $C_{12}H_{14}ClN_4O^+$ [M+H]$^+$: 265.0851, observed 265.0842.

5-((2-(aminomethyl)phenyl)amino)-4-chloro-2-methylpyridazin-3(2*H*)-one (2.16). Compound previously characterized in literature.[286] Following the general procedure A, (4,5-dichloro-2-methylpyridazin-3(2*H*)-one (250 mg, 1.39 mmol, 1.0 eq.), *tert*-butyl (2-aminobenzyl)carbamate (279 mg, 1.26 mmol, 0.9 eq.), *N,N*-Diisopropylethylamine (487 µL, 2.79 mmol, 2.0 eq.)), a portion of the crude product (12 mg, 3% yield) was then purified by reverse-phase HPLC (5-40% CH_3CN gradient over 30 minutes) to obtain product **2.16** as a brown solid.

^{1}H NMR (500 MHz, DMSO-d_6) δ 8.34 (s, 1H), 8.12 (s, 3H), 7.50 (m, 1H), 7.36 (m, 2H), 7.22 (m, 1H), 7.26 (s, 1H), 4.06 (q, *J* = 5.2 Hz, 2H), 3.61(s, 3H). HRMS (ESI-TOF) calculated for $C_{12}H_{14}ClN_4O^+$ [M+H]$^+$: 265.0851, observed 265.0840.

N-(4-((5-chloro-1-methyl-6-oxo-1,6-dihydropyridazin-4-yl)amino)benzyl)acetamide (2.17). 5-((4-(aminomethyl)phenyl)amino)-4-chloro-2-methylpyridazin-3(2H)-one **(2.10)** (20 mg, 0.05 mmol, 1.0 eq.) was stirred in dichloromethane (0.5 mL) followed by addition of acetic anhydride (6.4 mg, 0.06 mmol, 1.2 eq) and triethylamine (26 mg, 0.26 mmol, 5 eq.). The reaction mixture was stirred at room temperature for 0.5 h. Following completion of reaction, the reaction mixture was washed with diethyl ether. The solid was concentrated in vacuo and purified by flash column chromatography (CombiFlash Rf system: 12 g silica, dichloromethane/methanol, 0-10% methanol, 20 minutes). Product **2.17** was obtained as a white solid (9 mg, 56% yield). ^{1}H NMR (500 MHz, Chloroform-*d*) δ 7.66 (s, 1H), 7.35 (d, *J* = 8.4 Hz, 2H), 7.16 (d, *J* = 8.3 Hz, 2H), 4.46 (d, *J* = 8.3 Hz, 2H), 3.77 (s, 3H), 2.08 (s, 3H). ^{13}C NMR (126 MHz, Chloroform-*d*) δ 170.3, 157.9, 142.1, 136.8, 136.7, 129.4, 126.7, 124.2, 110.2, 43.2, 40.4, 23.4. HRMS (ESI-TOF) calculated for $C_{14}H_{16}ClN_4O_2^+$ [M+H]$^+$: 307.0956, observed 307.0949.

5-((4-(2-aminoethyl)phenyl)amino)-4-chloro-2-methylpyridazin-3(2*H*)-one (2.18/BZ1). Following the general procedure A, (4,5-dichloro-2-methylpyridazin-3(2*H*)-one (250 mg, 1.39 mmol, 1.0 eq.), *tert*-butyl (2-(4-amino-phenyl)-ethyl)carbamate (307 mg, 1.30 mmol, 0.9 eq.), *N,N*-Diisopropylethylamine (487 µL, 2.79 mmol, 2.0 eq.)), product **2.18** was obtained as a brown solid (140 mg, 21% yield over two steps). ^{1}H NMR (500 MHz, DMSO-d_6) δ 8.69 (s, 1 H), 7.61 (s, 1 H), 7.27 (d, *J* = 8.0 Hz, 2H), 7.20 (d, *J* = 7.9 Hz, 2H), 3.61 (s, 3 H), 2.93 (t, *J* = 7.5 Hz, 2 H), 2.76 (t, *J* = 7.6 Hz, 2H). ^{13}C NMR (126 MHz, DMSO-d_6) δ 157.1, 142.6, 136.7, 135.6, 129.7, 127.6, 123.9, 108.1, 41.5, 35.4 (one resonance obscured by solvent). HRMS (ESI-TOF) calculated for $C_{13}H_{16}ClN_4O^+$ [M+H]$^+$: 279.1007, observed 279.1002.

4-chloro-5-((4-(2-(dimethylamino)ethyl)phenyl)amino)-2-methylpyridazin-3(2H)-one (2.19). Following step 1 of the general procedure A, (4,5-dichloro-2-methylpyridazin-3(2*H*)-one (250 mg, 1.39 mmol, 1.0 eq.), 4-(2-dimethylamino-ethyl)aniline (214 mg, 1.26 mmol, 0.9 eq.), *N*,*N*-Diisopropylethylamine (487 μL, 2.79 mmol, 2.0 eq.)) and purification by flash column chromatography (CombiFlash Rf system: 4 g silica, DCM/methanol, 0-20% methanol, 20 minutes), product **2.19** (more polar fraction) was obtained as a yellow solid (42 mg, 11% yield). ^{1}H NMR (500 MHz, DMSO-d_6) δ 8.65 (s, 1H), 7.59 (s, 1H), 7.25 (d, *J* = 8.3 Hz, 2H), 7.16 (d, *J* = 8.4 Hz, 2H), 3.61 (s, 3 H), 2.70 (t, *J* = 7.6 Hz, 2H), 2.45 (t, *J* = 7.7 Hz, 2H), 2.18 (s, 6H). ^{13}C NMR (126 MHz, Chloroform-*d*) δ 158.0, 142.4, 139.1, 135.4, 130.3, 126.8, 124.4, 109.7, 61.4, 45.6, 40.4, 33.9. HRMS (ESI-TOF) calculated for $C_{15}H_{20}ClN_4O^+$ [M+H]$^+$: 307.1320, observed 307.1314.

5-chloro-4-((4-(2-(dimethylamino)ethyl)phenyl)amino)-2-methylpyridazin-3(2H)-one (2.20). Following step 1 of the general procedure A, (4,5-dichloro-2-methylpyridazin-3(2*H*)-one (250 mg, 1.39 mmol, 1.0 eq.), 4-(2-dimethylamino-ethyl)aniline (214 mg, 1.26 mmol, 0.9 eq.), *N*,*N*-Diisopropylethylamine (487 μL, 2.79 mmol, 2.0 eq.)) and purification by flash column chromatography (CombiFlash Rf system: 4 g silica, DCM/methanol, 0-20% methanol, 20 minutes), product **2.20** (less polar fraction) was obtained as a yellow solid (37 mg, 10% yield). ^{1}H NMR (500 MHz, DMSO-d_6) δ 8.70 (s, 1H), 7.75 (s, 1H), 7.11 (d, *J* = 8.4 Hz, 2H), 6.91 (d, *J* = 8.3 Hz, 2H), 3.67 (s, 3H), 2.66 (t, *J* = 7.7 Hz, 2H), 2.44 (t, *J* = 7.8 Hz, 2H), 2.18 (s, 6H). ^{13}C NMR (126 MHz, Chloroform-*d*) δ 158.0, 142.4, 139.1, 135.4, 130.3, 126.8, 124.4, 109.7, 61.4, 45.6, 40.4, 33.9. HRMS (ESI-TOF) calculated for $C_{15}H_{20}ClN_4O^+$ [M+H]$^+$: 307.1320, observed 307.1310.

5-((4-(2-aminoethyl)phenyl)amino)-4-bromo-2-methylpyridazin-3(2*H*)-one (2.21). Following the general procedure A, (4,5-dibromo-2-methylpyridazin-3(2*H*)-one (150 mg, 0.56

mmol, 1.0 eq.), *tert*-butyl (2-(4-amino-phenyl)-ethyl)carbamate (146 mg, 0.62 mmol, 1.1 eq.), *N*,*N*-Diisopropylethylamine (195 µL, 1.12 mmol, 2.0 eq.)), product **2.21** was obtained as a yellow solid (14 mg, 7% yield over two steps). ^{1}H NMR (500 MHz, DMSO-*d*$_6$) δ 7.48 (s, 1H), 7.24 (d, *J* = 8.4 Hz, 2H), 7.18 (d, *J* = 8.4 Hz, 2H), 3.61 (s, 3H), 2.82 (t, *J* = 7.3 Hz, 2H), 2.68 (d, *J* = 7.3 Hz, 2H). ^{13}C NMR (126 MHz, DMSO-*d*$_6$) δ 157.3, 144.6, 136.8, 136.5, 129.6, 127.4, 124.1, 100.1, 42.7, 37.8 (one resonance obscured by solvent). HRMS (ESI-TOF) calculated for $C_{13}H_{16}BrN_4O^+$ [M+H]$^+$: 323.0502, observed 323.0488.

4-chloro-5-((4-(3-(dimethylamino)propyl)phenyl)amino)-2-methylpyridazin-3(2*H*)-one (2.22). Following step 1 of the general procedure A, 4,5-dichloro-2-methylpyridazin-3(2H)-one (552mg, 3.08 mmol, 1.1 eq.), 4-(3-(dimethylamino)propyl)aniline (500mg, 2.80 mmol, 1.0 eq.) and N,N-Diisopropylethylamine (975 µL, 5.60 mmol, 2.0 eq.) and purification by flash column chromatography (CombiFlash Rf system: 4 g silica, DCM/methanol, 0-20% methanol, 20 minutes). A portion of the product (91 mg, 10% crude yield) was further purified by reverse-phase HPLC (5-45% CH_3CN gradient over 30 minutes) to obtain product **2.22** as a white solid. ^{1}H NMR (500 MHz, DMSO-*d$_6$*) δ 8.69 (s, 1H), 7.75 (s, 1H), 7.10 (d, J = 8.4 Hz, 2H), 6.92 (d, J = 8.3 Hz, 2H), 3.67 (s, 3H), 2.57 – 2.52 (m, 2H), 2.23 (t, J = 7.2 Hz, 2H), 2.14 (s, 6H), 1.68 (t, J = 7.4 Hz, 2H). ^{13}C NMR (126 MHz, DMSO-d6) δ 156.1, 138.2, 137.2, 136.6, 136.3, 127.6, 122.7, 111.0, 58.2, 44.9, 32.1, 28.6 (one resonance obscured by solvent). HRMS (ESI-TOF) calculated for $C_{16}H_{22}ClN_4O^+$ [M+H]$^+$: 321.1477, observed 321.1463.

5-((4-(aminomethyl)phenyl)amino)-4-chloro-2-ethylpyridazin-3(2*H*)-one (2.23). Following the general procedure A, (compound **2.26** (479 mg, 2.48 mmol, 1.0 eq.), *tert*-butyl (4-aminobenzyl)carbamate (607 mg, 2.73 mmol, 1.1 eq.), *N*,*N*-Diisopropylethylamine (864 µL, 4.96 mmol, 2.0 eq.)), product **2.23** was obtained as a yellow solid (62 mg, 9% yield over two steps). ^{1}H

NMR (500 MHz, DMSO-d_6) δ 7.61 (s, 1H), 7.36 (d, *J* = 8.4 Hz, 2H), 7.19 (d, *J* = 8.4 Hz, 2H), 4.03 (q, *J* = 7.2 Hz, 2H), 3.73 (s, 2H), 1.22 (t, *J* = 7.1 Hz, 3H) (NH not observed). ^{13}C NMR (126 MHz, DMSO-d_6) δ 156.5, 142.4, 140.9, 136.5, 128.0, 127.6, 123.8, 107.9, 46.2, 45.0, 13.5. HRMS (ESI-TOF) calculated for $C_{13}H_{16}ClN_4O^+$ [M+H]$^+$: 279.1007, observed 279.0995.

5-((4-(aminomethyl)phenyl)amino)-4-chloro-2-(prop-2-yn-1-yl)pyridazin-3(2*H*)-one (2.24). Following the general procedure A, (compound **2.27** (185 mg, 0.911 mmol, 1.0 eq.), *tert*-butyl (4-aminobenzyl)carbamate (223 mg, 1.00 mmol, 1.1 eq.), *N,N*-Diisopropylethylamine (317 µL, 1.82 mmol, 2.0 eq.)), a portion of the crude product was then purified by reverse-phase HPLC (5-45% CH_3CN gradient over 30 minutes) to obtain product **2.24** as a white solid (20 mg, 8% yield over two steps). ^{1}H NMR (500 MHz, DMSO-d_6) δ 8.95 (s, 1H), 8.20 (s, 3H), 7.66 (s, 1H), 7.48 (d, *J* = 8.5 Hz, 2H), 7.31 (d, *J* = 8.4 Hz, 2H), 4.94 (d, *J* = 10.3 Hz, 1H), 4.04 (s, 2H), 2.18 (s, 2H). ^{13}C NMR (126 MHz, DMSO-d_6) δ 156.8, 142.3, 138.6, 130.4, 130.1, 128.2, 125.5, 123.5, 108.7, 60.7, 41.8, 27.2. HRMS (ESI-TOF) calculated for $C_{14}H_{14}ClN_4O^+$ [M+H]$^+$: 289.0851, observed 298.0840.

5-((4-(aminomethyl)phenyl)amino)-4-chloro-2-isopropylpyridazin-3(2*H*)-one (2.25). Following the general procedure A, (compound **2.28** (270 mg, 1.31 mmol, 1.0 eq.), *tert*-butyl (4-aminobenzyl)carbamate (320 mg, 1.44 mmol, 1.1 eq.), *N,N*-Diisopropylethylamine (456 µL, 2.62 mmol, 2.0 eq.)), product **2.25** was obtained as a brown solid (65 mg, 17% yield over two steps). ^{1}H NMR (500 MHz, DMSO-d_6) δ 7.66 (s, 1H), 7.36 (d, *J* = 8.4 Hz, 2H), 7.20 (d, *J* = 8.4 Hz, 2H), 5.09 (hept, 6.6 Hz, 1H), 3.74 (s, 2H), 1.23 (d, *J* = 6.7 Hz, 6H). ^{13}C NMR (126 MHz, DMSO-d_6) δ 156.4, 141.9, 140.2, 136.6, 128.1, 127.4, 123.7, 107.8, 48.8, 44.8, 20.8 (NH_2 resonance not observed). HRMS (ESI-TOF) calculated for $C_{14}H_{18}ClN_4O^+$ [M+H]$^+$: 293.1164, observed 293.1153.

4,5-dichloro-2-ethylpyridazin-3(2*H*)-one (2.26). Following the general procedure B, (4,5-dichloropyridazin-3(2*H*)-one (1 g, 6.06 mmol, 1.0 eq.), ethyl bromide (680 µL, 9.09 mmol, 1.5 eq.), sodium hydride (160 mg, 6.67 mmol, 1.1 eq.)), product **2.26** was obtained as a white solid (525 mg, 45% yield). ^{1}H NMR (500 MHz, DMSO-d_6) δ 8.21 (s, 1H), 4.12 (d, *J* = 7.3 Hz, 2H), 1.27 (t, *J* = 7.3 Hz, 3H). ^{13}C NMR (126 MHz, DMSO-d_6) δ 155.5, 136.6, 135.8, 132.8, 47.4, 13.1. HRMS (ESI-TOF) calculated for $C_6H_7Cl_2N_2O^+$ [M+H]$^+$: 192.9930, observed 192.9925.

4,5-dichloro-2-(prop-2-yn-1-yl)pyridazin-3(2*H*)-one (2.27). Following the general procedure B, (4,5-dichloropyridazin-3(2*H*)-one (2 g, 12.1 mmol, 1.0 eq.), propargyl bromide 80 wt. % in toluene (2.02 mL, 18.2 mmol, 1.5 eq.), sodium hydride (320 mg, 13.3 mmol, 1.1 eq.)), product **2.27** was obtained as a white solid (493 mg, 20% yield). ^{1}H NMR (500 MHz, DMSO-d_6) δ 8.25 (s, 1H), 4.90 (d, *J* = 2.6 Hz, 2H), 3.42 (t, *J* = 2.5 Hz, 1H). ^{13}C NMR (126 MHz, DMSO-d_6) δ 155.1, 136.5, 136.4, 133.1, 77.5, 76.2, 41.9. HRMS (ESI-TOF) calculated for $C_7H_5Cl_2N_2O^+$ [M+H]$^+$: 202.9773, observed 202.9769.

4,5-dichloro-2-isopropylpyridazin-3(2H)-one (2.28). Following the general procedure B, (4,5-dichloropyridazin-3(2*H*)-one (1.5 g, 9.1 mmol, 1.0 eq.), isopropyl bromide (1.2 mL, 13.6 mmol, 1.5 eq.), sodium hydride (240 mg, 10.0 mmol, 1.1 eq.)), product **2.28** was obtained as a white solid (294 mg, 16% yield). ^{1}H NMR (500 MHz, DMSO-d_6) δ 8.25 (s, 1H), 5.15 – 5.00 (m, 1H), 1.29 (d, *J* = 6.7 Hz, 6H). ^{13}C NMR (126 MHz, DMSO-d_6) δ 155.4, 136.5, 135.6, 132.5, 50.6, 20.6.

Protein-Observed Fluorine (PrOF) NMR. Fluorinated BPTF, PCAF, CECR2 and BRD4 D1 were expressed and purified as described previously.[262] 40-50 µM of protein in 50 mM TRIS, 100 mM NaCl, and pH 7.4 was diluted by adding 25 µL of D_2O and 2 µL of 0.1% TFA for NMR locking and referencing purposes, respectively. Two spectra were taken of the control protein sample in the presence of 5 µL of DMSO (1% final concentration) at an O1P = -75 ppm, NS = 16, d1 = 1 s, AQ = 0.5 s (samples were referenced to trifluoroacetate at -75.25 ppm) and an O1P = -125 ppm, NS = 500-750, d1 = 0.7 s, AQ = 0.05 s (protein resonances). Ligands were titrated and the change in chemical shift relative to the control sample was plotted as a function of ligand concentration to generate binding isotherms. The data was processed in Mestrenova and isotherms were fit using GraphPad Prism with the equation below. $\Delta\delta_{obs}$ is the change in chemical shift, [L] is the total ligand concentration, and [P] is the total protein concentration:

$$\Delta\boldsymbol{\delta}_{\boldsymbol{obs}} = \Delta\boldsymbol{\delta}_{\boldsymbol{max}} \frac{(\boldsymbol{K_d} + [\boldsymbol{L}] + [\boldsymbol{P}]) - \sqrt{(\boldsymbol{K_d} + [\boldsymbol{L}] + [\boldsymbol{P}])^{\boldsymbol{2}} - \boldsymbol{4}[\boldsymbol{PL}]}}{\boldsymbol{2}[\boldsymbol{PL}]}$$

General procedure for AlphaScreen assay.[270] Unlabeled His_9-tagged BPTF and BRD4 D1 were expressed and purified as described previously.[270] The AlphaScreen assay procedures for BPTF and BRD4 bromodomains were adapted from the manufacturers protocol (PerkinElmer, USA). Nickel chelate (Ni-NTA) acceptor beads and streptavidin donor beads were purchased from PerkinElmer (Cat. #: 6760619M). The biotinylated Histone H4 KAc5,8,12,16 peptide was purchased from EpiCypher, with the sequence:

Ac-SGRGK(Ac)GGK(Ac)GLGK(Ac)GGAK(Ac)RHRKVLR-Peg(Biot).

All reagents were diluted in the assay buffer (50 mM HEPES-Na^+ (ChemImpex), 100 mM NaCl (SigmaAldrich), 0.05% CHAPS (RPI), 0.1% BSA (SigmaAldrich), pH 7.4). The final assay concentrations (after the addition of all assay components) of 30 nM for His_9-tagged BPTF bromodomain and 50 nM for the biotinylated peptide were used. For BRD4 D1, 7.5 nM His_9-BRD4 and 25 nM of the peptide were used. 3-fold serial dilutions were prepared with varying concentrations of the compounds and a fixed protein concentration, keeping the final DMSO concentration at either 0.25% or 0.5% v/v, depending upon the solubility of the compounds. 5 μL of these solutions were added to a 384-well plate (ProxiPlate-384, PerkinElmer). The plate was sealed and kept at room temperature for 30 min, followed by the addition of 5 μL of the biotinylated peptide. 5 µL of nickel chelate acceptor beads was added to each well under low light conditions (<100 lux), to a final concentration of 20 µg/mL, and the plate was incubated at room temperature in the dark for 30 minutes. This was followed by the addition of 5 µL (20 µg/mL final concentration) of streptavidin donor beads in low light conditions. After incubation for 30 min in the dark, the plate was read in AlphaScreen mode using a PerkinElmer EnSpire plate reader. Each compound was run in two technical replicates and the data was normalized against 0 µM inhibitor signal to obtain the % normalized AlphaScreen signal. IC_{50} values were calculated in GraphPad Prism 5 using sigmoidal 4-parameter logistic (4PL) curve fit.

Cell culture methods. 4T1 cells were grown to a confluency of 50-60% using media containing DMEM with 10% fetal bovine serum (FBS), 2 mM glutamine and penicillin-streptomycin. 4T1 cells with shRNA-mediated BPTF knockdown (KD) were prepared as described previously.[281] Figure S15 shows the western blot indicating BPTF KD. For NURF inhibitor toxicity study, 4000 cells/well were seeded in a 96-well plate and allowed to adhere overnight. The next day, 10 different dilutions of inhibitors were prepared starting with a highest concentration of 1.0 mM and further serially diluted 10 times to get the lowest concentration of 1.95 µM. Cells were treated with the inhibitors in complete media for 4 days. Thereafter, the MTS reagent was prepared using the CellTitre 96 aqueous MTS reagent (Promega, Cat #G1111) and phenazine methosulphate (Sigma, Cat #P9625). The MTS assay was performed as per manufacturer's protocol and the absorbance was recorded at a wavelength of 490 nm. Fraction cell survival was calculated using untreated control cells to indicate complete survival (1.0) and blank solutions as 0.0 survival. The data was derived from three independent experiments (N=3) and fraction survival was plotted as mean fraction survival ± SEM using GraphPad Prism software. For checking the toxicity on wildtype and BPTF knockdown cells, three doses were selected for each inhibitor based on their toxicity curves and treated for 4 days alone or in combination with 50 nM doxorubicin. Fraction survival was measured and calculated by MTS assay as mentioned above.

Cytotoxicity experiments with Eph4 cells. Eph4 cells were treated with either DMSO, AU1, **2.19** or **2.20** for 72 hours. Media containing each condition were changed every 12 hours. Cells were then incubated with Magic Red Caspase 3/7 (ImmunoChemistry Technologies, #936) to manufacturers specifications. Cells were also stained with Live/Dead Violet (Thermo Scientific, #L34964) in accordance to manufacturers specifications. All flow was performed on a Macsquant 10 (Miltenyi Biotec) and analyzed on FlowJo (TreeStar/BD). Statistically significant differences for cell line treatment groups were considered with a t-test p-value lower than 0.05 ($p<0.05$).

qPCR methods. Eph4 cells were treated for 24 h and harvested in trizol. RNA extraction was carried out via chloroform extractions. cDNA creation was completed via SuperScript III cDNA creation kit (Invitrogen, #12574026). All qpcrs are normalized to EPH4 DMSO and the house keeping gene beta actin. Bars represent 2 biological replicates and 3 technical replicates. All statistical analysis are student's t-test carried out on GraphPad. Reactions were carried out on the Quantstudio 6 platform using Sybr Green PCR Master Mix (Applied Biosystems, #4309155). Statistically significant differences for cell line treatment groups were considered with a one-way Anova p-value lower than 0.05 ($p<0.05$).

UV-Vis Methods. Compounds were diluted in DMSO at a top concentration of 100 mM. 2-fold serial dilutions in DMSO where performed followed by 1000-fold dilution into phosphate saline buffer (PBS) to get a final top concentration of 100 µM in 0.1% DMSO for each compound. UV-Vis measurements at 254 nm were taken on a Biomate 3S Spectrophotometer.

A) **B)**

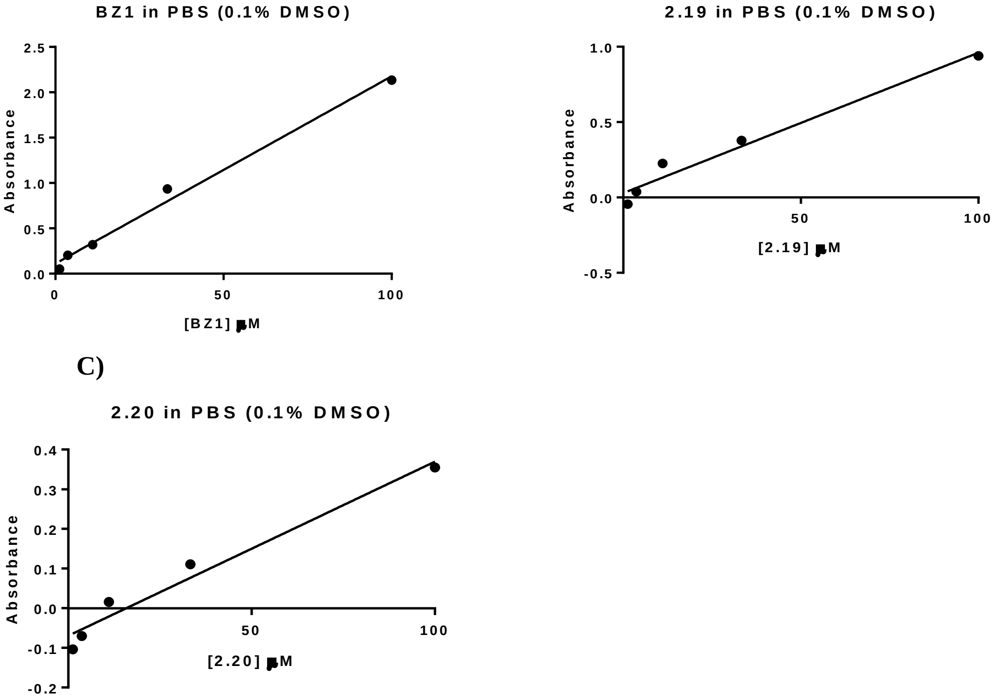

Figure 2.19: Solubility test for compounds 2.18 (BZ1), 2.19, and 2.20 in PBS. A) **BZ1**, B) **2.19**, C) **2.20** in 0.1% DMSO in Phosphate Buffered Saline (PBS) at 254 nm.

BROMOscan data and binding isotherms.

Table 2.7: BROMOscan single point measurements at 140 nM 2.18 (BZ1).

DiscoveRx Gene Symbol	**Entrez Gene Symbol**	**Percent Control**
ATAD2A	ATAD2	53
ATAD2B	ATAD2B	73
BAZ2A	BAZ2A	63
BAZ2B	BAZ2B	38
BRD1	BRD1	24
BRD2(1)	BRD2	100
BRD2(2)	BRD2	65
BRD3(1)	BRD3	50
BRD3(2)	BRD3	89
BRD4(1)	BRD4	29
BRD4(2)	BRD4	63
BRD7	BRD7	1.1
BRD9	BRD9	1.3
BRDT(1)	BRDT	97
BRDT(2)	BRDT	66

BRPF1	BRPF1	10
BRPF3	BRPF3	41
CECR2	CECR2	5.7
CREBBP	CREBBP	57
EP300	EP300	51
FALZ	BPTF	0
GCN5L2	KAT2A	34
PBRM1(2)	PBRM1	97
PBRM1(5)	PBRM1	100
PCAF	KAT2B	0
SMARCA2	SMARCA2	88
SMARCA4	SMARCA4	85
TAF1(2)	TAF1	34
TAF1L(2)	TAF1L	69
TRIM24(PHD,Bromo.)	TRIM24	81
TRIM33(PHD,Bromo.)	TRIM33	58
WDR9(2)	BRWD1	88

A)

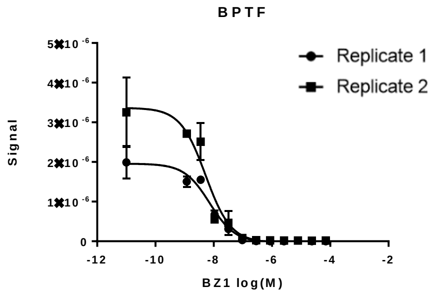

B)

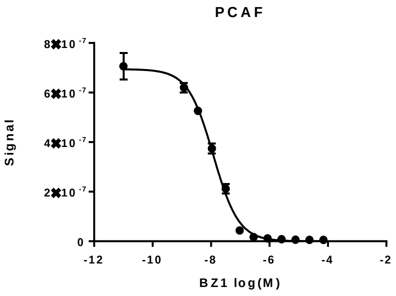

C)

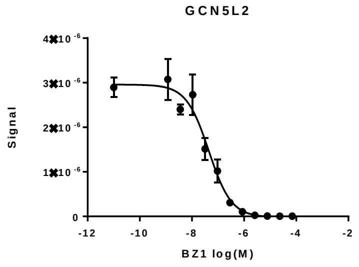

D)

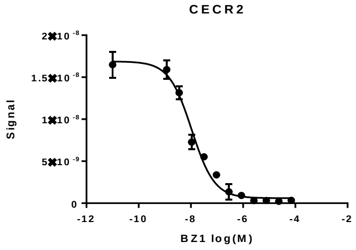

E)

F)

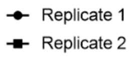

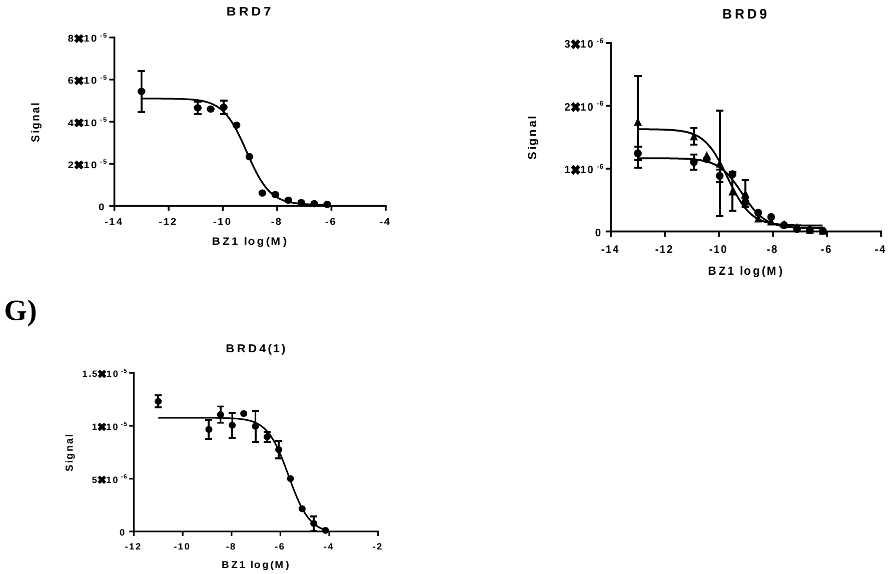

Figure 2.20: DiscoverX BROMOscan titrations of BZ1.

A) BPTF, B) PCAF, C) GCN5L2, D) CECR2, E) BRD7, F) BRD9 and G) BRD4 (1). Annotations replicate 1 and 2 in the graph legend indicate the two experimental replicates.

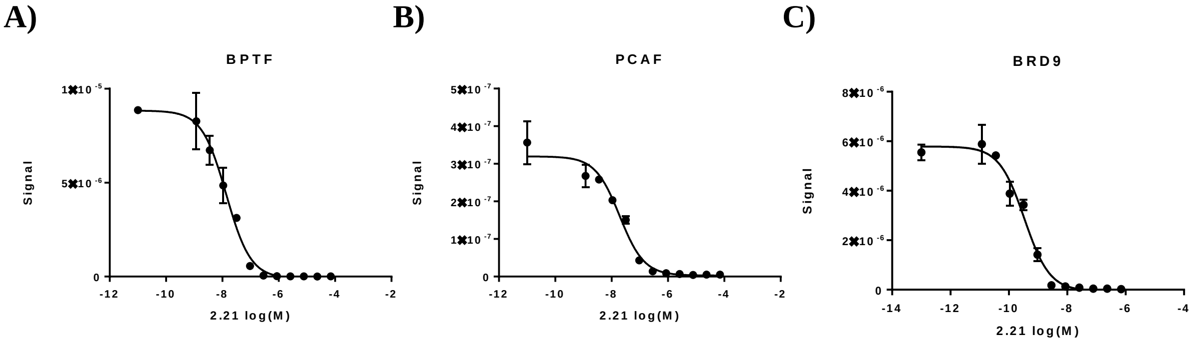

Figure 2.21: DiscoverX BROMOscan titrations of compound 2.21 with A) FALZ (BPTF) B) PCAF and C) BRD9 bromodomains.

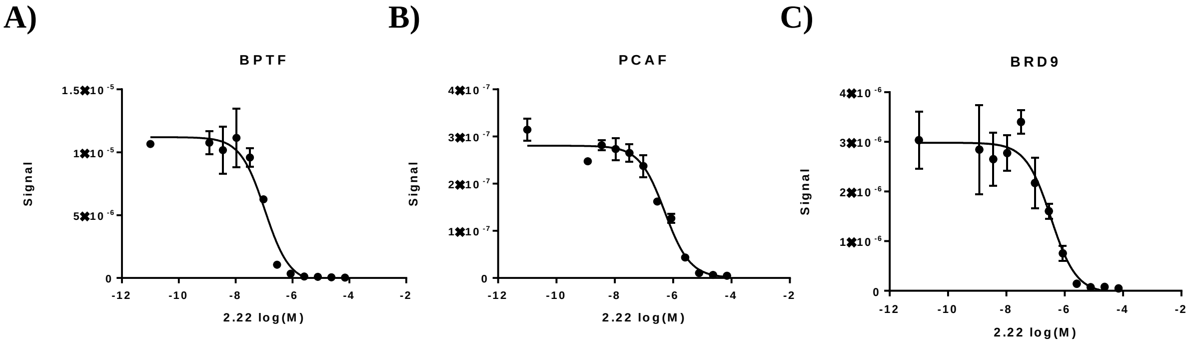

Figure 2.22: DiscoverX BROMOscan titrations of compound 2.22 with A) FALZ (BPTF) B) PCAF and C) BRD9. bromodomains.

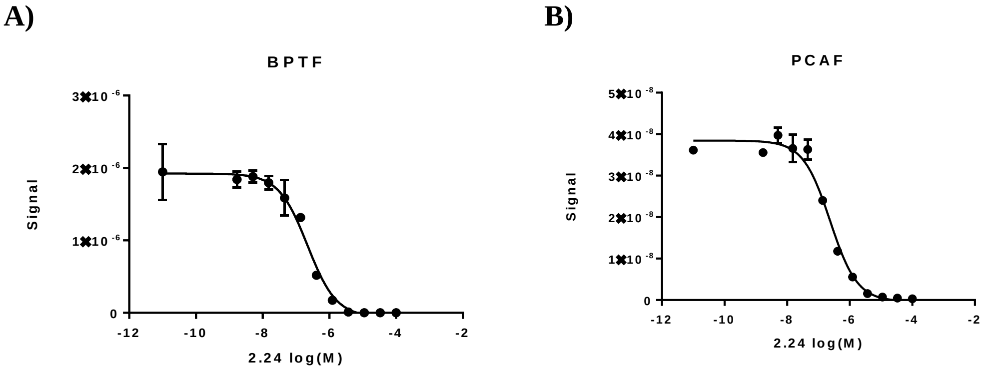

Figure 2.23: DiscoverX BROMOscan titrations of compound 2.24 with A) FALZ (BPTF) and B) PCAF bromodomains.

X-ray crystallography conditions and data collection methods.

<u>BPTF bromodomain purification and crystallography for compounds **2.1-2.4**:</u> Protein purification was performed at 4 °C by FPLC using columns and chromatography resins from GE Healthcare. Cell pellets were re-suspended in 50 mM Na/K Phosphate buffer (pH 7.4) containing 100 mM NaCl, 20 mM imidazole, 0.01% w/v lysozyme, 0.01% v/v Triton X-100 and 1mM DTT. Cells were lysed using a homogenizer, the lysate was clarified by centrifugation and subjected to purification on immobilized Ni^{2+}-affinity chromatography (Qiagen) using a linear gradient of 20 – 500 mM imidazole. Fractions containing BPTF were pooled and incubated overnight with TEV protease at 4 °C. Cleaved BPTF was subjected to a second Ni^{2+}-affinity chromatography run to remove His-TEV and the cleaved His-tag. The flow-through containing BPTF was concentrated and purified to homogeneity by size exclusion chromatography using a Superdex 26/60 column. Protein was eluted using 50 mM Tris/HCl (pH 8.0) containing 100 mM NaCl and 1 mM DTT. Peak fractions were combined, concentrated to 5 mg/mL, flash frozen in liquid N_2 and stored at -80 °C. Crystallization was performed at 18 °C with precipitant solutions from Hampton Research using a Mosquito liquid handler (TTP Labtech). Robust crystallization conditions were

established using 25% PEG 3,350, 0.2 M lithium sulfate monohydrate, 0.1 M Bis-Tris pH 6.5 mixed with an equal volume of protein in vapor diffusion hanging droplets. Compounds were cocrystallized with BPTF at 1 mM final concentration. Crystals were cryoprotected by addition of 20% ethylene glycol in the precipitant, flash frozen and stored in liquid N_2. During data collection, crystals were maintained under a constant stream of N_2 gas. X-ray diffraction data were recorded at beamlines 22-BM hosted by Ser-Cat and 23-ID-D hosted by GM/CA of Argonne National Laboratory. Data were indexed and scaled with XDS.[287] Phasing and refinement was performed using PHENIX[288] and model building with Coot.[289] PDB entry 7K6R served as the search model for molecular replacement. Initial models for small molecule ligands were generated through MarvinSketch (ChemAxon, Cambridge, MA) and ligands restraints through eLBOW of the PHENIX suite. All structures have been validated by MolProbity. Figures were prepared using PyMOL (Schrödinger, LLC). Data processing and refinement statistics are given in **Table 2.8**.

Crystallography methods for compounds **2.10-2.13**: Unlabeled BPTF was expressed and purified as described previously.[270] 200-300 µM BPTF (in 50 mM TRIS, 100 mM NaCl, 10% (v/v) ethylene glycol, pH 7.4) was crystallized with 700 µM of compounds 2.10-2.13 using the hanging drop method at 4 °C. Crystals grew to harvestable size in 3-4 days. 2.10 was crystallized using 200 mM potassium acetate and 20% (v/v) PEG 3350. 2.11 and 2.13 were crystallized using 200 mM manganese acetate and 20% (v/v) PEG 3350. 2.12 was crystallized with 200 mM magnesium chloride and 10% (v/v) PEG 3350. Crystals were harvested, cryoprotected with ethylene glycol and flash frozen. Data was acquired at the Advanced Photon Source with the NECAT 24-IDE beamline. The structures were solved using molecular replacement with Phaser-MR and the PDB structure 3UV2. PHENIX[288] and Coot[289] were used for structure refinement and model building. Data processing and refinement statistics are given in **Table 2.9**.

Crystallography method for compound **2.19**: Unlabeled BPTF was expressed and purified as described previously.[270] BPTF was concentrated to 16 mg/mL and previously reported crystallization conditions[290] were chosen for optimization using a Dragonfly liquid handler (TTP Labtech). Drops consisting of 150 nL reservoir solution and 150 nL protein solution were set up in 96-well hanging drop plates using a mosquito crystallization robot (TTP Labtech). Thin needles formed and grew over 14-16 days in 0.2M NaCl and 23% PEG 3350 at 277 K. Larger needle crystals were grown in 24-well VDX hanging drop plate using micro-seeding. These crystals were soaked in solutions containing 1 mM of compound 19 for 1 hour, cryo-protected using the well solution supplemented with additional 10% glycerol, flash frozen and X-ray diffraction data were collected at 100 K on beam line SER-CAT 22ID at the Advanced Photon Source. Diffraction images were indexed, integrated, and scaled using HKL2000 suite. Phases were obtained by rigid body refinement using 3UV2 as the initial model. Residues were renumbered using 7K6R as a template. Model building was carried out using Coot. The final model was refined using PHENIX, and torsion-angle molecular dynamics with a slow-cooling simulated annealing. Data processing and refinement statistics are given in **Table 2.10**.

Table 2.8: Data collection and refinement statistics for compounds 2.1-2.4.

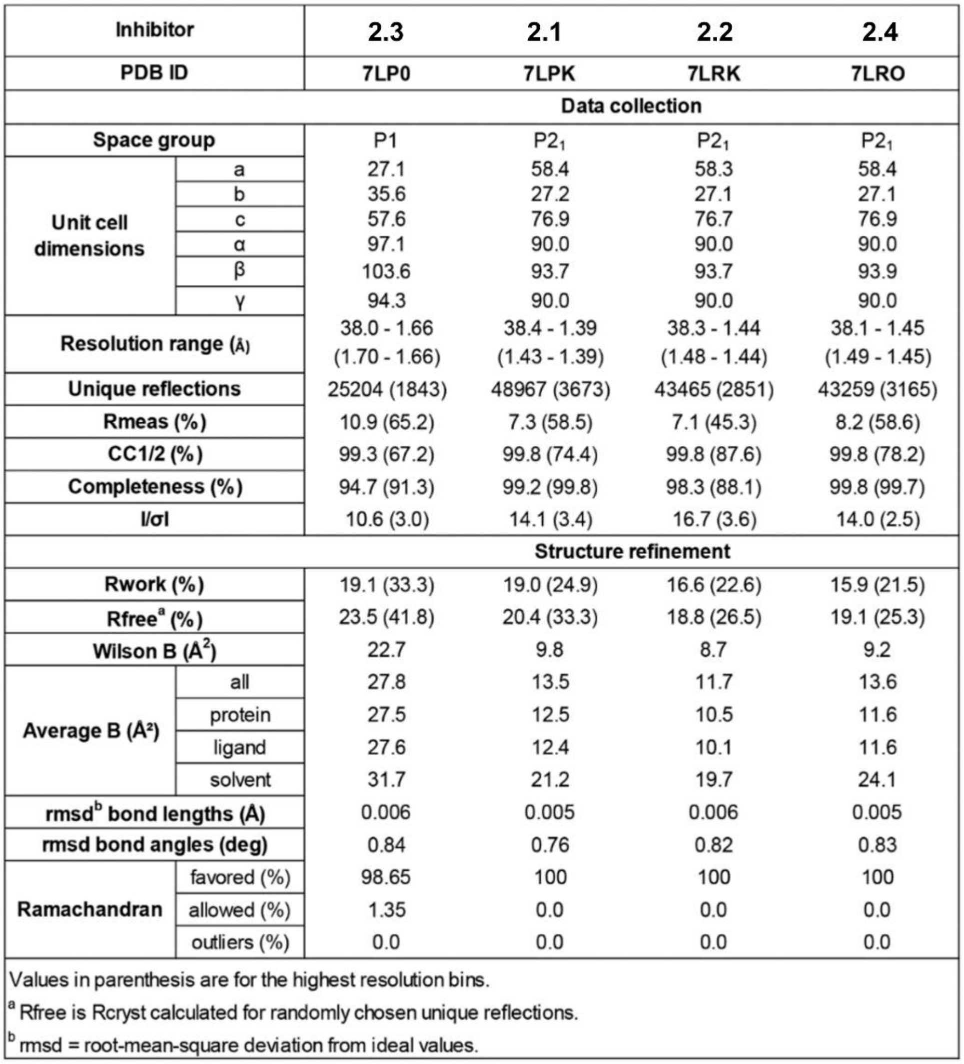

Inhibitor		2.3	2.1	2.2	2.4
PDB ID		7LP0	7LPK	7LRK	7LRO
		Data collection			
Space group		P1	$P2_1$	$P2_1$	$P2_1$
Unit cell dimensions	a	27.1	58.4	58.3	58.4
	b	35.6	27.2	27.1	27.1
	c	57.6	76.9	76.7	76.9
	α	97.1	90.0	90.0	90.0
	β	103.6	93.7	93.7	93.9
	γ	94.3	90.0	90.0	90.0
Resolution range (Å)		38.0 - 1.66 (1.70 - 1.66)	38.4 - 1.39 (1.43 - 1.39)	38.3 - 1.44 (1.48 - 1.44)	38.1 - 1.45 (1.49 - 1.45)
Unique reflections		25204 (1843)	48967 (3673)	43465 (2851)	43259 (3165)
Rmeas (%)		10.9 (65.2)	7.3 (58.5)	7.1 (45.3)	8.2 (58.6)
CC1/2 (%)		99.3 (67.2)	99.8 (74.4)	99.8 (87.6)	99.8 (78.2)
Completeness (%)		94.7 (91.3)	99.2 (99.8)	98.3 (88.1)	99.8 (99.7)
I/σI		10.6 (3.0)	14.1 (3.4)	16.7 (3.6)	14.0 (2.5)
		Structure refinement			
Rwork (%)		19.1 (33.3)	19.0 (24.9)	16.6 (22.6)	15.9 (21.5)
Rfree[a] (%)		23.5 (41.8)	20.4 (33.3)	18.8 (26.5)	19.1 (25.3)
Wilson B (Å^2)		22.7	9.8	8.7	9.2
Average B (Å^2)	all	27.8	13.5	11.7	13.6
	protein	27.5	12.5	10.5	11.6
	ligand	27.6	12.4	10.1	11.6
	solvent	31.7	21.2	19.7	24.1
rmsd[b] bond lengths (Å)		0.006	0.005	0.006	0.005
rmsd bond angles (deg)		0.84	0.76	0.82	0.83
Ramachandran	favored (%)	98.65	100	100	100
	allowed (%)	1.35	0.0	0.0	0.0
	outliers (%)	0.0	0.0	0.0	0.0

Values in parenthesis are for the highest resolution bins.

[a] Rfree is Rcryst calculated for randomly chosen unique reflections.

[b] rmsd = root-mean-square deviation from ideal values.

Table 2.9: Data collection and refinement statistics for compounds 2.10-2.13.

	2.10	2.11	2.12	2.13
Resolution range	48.31 - 1.73 (1.792 - 1.73)	38.28 - 1.39 (1.44 - 1.39)	35.61 - 1.9 (1.968 - 1.9)	33.32 - 1.58 (1.636 - 1.58)
Space group	P 2 21 21	P 1 21 1	P 2 21 21	P 1 21 1
Unit cell	27.131 66.337 70.506 90 90 90	27.148 66.854 39.706 90	27.18 66.346 71.216 90 90 90	27.098 66.638 39.288 90

		105.406 90		106.787 90
Total reflections	62016 (6463)	100196 (9373)	74932 (7559)	64535 (6691)
Unique reflections	13659 (1383)	27024 (2710)	10647 (1044)	17736 (1788)
Multiplicity	4.5 (4.7)	3.7 (3.5)	7.0 (7.2)	3.6 (3.7)
Completeness (%)	98.08 (99.64)	98.18 (98.44)	99.31 (99.71)	96.46 (98.24)
Mean I/sigma(I)	10.69 (2.14)	11.04 (2.57)	9.43 (2.04)	9.37 (2.08)
Wilson B-factor	17.42	11.59	20.6	14.60
R-merge	0.1015 (0.6784)	0.07337 (0.4816)	0.1636 (0.9022)	0.1067 (0.5826)
R-meas	0.114 (0.7611)	0.08561 (0.5697)	0.1767 (0.9711)	0.1265 (0.6807)
R-pim	0.05057 (0.3354)	0.04341 (0.2992)	0.06546 (0.3538)	0.06649 (0.3465)
CC1/2	0.998 (0.783)	0.997 (0.762)	0.994 (0.666)	0.934 (0.737)
CC*	0.999 (0.937)	0.999 (0.93)	0.999 (0.894)	0.983 (0.921)
Reflections used in refinement	13659 (1383)	27024 (2708)	10646 (1043)	17736 (1787)
Reflections used for R-free	1358 (137)	1985 (209)	1073 (106)	1771 (184)
R-work	0.2208 (0.2587)	0.1885 (0.2552)	0.2155 (0.3032)	0.1965 (0.2920)
R-free	0.2693 (0.3355)	0.2133 (0.3002)	0.2575 (0.3559)	0.2278 (0.3213)
CC(work)	0.942 (0.873)	0.955 (0.852)	0.948 (0.744)	0.930 (0.759)
CC(free)	0.911 (0.772)	0.941 (0.831)	0.880 (0.725)	0.835 (0.732)
Number of non-hydrogen atoms	1052	1140	1056	1109
macromolecules	983	1008	996	1019
ligands	19	20	21	20
solvent	50	112	39	70
Protein residues	117	120	119	120

RMS(bonds)	0.007	0.007	0.008	0.006
RMS(angles)	1.12	0.93	1.01	0.78
Ramachandran favored (%)	100.00	99.15	99.14	99.15
Ramachandran allowed (%)	0.00	0.85	0.86	0.85
Ramachandran outliers (%)	0.00	0	0	0.00
Rotamer outliers (%)	0.00	0	0.88	2.59
Clashscore	2.04	0.99	4.02	2.45
Average B-factor	18.69	14.93	22.14	16.32
macromolecules	18.46	14.17	22.15	16.09
ligands	26.57	19.51	23.17	17.37
solvent	20.11	20.9	21.23	19.49

Table 2.10: Data refinement and statistics for compound 2.19.

	2.19
PDB ID	7M2E
Data collection	
Resolution range	33.1 - 1.75 (1.81 - 1.75)
Wavelength (Å)	1.000
Space group	$P\ 2_1$
Unit cell (Å): *a*, *b*, *c* (°): β	27.01, 66.55, 39.62 105.61
Total number of observed reflections	47148 (4142)
Unique reflections	12317 (1033)
Average mosaicity	0.56

Multiplicity	3.8 (2.9)
Completeness (%)	90.33 (75.90)
Mean I/sigma(I)	9.6 (2.5)
Wilson B-factor	20.1
R_{merge} [a]	0.148 (0.391)
Structure refinement	
R_{work}	0.167 (0.199)
R_{free}	0.215 (0.253)
Molecules per asymmetric unit	1
Number of non-hydrogen atoms	1179
macromolecules	993
Ligand (CB02-092)	21
Solvent	165
Protein residues	121
RMS bond lengths (Å)	0.007
RMS bond angles (°)	0.81
Ramachandran favored (%)	100.0
Ramachandran allowed (%)	0.0
Ramachandran outliers (%)	0.0
Rotamer outliers (%)	0.92
Clashscore	0.51
Mean B values (Å^2)	
Overall	23.4
macromolecules	22.0
Ligand (CB02-092)	26.4
Solvent	31.3

Parentheses numbers represent the highest-resolution shell.

${}^{a}R_{\text{merge}} = \Sigma_{hkl}\Sigma_i|I_i(hkl)-I_{av}(hkl)|/\Sigma_{hkl}\Sigma_i I_i(hkl)$.

2.5 Acknowledgement

This work was conducted at the NE-CAT, GM/CA and SER-CAT beamlines at the Advanced Photon Source, which are supported by the NIH (P30-GM124165, Y1-CO-1020 and Y1-GM-1104). The Pilatus 6M detector on 24-ID-C beamline is funded by a NIH-ORIP HEI grant (S10-RR029205). We thank staff at the NE-CAT, GM/CA and SER-CAT beamlines for assistance in data collection. We thank the Moffitt Chemical Biology Core for use of the crystallization and crystallography facility (National Cancer Institute grant P30-CA076292). The authors thank Jose Valentin Lopez for contributing to the synthesis of related compounds published here. Figures were created with BioRender and PyMOL. Figure 2.1B and 2.5A adapted

by permission from Springer Nature, Applied Biophysics for Bromodomain Drug Discovery by William C. K. Pomerantz, Jorden A. Johnson, Peter D. Ycas Copyright 2019.

3) Future and On-Going Analysis of Cellular Activity of BZ1, Second Generation Inhibitors, and New Proximity-Inducing Molecules

This is unpublished and ongoing work (Section 3.2 manuscript in preparation).

Motivation: The goal of the work described in this chapter was to take the inhibitors described in Chapter 2 and further optimize selectivity, as well as use them as chemical probes in cellular models. Current progress in these specific areas based on collaborative studies is provided in the following sections. In Section 3.1, we tested the lead molecule, **BZ1**, and analogs in cancer cell models to test for sensitization. In Section 3.2, we also used the design rules established in Chapter 2 to design a more selective inhibitor, **BZ2**. Finally, in Section 3.3 we used the **BZ1** scaffold as a probe molecule to design two synthetic transcription factors (SynTFs) with the Ansari lab as a potential mechanism to alter the c-Myc transcriptional pathway. These molecules represent one example of a proximity-inducing ligand that is enabled by the structural biology described in Chapter 2.

3.1 Pyridazinone Sensitization in Cancer Cell Models

Contributions: Caroline R. Buchholz synthesized the compounds, and performed Alamar Blue and Western blot assays. Research directed by Laurie L. Parker and William C.K. Pomerantz.

3.1.1 Pyridazinone Sensitization in K562 cells

K562, a chronic myeloid leukemia (CML) cell line, has been shown to have increased BPTF gene expression, sensitivity to BPTF gene deletion, and high levels of Myc.[264] BPTF is correlated to the oncogene *Myc* in tumors as both a driver of Myc expression as well as formation of a complex with Myc that drives transcription of Myc signaling genes.[255,256] Therefore, we sought to evaluate K562 cells as a model cell line to test for sensitization to BZ1 and pyridazinone analogs. In addition to parental K562 cell lines, cell lines that have been cultured to be resistant against frontline tyrosine kinase inhibitors (TKI)[291] are of interest as a potential mechanism to overcome this resistance mechanism. Studies in these cell lines testing the efficacy of BPTF bromodomain inhibitors will be compelling because drug resistance is a significant clinical problem.

To test growth inhibition of our pyridazinones in K562 cells, we used the Alamar Blue assay. Resazurin, the Alamar Blue reagent, is blue and has low fluorescence, upon redox it can be converted to resorufin, a pink and highly fluorescent molecule. In the cellular context, normal healthy cells will metabolically convert resazurin to resorufin, which can be tracked by absorbance or fluorescence. Alamar Blue assays have become a common indicator of cell metabolic function and cellular health.[292]

Optimization of this assay started with varying cellular density and incubation time to determine the optimal signal to background. Incubating 5,000-10,000 cells over 2-4 hours gave more than enough signal to background (**Figure 3.1A**). Next, control molecule, Imatinib, a kinase inhibitor that is well characterized in K562 cells,[293] was tested under these conditions and approximated the literature growth inhibition IC_{50} of 387 nM with an IC_{50} of 160 nM(**Figure 3.1B**).

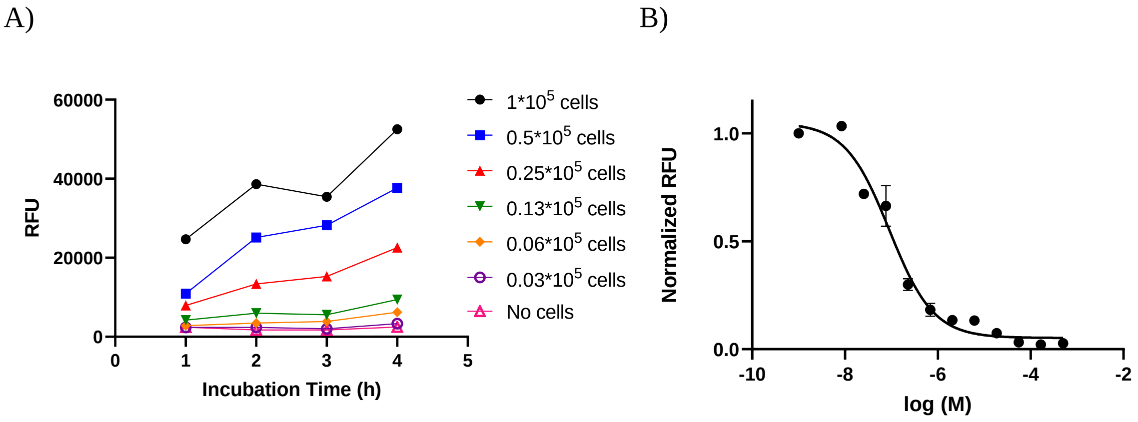

Figure 3.1: AlamarBlue assay optimization in K562 cells.

K562 cells were A) plated in varying cell densities and fluorescence was measured each hour and B) treated with a titration of Imatinib (IC_{50} = 160 nM), 2 technical replicates.

We next moved forward with testing growth inhibition of K562 cells upon treatment of various BPTF bromodomain inhibitors (**Figure 3.2**). We chose to test **BZ1**, our lead molecule, and **2.19** as it has a dimethyl amine compared to a free amine, potentially making it more cell penetrable. **BZ1** and **2.19** showed no effect even at 50 µM. **AU1**, another reported BPTF inhibitor from the Pomerantz lab,[264] and **TP-238**, a reported CECR2/BPTF inhibitor,[266] were also not a strong sensitizer of K562 cells. **AU1** had an IC_{50} of 67 uM and **TP-238** did not show any inhibition until 50 µM, which were likely due to general toxicity and not pursued further.

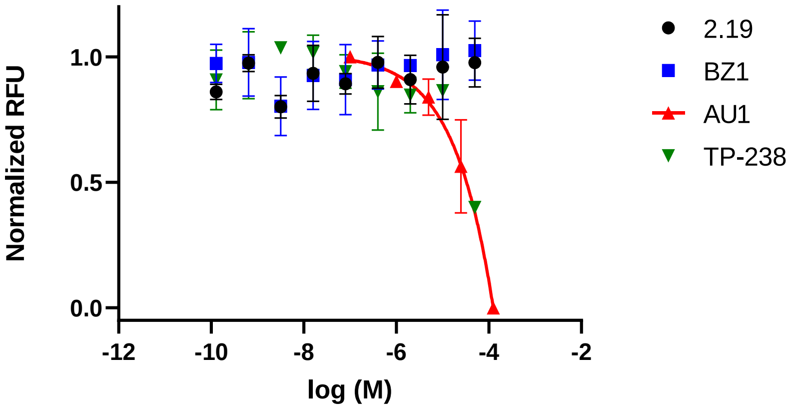

Figure 3.2: AlamarBlue assay in K562 cells treated with BPTF bromodomain inhibitors. K562 cells were treated with pyridazinone inhibitors **2.10**, **2.19,** and **AU1** & **TP-238**, 2 technical replicates.

Given the low toxicity of bromodomain inhibitors on their own we wanted to test them synergistically with Imatinib, similar to previous studies where we showed synergy between **BZ1** and chemotherapeutics in breast cancer cell models.[55] However similar to our previous results, our pyridazinone inhibitors did not show any toxicity as the growth inhibition by Imatinib was not amplified (**Figure 3.3**).

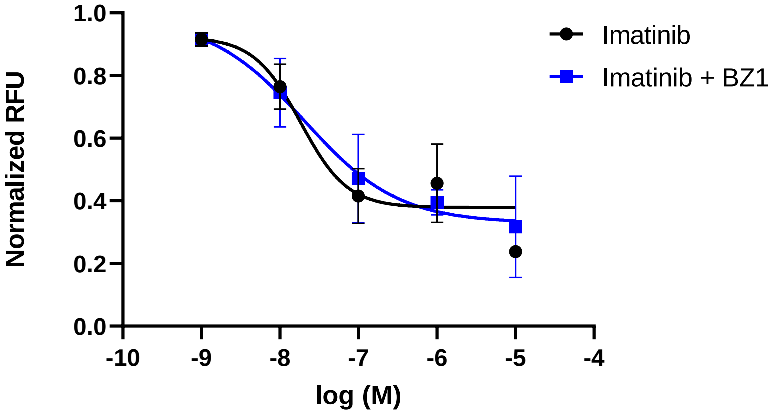

Figure 3.3: AlamarBlue assay in K562 cells testing synergy with BPTF bromodomain inhibitors. K562 cells were treated with Imatinib alone (IC_{50} = 120 nM) and Imatinib plus 5 μM pyridazinone **2.10** (IC_{50} = 110 nM), 2 technical replicates.

As a final exploration of this cell line, we tested frontline TKI resistant cell lines that had been cultured with doses of Imatinib over time to make them Imatinib resistant (IR) K562 cells (IR BA and IR VN). These cells were characterized as having a high level of carbonic anhydrase 1 (CA1), a marker that we used to confirm the cells were still Imatinib resistant,[291] as well as obtaining a growth inhibition IC_{50} to compare to the literature value of 6200 nM. We saw both higher levels of CA1 in IR versus WT K562 cells (**Figure 3.4A**), and a comparable IC_{50} of 3200 nM (**Figure 3.4B**) in the first IR cell line, IR VN. The other cell line, IR BA, did not show increased levels of CA1 by Western blot and visibly the cells looked pinker like red blood cells, so we did not continue to use this line. However, consistent with our prior findings, our pyridazinone inhibitors did not show any sensitization in the IR cell lines (**Figure 3.4C**). The low toxicity of pyridazinones in K562 cells indicated a need for a broader cellular screen to find a more sensitive system.

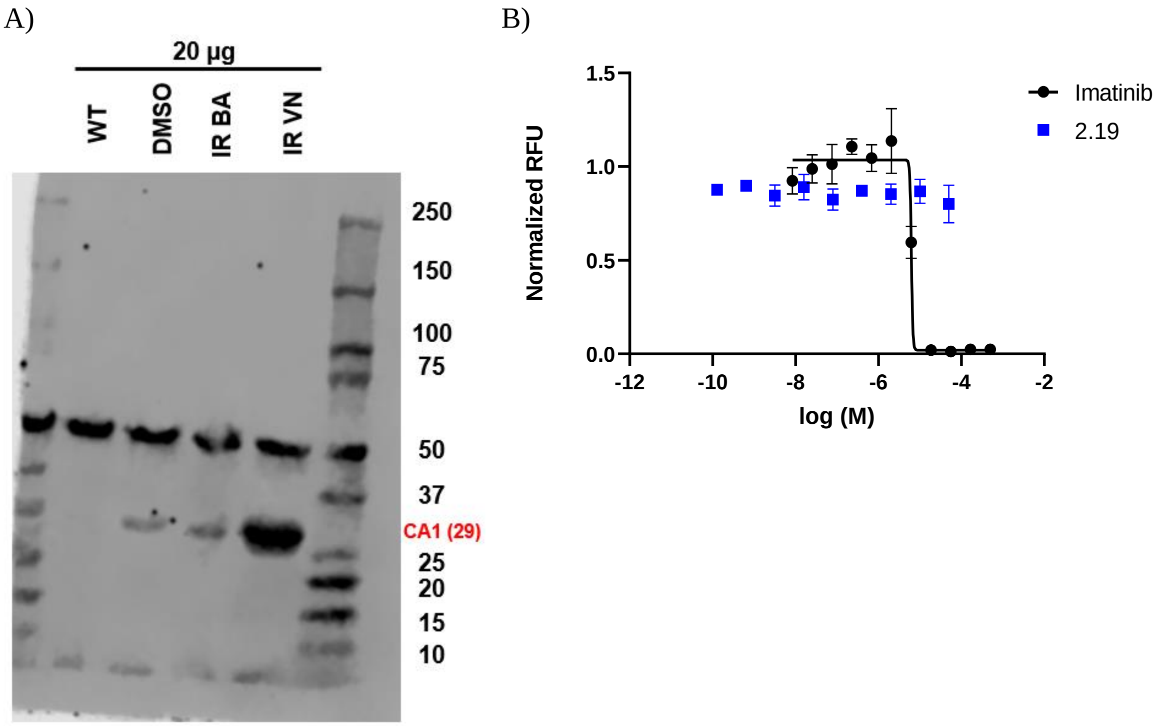

Figure 3.4: Imatinib Resistant K562 cells treated with BPTF bromodomain inhibitor.

A) K562 lysates from parental cell line (WT), DMSO treated cell line (DMSO), and Imatinib resistant treated cell lines (IR BA, IR VN) were blotted for CA1 (29 kDa) with loading control α-tubulin (50 kDa). B) K562 IR VN cells were treated with Imatinib and pyridazinone **2.19** and growth inhibition was measured by AlamarBlue assay, 2 technical replicates.

3.1.2 Pyridazinone Sensitization in NCI60 Tumor Screen

We next wanted to test our pyridazinone inhibitors across a broad array of cancer cell models to potentially target a BPTF bromodomain sensitive cell line. The NCI-60 Human Tumor Cell Lines Screen (NCI60) is widely used in the cancer research field and contains 60 different human tumor cell lines that can be dosed with submitted small molecules to assess growth inhibition and lethality.[294] **BZ1** and **2.22** were our top BPTF bromodomain inhibitors described in Chapter 2 and were submitted to the NCI60 panel. **BZ1** was the most potent for the BPTF bromodomain (K_d = 6.3 nM), and **2.22** was the most selective for BPTF over off-target BRD9 (3x-fold) with a small loss in potency (K_d = 70 nM).[55]

Overall, neither compound showed significant effects across all the paneled cell lines. **BZ1** at 10 μM showed some growth inhibition in MCF-7 (90% lethality), a breast cancer cell line that has increased BPTF gene expression levels and upon BPTF deletion or BPTF bromodomain inhibition by AU1 cell growth is inhibited.[264,295] Additionally, **BZ1** showed some growth inhibition in HCT-15, a colon cancer cell line, and SR, a lymphoma cell line (83% and 70% lethality respectively, **Figure 3.5**). Looking at K562 cells, **BZ1** had a low sensitivity of 24% lethality, comparable to the results found in Alamar Blue assays detailed in Section 3.1.1. **2.22** showed no significant sensitization across all cell lines (**Figure 3.6**). One recent cell line that has been identified as sensitive to BPTF bromodomain inhibition, MV-4-11, a leukemia cell line, was not tested in this panel but may be of interest in the future.[50]

The low toxicity of both pyridazinones across the NCI60 in contrast to their nanomolar affinity could indicate issues with cell permeability and cellular stability, or phenotypic differences from bromodomain inhibition versus genetic knockdown. Looking towards the future, these molecules do seem to be well tolerated but there is a need for a more sensitive cellular model system. Additionally, we are looking towards different mechanisms beyond BPTF bromodomain inhibition, including BPTF degraders[296] or BPTF PHD inhibitors (Chapter 4).

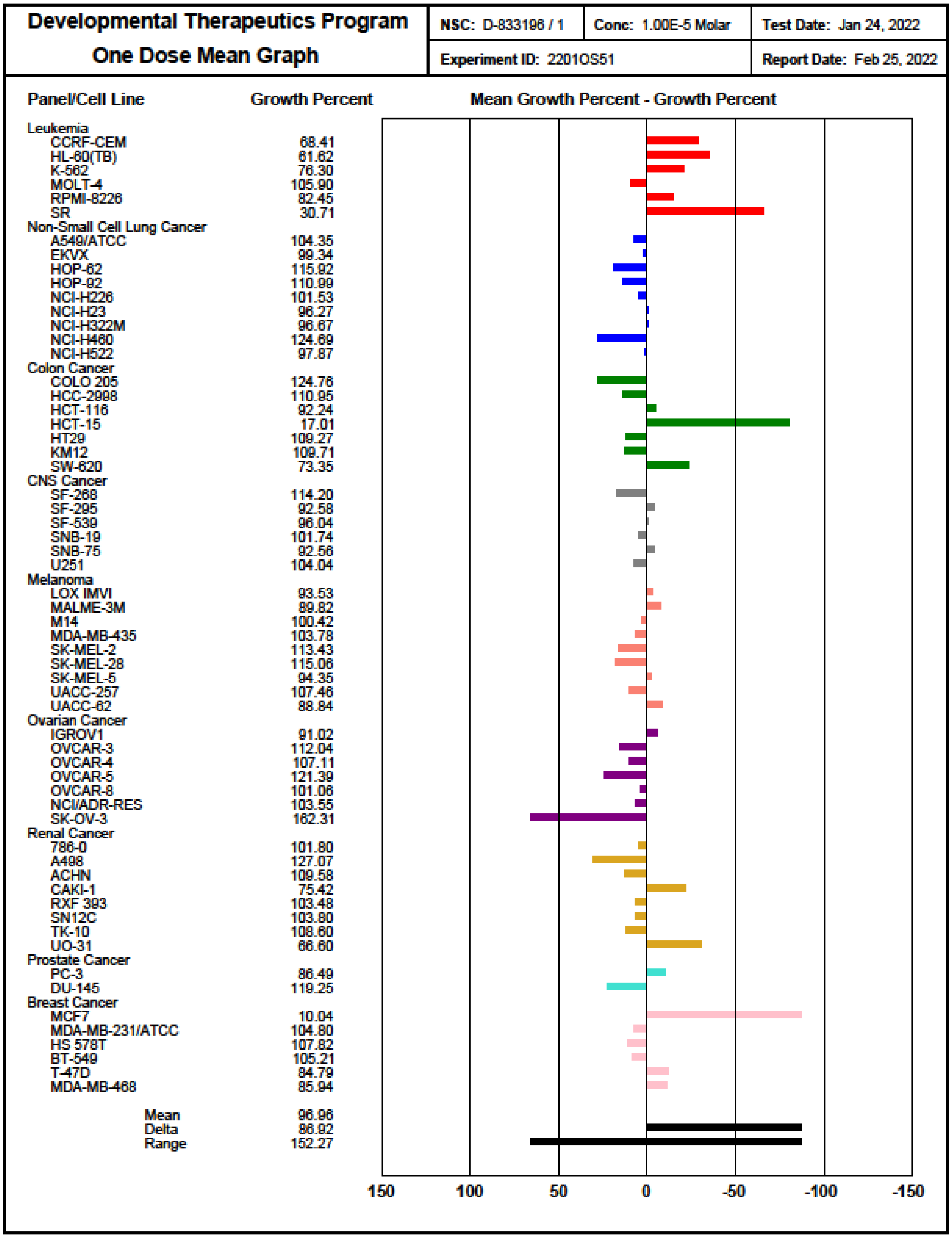

Developmental Therapeutics Program
One Dose Mean Graph

NSC: D-833196 / 1
Conc: 1.00E-5 Molar
Test Date: Jan 24, 2022
Experiment ID: 2201OS51
Report Date: Feb 25, 2022

Panel/Cell Line	Growth Percent
Leukemia	
CCRF-CEM	68.41
HL-60(TB)	61.62
K-562	76.30
MOLT-4	105.90
RPMI-8226	82.45
SR	30.71
Non-Small Cell Lung Cancer	
A549/ATCC	104.35
EKVX	99.34
HOP-62	115.92
HOP-92	110.99
NCI-H226	101.53
NCI-H23	96.27
NCI-H322M	96.67
NCI-H460	124.69
NCI-H522	97.87
Colon Cancer	
COLO 205	124.76
HCC-2998	110.95
HCT-116	92.24
HCT-15	17.01
HT29	109.27
KM12	109.71
SW-620	73.35
CNS Cancer	
SF-268	114.20
SF-295	92.58
SF-539	96.04
SNB-19	101.74
SNB-75	92.56
U251	104.04
Melanoma	
LOX IMVI	93.53
MALME-3M	89.82
M14	100.42
MDA-MB-435	103.78
SK-MEL-2	113.43
SK-MEL-28	115.06
SK-MEL-5	94.35
UACC-257	107.46
UACC-62	88.84
Ovarian Cancer	
IGROV1	91.02
OVCAR-3	112.04
OVCAR-4	107.11
OVCAR-5	121.39
OVCAR-8	101.06
NCI/ADR-RES	103.55
SK-OV-3	162.31
Renal Cancer	
786-0	101.80
A498	127.07
ACHN	109.58
CAKI-1	75.42
RXF 393	103.48
SN12C	103.80
TK-10	108.60
UO-31	66.60
Prostate Cancer	
PC-3	86.49
DU-145	119.25
Breast Cancer	
MCF7	10.04
MDA-MB-231/ATCC	104.80
HS 578T	107.82
BT-549	105.21
T-47D	84.79
MDA-MB-468	85.94
Mean	96.96
Delta	86.92
Range	152.27

Figure 3.5: BZ1 NCI60 Results

BZ1 growth inhibition at 10 µM

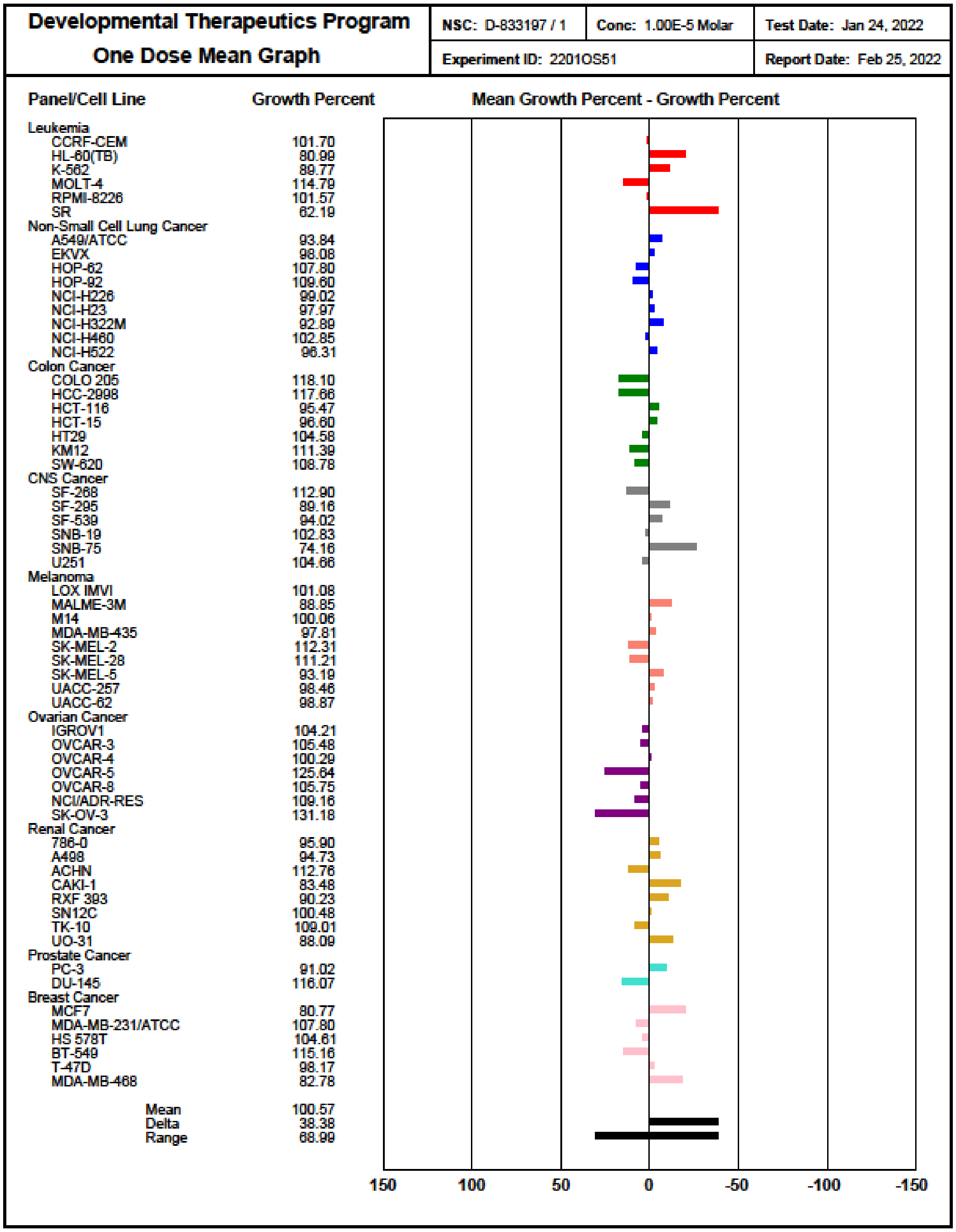

Developmental Therapeutics Program
One Dose Mean Graph

NSC: D-833197 / 1	**Conc:** 1.00E-5 Molar	**Test Date:** Jan 24, 2022
Experiment ID: 2201OS51		**Report Date:** Feb 25, 2022

Panel/Cell Line	Growth Percent
Leukemia	
CCRF-CEM	101.70
HL-60(TB)	80.99
K-562	89.77
MOLT-4	114.79
RPMI-8226	101.57
SR	62.19
Non-Small Cell Lung Cancer	
A549/ATCC	93.84
EKVX	98.08
HOP-62	107.80
HOP-92	109.60
NCI-H226	99.02
NCI-H23	97.97
NCI-H322M	92.89
NCI-H460	102.85
NCI-H522	96.31
Colon Cancer	
COLO 205	118.10
HCC-2998	117.66
HCT-116	95.47
HCT-15	96.60
HT29	104.58
KM12	111.39
SW-620	108.78
CNS Cancer	
SF-268	112.90
SF-295	89.16
SF-539	94.02
SNB-19	102.83
SNB-75	74.16
U251	104.66
Melanoma	
LOX IMVI	101.08
MALME-3M	88.85
M14	100.06
MDA-MB-435	97.81
SK-MEL-2	112.31
SK-MEL-28	111.21
SK-MEL-5	93.19
UACC-257	98.46
UACC-62	98.87
Ovarian Cancer	
IGROV1	104.21
OVCAR-3	105.48
OVCAR-4	100.29
OVCAR-5	125.64
OVCAR-8	105.75
NCI/ADR-RES	109.16
SK-OV-3	131.18
Renal Cancer	
786-0	95.90
A498	94.73
ACHN	112.76
CAKI-1	83.48
RXF 393	90.23
SN12C	100.48
TK-10	109.01
UO-31	88.09
Prostate Cancer	
PC-3	91.02
DU-145	116.07
Breast Cancer	
MCF7	80.77
MDA-MB-231/ATCC	107.80
HS 578T	104.61
BT-549	115.16
T-47D	98.17
MDA-MB-468	82.78
Mean	100.57
Delta	38.38
Range	68.99

Figure 3.6: Compound 2.22 NCI60 Results

2.22 growth inhibition at 10 µM

3.2 Selectivity Gains from BZ1

Manuscript in preparation

Contributions: Caroline R. Buchholz and Chun-Ju Tsou synthesized the compounds, Caroline R. Buchholz optimized AlphaScreen assays, Caroline R. Buchholz and Chun-Ju Tsou performed AlphaScreen assays. Research directed by Anang Shelat, Marcus Fischer, and William C.K. Pomerantz.

3.2.1 AlphaScreen Development for Off-Targets CECR2 and BRD9

Due to the off-target activities of **BZ1** for BRD9 and CECR2 we wanted to develop binding assays for each protein to rapidly assess selectivity moving forward as we designed second generation **BZ1** analogs. Previously, AlphaScreen had been used in our lab to quantitatively rank bromodomain inhibitors for BPTF[270] and BRD4.[278] **BZ1** was assayed against CECR2 using PrOF NMR, where the intermediate exchange regime of pyridazinone analogs did not allow for direct K_d determinations, and a commercial service, BROMOscan.[55] **BZ1** was also tested against BRD9 by BROMOscan. AlphaScreen was a complementary assay that could work well versus commercial services to rank-order BZ1 analogs.

Optimization started with testing the H4 tetra-acetylated biotinylated peptide as a probe. Commercial assays for BRD9 and CECR2, such as Reaction Biology, use H4 tetra-acetylation patterns as the probe suggesting a strong interaction between the two. A cross-titration was initially run to confirm complex formation between the histone probe and respective bromodomain-containing protein, as well as identify the concentration of probe and protein needed for optimal signal and approximation of K_d. Referring back to Section 1.5, where AlphaScreen methodology for epigenetic reader proteins is described, the concentration of each component must be high enough to generate signal above background, but significantly lower than the K_d of the probe for the target protein to be able to approximate tested compounds K_d from IC_{50}.

His-tagged BRD9 was tested with H4 tetra-acetylated probe in a 64-point titration. While the concentrations used were not high enough to see the full Hook effect, the general trend of lower (red) to higher signals (green) when moving from the bottom right to the top left held (**Figure 3.7**). Additionally, the signal response was ~4*10^6, enough for a large dynamic range upon inhibition. Similar results were seen for His-tagged CECR2 when tested with H4 tetra-acetylated probe in a 64-point titration (**Figure 3.8**). In both cases, this indicates the H4 tetra-acetylated probe will likely be viable for testing competitive inhibition of BRD9 and CECR2.

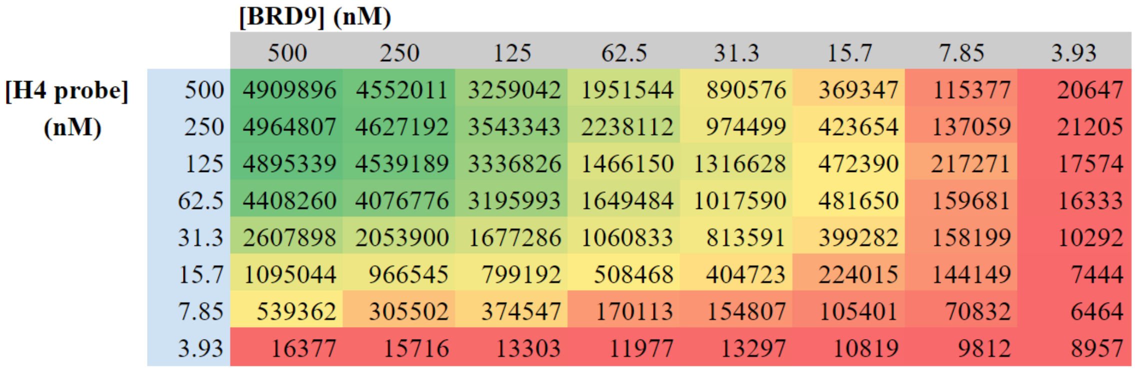

		[BRD9] (nM)							
		500	250	125	62.5	31.3	15.7	7.85	3.93
[H4 probe] (nM)	500	4909896	4552011	3259042	1951544	890576	369347	115377	20647
	250	4964807	4627192	3543343	2238112	974499	423654	137059	21205
	125	4895339	4539189	3336826	1466150	1316628	472390	217271	17574
	62.5	4408260	4076776	3195993	1649484	1017590	481650	159681	16333
	31.3	2607898	2053900	1677286	1060833	813591	399282	158199	10292
	15.7	1095044	966545	799192	508468	404723	224015	144149	7444
	7.85	539362	305502	374547	170113	154807	105401	70832	6464
	3.93	16377	15716	13303	11977	13297	10819	9812	8957

Figure 3.7: Complex Formation of BRD9 with H4 tetra-acetylated probe

Titration of [BRD9] across and titration of [H4 tetra-acetylated probe] down in 64-well plate. Highest AlphaScreen signals are shown in green, intermediate in yellow, and lowest in red.

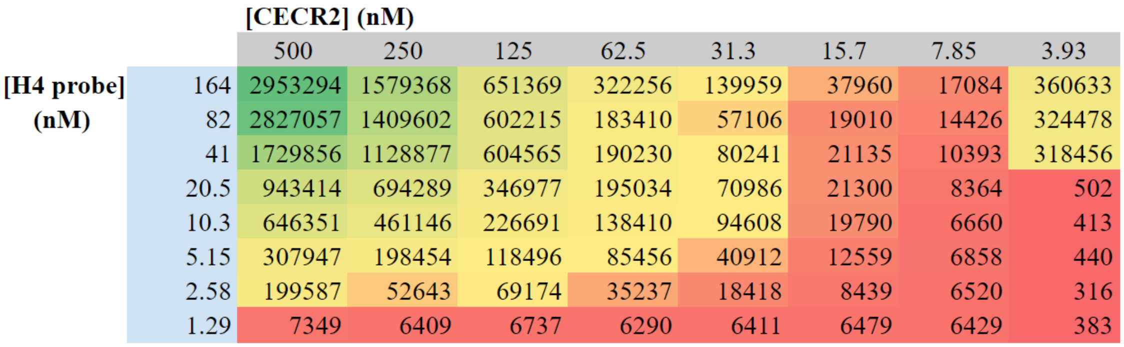

		[CECR2] (nM)							
		500	250	125	62.5	31.3	15.7	7.85	3.93
[H4 probe] (nM)	164	2953294	1579368	651369	322256	139959	37960	17084	360633
	82	2827057	1409602	602215	183410	57106	19010	14426	324478
	41	1729856	1128877	604565	190230	80241	21135	10393	318456
	20.5	943414	694289	346977	195034	70986	21300	8364	502
	10.3	646351	461146	226691	138410	94608	19790	6660	413
	5.15	307947	198454	118496	85456	40912	12559	6858	440
	2.58	199587	52643	69174	35237	18418	8439	6520	316
	1.29	7349	6409	6737	6290	6411	6479	6429	383

Figure 3.8: Complex Formation of CECR2 with H4 tetra-acetylated probe

Titration of [CECR2] across and titration of [H4 tetra-acetylated probe] down in 64-well plate. Highest AlphaScreen signals are shown in green, intermediate in yellow, and lowest in red.

Competition experiments were carried out using previously characterized control compounds, **BZ1** and **2.22** characterized in Chapter 2 for BRD9 by BROMOScan and **TP-238** characterized by the Structural Genomics Consortium for CECR2.

As a starting point, 100 nM His-BRD9 and 100 nM probe H4 tetra-acetylated probe was chosen as the complex gave a signal around three million in the cross titration. Under these conditions **BZ1** had an IC_{50} of 27 nM and **2.22** had an IC_{50} of 270 nM (**Figure 3.9**). This value was higher for **BZ1** than the K_d measured by BROMOscan (0.47 nM). We also saw this trend when testing **BZ1** against BPTF by BROMOscan versus AlphaScreen (10-fold). For **2.22** the measured IC_{50} and reported K_d (230 nM) were comparable. We selected these conditions as **2.22** was well approximated and lowering either the protein or probe concentrations would have likely resulted in a loss of the large dynamic range.

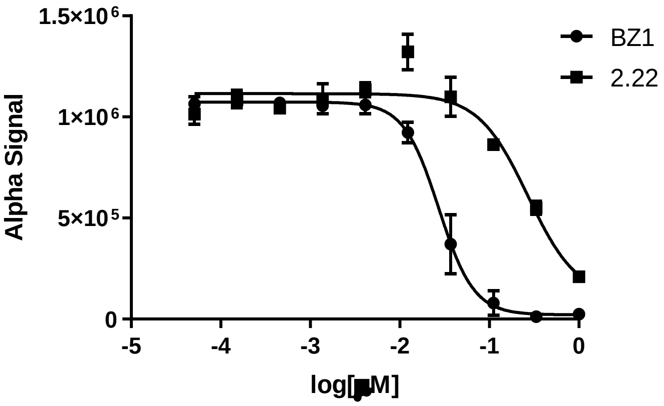

Figure 3.9: Competition experiment of BRD9 with BZ1 and 2.22.

For CECR2, as a starting point we chose 100 nM His-CECR2 and 100 nM probe H4 tetra-acetylated probe as the complex formation by cross titration was similar to that of BRD9. Under these conditions **TP-238** had an IC_{50} of 45 nM (**Figure 3.10A**), which was approximating the reported K_d of 10 nM and comparable to the reported IC_{50} of 30 nM.[266] To try and better approximate the K_d, we lowered the protein concentration to 60 nM and kept the probe at 100 nM, since the top signal was around 3 million this seemed reasonable. Under these conditions the measured IC_{50} of **TP-238** was 33 nM (**Figure 3.10B**), which was closer to the reported K_d, demonstrating how adjusting the protein concentration can improve K_d approximation in AlphaScreen competition assays.

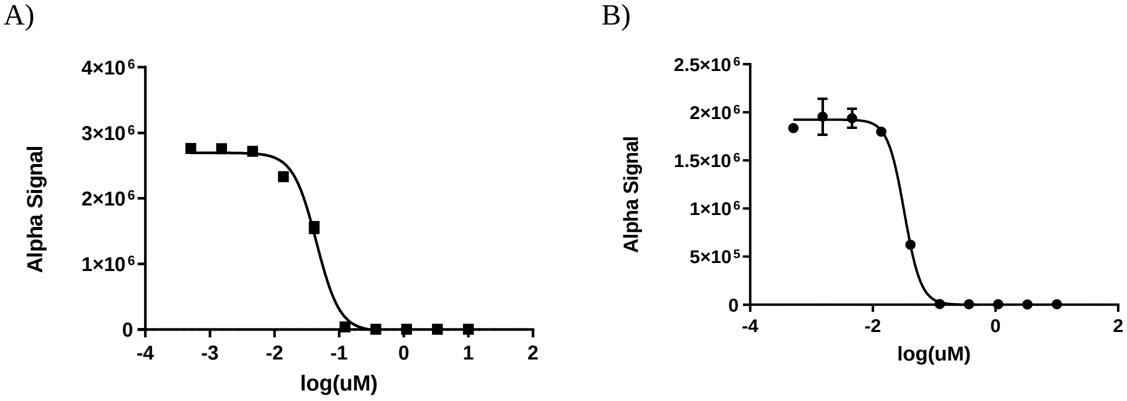

Figure 3.10: Competition experiment of BRD9 with BZ1 and 2.22.

A) 100 nM [CECR2] and 100 nM [probe] B) 60 nM [CECR2] and 100 nM [probe]

3.2.2 Design of Second Generation Pyridazinone Inhibitor BZ2

With binding assays in hand for off-targets BRD9 and CECR2 we moved forward with testing design ideas for more selective inhibitors. From work detailed in Chapter 2 we had hypothesized that targeting acidic residues in the BPTF binding pocket would afford both potency and selectivity. We had previously tested compounds with extended amines to interact with these acidic residues and landed on **BZ1** as our lead molecule. To further improve selectivity against BRD9 we turned to computational chemistry. In collaboration with St. Jude, we took our co-crystal structure of BPTF with **2.10**, a **BZ1** analog with one less methylene unit on the extended amine, and ran molecular dynamics studies. Through this work we hypothesized that we could target Asp2960 with a water mediated hydrogen bond by moving the nitrogen in the pyridazinone ring to form a pyrimidinone.

We designed **BZ2**, which has the same extended amine as **BZ1**, but a pyrimidinone ring instead of a pyridazinone ring. Testing by AlphaScreen (**Table 3.1, Figure 3.11A-C**), **BZ2** had a slight loss in potency for BPTF but was 10-fold more selective for BPTF over BRD9. Additionally, it gained more selectivity over CECR2 than **BZ1**. This made **BZ2** our most selective inhibitor. In a further test of selectivity, BROMOscan against Family I Bromodomains BPTF, CECR2, PCAF, and GCN5L2 showed **BZ2** to have increased selectivity for BPTF (**Figure 3.11D**). Additionally, activity against major **BZ1** off-targets BRD7 and BRD9 were greatly reduced with **BZ2** increasing selectivity to 77-fold.

Table 3.1: Selectivity Analysis of BZ1 and BZ2 by AlphaScreen.

Alpha Screen	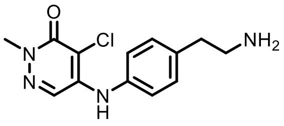 **BZ1**	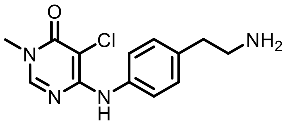 **BZ2**	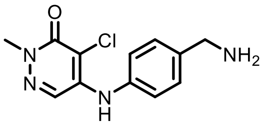 **10**
BPTF IC_{50}	0.140 ± 0.01 µM 0.070 ± 0.01 µM[55]	0.22 ± 0.02 µM	0.29 ± 0.08 µM[55]
CECR2 IC_{50}	0.45 ± 0.03 µM	1.4 ± 0.1 µM	2.0 ± 0.2 µM
BRD9 IC_{50}	0.054 ± 0.01 µM	2.8 ± 0.5 µM	0.11 ± 0.02 µM

AlphaScreen values were based on an average of three technical replicates, with N = 3. NB = No binding at top conc. of 50 µM. Binding isotherms shown in **Figure 3.11**.

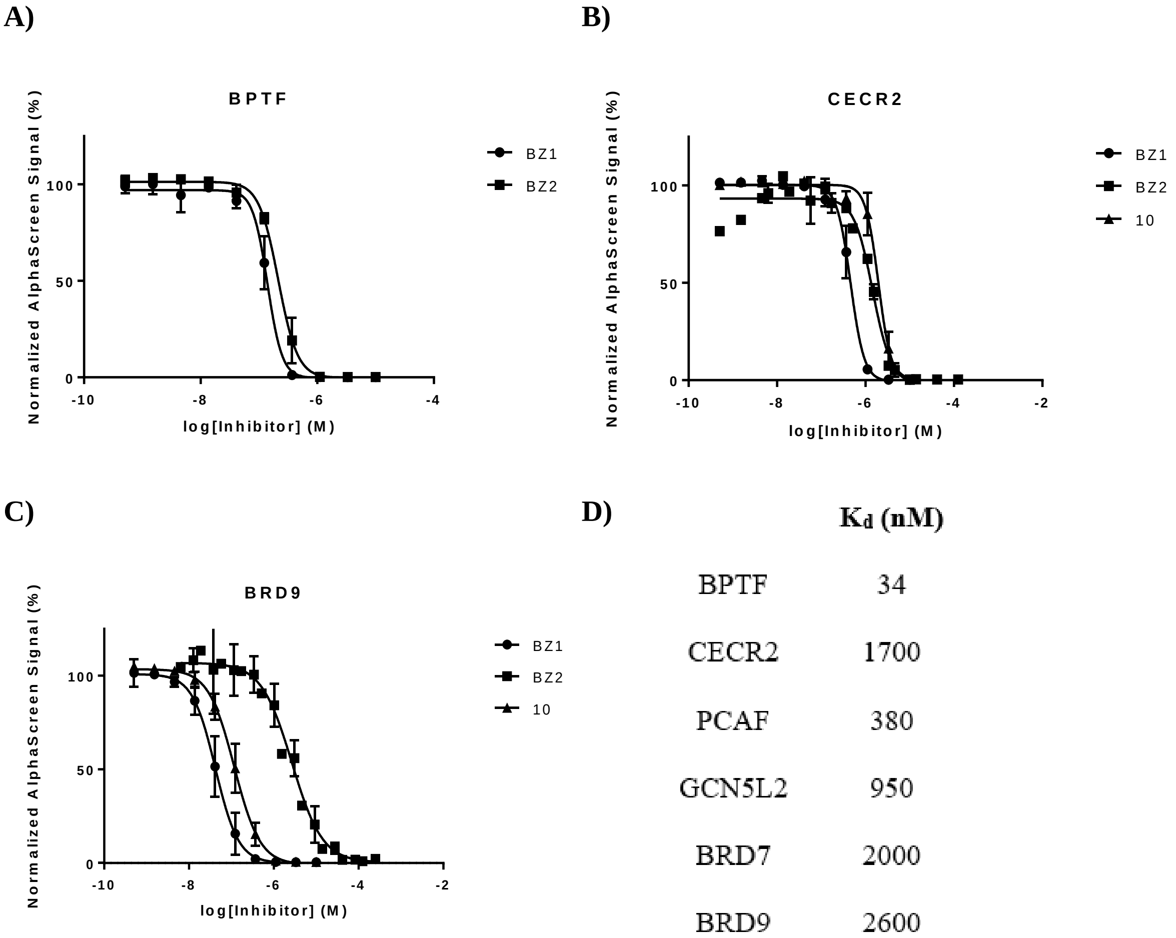

	K_d (nM)
BPTF	34
CECR2	1700
PCAF	380
GCN5L2	950
BRD7	2000
BRD9	2600

Figure 3.11: Selectivity analysis of BZ2

AlphaScreen titrations with **BZ1**, **BZ2**, and **2.10** for **A)** BPTF **B)** CECR2 **C)** BRD9. **D)** BROMOscan results for **BZ2**.

The selectivity results were encouraging, to confirm these results were due to a water mediated hydrogen bond we turned to crystallography. St. Jude obtained a co-crystal structure of **BZ2** with BPTF which did indeed show a water mediated hydrogen bond between Asp2960 and the nitrogen of the pyrimidone ring (**Figure 3.12**). Further design is being pushed forward by another graduate student in the Pomerantz lab, and in collaboration with St. Jude we are continuing to better understand the structural design of BPTF bromodomain inhibition by small molecules.

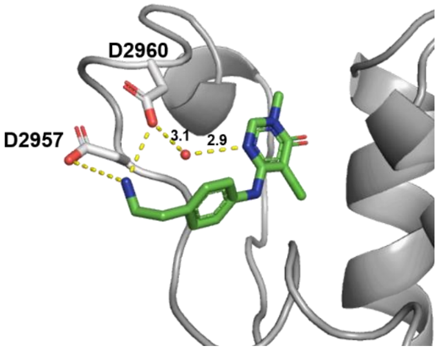

Figure 3.12: Co-crystal structure of BPTF bromodomain with BZ2.
Co-crystal structure of **BZ2** (green) with BPTF (gray); distance between D2960, water, and **BZ2** are shown.

In collaboration with St. Jude, we have also begun to preliminary test **BZ2** in cells. St. Jude has identified several neuroblastoma cell lines where knockdown of BPTF reduces the expression of Myc (**Figure 3.13A**). These Myc-driven cell lines were then shown to be sensitive to **BZ2** treatment, **BZ2** had a growth inhibition EC_{50} of 6.1 µM in WT SK-N-AS cells (**Figure 3.13B**). Furthermore, this inhibition was shown to be consistent with on target activity, as the BPTF BRD edited model had a ~6x-fold loss of **BZ2** activity, with a growth inhibition EC_{50} of 35.9 µM (**Figure 3.13C**). This show the promise of newly developed **BZ2** as a tool molecule for studying BPTF bromodomain inhibition, as well as a cell line that is sensitive to BPTF bromodomain inhibitor treatment.

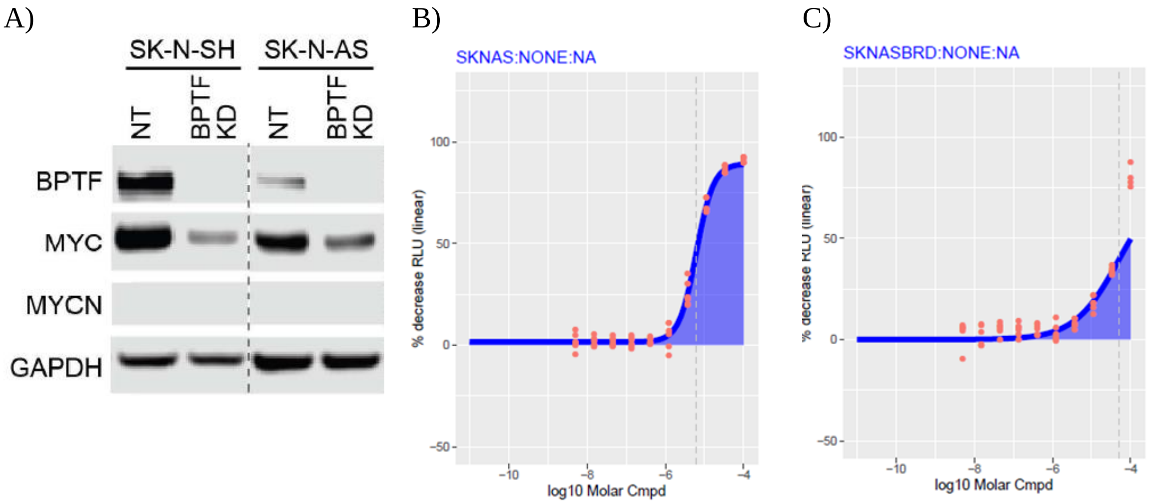

Figure 3.13: BPTF sensitivity in neuroblastoma cell lines (St. Jude).

A) Neuroblastoma cell lines (SK-N-SH and SK-N-AS) were treated with either non-targeting or BPTF-targeting siRNA and then blotted for BPTF and Myc. B) SK-N-AS cells were treated with **BZ2**. C) SK-N-AS cells with BPTF BRD KD were treated with **BZ2.**

3.3 BPTF Synthetic Transcription Factor (SynTF) Development

Contributions: Caroline R. Buchholz synthesized the precursors and performed AlphaScreen assays. St. Jude performed *FXN* mRNA expression assays and synthesized SynTFs. Research directed by Aseem Ansari and William C.K. Pomerantz.

Synthetic transcription factors (SynTF) are bifunctional molecules that can direct proteins of interest to targeted DNA sequences. They do this through a targeted protein ligand attached by linker to a programmable DNA binding polyamide.[297] We hypothesize that using BPTF bromodomain inhibitor scaffolds, we can alter the transcriptional pathway by redirecting remodeling complexes away from c-Myc oncogenic sites, which BPTF is associated with. Preliminary studies in collaboration with St. Jude have shown proof of concept by using BPTF SynTF to increase *FXN* expression, a loci in the genome that has been targeted previously for another class of bromodomain-containing proteins (BRD2, 3 and 4) by SynTFs, SynTEF1.[298] Pyridazinone **2.10** was used as the original targeting BPTF ligand to develop two preliminary BPTF SynTFs, **SynTF56** and **SynTF57**, which differ in linker length to the *FXN* intron specific polyamide (**Figure 3.13A**). **SynTF57** showed dose dependent increase of *FXN* expression, while **SynTF56** did not demonstrating the need for further design around targeted protein ligand and linker composition (**Figure 3.13B**).

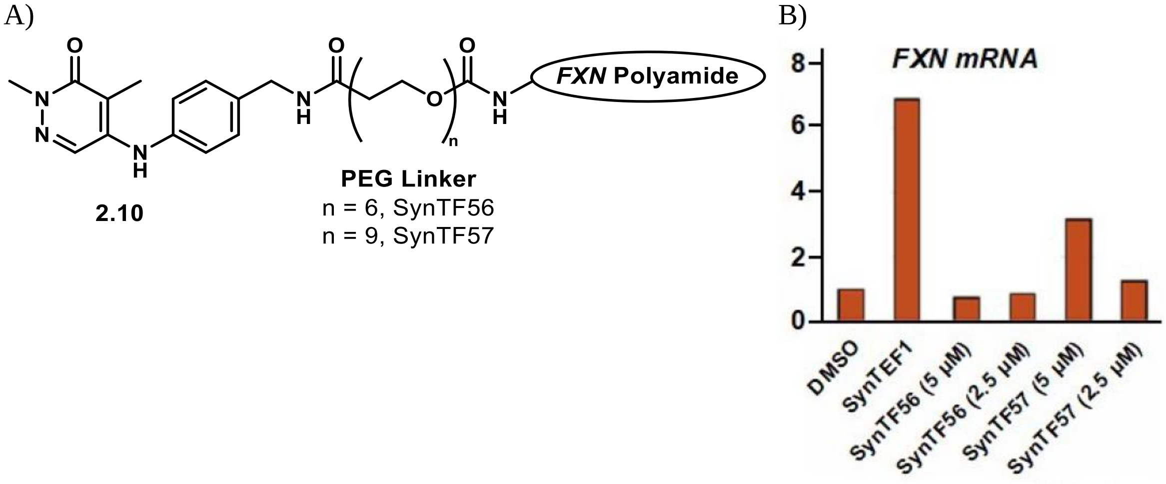

Figure 3.14: BPTF SynTFs Effect on *FXN* expression. (St. Jude).

A) **SynTF56** and **SynTF57** B) mRNA expression of *FXN* in GM04078 fibroblasts after treatment with SynTEF1 and BPTF SynTFs.

To further probe design of our BPTF SynTFs, we first examined the BPTF targeting element. Looking at our co-crystal structures of pyridazinones **2.12** and **2.13** with BPTF,[55] we noted two different exit vectors that we could explore for linker attachment by using these tetrahydroisoquinoline scaffolds, as well as using **BZ1**, our most potent bromodomain inhibitor, and **BZ2**, our most selective inhibitor, as scaffolds (**Figure 3.15A,B**). For the linker, from **SynTF56** and **SynTF57** it seemed a longer linker may be more advantageous. Using these scaffolds, we once again tested the SynTFs in the *FXN* expression system, and found the **BZ1** containing SynTF to be most comparable to **SynTF57** (**Figure 3.15C**).

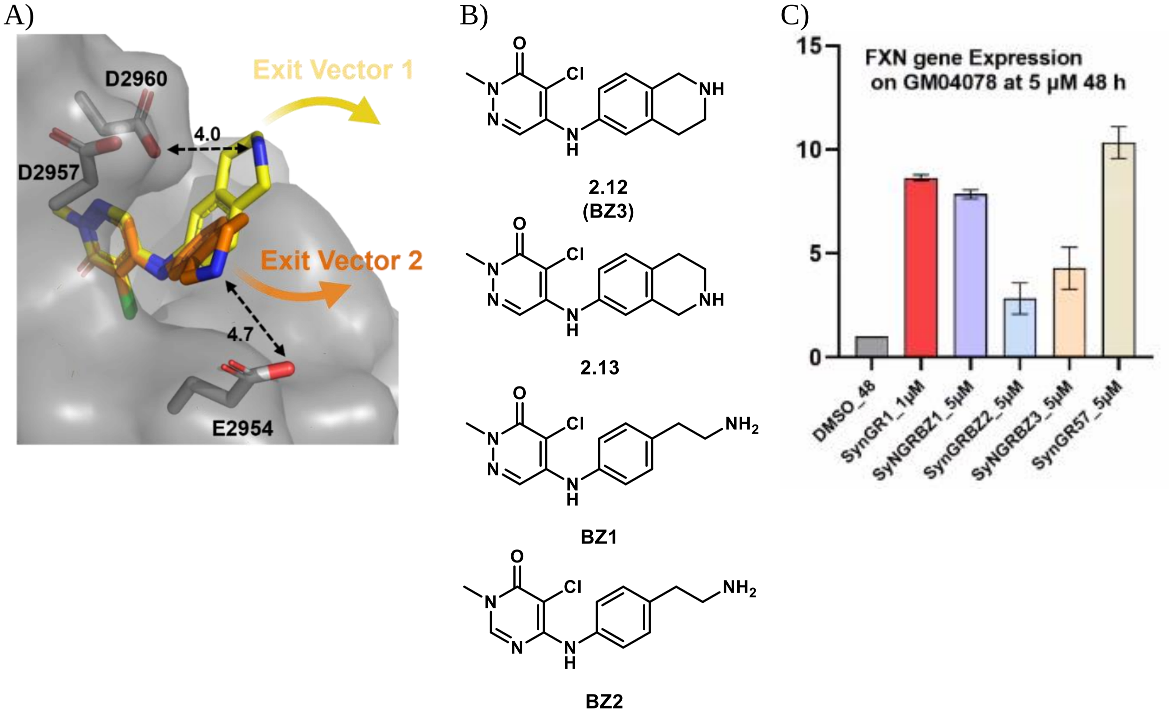

Figure 3.15: Design of BPTF SynTFs.

A) Exit vectors of **2.12** and **2.13** in BPTF co-crystal structures. B) Pyridazinones **2.12**, **2.13**, **BZ1**, **BZ2**. C) mRNA expression of *FXN* in GM04078 fibroblasts after treatment with SynTFs for 48 hours.

Future work by the Ansari lab will include designing new SynTFs for directing BPTF, and the NURF complex, away from c-Myc oncogenic sites and to c-Myc driven apoptotic genes. This will require new DNA-targeting polyamides to be designed that target the *ARF* locus, as ARF is a part of the p53 apoptotic regulatory loop. Before taking these newly designed BPTF SynTF molecules to cells, we wanted to confirm binding to the BPTF bromodomain. AlphaScreen was used to verify binding of two **BZ1** based SynTFs, **SynTF20** and **SynTF21**, that had linker lengths of PEG13 and PEG9 respectively (**Figure 3.16A**). Both showed binding comparative to the parent molecule BZ1 (**Figure 3.16B**). Since protein target engagement has been confirmed, new SynTFs will be tested in the ARF system.

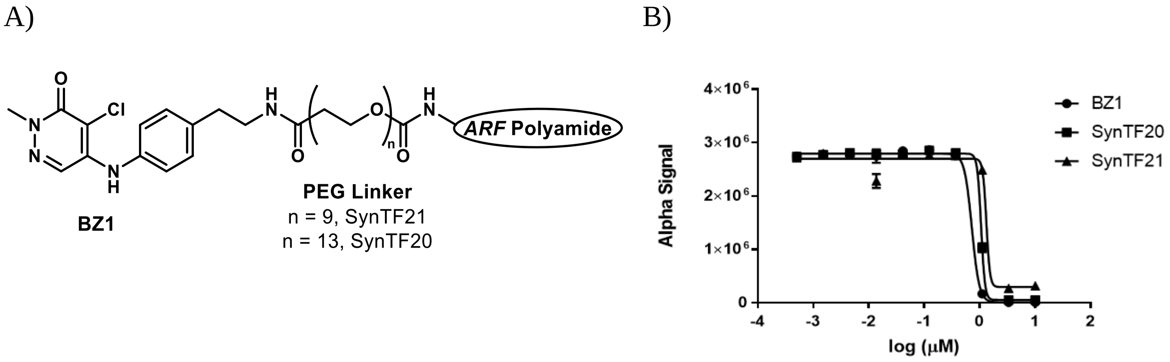

Figure 3.16: BPTF SynTFs Binding to BPTF.

A) **SynTF20** and **SynTF21**. B) AlphaScreen binding curves for BPTF with **BZ1**, **SynTF20**, and **SynTF21**.

3.4 Future Outlook

Future studies include looking at ADME properties and membrane permeability of our pyridazinone analogs as a potential explanation for the low micromolar cellular potencies compared to the nanomolar target potencies. Neuroblastoma cell lines will be continued to be studied as a BPTF sensitive cell line, and important cancer target, with new improved inhibitors like **BZ2**. Furthermore, in addition to SynTFs additional heterobifunctional molecules, such as degraders, are being designed in our lab based off our pyridazinone scaffold.[296] These approaches will allow a better understanding of BPTF's role in biology.

3.5 Experimental Section

Alamar Blue Assay. K562 cells were seeded at $0.2*10^6$ cells per well and dosed with DMSO or varying concentration of small molecule (0.1% DMSO). Plates were incubated at 37°C while rocking in a 5% CO_2 incubator for 3 days. Following incubation, 10% alamarBlue reagent (BUF012A, BioRad) was added and plates were again incubated at 37°C for 3 h. Fluorescence was measured on a Biotek Synergy4 plate with excitation set to 530-560 nm and emission set to 590 nm. Two technical replicates were normalized to the DMSO control for each titration, and plotted in GraphPad Prism using variable slope (four parameters) curve fit.

Western Blotting. K562 cells were collected during log phase of growth and media was removed, followed by rinsing with PBS and addition of urea lysis buffer (7 M urea, 2 M thiourea, 0.4 M TEAB, 4 mM DTT, 20% acetonitrile, protease inhibitor tablet, phosphatase inhibitor tablet, pH 8.0). After sonication for 30 seconds supernatant was collected and protein concentration was measured using the BSA assay. Normalized protein content (10, 20, 30, 40 µg) were mixed with loading dye and loaded onto NuPage 4–20% BisTris SDS Page gels and transferred to PVDF membrane using semi-wet transfer at 40 V for 45 minutes. Membranes were blocked in TBS buffer containing 1% BSA and 0.05% Tween for 1 h at room temperature. Next, they were incubated with primary antibody (Abnova α-CA1 mAb; α-tubulin) diluted 1:1,000 in blocking buffer for 1 h followed by secondary antibody (Invitrogen mouse, rabbit) diluted 1:10,000 for 1 h at room temperature. After washing with blocking buffer and and water, membranse were imaged on a BioRad imager at 700 and 800 nm.

AlphaScreen Cross-Titrations. All reagents were diluted in a buffer consisting of 50 mM HEPES, 100 mM NaCl, 0.1% BSA, and 0.05% CHAPS, pH 7.4. Biotinylated H4 KAc5,8,12,16 (Cat. # 12-0034, EpiCypher) and His-tagged protein were titrated across a 64-well array vertically and horizontally respectively. 20 µg/mL AlphaScreen streptavidin donor and nickel chelate acceptor beads (6760619M, Perkin Elmer) were added and then allowed to incubate for 30 minutes at room temperature. Emission was measured on a Tecan Spark reader using AlphaScreen filter settings.

AlphaScreen Competition. All reagents were diluted in a buffer consisting of 50 mM HEPES, 100 mM NaCl, 0.1% BSA, and 0.05% CHAPS, pH 7.4. Serial dilutions were prepared with varying concentration of small molecule and fixed His-tagged protein concentration (see **Table 3.2**) in 0.25% DMSO. 5 µL of these solutions were added to a 384-well white plate, followed by 5 µL biotinylated H4 KAc5,8,12,16 (Cat. # 12-0034, EpiCypher), to a final concentration of 100 nM. 10 µL of pre-mixed AlphaScreen streptavidin donor and nickel chelate acceptor beads (6760619M, Perkin Elmer) were added to a final concentration of 20 µg/mL and allowed to incubate for 30 minutes at room temperature. Emission was measured on a Tecan Spark reader using AlphaScreen filter settings. Data was plotted in GraphPad Prism 9 using a sigmoidal 4-parameter logistic (4PL) curve fit.

Table 3.2: Concentration of bromodomain used in AlphaScreen.

Protein	**Source**	**[Protein] nM**
BPTF	Expressed and purified as described previously[270]	30
BRD9	Cat. # RD-11-214, Reaction Biology	100
CECR2	Cat. # RD-11-210, Reaction Biology	60

3.6 Acknowledgement

We would like to thank Monica Kruk for her K562 cell culture expertise.

4) Fragment-Based NMR Screening of BPTF PHD Finger Uncovers New Chemical Matter for Methyl Lysine Reader

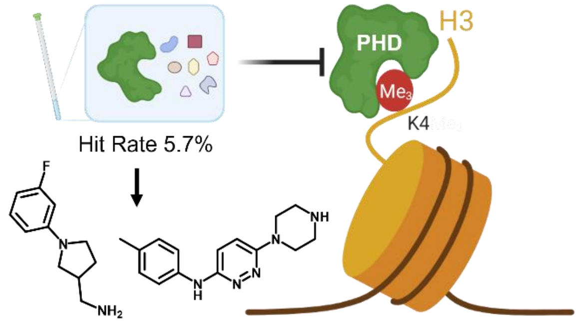

This work is a manuscript in preparation: Caroline R. Buchholz, Molly S. Vittengl, Sourav Das, Clifford T. Gee, Richard E. Lee, Anang A. Shelat, Daniel A. Harki, William C.K. Pomerantz.

Contribution of Authors: C.R.B. performed NMR experiments (^{1}H CPMG and HSQC) AlphaScreen assays, and FTMap analysis. C.T.G. and R.E.L. oversaw SPR experiments. S.D. and A.A.S. oversaw molecular docking. C.R.B. and M.V. synthesized fragments. W.C.K.P. oversaw the experiments and interpretation of data. C.R.B. and W.C.K.P. wrote the manuscript.

Motivation: The goal of the work described in this chapter is to conduct the first ligandability assessment of the BPTF PHD finger and uncover new chemical matter for methyl lysine reader inhibition. We sought to use FBDD to screen a library against the PHD finger as well as characterize the binding of hits by SPR, AlphaScreen, and HSQC NMR. We also began to conduct SAR by catalog and identified two scaffolds of interest for future lead development. This work is further carried on in Chapter 5.

4.1 Introduction

Plant homeodomain (PHD) fingers are one of the largest classes of epigenetic reader proteins, found in 291 human proteins.[59] They are characterized by 50-80 amino acid residues and a conserved zinc-binding motif.[60] While PHD fingers can recognize a diverse array of histone post-translational modifications (PTMs), the two major subsets bind to histone 3 trimethylated at lysine 4 (H3K4me3) and unmodified histone 3 at lysine 4 (H3K4me0) respectively, making them methyl lysine readers.[62] Structurally, PHD fingers that have high specificity for H3K4me3 have an aromatic cage, composed of two to four aromatic residues including a conserved tryptophan, that stabilizes the trimethylammonium group through van der Waals and cation-π interactions and contributes to the high nanomolar to low micromolar binding affinity for the trimethylated state. On the other hand, PHD fingers that have high specificity for H3K4me0 contain a cluster of acidic residues that form hydrogen bonds and salt bridges that results in low micromolar binding affinity to this unmodified state.[60] Binding of PHD fingers to histone H3 facilitates essential biological processes, including nucleosome remodeling and gene regulation, transcriptional activation or repression.[62]

When dysregulated, numerous PHD fingers have been implicated in human diseases, including immunological disorders, neurological diseases, and cancers.[64] For example, in acute myeloid leukemia (AML) one of the most promiscuous chromosomal abnormalities is the translocation of nucleoporin 98 (NUP98). NUP98 has over 30 identified fusion partners, including the PHD finger-containing proteins KDM5A,[65] PHF23,[66] and BPTF.[67,68] These translocations are often associated with a high fatality pediatric subset of AML, AMKL. It has been demonstrated that in these fusions the PHD finger plays a critical role in driving leukemogenesis and blocking the PHD finger-H3K4me3 interaction results in cell death.[69] Additionally, when two of the key aromatic cage residues in the BPTF PHD, which drive the interaction between the PHD finger and H3K4me3, were mutated systematically to alanine (W32A; Y10A), the mutant fusions were no longer able to induce the oncogenic transformation of AML cells. These results highlight a potential role for PHD finger inhibitors for regulating disease. However, PHD fingers are also considered difficult targets due to their shallow binding pockets,[70] currently only three studies have evaluated the ligandability of PHD fingers (**Figure 1.6).** The first of which screened the NIH Clinical Collection against PHD3 of KDM5A (also referred to as JARID1A) and identified the drug amiodarone as a hit; however, limited structural information was obtained.[71] A follow-up study demonstrated the low potency and promiscuous binding of amiodarone derivatives, indicating that scaffold optimization is needed to develop a useful chemical probe.[72] The PHD finger of Pygo was also screened using a fragment library and competitive binding of benzimidazole hits compared to the H3K4me3 peptide were demonstrated by HSQC NMR.[73] Most recently, the PHD fingers of BAZ2A and BAZ2B were screened *in silico* and the resulting fragment hits were validated by HSQC NMR and co-crystal structures giving valuable information for future structure based design.[74]

Here we conducted a fragment screen against the C-terminal PHD finger of BPTF (BPTF PHD), leading to the first reported small molecule ligands for this PHD finger. The BPTF PHD recognizes H3K4me3 on chromatin and recruits the nucleosome remodeling factor (NURF) to activate downstream genes.[14] BPTF itself was first implicated in cancer after a translocation breakpoint in *BPTF* was shown to drive malignancy,[19] and other oncogenic roles are emerging,[32] particularly in Myc-driven cancers.[30,31] With the exception of the BPTF PHD fingers role in NUP98 fusions in AML,[69] the role of this chromatin binding domain in other cancers has yet to be elucidated. We chose the BPTF PHD both because of its relevance in disease and our preliminary results from a computational analysis supporting its druggability. After screening a fragment library using ^{1}H CPMG NMR with an 5.7% hit rate, 8 hits were identified and confirmed to bind directly by SPR, and competitively with histone peptides by AlphaScreen. Further structure activity relationship (SAR) and molecular docking studies led to the prioritization of two scaffolds, pyrrolidine- and pyridazine-containing fragments respectively. Additionally, we performed preliminary selectivity analysis against KDM5A PHD3 and found our fragments had low levels of binding. Discovery of the first small molecule ligands for the BPTF PHD provides the basis for developing future methyl lysine reader probes for studying the functional role of this emerging protumorigenic protein.

4.2 Results and Discussion

4.2.1 Computational Analysis

Currently no high throughput or fragment-based screens have been reported in the literature for the BPTF PHD. Therefore, in order to first evaluate the tractability of this structural domain for inhibitor development, we assessed the ligandability of the histone binding pocket of BPTF PHD by the computational server FTMap[299,300] and compared it to KDM5A PHD3, a PHD finger that has been previously screened in literature.[71] After probing the *apo* BPTF PHD structure, a strong hot spot (**Figure 4.1A**, CS = 18, yellow) was identified next to the aromatic cage with a nearby (< 8 Å) hot spot in the histone binding pocket (**Figure 4.1A**, CS = 24, blue), predicting it to be highly druggable (CS > 16) at this site.[299,300] On the other hand, after probing *apo* KDM5A PHD3 two strong clusters were identified near the histone binding pocket (**Figure 4.1B**, CS = 18, blue; CS = 15, yellow), but they were not close enough (> 8 Å) to predict a highly druggable site. This analysis suggested that BPTF PHD would be ligandable and a promising target as it scored higher in comparison to KDM5A PHD3, which has been successfully screened against. Additionally, when comparing the two histone bound structures of BPTF PHD and KDM5A PHD3, which have a large conformational change, a similar conclusion was made (**Figure 4.2**). Based on this favorable druggability analysis, we moved forward with an NMR screen to experimentally evaluate the ligandability of the BPTF PHD.

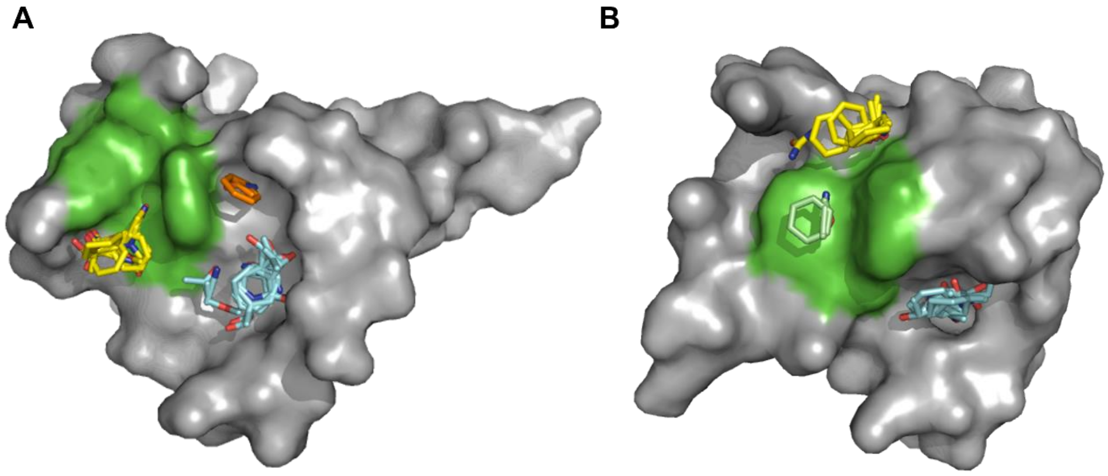

Figure 4.1: FTMap Analysis of *apo* BPTF PHD and KDM5A PHD3

FTMap analysis of (A) BPTF PHD (PDB: 2F6N) and (B) KDM5A PHD3 (PDB: 2KGG) where green surface represents aromatic cage residues and consensus sites (CS) are represented as sticks and characterized by having the same color.

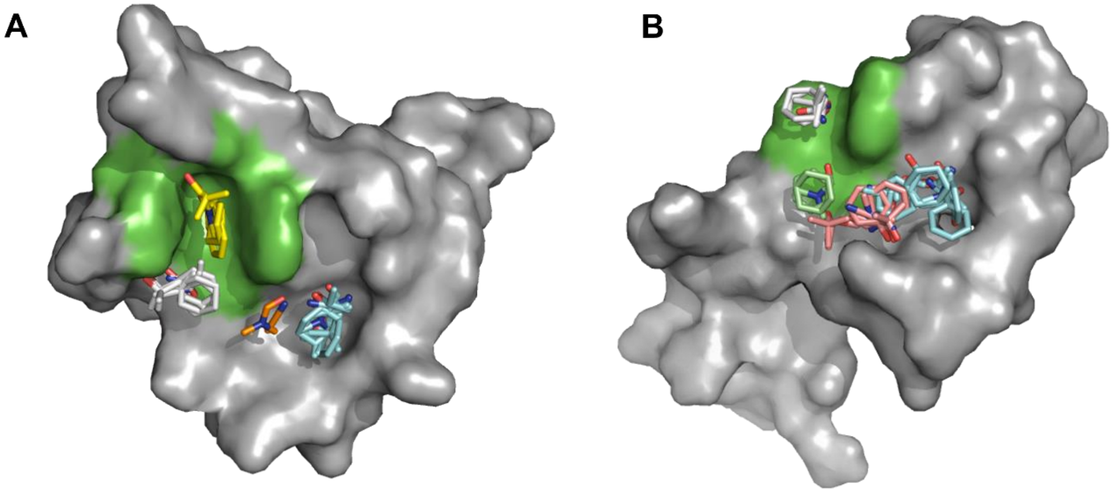

Figure 4.2: FTMap Analysis of Histone 3 Complexes of BPTF PHD and KDM5A PHD3

FTMap analysis of (A) BPTF PHD (PDB: 2F6J) and (B) KDM5A PHD3 (PDB: 3GL6) where green surface represents aromatic cage residues and consensus sites (CS) are represented as sticks and characterized by having the same color.

4.2.2 Fragment-Based Screening

We used ^{1}H CPMG NMR to screen a library of 1,056 fragments purchased from Life Chemicals against BPTF PHD (**Figure 4.3A**). Fragment-based screening is an approach that allows for effective sampling of chemical space with a smaller library in comparison to traditional high throughput screening. Biomolecular NMR is a sensitive biophysical technique that can detect weaker interaction typically exhibited by fragments,[1] which is ideal for a target that is more challenging. The library was assembled with minimal thiols and PAINS compounds with Rule of 3 compliant fragments. Protein sensitivity to the H3K4me2 peptide was used as a control. Fragments were pooled in mixtures of up to five at 100 µM. 61 active fragments came out of this primary screen after deconvolution (5.7% hit rate), a hit was defined as at least 20% reduction in proton resonance intensity upon addition of 10 µM BPTF PHD (**Figure 4.3B**).[120] Following validation both in singleton and repurchased material, ten fragments reproduced binding activity in the ^{1}H CPMG NMR assay (**Figure 4.3C**). As a preliminary selectivity analysis, the top fragments were used in an identical ^{1}H CPMG NMR assay with KDM5A PHD3. Encouragingly, none of the fragments showed a significant drop in resonance intensity upon addition of KDM5A PHD3 in contrast to the control histone peptide, indicating a rough estimate of the selectivity of our fragments for BPTF PHD.

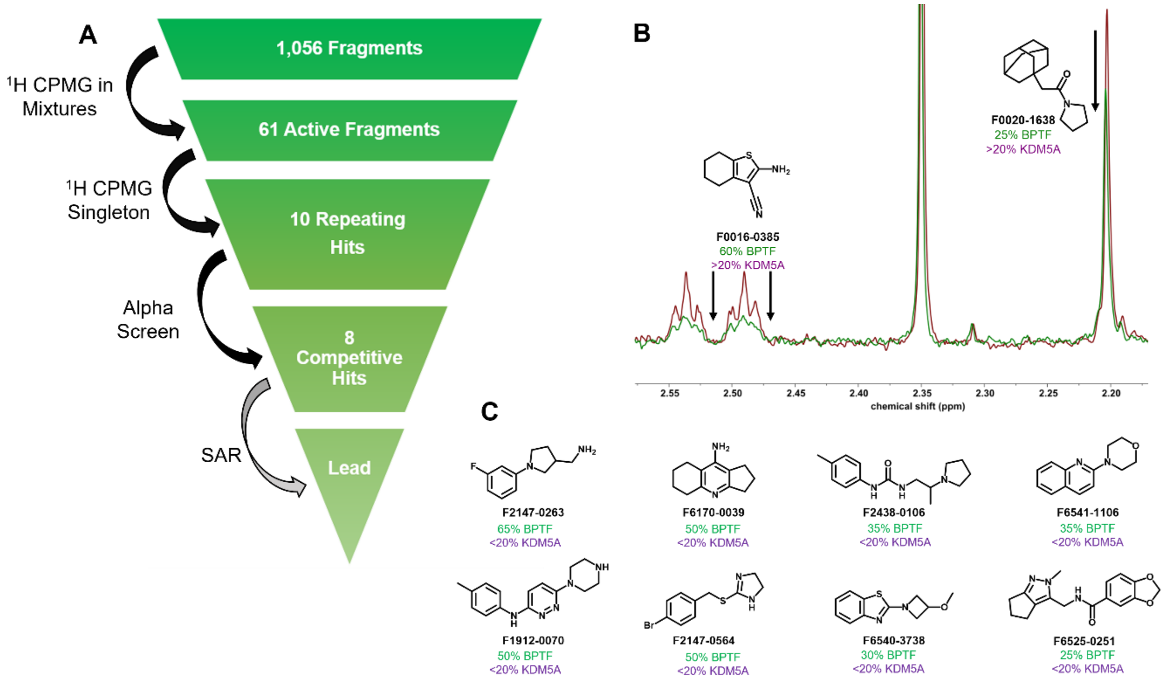

Figure 4.3: Fragment-Based Screening of BPTF PHD

(A) Screening Tree. (B) Analysis of Mixture Only ^{1}H CPMG NMR spectra in red and Mixture plus BPTF PHD (10:1) in green, where F0016-0385 and F0020-1638 both see resonance intensity drops >20%. (C) Remaining fragment hits identified from CPMG screening with % intensity drop with BPTF PHD and KDM5A PHD3.

After primary screening and hit validation in the same NMR assay, we used surface plasmon resonance (SPR) as a complementary assay to confirm binding. Fragments were tested at a single concentration of 400 μM, and binders were validated at 1.6 mM. Six fragments were confirmed to bind to BPTF PHD (**Table 4.1, Figure 4.4**), although weakly preventing K_d determinations under these conditions. In some cases, reference channel binding prohibited affinity determination as well. Based on the results of these two complementary assays we concluded we had identified several new binders of BPTF PHD, but of unknown binding mechanism.

Table 4.1: Binding of fragments to BPTF PHD by ^{1}H CPMG NMR, AlphaScreen, and SPR. CPMG Responses defined as strong: >40%, intermediate: 30-40%, and weak: 20 - 30% drop. SPR run at 400 uM. n=3 for AlphaScreen. NB = No binding. ND = assay interference.

Fragment	CPMG Response	SPR Binding (+ or -)	Alpha IC$_{50}$ (µM) or %I at 2 mM
F2147-0263	Strong	+	540 ± 20
F1912-0070	Strong	+	910 ± 20
F6170-0039	Strong	+	590 ± 20
F0016-0385	Strong	-	130 ± 7
F3308-0593	Strong	+	NB
F2438-0273	Intermediate	+	45%
F6540-3738	Intermediate	+	46%
F6541-1106	Intermediate	-	ND
F0020-1638	Weak	-	750
F6525-0251	Weak	-	64%

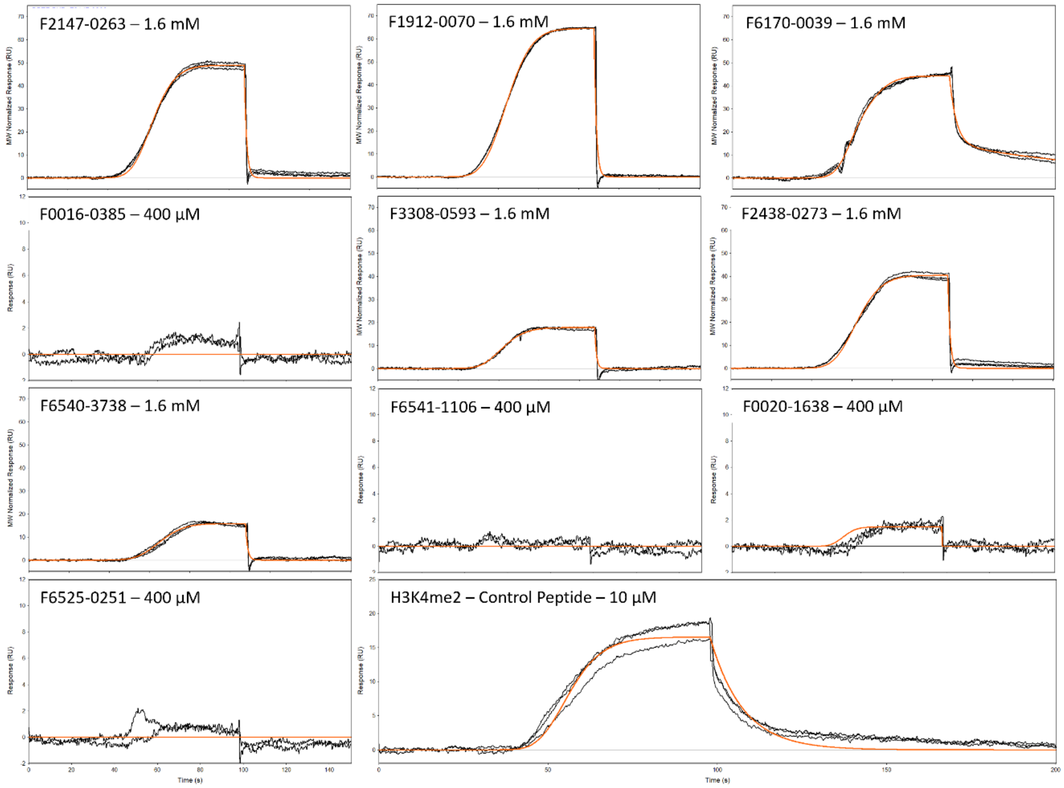

Figure 4.4: SPR Binding Curves of BPTF-PHD with Fragments

SPR binding curves with 2 technical replicates, where control peptide has a measured K_d of 7.4 µM.

4.2.3 Competitive Binding to the Histone Pocket

Following identification of fragment binders, we next set out to evaluate fragments that bound competitively to the histone binding pocket in a dose-dependent manner. AlphaScreen was used as a technique that has been applied to PHD fingers previously,[71,72] and is also well-suited for characterization of weak binding ligands. In this setup, a complex between the PHD domain and an H3K4me2-biotinylated peptide was competed away by addition of inhibitor (0-2 mM). Self-competition with the unlabeled H3K4me2, which has a comparable affinity to that of H3K4me3 for BPTF PHD (5.0 vs. 2.7 μM),[63] supported a functional assay (**Figure 4.5**). Subsequently, eight fragments were confirmed to compete off the H3K4me2 peptide, with three fragments leading to incomplete inhibition of the histone peptide at the top tested concentration (**Table 4.1, Figure 4.6**). We also tested Amiodarone by AlphaScreen, as it was identified to bind to the similar PHD finger, KDM5A PHD3.[71] Amiodarone had an IC_{50} of 720 μM for BPTF PHD (**Figure 4.6D**).

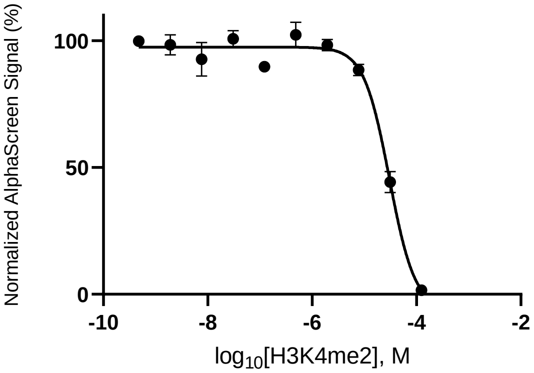

Figure 4.5: AlphaScreen Binding Curve of BPTF PHD with H3K4me3

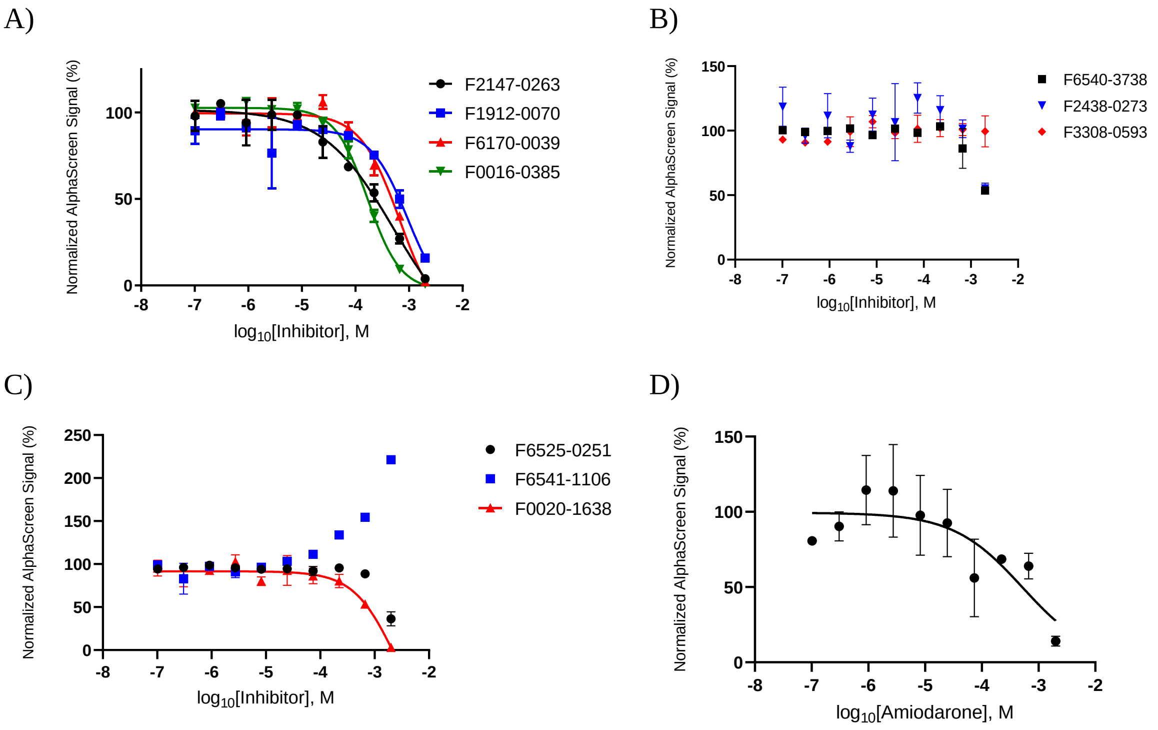

Figure 4.6: AlphaScreen Binding Curve of BPTF PHD with Fragments and Amiodarone

Comparing the results of each respective assay, F2147-0263 (**F1**), F1912-0070 (**F2**), and F6170-0039 (**F3**) were identified as strong hits in all three assays. Each fragment led to greater than a 40% drop in resonance intensity by CPMG, qualitatively bound by SPR, and exhibited full inhibition by 2 mM in AlphaScreen. F0016-0385 (**F4**) showed strong binding in both CPMG and AlphaScreen, but no binding in SPR. Even with this discrepancy, we moved forward with this fragment into structure activity relationships given its performance in the first two assays. F3308-0593 (**F5**) showed strong response by CPMG and qualitatively bound by SPR, but did not show any binding by AlphaScreen even at a high concentration of 2 mM. This molecule was not moved forward due to assay inconsistencies and concerns about different oxidation states of the sulfur atom. F2438-0273 (**F6**) and F6540-3738 (**F7**) showed binding by SPR, but had intermediate responses by CPMG and did not fully compete off the histone peptide at 2 mM, so were deprioritized. F6541-1106 (**F8**) while showing intermediate binding by CPMG, had interference in the AlpahScreen assay and no binding by SPR, so we did not move forward with this fragment either. F0020-1638 (**F9**) and F6525-0251 (**F10**) were also not prioritized as they showed a weak response by CPMG, moderate inhibition by AlphaScreen, and no binding by SPR. It should be noted that the first round of testing by SPR was tested at 400 µM which may have been too low to see binding of these weaker inhibitors.

4.2.4 SAR by Catalog

To further prioritize our hit fragments, we proceeded with SAR by catalog for each scaffold. We selected fragment analogs with greater than 70% similarity for purchase at LifeChemicals and tested them by AlphaScreen (**Figure 4.7-Figure 4.8**).

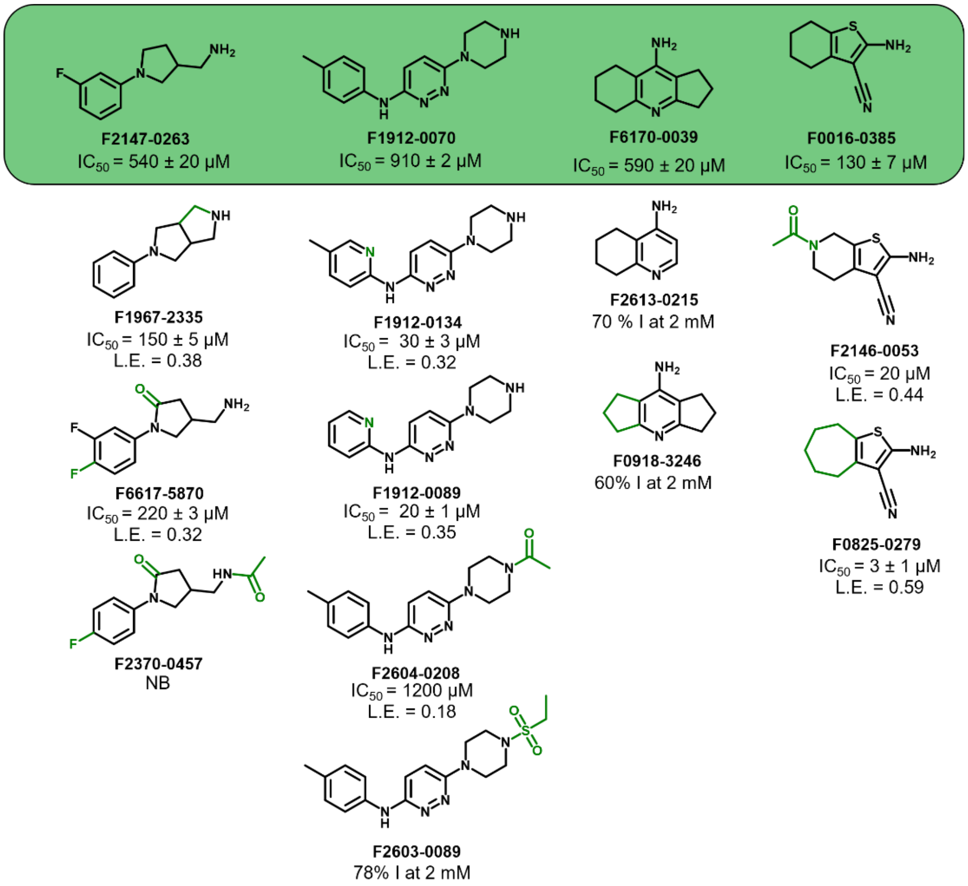

Figure 4.7: SAR by Catalog against BPTF PHD.

Binding affinity by Alphascreen of parent fragment analogs for BPTF PHD, n = 2.

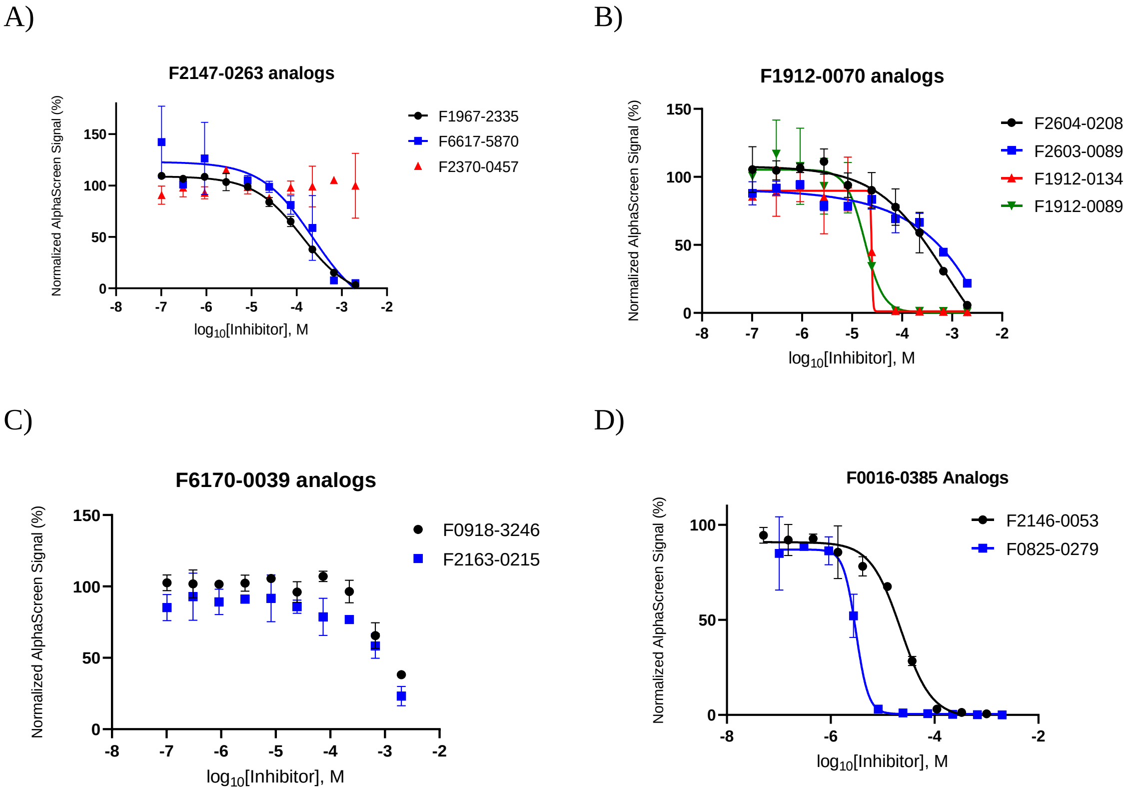

Figure 4.8: AlphaScreen Binding Curve of BPTF PHD with Purchased Analogs

F1's purchased analogs did not have any single point changes making it difficult to draw direct conclusions about functional group importance, however the varied potencies of the analogs supported a tractable SAR for future analog development. Specifically, F1967-2335 (**F1.1**), which had a constrained amine in comparison to the free amine and no aryl fluorine, had an improved affinity with an IC_{50} of 150 μM compared to 540 μM for **F1**. F6617-5870 (**F1.2**), which had an extra fluorine at the para position and a carbonyl on the pyrrolidine ring, had an improved affinity with an IC_{50} of 220 μM. F2370-0457 (**F1.3**) had a fluorine only at the para position, a carbonyl on the pyrrolidine ring, and an acetylated amine, exhibited no inhibition. Due to our interest in this scaffold, we resynthesized the parent compound to revalidate binding, and to access a pathway for facile synthesis of simpler analogs (**Figure 4.9**), which will be used in future studies.

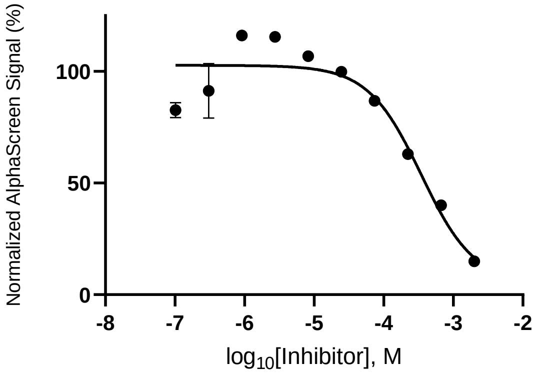

Figure 4.9: Resynthesis of F1.

AlphaScreen Binding Curve of BPTF PHD with F1* (IC_{50} = 380 ± 30 µM).

Comparing **F2** (IC_{50} = 910 µM) to its analogs, those that had modifications on the piperazine in general had weaker binding than the parent fragment. F2604-0208 (**F2.1**), which had an acetylated nitrogen on the piperazine ring, had an IC_{50} of 1200 µM, and F2603-0089 (**F2.2**), which had an ethyl sulfonyl group added to the nitrogen on the piperazine ring, had only 78% inhibition at 2 mM. The positive charge on the piperazine may be either critical for binding interactions or that the larger functional group is no longer accommodated in the protein binding pocket. On the other side of the fragment, addition of a nitrogen to the arene ring provided a significant gain in affinity. F1912-0134 (**F2.3**), which only differs from the parent fragment by a nitrogen at position 2 of the arene ring, has ~30 fold increase in affinity (IC_{50} = 30 µM) and F1912-0089 (**F2.4**), which is identical to F2.3 besides the loss of the para-methyl group on the arene ring, has ~45 fold increase in affinity (IC_{50} = 20 µM). These results suggest that the **F2** is amenable to modifications and can be explored further by SAR. We have also developed a synthetic route to resynthesize the parent fragment of this scaffold to validate binding, as well as to deconstruct the fragments to validate functional group contributions. Removal of the aryl group (**F2.5**) resulted in a loss of affinity compared to the resynthesized parent fragment (**F2***), indicating that functional group is critical for binding (**Figure 4.10**).

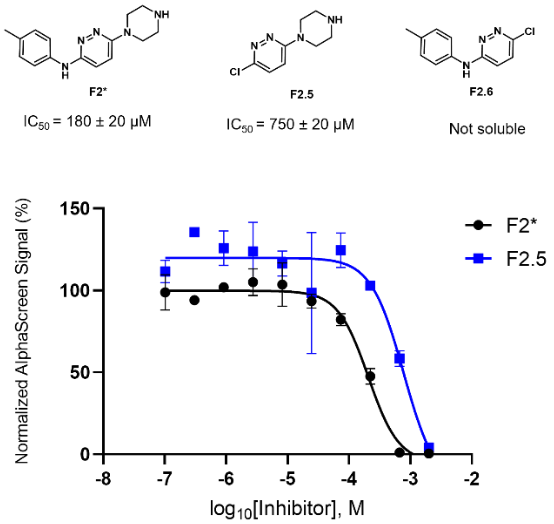

Figure 4.10: Deconstruction of F2.

AlphaScreen Binding Curve of BPTF PHD with F2*, F2.5, and F2.6.

F3's analogs had modifications at the two aliphatic rings and did not show full inhibition at 2 mM compared to the parent fragment (IC_{50} = 590 µM). F2163-0215 (**F3.1**), which only had one 6-membered aliphatic ring, had only 70% inhibition at 2 mM and F0918-3246 (**F3.2**), which had two 5-membered aliphatic rings versus a 5- and 6- membered ring, had only 60% inhibition at 2 mM. This result could indicate each aliphatic ring is important for the binding affinity. With the lack of concrete SAR and the synthesis we decided to not prioritize this fragment scaffold.

Finally, examining **F4**, which had the highest hit binding affinity (IC_{50} = 130 µM), led to several analogs with stronger affinities. F2146-0053 (**F4.1**), which as an amide group added to the aliphatic group, had an IC_{50} of 20 µM, ~6-fold higher than the parent fragment. F0825-0279 (**F4.2**), which had an expanded 7-member aliphatic ring had a IC_{50} of 3 µM, ~40-fold higher than the parent fragment. While these binding affinities were all in the low micromolar range, we had some concerns with this scaffold's promiscuity. A report that analyzed substructures that are potentially PAINS in screening identified 2-aminothiophenes as problematic.[301] This substructure has also been identified in a prior fragment screen against an unrelated protein from our lab, as well as being reported as a fragment hit that has been optimized into a lead for KRAS^{G12C}.[302] We found it to be a promiscuous binder to another reader domain, the bromodomain BRD4-D1, but not a denaturant (**Figure 4.11**). Future structural analysis of the compound binding mode will be important guiding future designs.

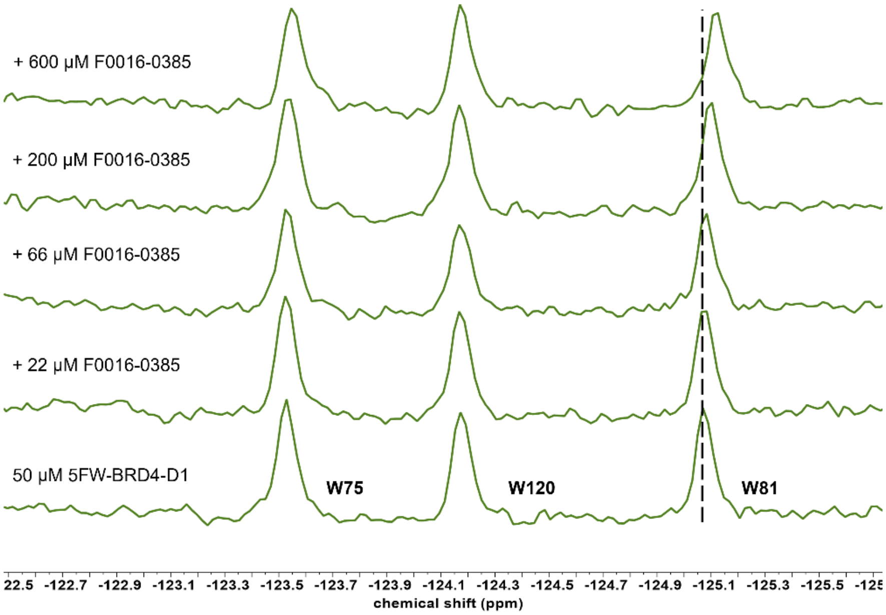

Figure 4.11: F4 Binding to Bromodomain BRD4-D1 by PrOF NMR

PrOF NMR spectra of 50 µM 5FW-BRD4-D1 titrated with 0-600 µM F0016-0385 (F4), where W81, the W in the binding pocket sees a significant CSP.

4.2.5 Molecular Docking

We used molecular docking predictions to explore potential binding interactions of 20 of our initial NMR hits with BPTF PHD (**Figure 4.12-Figure 4.13**). Perhaps unsurprisingly, 19 of the fragments docked in the aromatic cage. For example, **F1**, one of our prioritized hits, docks in the histone binding pocket, with the amine pointing towards the top of the aromatic cage where the methylated nitrogen in H3K4me3 binds (**Figure 4.12A**). However, **F2**, one of our prioritized hits, has a unique predicted interaction mode in the histone backbone binding pocket. The piperazine is oriented at the N-terminal end of histone binding pocket where H3A1 binds and the aryl ring is pointed towards the edge of the pocket where the backbone of H3K4 and H3Q5 bind (**Figure 4.12B).**

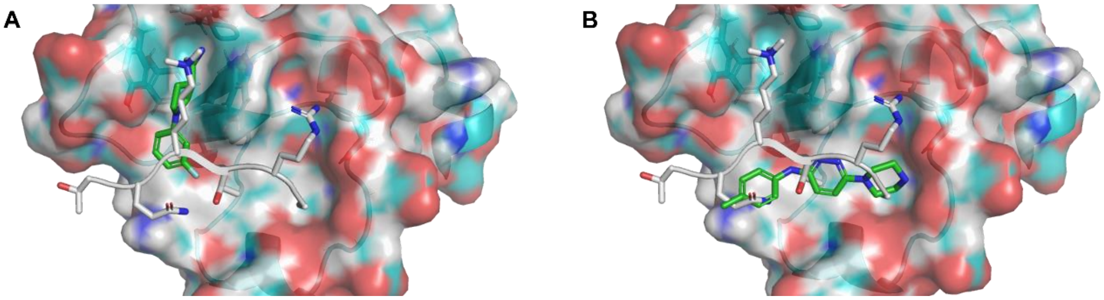

Figure 4.12: Molecular Docking with BPTF PHD

BPTF PHD represented by electrostatic surface, with F1 (A) and F2 (B) where fragments are represented as green sticks and H3K4me3 (1-15) is overlayed in white (PDB: 2F6J).

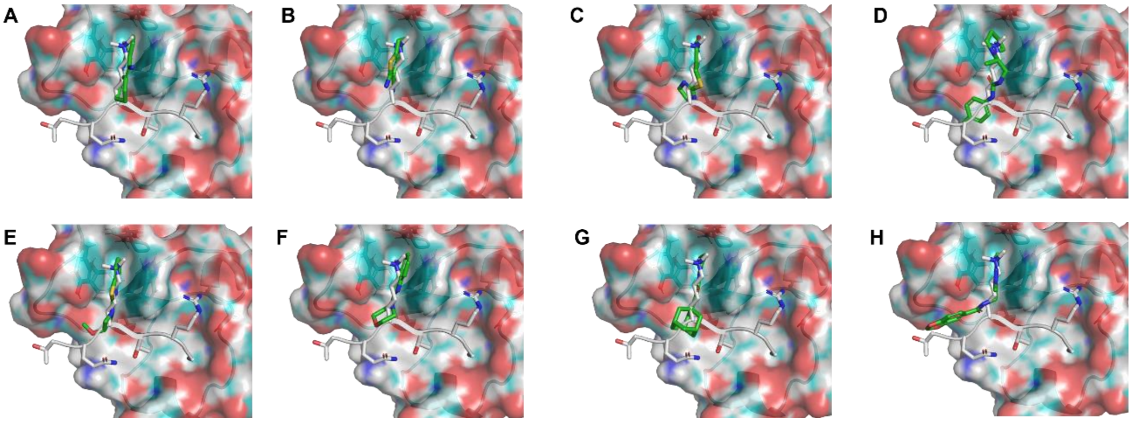

Figure 4.13: Extended Molecular Docking with BPTF PHD

BPTF PHD represented by electrostatic surface, where fragments are represented as green sticks and H3K4me3 (1-15) is overlayed in white (PDB: 2F6J). A) F3 B) F4 C) F5 D) F6 E) F7 F) F8 G) F9 H) F10.

4.2.6 HSQC NMR

To further explore binding interactions *in vitro*, we employed $^{1}H,^{15}N$ HSQC NMR spectroscopy for our top two fragments (**F1** and **F2**) and a third fragment **F4**. Under our NMR conditions, previously assigned resonances of the uniformly ^{15}N-labeled BPTF PHD were used to assign the majority of resonances.[16,63] At 1 mM fragment, the magnitude of chemical shift perturbations (CSP) was significantly lower than perturbations seen upon addition of histone peptide (up to CSP = 0.6)[16] but comparable to fragment perturbations seen in a previously screened PHD finger, BAZ2B, upon addition of 5 mM of two of their hit fragments (up to CSP = 0.035).[74] While we did not see distinct binding fingerprints for our fragments, we were able to glean some structural information. **F1** has one residue that is significantly perturbed two standard deviations from the average CSP, Y17, which is a part of the aromatic cage (**Figure 4.14A**). Two other aromatic cage residues (Y23, Wε32) were perturbed one standard deviations from the average CSP as well. While the resonances for Y17 and Wε32 were less effected, in general **F2** had less significant perturbations overall, making it difficult to confirm or reject the binding mode predicted through molecular docking (**Figure 4.14B**). The last fragment, **F4**, which we suspected to be a promiscuous binder, or potential denaturant, did not show evidence of denaturing the protein and aromatic cage residues (Y17, Y23) were perturbed one standard deviation from the average CSP (**Figure 4.14C**). Additionally, H34 was most significantly perturbed; however H34 perturbation could potentially be due to a pH effect.[303] Future studies will be needed to develop more elaborated fragments with higher affinity for assessing how these scaffolds interact with the BPTF PHD.

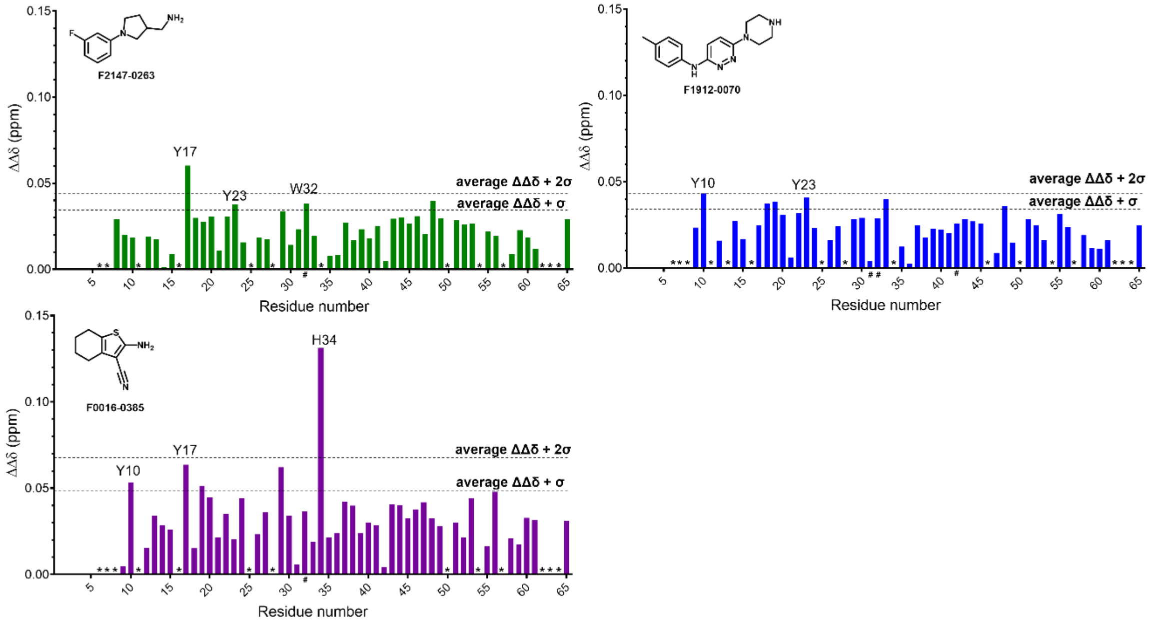

Figure 4.14: CSP Plots of BPTF PHD Upon Addition of Fragments F1, F2, and F4. Chemical shift perturbation (CSP) of 40 µM BPTF PHD in the presence of (A) **F1** (1 mM), (B) **F2** (1 mM), and (C) **F4** (1 mM). * indicates an unresolved resonance. # indicates a sidechain residue due to unresolved backbone residue.

4.2.7 KDM5A Selectivity

As a final analysis of our hit fragments, we wanted to further assess their selectivity against KDM5A PHD3. We used TR-FRET to quantitively examine binding to KDM5A PHD3. Top fragment hits, **F1**, **F2**, and **F4**, as well as potent analog **F2.3**, were tested up to a concentration of 400 µM (Figure 4.15). In comparison to control peptide H3Kme3, which has a measured IC_{50} of 799 nM comparable to the reported literature K_d of 930 nM, none of the tested fragments saw greater than 30% inhibition. Based on these results we conclude that our fragments show low level of binding to KDM5A PHD3.

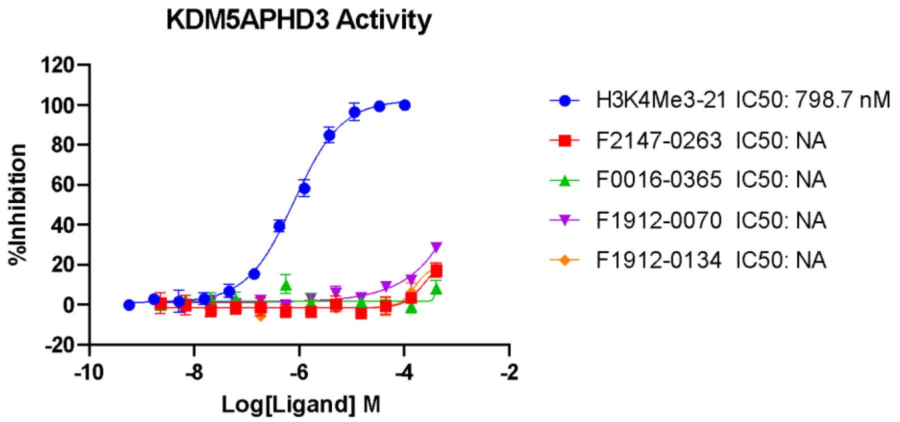

Figure 4.15: KDM5A PHD3 Acitivity by TR-FRET for F1, F2, F4, and F2.3. All fragments tested from 0-400 μM in triplicate, H3K4me3 0-100 μM.

4.3 Conclusions

We describe here a ligandability analysis for a methyl lysine reader, BPTF, which led to the discovery of the first reported small molecules for the BPTF PHD finger. We use NMR-based fragment screening, followed up by SPR and AlphaScreen to validate binding and prioritize our top two hit scaffolds, which are pyrrolidine- and pyridazine- based respectively. Competitive binding experiments show these hits competitively bind to the histone binding pocket. Preliminary SAR indicate these hit scaffolds are amenable to modifications for further gains in potency. We use molecular docking and HSQC NMR to further explore these hit scaffolds binding modes. These hits are suitable for further SAR optimization and development into future methyl lysine reader chemical probes to study their oncogenic functions.

4.4 Experimental Section

General Reagents: Fragment library assembled by Harki Lab from LifeChemicals. Fragments were purchased from LifeChemicals. Amiodarone HCl was purchased from Spectrum Chemical. His-KDM5A PHD3 gifted from St. Jude.

FTMap: Computational analyses of the druggability of the PHD fingers were carried out using FTMap.[299,300] The *apo* structures of BPTF PHD PHD3 (PDB: 2F6N) and KDM5A PHD3 (PDB: 2KGG) were submitted to the FTMap server using PPI mode. The structures of BPTF PHD PHD3 in complex with H3(1-15)K4me3 (PDB: 2F6J) and KDM5A PHD3 in complex with H3(1-9)K4me3 (PDB: 3GL6) with the ligand removed were submitted to the FTMap server using PPI mode.

BPTF PHD Expression and Purification: BPTF PHD construct was prepared as previously described.[15] The BPTF PHD construct was cloned into pET-28a(+)-TEV vector encoding residues 2722-2781 from human BPTF isoform 2 (gi:38788260) with a N-terminal His9 tag followed by a TEV cleavage site (Genscript). Protein was expressed in BL21Star (DE3) *E. coli* cells supplemented with 0.1 mM $ZnCl_2$ and induced by 0.4 mM isopropyl β-D-thiogalactoside at 20º C overnight. Cells were lysed and filtered before supernatant was applied to a HisTrap HP column (Cytiva) and eluted with 50 mM phosphate, 100 mM NaCl, 400 mM imidazole, and 5 µM $ZnCl_2$, pH 7.4. Purified protein was buffer exchanged into 50 mM HEPES, 100 mM NaCl, pH 7.4 and stored at -20 °C after being flash frozen.

^{15}N-Labeled BPTF PHD Expression: Following the procedure for unlabeled proteins, the LB media was swapped for minimal media M9 with twice the buffering capacity as reported in Azation et al.[304] At the induction step 1 g/L ^{15}N ammonium chloride was added.

^{1}H CPMG NMR: Data was acquired on a Bruker 700 MHz Avance with a CryoProbe 5 mm TXI and excitation sculpting water suppression. ^{1}H CPMG NMR parameters were as follows, NS = 128, acquisition time = 2 s, and L = 50. Samples were prepared in separate NMR tubes as 1) ligand only with each molecule at 100 µM in 50 mM phosphate, 100 mM NaCl, pH 7.4 in 100% D_2O and 2) ligand plus protein with the addition of 10 µM protein to 1).

Surface Plasmon Resonance: Surface Plasmon Resonance experiments were performed on a PioneerFE instrument (Sartorius). All experiments were carried out in 10 mM HEPES 150 mM NaCl, 0.005% NP40, pH 7.5 + DMSO as a running buffer with a flow rate of 120 μL/min at 25 ◦C. The Ni-NTA-coated biosensor chip (Xantec NiHC200M) surface was activated using using 0.5 M EDTA (125 μL at 25 μL/min) followed by 5 mM NiCl2 (75 μL at 25 μL/min). Protein was then diluted in running buffer and immobilized onto FC3 (~1300 RU), leaving FC1 and FC2 blank to be used as references. Compounds were diluted from 40 mM DMSO stocks to 400 μM with running buffer to yield 1% DMSO solutions. The first round of experiments were tested at a top analyte concentration of 400 μM using the OneStep® injection method on the Pioneer system to obtain binding kinetics data. A top concentration of 10 μM was used for the positive control H3K4me2 peptide. Data for the test compounds was analyzed with the Qdat software using the affinity model due to the fast dissociation rates. Compounds that yielded sensorgrams with significant binding responses were retested at a higher concentration (1.6 mM, 4% DMSO) but still only yielded qualitative instead of quantitative binding data.

H3K4me2 Peptide Synthesis: H3K4me2(H_2N-ARTKme2QTARKSTGGKA-C(O)NH_2) was synthesized on NovaSyn TGR resin (Novabiochem) using standard *N*-9-fluorenylmethoxycarbonyl (Fmoc) solid-phase synthesis methods on a Liberty Blue microwave synthesizer (CEM). The peptide was cleaved from resin using a 95:2.5:2.5 trifluoroacetic acid:triisopropylsilane:water mixture for 5 h followed by evaporation of the solvent under a nitrogen stream. The crude peptide was precipitated into cold diethyl ether and purified by reverse-phase (RP) high-performance liquid chromatography (HPLC) on a C-18 column using 0.1% TFA water and acetonitrile as solvents (5-20% ACN gradient over 60 min). Peptide molecular weight was confirmed using an Ab-Sciex 5800 matrix-assisted laser desorption ionization (MALDI) time-of-flight mass spectrometer.

AlphaScreen Assay: All samples were prepared in a buffer consisting of 50 mM HEPES, 100 mM NaCl, 0.1% BSA, and 0.05% CHAPS, pH 7.4. Serial dilutions were prepared with varying concentration of ligand and 100 µM His9-tagged BPTF PHD in 5% DMSO. 5 µL of these solutions were added to a 384-well white plate, followed by 5 µL biotinylated H3K4me2 (Cat. # 12-0008, EpiCypher), to a final concentration of 100 nM. 10 µL of pre-mixed AlphaScreen streptavidin donor and nickel chelate acceptor beads (6760619M, Perkin Elmer) were added to a final concentration of 40 µg/mL and allowed to incubate for 1 hour at room temperature under low light conditions. Emission was measured on a Tecan Spark reader using AlphaScreen filter settings. Data was plotted in GraphPad Prism 9 using a sigmoidal 4-parameter logistic (4PL) curve fit.

Synthesis of F1*, F2*, F2.5, and F2.6:

(1-(3-fluorophenyl)pyrrolidin-3-yl)methanamine (F1*). <u>Step 1</u>: 1-fluoro-3-iodozbenzene (1.0 g, 4.50 mmol,1 eq.), 3-Boc-aminomethyl-pyrrolidine (1.6 g, 6.76 mmol, 6.5 eq.), copper iodide (0.086 g, 0.450 mmol, 0.1 eq.), L-proline 0.104 g (0.901 mmol, 0.2 eq.), and potassium carbonate (1.245 g, 9.01 mmol, 2 eq.) added to 10.14 mL DMSO and bubbled in N_2 gas for 5 minutes. Reaction was heated to 70°C and stirred overnight. Reaction was quenched with 15 mL NH_4Cl, extracted 3 times with ethyl acetate, washed with H_2O and brine. Product was dried with $MgSO_4$ and concentrated under vacuum. Flash column chromatography purification was performed (CombiFlash Rf system: 12 g silica, hexanes/0-100% ethyl acetate, 30 min). Intermediate product was obtained as a yellow oil (1.137 g, 86% yield). Step 2: Intermediate product was deprotected with 10% TFA in DCM and extracted with 1 M NaOH (pH<10), dried over magnesium sulfate, and concentrated in vacuo. Flash column chromatography purification was performed (CombiFlash Rf system: 4 g silica, 0 - 100% DCM/MeOH over 30 min). Product **F1*** was obtained as a yellow oil (0.615 g, 82% yield). ^1H NMR (500 MHz, $CDCl_3$) δ 7.13 (q, *J* =

8.3 Hz, 1H), 6.34 (td, 1H), 6.30 (dd, 1H), 6.22 (dt, 1H), 3.43 (m, 1H), 3.34 (m, 1H), 3.27 (m, 1H), 3.00 (m, 1H), 2.80 (m, 2H), 2.39 (m, 1H), 2.16 (m, 1H), 1.74 (m, 3H). ^{13}C NMR (500 MHz, $CDCl_3$) δ 165.08, 163.19, 149.45, 107.27, 101.99, 98.44, 51.49, 47.16, 45.49, 41.90, 29.25. HRMS (ESI-TOF) calculated for $C_{15}H_{19}N_5^+$ [M+H]$^+$: 195.13, observed 195.1287.

6-(piperazin-1-yl)-N-(p-tolyl)pyridazin-3-amine (F2*). 1-Boc-4-(6-Chloropfyridazin-3-yl)piperazine (200 mg, 0.8 mmol, 1 eq.) and p-toluidine (144 mg, 1.6 mmol, 2 eq.) were added to 2 mL 1,4 dioxane and stirred at reflux overnight. Following completion of reaction, the reaction mixture was concentrated in vacuo and purified by flash column chromatography (CombiFlash Rf system: 4 g silica, hexanes/0-100% ethyl acetate, 20 min). Intermediate product was deprotected with 10% TFA in DCM and extracted with 1 M NaOH (pH<10), dried over magnesium sulfate, and concentrated in vacuo. Product **F2*** was obtained as a yellow solid (23 mg, 10% yield). ^{1}H NMR (500 MHz, DMSO-d_6) δ 9.28 (s, 1H), 8.84 (s, 2H), 7.56 (m, 1H), 7.52 (d, J = 8.6 Hz, 2H), 7.26 (d, J = 7.5 Hz, 1H), 7.14 (d, J = 8.4 Hz, 2H), 3.68 (t, J = 5.5 Hz, 4H), 3.25 (m, 4H), 2.27 (s, 3H). ^{13}C NMR (500 MHz, DMSO-d_6) δ 153.29, 151.43, 137.46, 131.92, 129.95, 123.94, 122.21, 119.90, 43.43, 42.57, 20.89. HRMS (ESI-TOF) calculated for $C_{15}H_{19}N_5^+$ [M+H]$^+$: 270.36, observed 270.1706.

3-chloro-6-(piperazin-1-yl)pyridazine (F2.5). 3,6-dichloropyridazine (500 mg, 3.3 mmol, 1 eq.) and 1-Boc-piperazine (653 mg, 3.3 mmol, 1 eq.) were added to 2 mL ethanol and stirred at reflux overnight. Following completion of reaction, the reaction mixture was concentrated in vacuo and purified by flash column chromatography (CombiFlash Rf system: 12 g silica, hexanes/0-100% ethyl acetate, 20 min). Product **F2.5** was obtained as a white solid (134 mg, 13% yield). ^{1}H NMR (500 MHz, DMSO-d_6) δ 7.50 (d, J = 9.6 Hz, 1H), 7.34 (d, J = 9.6 Hz, 1H), 3.49 (t, J = 5.2 Hz, 4H), 2.79 (t, J = 5.0 Hz, 4H). HRMS (ESI-TOF) calculated for $C_8H_{12}ClN_4^+$ [M+H]$^+$: 199.07, observed 199.0740.

6-chloro-N-(*p*-tolyl)pyridzin-3-amine (F2.6). 3,6-dichloropyridazine (50 mg, 0.3 mmol, 1 eq.) and p-toluidine (31 mg, 0.3 mmol, 1 eq.) were added to 0.5 mL ethanol and stirred at reflux overnight. Following completion of reaction, the reaction mixture was concentrated in vacuo and purified by flash column chromatography (CombiFlash Rf system: 4 g silica, hexanes/0-100% ethyl acetate, 20 min). Product **F2.6** was obtained as a white solid (19 mg, 26% yield). ^{1}H NMR (500 MHz, $CDCl_3$) δ 7.22 (d, *J* = 9.3 Hz, 1H), 7.18 (m, 4H), 7.00 (d, *J* = 9.3 Hz, 1H), 2.35 (s, 3H). ^{13}C NMR (500 MHz, DMSO-d_6) δ 157.3, 147.5, 138.1, 131.2, 129.7, 129.6, 120.5, 119.5. HRMS (ESI-TOF) calculated for $C_{11}H_{11}ClN_3^+$ $[M+H]^+$: 220.68, observed 220.0263.

HSQC NMR: Data was acquired on a Bruker 850 MHz Avance III with a CryoProbe 5 mm TXI. IBS_SOFAST parameters were as follows, NS =128, acquisition time = 0.08 s, and 0.2 s delay. Samples were prepared with 40 µM BPTF PHD in 50 mM phosphate, 100 mM NaCl, pH 7.4 and 10% D_2O. Data were processed with TopSpin and CSP was calculated using eq 1.[305]

$$\mathrm{CSP} = \sqrt{(\Delta\delta\ ^{1}H)^2 + (0.1\Delta\delta^{15}N)^2} \qquad (1)$$

4.5 Acknowledgement

We would like to acknowledge Michael Grillo and Jared Anderson for previous ^{1}H spectra that aided deconvolution. We acknowledge Joe E. McPherson for contributions to synthesis. TOC created with BioRender.

5) Future Directions of BPTF PHD Inhibitor Development: Preliminary SAR, Binding Interactions, and Selectivity Analysis

This is unpublished and ongoing work.

Contribution of Authors Caroline R. Buchholz synthesized the compounds, performed NMR and AlphaScreen assays, and designed primers. Research directed by William C.K. Pomerantz.

Motivation: The goal of the work described in this chapter is to take the hit scaffolds discovered in Chapter 4 and further explore SAR, as well as develop assays to investigate binding interactions and selectivity of these fragments. In Section 5.1 we started to explore SAR around the aniline of F1912-0070. In Section 5.2 we generated resolved ^{1}H,^{15}N spectra of ^{15}N-BPTF PHD and designed primers for site directed mutagenesis to investigate protein-ligand interactions. Finally, in Section 5.3 we started to optimize an AlphaScreen assay against KDM5A PHD3 to assess selectivity.

5.1 Preliminary SAR Around Aniline of F1912-0070 (F2)

Given the importance of the anilino-group for binding in **F2** for BPTF PHD shown through deconstruction of the fragment and the more potent pyridine ring modification from Chapter 4, we wanted to further explore modifications around the aniline ring of **F2**. Our original synthetic route started with nucleophilic aromatic substitution of the piperazine to 3,6-dichloropyridazine, followed by another substitution to add on the aniline, and a final TFA deprotection (Scheme 5.1). Using this route, we wanted to generate a small library to test a range of EWG to EDG at the para position (**Figure 5.1A**). However, the low yields of the second

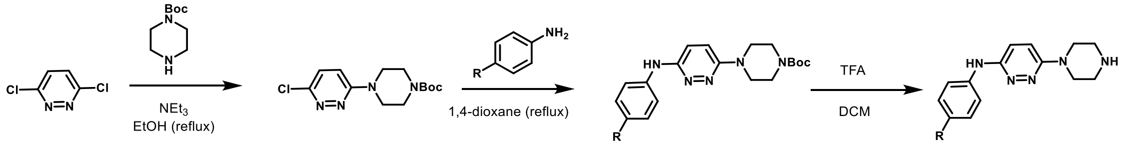

substitution (>15% yield) were not amenable to some of the anilines, including pyridine rings and more EWG substituents. In the future, we are considering metal-catalyzed coupling routes, like the Ullman coupling, to access a wider array of substituents. We also wanted to investigate different connections on the pyridazine ring. We hypothesized that we could orient the piperazine towards the R2 pocket based on molecular docking predictions and gain binding affinity by going from the 3,6-dichloropyridazine as our starting block to 2,4-dichloropyrimidine (**Figure 5.1A**).

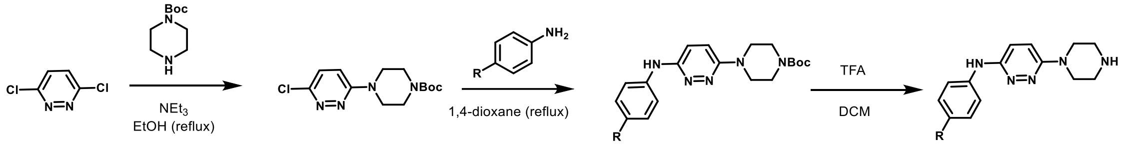

Scheme 5.1: Nucleophilic aromatic substitution with dichloropyridazine to synthesize F2 analogs.

To assess affinity of each synthesized fragment for BPTF PHD we used AlphaScreen (**Figure 5.1B**). A more electron donating group, like the para-amine of **F2.7**, was comparable to the resynthesized **F2***. **F2.8**, which did not have any para substitution, was also comparable to **F2***. However, when a p-fluoro group was added in **F2.9**, a significant increase in affinity was observed (~ 4-fold). This warrants further characterization to investigate what makes this fragment more potent. Looking at the change in ring connection, **F2.10** did not show full inhibition at 2 mM pointing towards this modification being detrimental to binding. Following optimization of synthetic routes, we want to further explore the para-F analog and incorporate more electronic deficient systems, like the pyridine rings similar to those from our SAR by catalog in Chapter 4 or p-NO_2 and p-CF_3.

A) B)

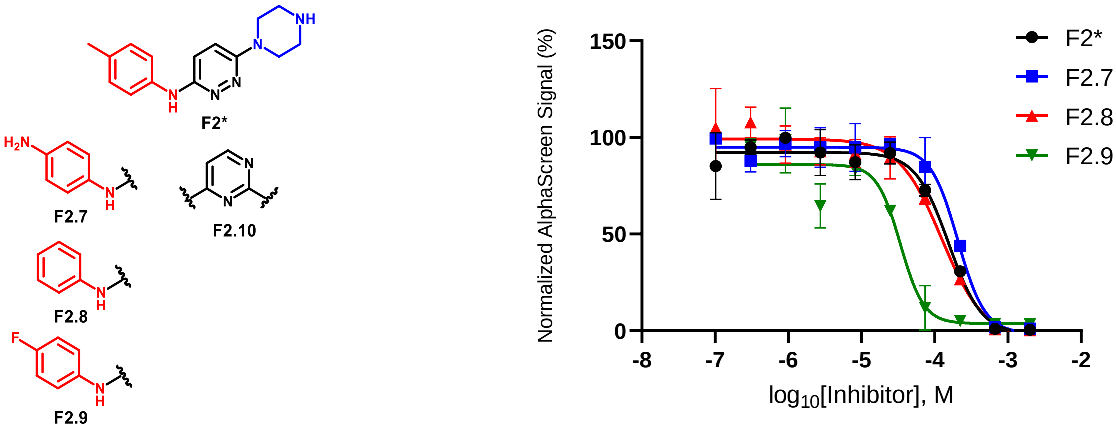

Figure 5.1: F2 Analogs Binding to BPTF PHD.

A) Structure of **F2** analogs. B) AlphaScreen titration of **F2*** and **F2.7-F2.9**.

5.2 Examining Binding Interaction of Fragments with BPTF PHD

To better understand changes in affinity between our two hit scaffolds from Chapter 4, **F1** and **F2**, we wanted to further investigate binding interactions beyond molecular docking.

5.2.1 ^{1}H,^{15}N HSQC NMR

^{1}H,^{15}N HSQC NMR is a technique that can be used to discern protein structure and perturbations upon ligand binding, as discussed in Section 1.5. An assigned spectra for ^{15}N-labeled BPTF PHD has already been reported in literature, as well as chemical shift perturbations (CSPs) upon addition of H3K4me3 peptide and histone.[16,63] We were able to obtain an *apo* spectra of ^{15}N-BPTF PHD, which was well dispersed, and assign residues 8-65 reports (**Figure 5.2**). We were also able to see CSPs comparable to literature upon addition of H3K4me2 (**Figure 5.3),** as in the downfield shift on the ^{1}H axis and upfield shift on the ^{15}N axis of Y23, which is a part of the aromatic cage, and an upfield shift on the ^{15}N axis of D27, which is a part of the R2 pocket (**Figure 5.3 inset**).

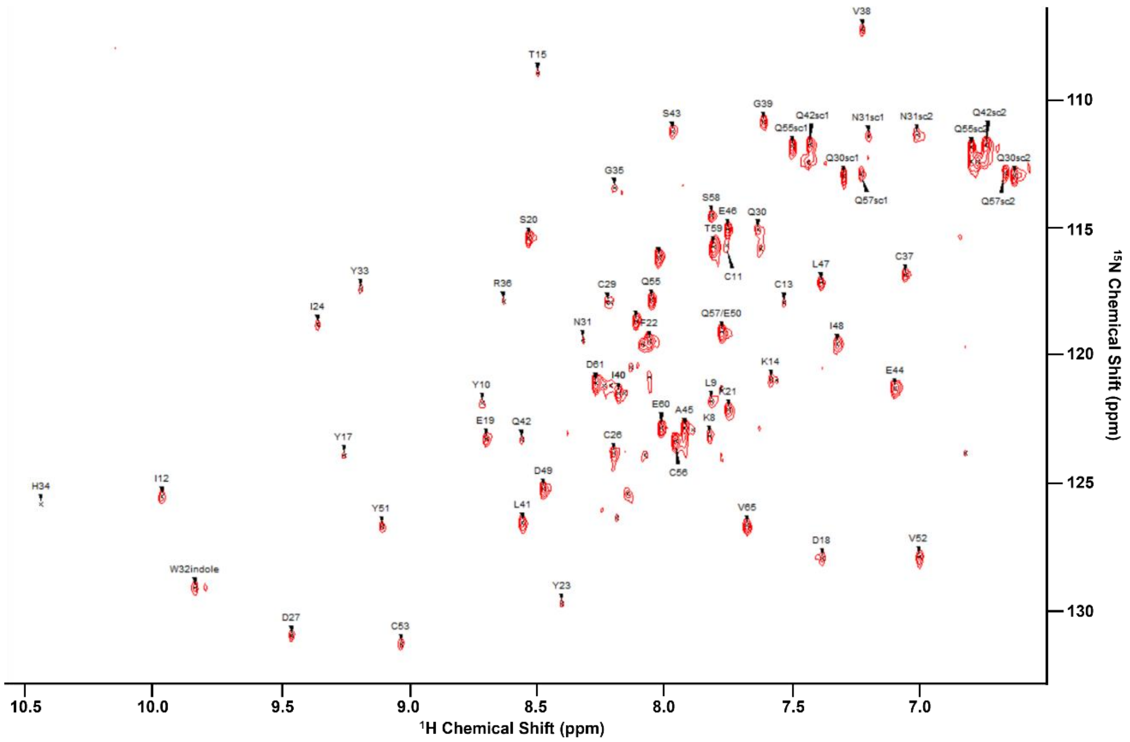

Figure 5.2: ^{1}H,^{15}N HSQC NMR Spectra of *apo* ^{15}N-labeled BPTF PHD.

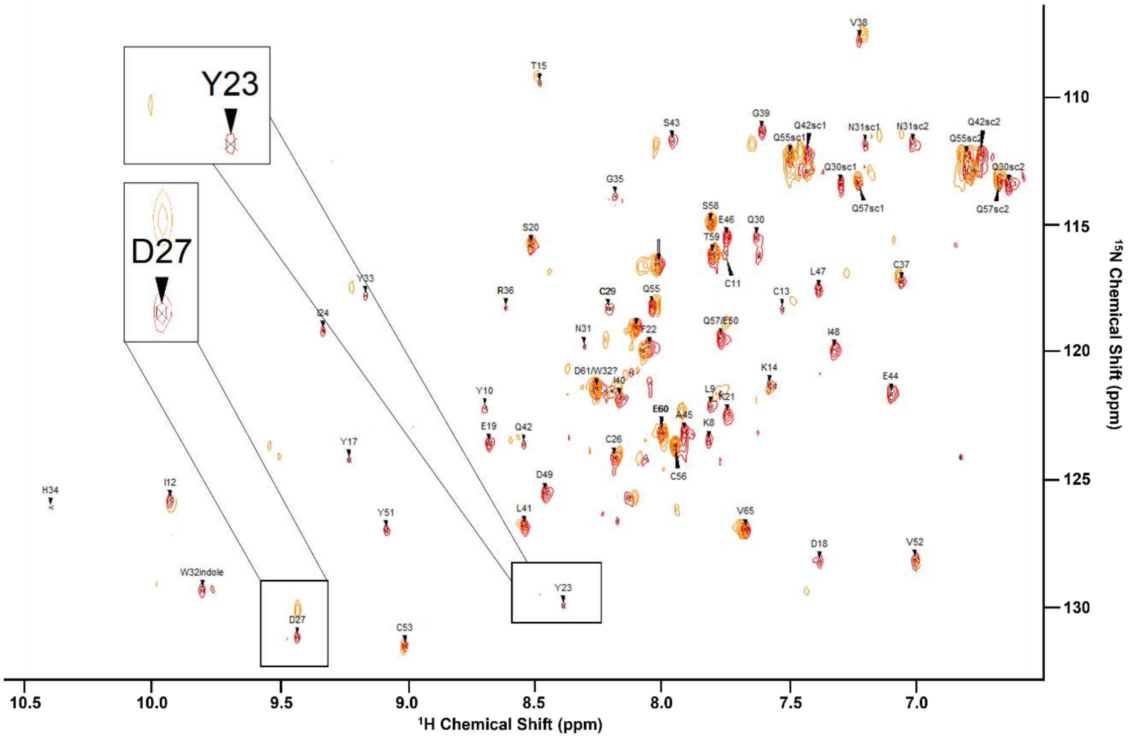

Figure 5.3: ^{1}H,^{15}N HSQC NMR Spectra of ^{15}N-BPTF PHD + H3K3me2.

Spectra of *apo* ^{15}N-BPTF PHD (red) overlayed with 40 μM ^{15}N-BPTF PHD + 5 equiv. H3K4me2 (orange). Inset magnified spectra of Y23 and D27 residues.

To look at fragment binding perturbations we recorded spectra with 1 mM each respective fragment, **F1**, **F2**, and **F4**, added to ^{15}N-BPTF PHD. We did not see any distinct binding fingerprints when examining CSPs (Figure 4.14) and were not able to determine K_d due to the low CSPs. We can conclude that are fragments are not denaturants. Additionally, we did note a subset of significant shift in the W32 sidechain and Y17 residues, which are a part of the aromatic cage, upon addition of **F1** and **F2** (**Figure 4.14** and **Figure 5.4)**. Experiments with more potent fragment analogs will be run in the future to elucidate a binding pattern for these fragment scaffolds.

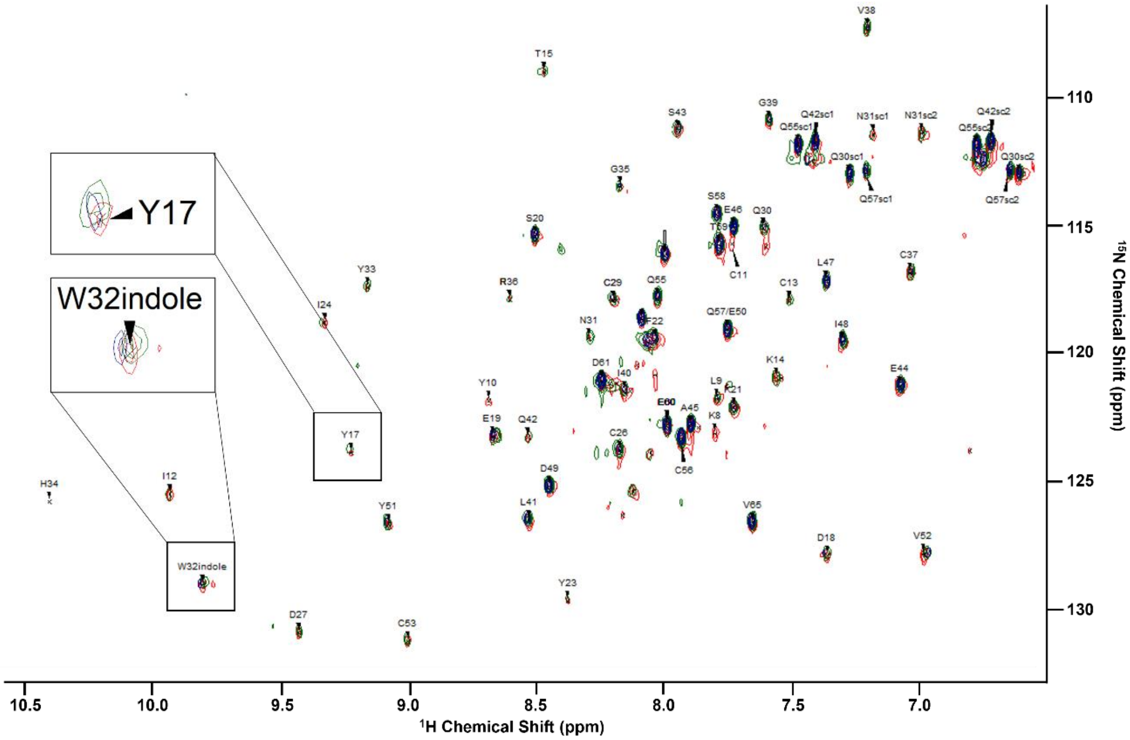

Figure 5.4:^{1}H,^{15}N HSQC NMR Spectra of ^{15}N-labeled BPTF PHD + Fragments.
Spectra of *apo* ^{15}N-BPTF PHD (red) overlayed with 40 μM ^{15}N-BPTF PHD + 1 mM **F1** (green) or 1 mM **F2** (blue). Insets magnified spectra of Y17 and W32 sidechain residues.

5.2.2 Site Directed Mutants

Site directed mutagenesis (SDM) is a technique that can be used to add point mutations, amino acid mutations, or amino acid insertions/deletions to protein constructs. We hypothesize that by introducing amino acid mutations at critical binding residues using SDM, we will be able to study binding interactions between BPTF PHD and hit fragment scaffolds. Mutations at W32 (W32F) and D27 (D27A, D27N) have been shown to report binding interactions in the aromatic cage and R2 pocket respectively (**Figure 5.5**). The histone tail, H3K4me3, loses affinity for these mutants.[63] Fragments that also bind in either the aromatic cage or R2 pocket would lose potency for these mutants. **F1** was predicted by molecular docking to bind in the aromatic cage, so a first test would be with a W32F mutant (**Figure 5.5**). We are also interested in examining G25 mutants as a method to report on binding interactions. G25 sits on the edge of the pocket where the histone backbone binds (**Figure 5.5**). If bulkier residues are added at G25 (G25V, G25I, G25V) they could block binding interactions at this site. This is relevant for **F2**, which is predicted by molecular docking to bind near the backbone binding site.

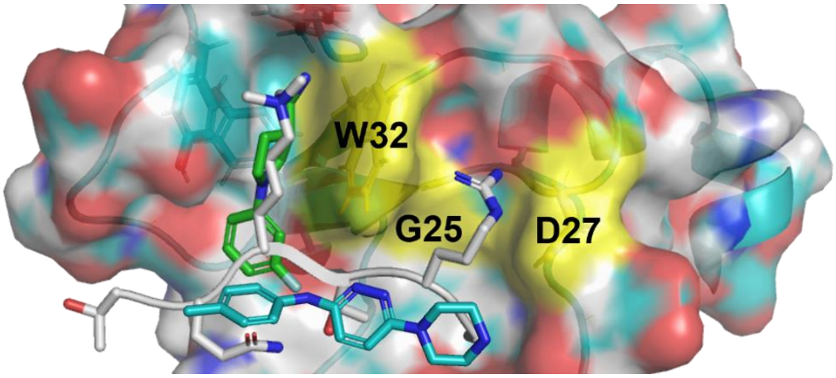

Figure 5.5: Mutation Sites to Report on BPTF PHD Binding Interactions

BPTF PHD (electrostatic surface) molecular docking with F1 (green sticks) and F2 (blue sticks), overlayed with histone tail (white sticks), with mutation sites highlight in yellow.

To perform SDM, primers specific to each desired mutant must be designed. A forward and reverse primer are needed that contain the desired mutation and can anneal to the same location on the DNA template. Generally, they need to be 25-45 bases in length, with 10-15 bases on either side of the mutation site to anneal. Additionally, they should be made up of at least 40% G or C bases and have a melting temperature of greater than 78°C. This allows for annealing of primer to DNA template, followed by primer extension under a thermal cycle to form the mutant plasmid. Digestion of the template affords only the mutated plasmid which can then by transformed into competent cells for subsequent expression of mutant protein.[306]

We designed forward primers for mutations at W32, G25, and D27 (**Table 5.1**) and their corresponding reverse primers, and then ordered them from Integrated DNA Technologies. In the future these mutagenic primers can be used to create BPTF PHD mutants that can monitor residues critical for binding interactions of our fragment scaffolds.

Table 5.1: Forward Primers for Site Directed Mutagenesis

(mutated codon highlighted in yellow)

Mutation	**Forward Primer (5'-3')**
W32F	cgatcgttgccagaacttctatcacggtcgttgcgt
G25A	acgaaagcaagttttatattgcctgcgatcgttgccag
G25L	ccccgtacgacgaaagcaagttttatattctatgcgatcgttgccag
G25I	cgtacgacgaaagcaagttttatattatctgcgatcgttgcc
G25V	acgaaagcaagttttatattgtctgcgatcgttgccag
D27A	gttttatattggctgcgctcgttgccagaactggt
D27N	caagttttatattggctgcaatcgttgccagaactggta

5.3 Selectivity Analysis of Fragments Against KDM5A PHD3

With BPTF PHD binders in hand, we wanted to begin to assess their selectivity against other PHD fingers. We chose to start with KDM5A PHD3, which has been screened previously in literature,[71] as it also recognizes H3K4me3 marks while having an aromatic cage composed of only two tryptophans in comparison to BPTF PHD's three tyrosines and one tryoptophan.[60] ^{1}H CPMG NMR was used as a binding assay to directly compare to the BPTF PHD screen, as detailed in Chapter 4 none of our top fragments showed significant binding to KDM5A PHD3. We validated this approach using the H3K4me2 peptide. H3K4me2 has a K_d of 930 nM for KDMD5A.[307] Upon addition of the protein, with a 10-fold excess of peptide as in the BPTF PHD assays, a 30% drop in resonance was observed (**Figure 5.6**). This drop was lower than expected for such a strong binder, which may indicate oversaturation of peptide. Upon lowering the ratio of peptide to protein to 3:1 and 2:1, larger drops of 50% and 60% were observed, indicating active protein (**Figure 5.6**).

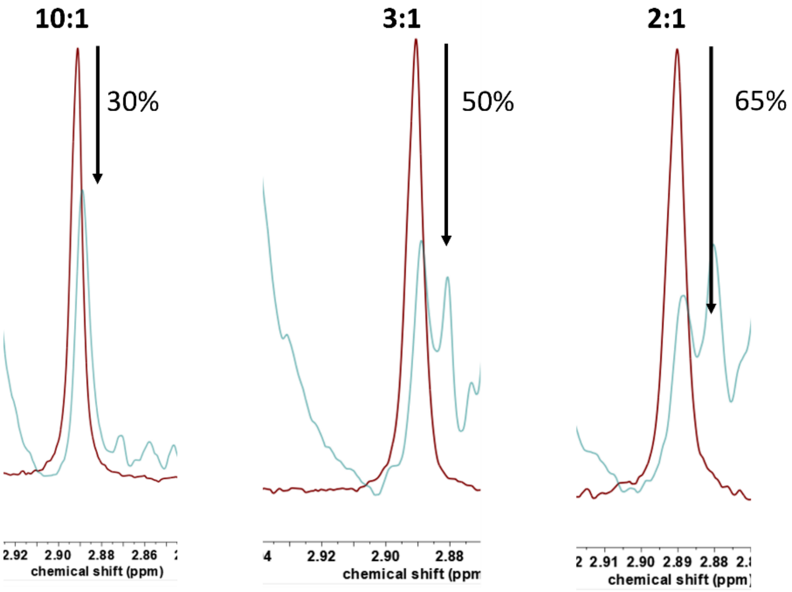

Figure 5.6: ^{1}H CPMG assay of KDM5A PHD3 and H3K4me2 with differing ratios. 1H CPMG experiments with peptide only in red and peptide plus protein in green, where the methyl peak is monitored at 2.88 ppm.

To validate these results, we chose AlphaScreen, a competitive inhibition assay we had also used for BPTF PHD. Optimization of a KDM5A PHD3 AlphaScreen assay began with testing H3K4me3 biotinylated peptide as a probe. To confirm complex formation between the histone probe and KDM5A a 64-point cross-titration was run (**Figure 5.7**).

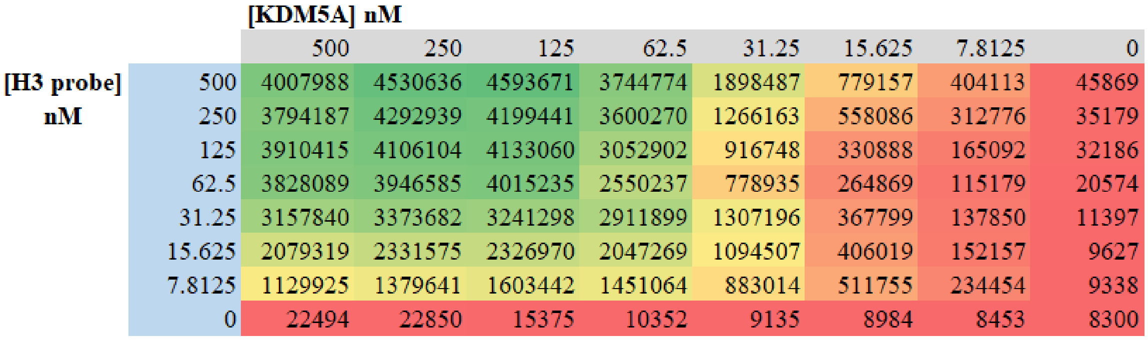

		[KDM5A] nM							
		500	250	125	62.5	31.25	15.625	7.8125	0
[H3 probe] nM	500	4007988	4530636	4593671	3744774	1898487	779157	404113	45869
	250	3794187	4292939	4199441	3600270	1266163	558086	312776	35179
	125	3910415	4106104	4133060	3052902	916748	330888	165092	32186
	62.5	3828089	3946585	4015235	2550237	778935	264869	115179	20574
	31.25	3157840	3373682	3241298	2911899	1307196	367799	137850	11397
	15.625	2079319	2331575	2326970	2047269	1094507	406019	152157	9627
	7.8125	1129925	1379641	1603442	1451064	883014	511755	234454	9338
	0	22494	22850	15375	10352	9135	8984	8453	8300

Figure 5.7: Complex Formation of KDM5A PHD3 with H3K4me3 probe.

Titration of [KDM5A] across and titration of [H3K4me3 probe] down in 64-well plate. Highest AlphaScreen signals are shown in green, intermediate in yellow, and lowest in red.

Complex formation was indicated by signals up to four million and a general trend of lower (red) to higher (green) signals when going across the plate from the bottom right to top left. H3K4me2 was used a control for a self-competition experiment. As a starting point, 60 nM His-KDM5A and 100 nM H3K4me3 probe was chosen, to try and best approximate K_d. This allows the [probe] to be significantly lower than the complex K_d of 930 nM, and the [target] to be lower than the [probe] to avoid excess protein. Under these conditions, the H3K4me2 peptide did not fully compete off the probe at 250 µM, the IC_{50} was far from approximating the K_d (**Figure 5.8**). Another control may be needed to continue to optimize this assay in the future.

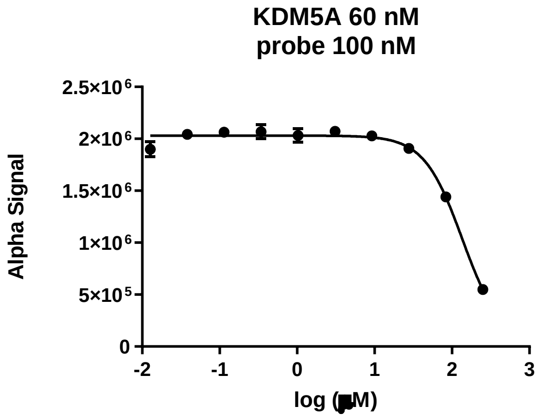

Figure 5.8: Competition experiment of KDM5A with H3K4me2.

5.4 Conclusions and Future Outlook

In conclusion, we have begun to perform SAR around **F2** indicating the importance of the aniline moiety, and are currently optimizing an Ullman coupling to access a diverse array of analogs. Additionally, SAR around **F1** will be explored. ITC and tryptophan fluorescence assays are currently being optimized to be able to measure K_d for our analogs. To better understand binding interactions, HSQC NMR will continue to be used as well as setting up crystallography, for which the histone tail complex has been crystallized previously.[63] In the future we aim to connect this work to our bromodomain inhibitors, and monitor in cell effects of both PHD inhibitors alone and in combination with bromodomain inhibitors. In collaboration with St. Jude a fluorescence recovery after photobleaching (FRAP) assay will be used to assess chromatin engagement upon cell treatment. These approaches will allow for understanding of the PHD fingers biological role in disease, as well as dual domain inhibition. Specifically, we want to study neuroblastoma systems, as described in Section 3.2. Bromodomain inhibitor **BZ2** has already been tested in WT SK-N-AS cells and exhibited growth inhibition, and BPTF knockdown showed downregulation of c-Myc expression (**Figure 3.13**).

5.5 Experimental Section

In addition to methods detailed in Chapter 4:

General procedure for the synthesis of compounds F2.7-2.9 1-Boc-4-(6-Chloropyridazin-3-yl)piperazine was stirred in 1,4-dioxane followed by addition of primary amine (2 eq.) and heated at reflux overnight. Following completion of reaction, the reaction mixture was concentrated in vacuo and purified by flash column chromatography (CombiFlash Rf system: 12 g silica, hexanes/0-100% ethyl acetate, 20 min). Intermediate product was deprotected with 10% TFA in DCM and extracted with 1 M NaOH, dried over magnesium sulfate, and concentrated in vacuo.

N1-(6-(piperazin-1-yl)pyridazin-3-yl)benzene-1,4-diamine (F2.7). Following the general procedure, (1-Boc-4-(6-Chloropyridazin-3-yl)piperazine (250 mg, 0.8 mmol, 1 eq.), N-Boc-p-phenylenediamine (349 mg, 1.6 mmol, 2 eq.)), product **F2.7** was obtained as a yellow solid (9 mg, 4% yield). ^{1}H NMR (500 MHz, DMSO-*d$_6$*) δ 8.24 (s, 1H), 7.27 (m, 2 H), 7.16 (d, *J* = 9.8 Hz, 1H), 6.88 (d, *J* = 9.8 Hz, 1H), 6.51 (m, 2H), 4.66 (s, 2H), 3.26 (t, *J* = 4 Hz, 4H), 2.81 (t, *J* = 3.9 Hz, 4H).

N-phenyl-6-(piperazin-1-yl)pyridazin-3-amine (F2.8). Following the general procedure, (1-Boc-4-(6-Chloropyridazin-3-yl)piperazine (250 mg, 0.8 mmol, 1 eq.), aniline (78 mg, 1.6 mmol, 2 eq.)), product **F2.8** was obtained as a yellow solid (31 mg, 15% yield). ^{1}H NMR (500 MHz, DMSO- *d$_6$*) δ 9.35 (s, 1H), 8.87 (s, 2H), 7.62 (d, *J* = 9.8 Hz, 2H), 7.57 (d, *J* = 11.2 Hz, 1 H), 7.31 (m, 3H), 6.97 (t, *J* = 7.4 Hz, 1H), 3.68 (t, *J* = 5.8 Hz, 4H), 3.25 (m, 4H).

N-(4-fluorophenyl)-6-(piperazin-1-yl)pyridazin-3-amine (F2.9). Following the general procedure, (1-Boc-4-(6-Chloropyridazin-3-yl)piperazine (166 mg, 0.55 mmol, 1 eq.), 4-fluoroaniline (123 mg, 1.1 mmol, 2 eq.)), product **F2.9** was obtained as a yellow solid (9 mg, 5% yield). ^{1}H NMR (500 MHz, DMSO- *d$_6$*) δ 8.83 (s, 1H), 7.70 (m,, 2H). 7.26 (d, *J* = 9.6 Hz, 1H), 7.08 (m, 2H), 6.99 (d, *J* = 9.7 Hz, 1H), 3.30 (m, 4H), 2.80 (m, 4H).

2-(piperazin-1-yl)-N-(p-tolyl)pyrimidin-4-amine (F2.10). Step 1: 2,4-dichloropyrimidine (200 mg, 1.3 mmol, 1 eq.) and 1-Boc-piperazine (261 mg, 1.3 mmol, 1 eq.) were added to 1 mL ethanol and stirred at reflux overnight. Following completion of reaction, the reaction mixture was concentrated in vacuo and purified by flash column chromatography (CombiFlash Rf system: 12 g silica, hexanes/0-100% ethyl acetate, 20 min). Step 2: Intermediate product was added with p-toluidine (2 eq.) to 1,4-dioxane and stirred at reflux overnight. Following completion of reaction, the reaction mixture was concentrated in vacuo and purified by flash column chromatography (CombiFlash Rf system: 12 g silica, hexanes/0-100% ethyl acetate, 20 min). Intermediate product was deprotected with 10% TFA in DCM and extracted with 1 M NaOH, dried over magnesium sulfate, and concentrated in vacuo. Product **F2.10** was obtained as a yellow solid (15 mg, 4% yield). ^{1}H NMR (500 MHz, DMSO-d_6) δ 8.87 (s, 2H), 7.93 (d, J = 6.1 Hz, 1H), 7.57 (d, J = 8.6 Hz, 2H), 7.04 (d, J = 8.3 Hz, 2H), 6.20 (d, J = 6.1 Hz, 1H), 3.51 (t, J = 5.2 Hz, 4H), 2.75 (t, J = 4.9 Hz, 4H), 2.23 (s, 3H).

AlphaScreen Cross-Titrations. All reagents were diluted in a buffer consisting of 50 mM HEPES, 100 mM NaCl, 0.1% BSA, and 0.05% CHAPS, pH 7.4. Biotinylated H3 K4me3 (Cat. # 81042, Active Motif) and His-tagged protein were titrated across a 64-well array vertically and horizontally respectively. #0 µg/mL AlphaScreen streptavidin donor and nickel chelate acceptor beads (6760619M, Perkin Elmer) were added and then allowed to incubate for 30 minutes at room temperature. Emission was measured on a Tecan Spark reader using AlphaScreen filter settings.

5.6 Acknowledgement

We would like to acknowledge Brandon Schuldt, Kostana Ligori, and Joe McPherson for assistance with synthesis.

Rights and Permissions

^{19}F NMR viewed through two different lenses: ligand-observed and protein-observed ^{19}F NMR applications for fragment-based drug discovery

C. R. Buchholz and W. C. K. Pomerantz, *RSC Chem. Biol.*, 2021, **2**, 1312 **DOI:** 10.1039/D1CB00085C

This article is licensed under a Creative Commons Attribution 3.0 Unported Licence. **You can use material from this article in other publications without requesting further permissions** from the RSC, provided that the correct acknowledgement is given.

Read more about how to correctly acknowledge RSC content.

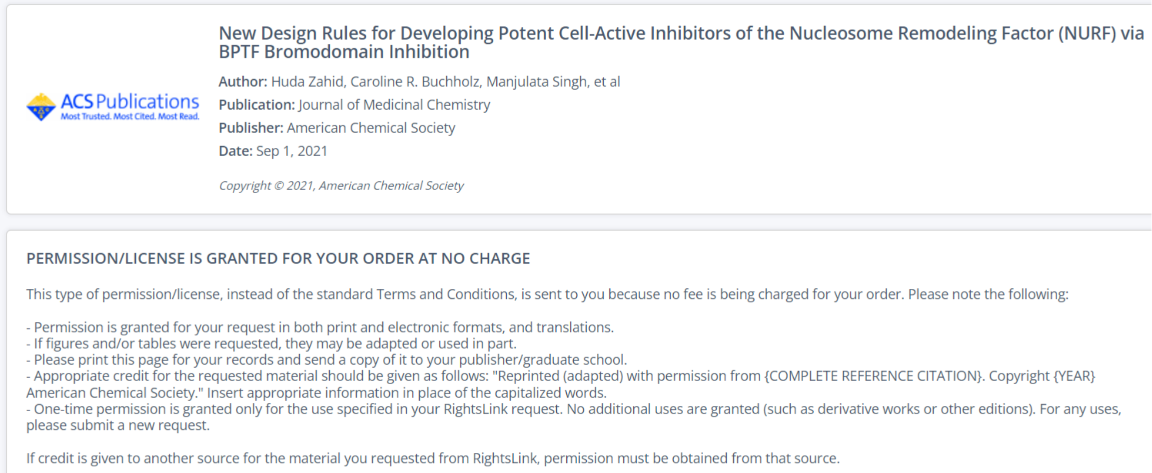

New Design Rules for Developing Potent Cell-Active Inhibitors of the Nucleosome Remodeling Factor (NURF) via BPTF Bromodomain Inhibition

Author: Huda Zahid, Caroline R. Buchholz, Manjulata Singh, et al
Publication: Journal of Medicinal Chemistry
Publisher: American Chemical Society
Date: Sep 1, 2021

Copyright © 2021, American Chemical Society

PERMISSION/LICENSE IS GRANTED FOR YOUR ORDER AT NO CHARGE

This type of permission/license, instead of the standard Terms and Conditions, is sent to you because no fee is being charged for your order. Please note the following:

- Permission is granted for your request in both print and electronic formats, and translations.
- If figures and/or tables were requested, they may be adapted or used in part.
- Please print this page for your records and send a copy of it to your publisher/graduate school.
- Appropriate credit for the requested material should be given as follows: "Reprinted (adapted) with permission from {COMPLETE REFERENCE CITATION}. Copyright {YEAR} American Chemical Society." Insert appropriate information in place of the capitalized words.
- One-time permission is granted only for the use specified in your RightsLink request. No additional uses are granted (such as derivative works or other editions). For any uses, please submit a new request.

If credit is given to another source for the material you requested from RightsLink, permission must be obtained from that source.

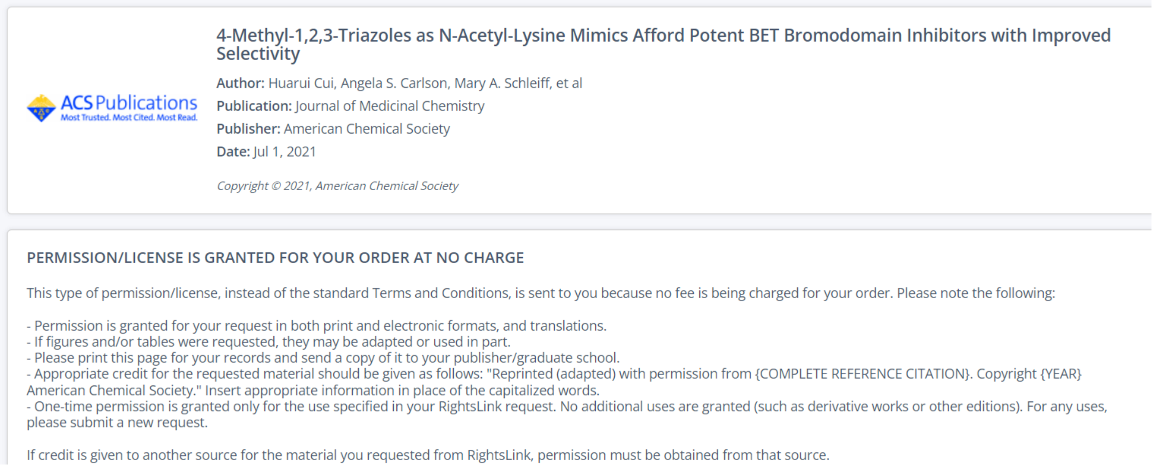

4-Methyl-1,2,3-Triazoles as N-Acetyl-Lysine Mimics Afford Potent BET Bromodomain Inhibitors with Improved Selectivity

Author: Huarui Cui, Angela S. Carlson, Mary A. Schleiff, et al
Publication: Journal of Medicinal Chemistry
Publisher: American Chemical Society
Date: Jul 1, 2021

Copyright © 2021, American Chemical Society

PERMISSION/LICENSE IS GRANTED FOR YOUR ORDER AT NO CHARGE

This type of permission/license, instead of the standard Terms and Conditions, is sent to you because no fee is being charged for your order. Please note the following:

- Permission is granted for your request in both print and electronic formats, and translations.
- If figures and/or tables were requested, they may be adapted or used in part.
- Please print this page for your records and send a copy of it to your publisher/graduate school.
- Appropriate credit for the requested material should be given as follows: "Reprinted (adapted) with permission from {COMPLETE REFERENCE CITATION}. Copyright {YEAR} American Chemical Society." Insert appropriate information in place of the capitalized words.
- One-time permission is granted only for the use specified in your RightsLink request. No additional uses are granted (such as derivative works or other editions). For any uses, please submit a new request.

If credit is given to another source for the material you requested from RightsLink, permission must be obtained from that source.

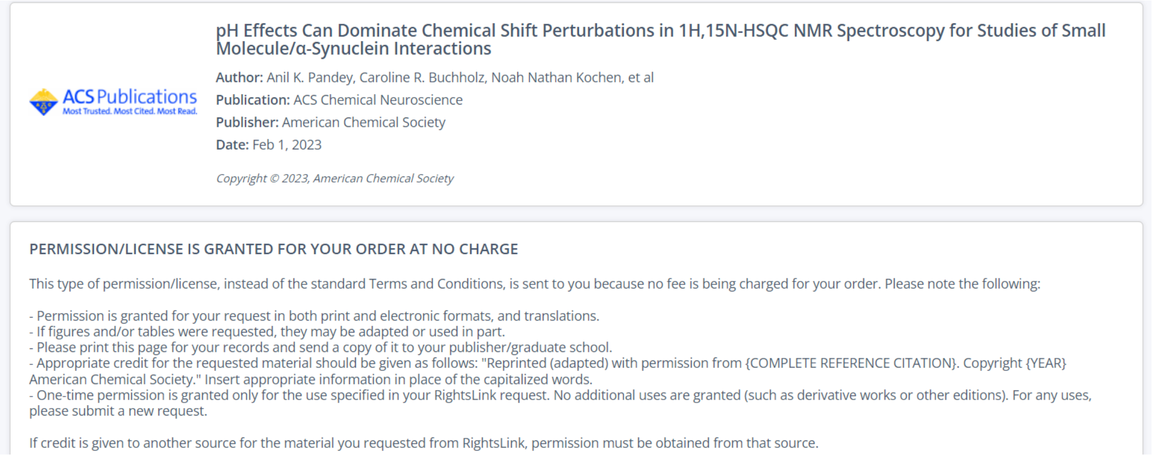

pH Effects Can Dominate Chemical Shift Perturbations in 1H,15N-HSQC NMR Spectroscopy for Studies of Small Molecule/α-Synuclein Interactions

Author: Anil K. Pandey, Caroline R. Buchholz, Noah Nathan Kochen, et al
Publication: ACS Chemical Neuroscience
Publisher: American Chemical Society
Date: Feb 1, 2023

Copyright © 2023, American Chemical Society

PERMISSION/LICENSE IS GRANTED FOR YOUR ORDER AT NO CHARGE

This type of permission/license, instead of the standard Terms and Conditions, is sent to you because no fee is being charged for your order. Please note the following:

- Permission is granted for your request in both print and electronic formats, and translations.
- If figures and/or tables were requested, they may be adapted or used in part.
- Please print this page for your records and send a copy of it to your publisher/graduate school.
- Appropriate credit for the requested material should be given as follows: "Reprinted (adapted) with permission from {COMPLETE REFERENCE CITATION}. Copyright {YEAR} American Chemical Society." Insert appropriate information in place of the capitalized words.
- One-time permission is granted only for the use specified in your RightsLink request. No additional uses are granted (such as derivative works or other editions). For any uses, please submit a new request.

If credit is given to another source for the material you requested from RightsLink, permission must be obtained from that source.

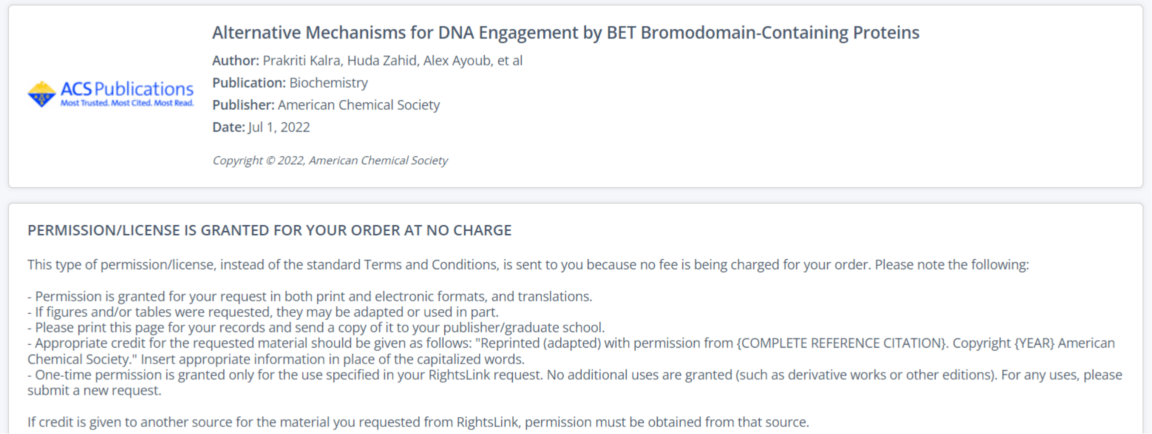

Alternative Mechanisms for DNA Engagement by BET Bromodomain-Containing Proteins

Author: Prakriti Kalra, Huda Zahid, Alex Ayoub, et al
Publication: Biochemistry
Publisher: American Chemical Society
Date: Jul 1, 2022

Copyright © 2022, American Chemical Society

PERMISSION/LICENSE IS GRANTED FOR YOUR ORDER AT NO CHARGE

This type of permission/license, instead of the standard Terms and Conditions, is sent to you because no fee is being charged for your order. Please note the following:

- Permission is granted for your request in both print and electronic formats, and translations.
- If figures and/or tables were requested, they may be adapted or used in part.
- Please print this page for your records and send a copy of it to your publisher/graduate school.
- Appropriate credit for the requested material should be given as follows: "Reprinted (adapted) with permission from {COMPLETE REFERENCE CITATION}. Copyright {YEAR} American Chemical Society." Insert appropriate information in place of the capitalized words.
- One-time permission is granted only for the use specified in your RightsLink request. No additional uses are granted (such as derivative works or other editions). For any uses, please submit a new request.

If credit is given to another source for the material you requested from RightsLink, permission must be obtained from that source.

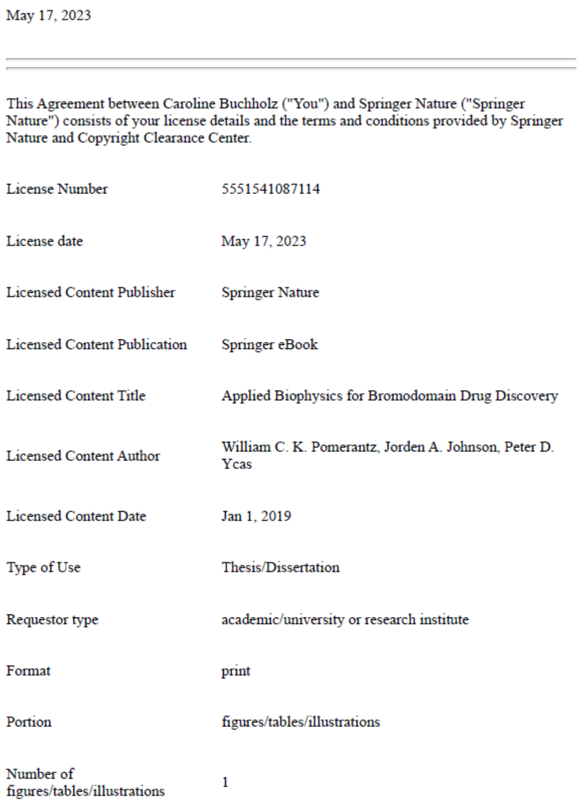

May 17, 2023

This Agreement between Caroline Buchholz ("You") and Springer Nature ("Springer Nature") consists of your license details and the terms and conditions provided by Springer Nature and Copyright Clearance Center.

License Number	5551541087114
License date	May 17, 2023
Licensed Content Publisher	Springer Nature
Licensed Content Publication	Springer eBook
Licensed Content Title	Applied Biophysics for Bromodomain Drug Discovery
Licensed Content Author	William C. K. Pomerantz, Jorden A. Johnson, Peter D. Ycas
Licensed Content Date	Jan 1, 2019
Type of Use	Thesis/Dissertation
Requestor type	academic/university or research institute
Format	print
Portion	figures/tables/illustrations
Number of figures/tables/illustrations	1

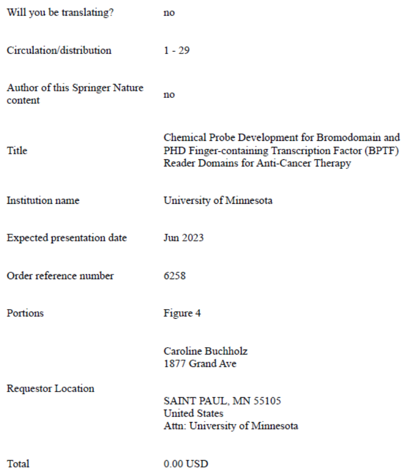

Will you be translating?	no
Circulation/distribution	1 - 29
Author of this Springer Nature content	no
Title	Chemical Probe Development for Bromodomain and PHD Finger-containing Transcription Factor (BPTF) Reader Domains for Anti-Cancer Therapy
Institution name	University of Minnesota
Expected presentation date	Jun 2023
Order reference number	6258
Portions	Figure 4
Requestor Location	Caroline Buchholz 1877 Grand Ave SAINT PAUL, MN 55105 United States Attn: University of Minnesota
Total	0.00 USD

Bibliography

(1) Buchholz, C. R.; Pomerantz, W. C. K. 19F NMR Viewed through Two Different Lenses: Ligand-Observed and Protein-Observed 19F NMR Applications for Fragment-Based Drug Discovery. *RSC Chem. Biol.* **2021**, *2* (5), 1312–1330. https://doi.org/10.1039/D1CB00085C.

(2) Goldberg, A. D.; Allis, C. D.; Bernstein, E. Epigenetics: A Landscape Takes Shape. *Cell* **2007**, *128* (4), 635–638. https://doi.org/10.1016/j.cell.2007.02.006.

(3) Workman, J. L.; Kingston, R. E. Alteration of Nucleosome Structure as a Mechanism of Transcriptional Regulation. *Annu. Rev. Biochem.* **1998**, *67* (1), 545–579. https://doi.org/10.1146/annurev.biochem.67.1.545.

(4) Portela, A.; Esteller, M. Epigenetic Modifications and Human Disease. *Nat. Biotechnol.* **2010**, *28* (10), 1057–1068. https://doi.org/10.1038/nbt.1685.

(5) Feinberg, A. P.; Koldobskiy, M. A.; Göndör, A. Epigenetic Modulators, Modifiers and Mediators in Cancer Aetiology and Progression. *Nat. Rev. Genet.* **2016**, *17* (5), 284–299. https://doi.org/10.1038/nrg.2016.13.

(6) Jenuwein, T.; Allis, C. D. Translating the Histone Code. *Science* **2001**, *293* (5532), 1074–1080. https://doi.org/10.1126/science.1063127.

(7) Strahl, B. D.; David Allis, C. *The Language of Covalent Histone Modi®cations*; 2000; Vol. 403. www.nature.com (accessed 2019-06-04).

(8) Fujimori D.G., C. S. J. Editorial Overview: Chemical Genetics and Epigenetics. *Curr Opin Chem Biol* **2016**, *33*, vi–vii.

(9) Barak, O.; Lazzaro, M. A.; Lane, W. S.; Speicher, D. W.; Picketts, D. J.; Shiekhattar, R. Isolation of Human NURF: A Regulator of Engrailed Gene Expression. *EMBO J.* **2003**, *22* (22), 6089–6100. https://doi.org/10.1093/emboj/cdg582.

(10) Alkhatib, S. G.; Landry, J. W. The Nucleosome Remodeling Factor. *FEBS Lett.* **2011**, *585* (20), 3197–3207. https://doi.org/10.1016/j.febslet.2011.09.003.

(11) Hamiche, A.; Sandaltzopoulos, R.; Gdula, D. A.; Wu, C. ATP-Dependent Histone Octamer Sliding Mediated by the Chromatin Remodeling Complex NURF. *Cell* **1999**, *97* (7), 833–842. https://doi.org/10.1016/S0092-8674(00)80796-5.

(12) Mizuguchi, G.; Tsukiyama, T.; Wisniewski, J.; Wu, C. Role of Nucleosome Remodeling Factor NURF in Transcriptional Activation of Chromatin. *Mol. Cell* **1997**, *1* (1), 141–150. https://doi.org/10.1016/S1097-2765(00)80015-5.

(13) Landry, J.; Sharov, A. A.; Piao, Y.; Sharova, L. V.; Xiao, H.; Southon, E.; Matta, J.; Tessarollo, L.; Zhang, Y. E.; Ko, M. S. H.; Kuehn, M. R.; Yamaguchi, T. P.; Wu, C. Essential Role of Chromatin Remodeling Protein Bptf in Early Mouse Embryos and

Embryonic Stem Cells. *PLoS Genet.* **2008**, *4* (10), e1000241. https://doi.org/10.1371/journal.pgen.1000241.

(14) Wysocka, J.; Swigut, T.; Xiao, H.; Milne, T. A.; Kwon, S. Y.; Landry, J.; Kauer, M.; Tackett, A. J.; Chait, B. T.; Badenhorst, P.; Wu, C.; Allis, C. D. A PHD Finger of NURF Couples Histone H3 Lysine 4 Trimethylation with Chromatin Remodelling. *Nature* **2006**, *442* (7098), 86–90. https://doi.org/10.1038/nature04815.

(15) Ruthenburg, A. J.; Li, H.; Milne, T. A.; Dewell, S.; McGinty, R. K.; Yuen, M.; Ueberheide, B.; Dou, Y.; Muir, T. W.; Patel, D. J.; Allis, C. D. Recognition of a Mononucleosomal Histone Modification Pattern by BPTF via Multivalent Interactions. *Cell* **2011**, *145* (5), 692–706. https://doi.org/10.1016/j.cell.2011.03.053.

(16) Morrison, E. A.; Bowerman, S.; Sylvers, K. L.; Wereszczynski, J.; Musselman, C. A. The Conformation of the Histone H3 Tail Inhibits Association of the BPTF PHD Finger with the Nucleosome. *eLife* **2018**, *7*. https://doi.org/10.7554/eLife.31481.

(17) Marunde, M.; Fuchs, H.; Burg, J.; Popova, I.; Vaidya, A.; Hall, N.; Meiners, M.; Watson, R.; Howard, S.; Novitzky, K.; McAnarney, E.; Cheek, M.; Sun, Z.-W.; Venters, B.; Keogh, M.-C.; Musselman, C. Nucleosome Conformation Dictates the Histone Cod. 2022. https://doi.org/10.1101/2022.02.21.481373.

(18) Jones, M. H.; Hamana, N.; Shimane, M. Identification and Characterization of BPTF, a Novel Bromodomain Transcription Factor. *Genomics* **2000**, *63* (1), 35–39. https://doi.org/10.1006/geno.1999.6070.

(19) Buganim, Y.; Goldstein, I.; Lipson, D.; Milyavsky, M.; Polak-Charcon, S.; Mardoukh, C.; Solomon, H.; Kalo, E.; Madar, S.; Brosh, R.; Perelman, M.; Navon, R.; Goldfinger, N.; Barshack, I.; Yakhini, Z.; Rotter, V. A Novel Translocation Breakpoint within the BPTF Gene Is Associated with a Pre-Malignant Phenotype. **2010**. https://doi.org/10.1371/journal.pone.0009657.

(20) Pan, Y.; Yuan, F.; Li, Y.; Wang, G.; Lin, Z.; Chen, L. Bromodomain PHD-Finger Transcription Factor Promotes Glioma Progression and Indicates Poor Prognosis. *Oncol. Rep.* **2019**, *41* (1), 246–256. https://doi.org/10.3892/or.2018.6832.

(21) Green, A. L.; DeSisto, J.; Flannery, P.; Lemma, R.; Knox, A.; Lemieux, M.; Sanford, B.; O'Rourke, R.; Ramkissoon, S.; Jones, K.; Perry, J.; Hui, X.; Moroze, E.; Balakrishnan, I.; O'Neill, A. F.; Dunn, K.; DeRyckere, D.; Danis, E.; Safadi, A.; Gilani, A.; Hubbell-Engler, B.; Nuss, Z.; Levy, J. M. M.; Serkova, N.; Venkataraman, S.; Graham, D. K.; Foreman, N.; Ligon, K.; Jones, K.; Kung, A. L.; Vibhakar, R. BPTF Regulates Growth of Adult and Pediatric High-Grade Glioma through the MYC Pathway. *Oncogene* **2020**, *39* (11), 2305–2327. https://doi.org/10.1038/s41388-019-1125-7.

(22) Dar, A. A.; Majid, S.; Bezrookove, V.; Phan, B.; Ursu, S.; Nosrati, M.; De Semir, D.; Sagebiel, R. W.; Miller, J. R.; Debs, R.; Cleaver, J. E.; Kashani-Sabet, M.; Kashani-Sabet, M. BPTF Transduces MITF-Driven Prosurvival Signals in Melanoma Cells. *Proc.*

Natl. Acad. Sci. U. S. A. **2016**, *113* (22), 6254–6258. https://doi.org/10.1073/pnas.1606027113.

(23) Frey, W. D.; Chaudhry, A.; Slepicka, P. F.; Ouellette, A. M.; Kirberger, S. E.; Pomerantz, W. C. K.; Hannon, G. J.; dos Santos, C. O. BPTF Maintains Chromatin Accessibility and the Self-Renewal Capacity of Mammary Gland Stem Cells. *Stem Cell Rep.* **2017**, *9* (1), 23–31. https://doi.org/10.1016/j.stemcr.2017.04.031.

(24) Dai, M.; Lu, J.-J.; Guo, W.; Yu, W.; Wang, Q.; Tang, R.; Tang, Z.; Xiao, Y.; Li, Z.; Sun, W.; Sun, X.; Qin, Y.; Huang, W.; Deng, W.; Wu, T. BPTF Promotes Tumor Growth and Predicts Poor Prognosis in Lung Adenocarcinomas. *Oncotarget* **2015**, *6* (32), 33878–33892. https://doi.org/10.18632/oncotarget.5302.

(25) Xiao, S.; Liu, L.; Lu, X.; Long, J.; Zhou, X.; Fang, M. The Prognostic Significance of Bromodomain PHD-Finger Transcription Factor in Colorectal Carcinoma and Association with Vimentin and E-Cadherin. *J. Cancer Res. Clin. Oncol.* **2015**, *141* (8), 1465–1474. https://doi.org/10.1007/s00432-015-1937-y.

(26) Kim, K.; Punj, V.; Choi, J.; Heo, K.; Kim, J. M.; Laird, P. W.; An, W. Gene Dysregulation by Histone Variant H2A.Z in Bladder Cancer. *Epigenetics Chromatin* **2013**, *6* (1), 34. https://doi.org/10.1186/1756-8935-6-34.

(27) Xiao, S.; Liu, L.; Fang, M.; Zhou, X.; Peng, X.; Long, J.; Lu, X. BPTF Associated with EMT Indicates Negative Prognosis in Patients with Hepatocellular Carcinoma. *Dig. Dis. Sci.* **2015**, *60* (4), 910–918. https://doi.org/10.1007/s10620-014-3411-0.

(28) Zhao, X.; Zheng, F.; Li, Y.; Hao, J.; Tang, Z.; Tian, C.; Yang, Q.; Zhu, T.; Diao, C.; Zhang, C.; Chen, M.; Hu, S.; Guo, P.; Zhang, L.; Liao, Y.; Yu, W.; Chen, M.; Zou, L.; Guo, W.; Deng, W. BPTF Promotes Hepatocellular Carcinoma Growth by Modulating HTERT Signaling and Cancer Stem Cell Traits. *Redox Biol.* **2019**, *20*, 427–441. https://doi.org/10.1016/J.REDOX.2018.10.018.

(29) Zhang, C.; Chen, L.; Liu, Y.; Huang, J.; Liu, A.; Xu, Y.; Shen, Y.; He, H.; Xu, D. Downregulated METTL14 Accumulates BPTF That Reinforces Super-Enhancers and Distal Lung Metastasis via Glycolytic Reprogramming in Renal Cell Carcinoma. *Theranostics* **2021**, *11* (8), 3676–3693. https://doi.org/10.7150/thno.55424.

(30) Richart, L.; Carrillo-de Santa Pau, E.; Río-Machín, A.; de Andrés, M. P.; Cigudosa, J. C.; Sánchez-Arévalo Lobo, V. J.; Real, F. X. BPTF Is Required for C-MYC Transcriptional Activity and in Vivo Tumorigenesis. *Nat. Commun.* **2015**, *7*. https://doi.org/10.1038/ncomms10153.

(31) Richart, L.; Real, F. X.; Sanchez-Arevalo Lobo, V. J. C-MYC Partners with BPTF in Human Cancer. *Mol. Cell. Oncol.* **2016**, *3* (3). https://doi.org/10.1080/23723556.2016.1152346.

(32) Zahid, H.; Olson, N. M.; Pomerantz, W. C. K. Opportunity Knocks for Uncovering the New Function of an Understudied Nucleosome Remodeling Complex Member, the

Bromodomain PHD Finger Transcription Factor, BPTF. *Curr. Opin. Chem. Biol.* **2021**, *63*, 57–67. https://doi.org/10.1016/j.cbpa.2021.02.003.

(33) Tamkun, J. W.; Deuring, R.; Scott, M. P.; Kissinger, M.; Pattatucci, A. M.; Kaufman, T. C.; Kennison, J. A. Brahma: A Regulator of Drosophila Homeotic Genes Structurally Related to the Yeast Transcriptional Activator SNF2SWI2. *Cell* **1992**, *68* (3), 561–572. https://doi.org/10.1016/0092-8674(92)90191-E.

(34) Filippakopoulos, P.; Picaud, S.; Mangos, M.; Keates, T.; Lambert, J.-P.; Barsyte-Lovejoy, D.; Felletar, I.; Volkmer, R.; Müller, S.; Pawson, T.; Gingras, A.-C.; Arrowsmith, C. H.; Knapp, S. Histone Recognition and Large-Scale Structural Analysis of the Human Bromodomain Family. *Cell* **2012**, *149* (1), 214–231. https://doi.org/10.1016/j.cell.2012.02.013.

(35) Pomerantz, W. C. K.; Johnson, J. A.; Ycas, P. D. Applied Biophysics for Bromodomain Drug Discovery. In *Chemical Epigenetics*; Mai, A., Ed.; Topics in Medicinal Chemistry; Springer International Publishing: Cham, 2020; pp 287–337. https://doi.org/10.1007/7355_2019_79.

(36) Jeanmougin, F.; Wurtz, J.-M.; Le Douarin, B.; Chambon, P.; Losson, R. The Bromodomain Revisited. *Trends Biochem. Sci.* **1997**, *22* (5), 151–153. https://doi.org/10.1016/S0968-0004(97)01042-6.

(37) Dhalluin, C.; Carlson, J. E.; Zeng, L.; He, C.; Aggarwal, A. K.; Zhou, M.-M. Structure and Ligand of a Histone Acetyltransferase Bromodomain. *Nature* **1999**, *399* (6735), 491–496. https://doi.org/10.1038/20974.

(38) Owen, D. J.; Ornaghi, P.; Yang, J.-C.; Lowe, N.; Evans, P. R.; Ballario, P.; Neuhaus, D.; Filetici, P.; Travers, A. A. The Structural Basis for the Recognition of Acetylated Histone H4 by the Bromodomain of Histone Acetyltransferase Gcn5p. *EMBO J.* **2000**, *19* (22), 6141–6149. https://doi.org/10.1093/emboj/19.22.6141.

(39) Vidler, L. R.; Brown, N.; Knapp, S.; Hoelder, S. Druggability Analysis and Structural Classification of Bromodomain Acetyl-Lysine Binding Sites. *J. Med. Chem.* **2012**, *55* (17), 7346–7359. https://doi.org/10.1021/jm300346w.

(40) Sharma, T. The Role of Bromodomain-Containing Proteins in Development and Disease. *Curr. Mol. Biol. Rep.* **2023**, *9* (2), 9–19. https://doi.org/10.1007/s40610-023-00152-7.

(41) Dawson, M. A.; Kouzarides, T.; Huntly, B. J. P. Targeting Epigenetic Readers in Cancer. *N. Engl. J. Med.* **2012**, *367* (7), 647–657. https://doi.org/10.1056/NEJMra1112635.

(42) Zeng, L.; Li, J.; Muller, M.; Yan, S.; Mujtaba, S.; Pan, C.; Wang, Z.; Zhou, M.-M. Selective Small Molecules Blocking HIV-1 Tat and Coactivator PCAF Association. *J. Am. Chem. Soc.* **2005**, *127* (8), 2376–2377. https://doi.org/10.1021/ja044885g.

(43) Hu, P.; Wang, X.; Zhang, B.; Zhang, S.; Wang, Q.; Wang, Z. Fluorescence Polarization for the Evaluation of Small-Molecule Inhibitors of PCAF BRD/Tat-AcK50 Association. *ChemMedChem* **2014**, *9* (5), 928–931. https://doi.org/10.1002/cmdc.201300499.

(44) Nicodeme, E.; Jeffrey, K. L.; Schaefer, U.; Beinke, S.; Dewell, S.; Chung, C.; Chandwani, R.; Marazzi, I.; Wilson, P.; Coste, H.; White, J.; Kirilovsky, J.; Rice, C. M.; Lora, J. M.; Prinjha, R. K.; Lee, K.; Tarakhovsky, A. Suppression of Inflammation by a Synthetic Histone Mimic. *Nature* **2010**, *468* (7327), 1119–1123. https://doi.org/10.1038/nature09589.

(45) Filippakopoulos, P.; Qi, J.; Picaud, S.; Shen, Y.; Smith, W. B.; Fedorov, O.; Morse, E. M.; Keates, T.; Hickman, T. T.; Felletar, I.; Philpott, M.; Munro, S.; McKeown, M. R.; Wang, Y.; Christie, A. L.; West, N.; Cameron, M. J.; Schwartz, B.; Heightman, T. D.; La Thangue, N.; French, C. A.; Wiest, O.; Kung, A. L.; Knapp, S.; Bradner, J. E. Selective Inhibition of BET Bromodomains. *Nature* **2010**, *468* (7327), 1067–1073. https://doi.org/10.1038/nature09504.

(46) Urick, A. K.; Hawk, L. M. L.; Cassel, M. K.; Mishra, N. K.; Liu, S.; Adhikari, N.; Zhang, W.; Dos Santos, C. O.; Hall, J. L.; Pomerantz, W. C. K. Dual Screening of BPTF and Brd4 Using Protein-Observed Fluorine NMR Uncovers New Bromodomain Probe Molecules. *ACS Chem Biol* **2015**, *10* (10), 2246–2256. https://doi.org/10.1021/acschembio.5b00483.

(47) Kirberger, S. E.; Ycas, P. D.; Johnson, J. A.; Chen, C.; Ciccone, M. F.; Woo, R. W. L.; Urick, A. K.; Zahid, H.; Shi, K.; Aihara, H.; McAllister, S. D.; Kashani-Sabet, M.; Shi, J.; Dickson, A.; Dos Santos, C. O.; Pomerantz, W. C. K. Selectivity, Ligand Deconstruction, and Cellular Activity Analysis of a BPTF Bromodomain Inhibitor. *Org. Biomol. Chem.* **2019**, *17* (7), 2020–2027. https://doi.org/10.1039/c8ob02599a.

(48) *TP-238*. SGC. https://www.thesgc.org/chemical-probes/TP-238 (accessed 2023-04-17).

(49) *NVS-BPTF-1*. SGC. https://www.thesgc.org/chemical-probes/NVS-BPTF-1 (accessed 2023-05-08).

(50) Lu, T.; Lu, H.; Duan, Z.; Wang, J.; Han, J.; Xiao, S.; Chen, H.; Jiang, H.; Chen, Y.; Yang, F.; Li, Q.; Chen, D.; Lin, J.; Li, B.; Jiang, H.; Chen, K.; Lu, W.; Lin, H.; Luo, C. Discovery of High-Affinity Inhibitors of the BPTF Bromodomain. *J. Med. Chem.* **2021**, *64* (16), 12075–12088. https://doi.org/10.1021/acs.jmedchem.1c00721.

(51) Lu, H.; Lu, T.; Zu, S.; Duan, Z.; Guang, Y.; Li, Q.; Ma, J.; Chen, D.; Li, B.; Lu, W.; Jiang, H.; Luo, C.; Ye, D.; Chen, K.; Lin, H. Discovery of a Highly Potent CECR2 Bromodomain Inhibitor with 7H-Pyrrolo[2,3-d] Pyrimidine Scaffold. *Bioorganic Chem.* **2022**, *123*, 105768. https://doi.org/10.1016/j.bioorg.2022.105768.

(52) Ycas, P. D.; Zahid, H.; Chan, A.; Olson, N. M.; Johnson, J. A.; Talluri, S. K.; Schonbrunn, E.; Pomerantz, W. C. K. New Inhibitors for the BPTF Bromodomain Enabled by Structural Biology and Biophysical Assay Development. *Org. Biomol. Chem.* **2020**. https://doi.org/10.1039/D0OB00506A.

(53) Johnson, J. A.; Nicolaou, C. A.; Kirberger, S. E.; Pandey, A. K.; Hu, H.; Pomerantz, W. C. K. Evaluating the Advantages of Using 3D-Enriched Fragments for Targeting BET Bromodomains. *ACS Med. Chem. Lett.* **2019**, *10* (12), 1648–1654. https://doi.org/10.1021/acsmedchemlett.9b00414.

(54) Humphreys, P. G.; Bamborough, P.; Chung, C.; Craggs, P. D.; Gordon, L.; Grandi, P.; Hayhow, T. G.; Hussain, J.; Jones, K. L.; Lindon, M.; Michon, A.-M.; Renaux, J. F.; Suckling, C. J.; Tough, D. F.; Prinjha, R. K. Discovery of a Potent, Cell Penetrant, and Selective P300/CBP-Associated Factor (PCAF)/General Control Nonderepressible 5 (GCN5) Bromodomain Chemical Probe. *J. Med. Chem.* **2017**, *60* (2), 695–709. https://doi.org/10.1021/acs.jmedchem.6b01566.

(55) Zahid, H.; Buchholz, C. R.; Singh, M.; Ciccone, M. F.; Chan, A.; Nithianantham, S.; Shi, K.; Aihara, H.; Fischer, M.; Schönbrunn, E.; dos Santos, C. O.; Landry, J. W.; Pomerantz, W. C. K. New Design Rules for Developing Potent Cell-Active Inhibitors of the Nucleosome Remodeling Factor (NURF) via BPTF Bromodomain Inhibition. *J. Med. Chem.* **2021**, *64* (18), 13902–13917. https://doi.org/10.1021/acs.jmedchem.1c01294.

(56) Xiong, L.; Mao, X.; Guo, Y.; Zhou, Y.; Chen, M.; Chen, P.; Yang, S.; Li, L. Discovery of Selective BPTF Bromodomain Inhibitors by Screening and Structure-Based Optimization. *Biochem. Biophys. Res. Commun.* **2021**, *545*, 125–131. https://doi.org/10.1016/j.bbrc.2021.01.067.

(57) Martinelli, P.; Schaaf, O.; Mantoulidis, A.; Martin, L. J.; Fuchs, J. E.; Bader, G.; Gollner, A.; Wolkerstorfer, B.; Rogers, C.; Balıkçı, E.; Lipp, J. J.; Mischerikow, N.; Doebel, S.; Gerstberger, T.; Sommergruber, W.; Huber, K. V. M.; Böttcher, J. Discovery of a Chemical Probe to Study Implications of BPTF Bromodomain Inhibition in Cellular and in Vivo Experiments. *ChemMedChem* **2023**, *18* (6), e202200686. https://doi.org/10.1002/cmdc.202200686.

(58) Schindler, U.; Beckmann, H.; Cashmore, A. R. HAT3.1, a Novel Arabidopsis Homeodomain Protein Containing a Conserved Cysteine-Rich Region. *Plant J.* **1993**, *4* (1), 137–150. https://doi.org/10.1046/j.1365-313X.1993.04010137.x.

(59) Sbardella, G. Methyl-Readers and Inhibitors. In *Chemical Epigenetics;* Mai, A., Ed.; Topics in Medicinal Chemistry; Springer International Publishing: Cham, 2020; pp 339–399. https://doi.org/10.1007/7355_2019_78.

(60) Sanchez, R.; Zhou, M.-M. The PHD Finger: A Versatile Epigenome Reader. *Trends Biochem. Sci.* **2011**, *36* (7), 364–372. https://doi.org/10.1016/j.tibs.2011.03.005.

(61) Shi, X.; Hong, T.; Walter, K. L.; Ewalt, M.; Michishita, E.; Hung, T.; Carney, D.; Peña, P.; Lan, F.; Kaadige, M. R.; Lacoste, N.; Cayrou, C.; Davrazou, F.; Saha, A.; Cairns, B. R.; Ayer, D. E.; Kutateladze, T. G.; Shi, Y.; Côté, J.; Chua, K. F.; Gozani, O. ING2 PHD Domain Links Histone H3 Lysine 4 Methylation to Active Gene Repression. *Nature* **2006**, *442* (7098), 96–99. https://doi.org/10.1038/nature04835.

(62) Musselman, C. A.; Kutateladze, T. G. Handpicking Epigenetic Marks with PHD Fingers. *Nucleic Acids Res.* **2011**, *39* (21), 9061–9071. https://doi.org/10.1093/nar/gkr613.

(63) Li, H.; Ilin, S.; Wang, W.; Duncan, E. M.; Wysocka, J.; Allis, C. D.; Patel, D. J. Molecular Basis for Site-Specific Read-out of Histone H3K4me3 by the BPTF PHD Finger of NURF. *Nature* **2006**, *442* (7098), 91–95. https://doi.org/10.1038/nature04802.

(64) Baker, L. A.; Allis, C. D.; Wang, G. G. PHD Fingers in Human Diseases: Disorders Arising from Misinterpreting Epigenetic Marks. *Mutat. Res.* **2008**, *647* (1–2), 3–12. https://doi.org/10.1016/j.mrfmmm.2008.07.004.

(65) de Rooij, J. D. E.; Masetti, R.; van den Heuvel-Eibrink, M. M.; Cayuela, J.-M.; Trka, J.; Reinhardt, D.; Rasche, M.; Sonneveld, E.; Alonzo, T. A.; Fornerod, M.; Zimmermann, M.; Pigazzi, M.; Pieters, R.; Meshinchi, S.; Zwaan, C. M.; Locatelli, F. Recurrent Abnormalities Can Be Used for Risk Group Stratification in Pediatric AMKL: A Retrospective Intergroup Study. *Blood* **2016**, *127* (26), 3424–3430. https://doi.org/10.1182/blood-2016-01-695551.

(66) Gough, S. M.; Lee, F.; Yang, F.; Walker, R. L.; Zhu, Y. J.; Pineda, M.; Onozawa, M.; Chung, Y. J.; Bilke, S.; Wagner, E. K.; Denu, J. M.; Ning, Y.; Xu, B.; Wang, G. G.; Meltzer, P. S.; Aplan, P. D. NUP98–PHF23 Is a Chromatin-Modifying Oncoprotein That Causes a Wide Array of Leukemias Sensitive to Inhibition of PHD Histone Reader Function. *Cancer Discov.* **2014**, *4* (5), 564–577. https://doi.org/10.1158/2159-8290.CD-13-0419.

(67) Roussy, M.; Bilodeau, M.; Jouan, L.; Tibout, P.; Laramée, L.; Lemyre, E.; Léveillé, F.; Tihy, F.; Cardin, S.; Sauvageau, C.; Couture, F.; Louis, I.; Choblet, A.; Patey, N.; Gendron, P.; Duval, M.; Teira, P.; Hébert, J.; Wilhelm, B. T.; Choi, J. K.; Gruber, T. A.; Bittencourt, H.; Cellot, S. NUP98-BPTF Gene Fusion Identified in Primary Refractory Acute Megakaryoblastic Leukemia of Infancy. *Genes. Chromosomes Cancer* **2018**, *57* (6), 311–319. https://doi.org/10.1002/gcc.22532.

(68) Kawaguchi, K.; Azumi, S.; Itakura, Y.; Takachi, T.; Ogura, T.; Horikoshi, Y.; Suzuki, K.; Muramatsu, H.; Hama, A.; Takahashi, Y.; Watanabe, K. Acquisition of a Rare NUP98–BPTF Fusion Gene Associated with Recurrence of Acute Myeloid Leukemia. *Pediatr. Blood Cancer* **2021**, e29201. https://doi.org/10.1002/PBC.29201.

(69) Zhang, Y.; Guo, Y.; Gough, S. M.; Zhang, J.; Vann, K. R.; Li, K.; Cai, L.; Shi, X.; Aplan, P. D.; Greg Wang, G.; Kutateladze, T. G. Mechanistic Insights into Chromatin Targeting by Leukemic NUP98-PHF23 Fusion. *Nat. Commun.* **2020**, *11* (3339). https://doi.org/10.1038/s41467-020-17098-4.

(70) Santiago, C.; Nguyen, K.; Schapira, M. Druggability of Methyl-Lysine Binding Sites. *J. Comput. Aided Mol. Des.* **2011**, *25* (12), 1171–1178. https://doi.org/10.1007/s10822-011-9505-2.

(71) Wagner, E. K.; Nath, N.; Flemming, R.; Feltenberger, J. B.; Denu, J. M. Identification and Characterization of Small Molecule Inhibitors of a PHD Finger. *Biochemistry* **2012**, *51* (41), 8293. https://doi.org/10.1021/BI3009278.

(72) Bhushan, B.; Erdmann, A.; Zhang, Y.; Belle, R.; Johannson, C.; Oppermann, U.; Hopkinson, R. J.; Schofield, C. J.; Kawamura, A. Investigations on Small Molecule Inhibitors Targeting the Histone H3K4 Tri-Methyllysine Binding PHD-Finger of JmjC Histone Demethylases. *Bioorg. Med. Chem.* **2018**, *26* (11), 2984–2991. https://doi.org/10.1016/J.BMC.2018.03.030.

(73) Miller, T. C. R.; Rutherford, T. J.; Birchall, K.; Chugh, J.; Fiedler, M.; Bienz, M. Competitive Binding of a Benzimidazole to the Histone-Binding Pocket of the Pygo PHD Finger. *ACS Chem. Biol.* **2014**, *9* (12), 2864–2874. https://doi.org/10.1021/CB500585S/SUPPL_FILE/CB500585S_SI_001.PDF.

(74) Amato, A.; Lucas, X.; Bortoluzzi, A.; Wright, D.; Ciulli, A. Targeting Ligandable Pockets on Plant Homeodomain (PHD) Zinc Finger Domains by a Fragment-Based Approach. *ACS Chem. Biol.* **2018**, *13* (4), 915–921. https://doi.org/10.1021/acschembio.7b01093.

(75) Ali, M.; Daze, K. D.; Strongin, D. E.; Rothbart, S. B.; Rincon-Arano, H.; Allen, H. F.; Li, J.; Strahl, B. D.; Hof, F.; Kutateladze, T. G. Molecular Insights into Inhibition of the Methylated Histone-Plant Homeodomain Complexes by Calixarenes. *J. Biol. Chem.* **2015**, *290* (38), 22919–22930. https://doi.org/10.1074/jbc.M115.669333.

(76) Bosse, R.; Illy, C.; Chelsky, D. Principles of AlphaScreen.

(77) *The Hook Effect | Application Support Knowledgebase | Lab Products & Services*. PerkinElmer. https://www.perkinelmer.com/lab-products-and-services/application-support-knowledgebase/alphalisa-alphascreen-no-wash-assays/hook-effect.html (accessed 2023-05-12).

(78) Gossert, A. D.; Jahnke, W. NMR in Drug Discovery: A Practical Guide to Identification and Validation of Ligands Interacting with Biological Macromolecules. *Prog. Nucl. Magn. Reson. Spectrosc.* **2016**, *97*, 82–125. https://doi.org/10.1016/j.pnmrs.2016.09.001.

(79) Kalra, P.; Zahid, H.; Ayoub, A.; Dou, Y.; Pomerantz, W. C. K. Alternative Mechanisms for DNA Engagement by BET Bromodomain-Containing Proteins. *Biochemistry* **2022**, *61* (13), 1260–1272. https://doi.org/10.1021/acs.biochem.2c00157.

(80) Struck, H. C.; Plattner, E. B. A Study of the Pharmacological Properties of Certain Saturated Fluorocarbons. *J. Pharmacol. Exp. Ther.* **1940**, *68* (2), 217–219.

(81) Alauddin, M. M. Positron Emission Tomography (PET) Imaging with (18)F-Based Radiotracers. *Am. J. Nucl. Med. Mol. Imaging* **2012**, *2* (1), 55–76.

(82) Ruiz-Cabello, J.; Barnett, B. P.; Bottomley, P. A.; Bulte, J. W. M. Fluorine (19F) MRS and MRI in Biomedicine. *NMR Biomed.* **2011**, *24* (2), 114–129. https://doi.org/10.1002/nbm.1570.

(83) Gimenez, D.; Phelan, A.; Murphy, C. D.; Cobb, S. L. 19 F NMR as a Tool in Chemical Biology. *Beilstein J. Org. Chem.* **2021**, *17*, 293–318. https://doi.org/10.3762/bjoc.17.28.

(84) Müller, K.; Faeh, C.; Diederich, F. Fluorine in Pharmaceuticals: Looking beyond Intuition. *Science* **2007**, *317* (5846), 1881–1886. https://doi.org/10.1126/science.1131943.

(85) Lemal, D. M. Perspective on Fluorocarbon Chemistry. *J. Org. Chem.* **2004**, *69* (1), 1–11. https://doi.org/10.1021/jo0302556.

(86) Huchet, Q. A.; Kuhn, B.; Wagner, B.; Kratochwil, N. A.; Fischer, H.; Kansy, M.; Zimmerli, D.; Carreira, E. M.; Müller, K. Fluorination Patterning: A Study of Structural Motifs That Impact Physicochemical Properties of Relevance to Drug Discovery. *J. Med. Chem.* **2015**, *58* (22), 9041–9060. https://doi.org/10.1021/acs.jmedchem.5b01455.

(87) Gillis, E. P.; Eastman, K. J.; Hill, M. D.; Donnelly, D. J.; Meanwell, N. A. Applications of Fluorine in Medicinal Chemistry. *J. Med. Chem.* **2015**, *58* (21), 8315–8359. https://doi.org/10.1021/acs.jmedchem.5b00258.

(88) Dunitz, J. D.; Taylor, R. Organic Fluorine Hardly Ever Accepts Hydrogen Bonds. *Chem. - Eur. J.* **1997**, *3* (1), 89–98. https://doi.org/10.1002/chem.19970030115.

(89) Mullard, A. 2011 FDA Drug Approvals. *Nat. Rev. Drug Discov.* **2012**, *11* (2), 91–94. https://doi.org/10.1038/nrd3657.

(90) G. de la Torre, B.; Albericio, F. The Pharmaceutical Industry in 2018. An Analysis of FDA Drug Approvals from the Perspective of Molecules. *Molecules* **2019**, *24* (4), 809. https://doi.org/10.3390/molecules24040809.

(91) *Novel Drug Approvals for 2019 | FDA*. https://www.fda.gov/drugs/new-drugs-fda-cders-new-molecular-entities-and-new-therapeutic-biological-products/novel-drug-approvals-2019 (accessed 2021-03-23).

(92) *Novel Drug Approvals for 2020 | FDA*. https://www.fda.gov/drugs/new-drugs-fda-cders-new-molecular-entities-and-new-therapeutic-biological-products/novel-drug-approvals-2020 (accessed 2021-03-23).

(93) Liu, Z.; Li, J.; Li, S.; Li, G.; Sharpless, K. B.; Wu, P. SuFEx Click Chemistry Enabled Late-Stage Drug Functionalization. *J. Am. Chem. Soc.* **2018**, *140* (8), 2919–2925. https://doi.org/10.1021/jacs.7b12788.

(94) Gouverneur, V.; Seppelt, K. Introduction: Fluorine Chemistry. *Chem. Rev.* **2015**, *115* (2), 563–565. https://doi.org/10.1021/cr500686k.

(95) Dalvit, C.; Vulpetti, A. Ligand-Based Fluorine NMR Screening: Principles and Applications in Drug Discovery Projects. *J. Med. Chem.* **2019**, *62* (5), 2218–2244. https://doi.org/10.1021/acs.jmedchem.8b01210.

(96) Dalvit, C. Ligand- and Substrate-Based 19F NMR Screening: Principles and Applications to Drug Discovery. *Prog. Nucl. Magn. Reson. Spectrosc.* **2007**, *51* (4), 243–271. https://doi.org/10.1016/j.pnmrs.2007.07.002.

(97) Dalvit, C.; Veronesi, M.; Vulpetti, A. Fluorine NMR Functional Screening: From Purified Enzymes to Human Intact Living Cells. *J. Biomol. NMR* **2020**, *74*, 613–631. https://doi.org/10.1007/s10858-020-00311-3.

(98) Arntson, K. E.; Pomerantz, W. C. K. Protein-Observed Fluorine NMR: A Bioorthogonal Approach for Small Molecule Discovery. *J. Med. Chem.* **2016**, *59* (11), 5158–5171. https://doi.org/10.1021/acs.jmedchem.5b01447.

(99) Divakaran, A.; Kirberger, S. E.; Pomerantz, W. C. K. SAR by (Protein-Observed) 19F NMR. *Acc. Chem. Res.* **2019**, *52* (12), 3407–3418. https://doi.org/10.1021/acs.accounts.9b00377.

(100) Norton, R. S.; Leung, E. W. W.; Chandrashekaran, I. R.; MacRaild, C. A. Applications of 19F-NMR in Fragment-Based Drug Discovery. *Molecules* **2016**, *21* (7), 860. https://doi.org/10.3390/molecules21070860.

(101) Dickinson, W. C. Dependence of the F19 Nuclear Resonance Position on Chemical Compound [32]. *Phys. Rev.* **1950**, *77* (5), 736–737. https://doi.org/10.1103/PhysRev.77.736.2.

(102) Gutowsky, H. S.; Hoffman, C. J. Chemical Shifts in the Magnetic Resonance of F19. *Phys. Rev.* **1950**, *80* (1), 110–111. https://doi.org/10.1103/PhysRev.80.110.

(103) Spotswood, T. M. L.; Evans, J. M.; Richards, J. H. Enzyme-Substrate Interaction by Nuclear Magnetic Resonance. *J. Am. Chem. Soc.* **1967**, *89* (19), 5052–5054. https://doi.org/10.1021/ja00995a047.

(104) Mitchell, H. K.; Niemann, C. The Competitive Inhibition of the Metabolism of α-Amino Acids by Their Halogenated Analogs. *J. Am. Chem. Soc.* **1947**, *69* (5), 1232. https://doi.org/10.1021/ja01197a525.

(105) Atkinson, D. E.; Melvin, S.; Fox, S. W. Effects of P-Fluorophenylalanine on the Growth of Lactobacillus Arabinosus. *Arch. Biochem. Biophys.* **1951**, *31* (2), 205–211. https://doi.org/10.1016/0003-9861(51)90207-X.

(106) Westhead, E. W.; Boyer, P. D. The Incorporation of P-Fluorophenylalanine into Some Rabbit Enzymes and Other Proteins. *Biochim Biophys Acta* **1961**, *54*, 45–50.

(107) Hull, W. E.; Sykes, B. D. Fluorotyrosine Alkaline Phosphatase. 19F Nuclear Magnetic Resonance Relaxation Times and Molecular Motion of the Individual Fluorotyrosines. *Biochemistry* **1974**, *13* (17), 3431–3437. https://doi.org/10.1021/bi00714a002.

(108) Dalvit, C.; Ardini, E.; Flocco, M.; Fogliatto, G. P.; Mongelli, N.; Veronesi, M. A General NMR Method for Rapid, Efficient, and Reliable Biochemical Screening. *J. Am. Chem. Soc.* **2003**, *125* (47), 14620–14625. https://doi.org/10.1021/ja038128e.

(109) Dalvit, C.; Fagerness, P. E.; Hadden, D. T. A.; Sarver, R. W.; Stockman, B. J. Fluorine-NMR Experiments for High-Throughput Screening: Theoretical Aspects, Practical Considerations, and Range of Applicability. *J. Am. Chem. Soc.* **2003**, *125* (25), 7696–7703. https://doi.org/10.1021/ja034646d.

(110) Dalvit, C.; Flocco, M.; Veronesi, M.; Stockman, B. J. Fluorine-NMR Competition Binding Experiments for High-Throughput Screening of Large Compound Mixtures. *Comb. Chem. High Throughput Screen.* **2002**, *5* (8), 605–611. https://doi.org/10.2174/1386207023329923.

(111) Danielson, M. A.; Falke, J. J. Use of 19F NMR to Probe Protein Structure and Conformational Changes. *Annu. Rev. Biophys. Biomol. Struct.* **1996**, *25*, 163–195. https://doi.org/10.1146/annurev.bb.25.060196.001115.

(112) Hull, W. E.; Sykes, B. D. Fluorotyrosine Alkaline Phosphatase: Internal Mobility of Individual Tyrosines and the Role of Chemical Shift Anisotropy as a 19F Nuclear Spin Relaxation Mechanism in Proteins. *J. Mol. Biol.* **1975**, *98* (1), 121–153. https://doi.org/10.1016/S0022-2836(75)80105-7.

(113) Liu, J. J.; Horst, R.; Katritch, V.; Stevens, R. C.; Wüthrich, K. Biased Signaling Pathways in B2-Adrenergic Receptor Characterized by 19F-NMR. *Science* **2012**, *335* (6072), 1106–1110. https://doi.org/10.1126/science.1215802.

(114) Pomerantz, W. C.; Wang, N.; Lipinski, A. K.; Wang, R.; Cierpicki, T.; Mapp, A. K. Profiling the Dynamic Interfaces of Fluorinated Transcription Complexes for Ligand Discovery and Characterization. *ACS Chem. Biol.* **2012**, *7* (8), 1345–1350. https://doi.org/10.1021/cb3002733.

(115) Boeszoermenyi, A.; Chhabra, S.; Dubey, A.; Radeva, D. L.; Burdzhiev, N. T.; Chanev, C. D.; Petrov, O. I.; Gelev, V. M.; Zhang, M.; Anklin, C.; Kovacs, H.; Wagner, G.; Kuprov, I.; Takeuchi, K.; Arthanari, H. Aromatic 19F-13C TROSY: A Background-Free Approach to Probe Biomolecular Structure, Function, and Dynamics. *Nat. Methods* **2019**, *16*, 333–340. https://doi.org/10.1038/s41592-019-0334-x.

(116) Li, C.; Wang, G. F.; Wang, Y.; Creager-Allen, R.; Lutz, E. A.; Scronce, H.; Slade, K. M.; Ruf, R. A. S.; Mehl, R. A.; Pielak, G. J. Protein 19F NMR in Escherichia Coli. *J. Am. Chem. Soc.* **2010**, *132* (1), 321–327. https://doi.org/10.1021/ja907966n.

(117) Ye, Y.; Li, C. Chapter 8. 19 F In-Cell NMR. In *In-cell NMR Spectroscopy: From Molecular Sciences to Cell Biology*; 2019; pp 117–130. https://doi.org/10.1039/9781788013079-00117.

(118) Kemp, W. Fluorine-19 NMR Spectra. In *NMR in Chemistry*; Macmillan Education UK, 1986; pp 169–175. https://doi.org/10.1007/978-1-349-18348-7_9.

(119) Vulpetti, A.; Dalvit, C. Design and Generation of Highly Diverse Fluorinated Fragment Libraries and Their Efficient Screening with Improved ^{19} F NMR Methodology. *ChemMedChem* **2013**, *8* (12), 2057–2069. https://doi.org/10.1002/cmdc.201300351.

(120) Urick, A. K.; Calle, L. P.; Espinosa, J. F.; Hu, H.; Pomerantz, W. C. K. Protein-Observed Fluorine NMR Is a Complementary Ligand Discovery Method to 1 H CPMG Ligand-Observed NMR. *ACS Chem. Biol.* **2016**, *11* (11), 3154–3164. https://doi.org/10.1021/acschembio.6b00730.

(121) Gerig, J. T. Fluorine NMR of Proteins. *Prog. Nucl. Magn. Reson. Spectrosc.* **1994**, *26* (PART 4), 293–370. https://doi.org/10.1016/0079-6565(94)80009-X.

(122) Kitevski-LeBlanc, J. L.; Evanics, F.; Prosser, R. S. Approaches for the Measurement of Solvent Exposure in Proteins by 19 F NMR. *J Biomol NMR* **2009**, *45* (3), 255–264. https://doi.org/10.1007/s10858-009-9359-2.

(123) Dahanayake, J. N.; Kasireddy, C.; Karnes, J. P.; Verma, R.; Steinert, R. M.; Hildebrandt, D.; Hull, O. A.; Ellis, J. M.; Mitchell-Koch, K. R. Progress in Our Understanding of 19F Chemical Shifts. *Annu. Rep. NMR Spectrosc.* **2018**, *93,* 281–365. https://doi.org/10.1016/bs.arnmr.2017.08.002.

(124) Saunders, C.; Khaled, M. B.; Weaver, J. D.; Tantillo, D. J. Prediction of 19 F NMR Chemical Shifts for Fluorinated Aromatic Compounds. *J Org Chem* **2018**, *83* (6), 3220–3225. https://doi.org/10.1021/acs.joc.8b00104.

(125) Pearson, J. G.; Oldfield, E.; Lee, F. S.; Warshel, A. Chemical Shifts in Proteins: A Shielding Trajectory Analysis of the Fluorine Nuclear Magnetic Resonance Spectrum of the Escherichia Coli Galactose Binding Protein Using a Multipole Shielding Polarizability-Local Reaction Field-Molecular Dynamics Approach. *J. Am. Chem. Soc.* **1993**, *115* (15), 6851–6862. https://doi.org/10.1021/ja00068a049.

(126) Lau, E. Y.; Gerig, J. T. Origins of Fluorine NMR Chemical Shifts in Fluorine-Containing Proteins. *J. Am. Chem. Soc.* **2000**, *122* (18), 4408–4417. https://doi.org/10.1021/ja992107w.

(127) Isley, W. C.; Urick, A. K.; Pomerantz, W. C. K.; Cramer, C. J. Prediction of 19F NMR Chemical Shifts in Labeled Proteins: Computational Protocol and Case Study. *Mol. Pharm.* **2016**, *13* (7), 2376–2386. https://doi.org/10.1021/acs.molpharmaceut.6b00137.

(128) Gerig, J. T. *Fluorine NMR*. SelfPublished.

(129) Nußbaumer, F.; Plangger, R.; Roeck, M.; Kreutz, C. Aromatic ^{19}F–^{13}C TROSY—[^{19}F, ^{13}C]-Pyrimidine Labeling for NMR Spectroscopy of RNA. *Angew. Chem. Int. Ed.* **2020**, *59* (39), 17062–17069. https://doi.org/10.1002/anie.202006577.

(130) Klein, B. A.; Sykes, B. D. Feasibility of Trifluoromethyl TROSY NMR at High Magnetic Fields. *J. Biomol. NMR* **2019**, *73* (10–11), 519–523. https://doi.org/10.1007/s10858-019-00266-0.

(131) Shuker, S. B.; Hajduk, P. J.; Meadows, R. P.; Fesik, S. W. Discovering High-Affinity Ligands for Proteins: SAR by NMR. *Science* **1996**, *274* (5292), 1531–1534. https://doi.org/10.1126/science.274.5292.1531.

(132) Dalvit, C.; Flocco, M.; Knapp, S.; Mostardini, M.; Perego, R.; Stockman, B. J.; Veronesi, M.; Varasi, M. High-Throughput NMR-Based Screening with Competition Binding Experiments. *J. Am. Chem. Soc.* **2002**, *124* (26), 7702–7709. https://doi.org/10.1021/ja020174b.

(133) Tsai, J.; Lee, J. T.; Wang, W.; Zhang, J.; Cho, H.; Mamo, S.; Bremer, R.; Gillette, S.; Kong, J.; Haass, N. K.; Sproesser, K.; Li, L.; Smalley, K. S. M.; Fong, D.; Zhu, Y. L.; Marimuthu, A.; Nguyen, H.; Lam, B.; Liu, J.; Cheung, I.; Rice, J.; Suzuki, Y.; Luu, C.; Settachatgul, C.; Shellooe, R.; Cantwell, J.; Kim, S. H.; Schlessinger, J.; Zhang, K. Y. J.; West, B. L.; Powell, B.; Habets, G.; Zhang, C.; Ibrahim, P. N.; Hirth, P.; Artis, D. R.; Herlyn, M.; Bollag, G. Discovery of a Selective Inhibitor of Oncogenic B-Raf Kinase with Potent Antimelanoma Activity. *Proc. Natl. Acad. Sci. U. S. A.* **2008**, *105* (8), 3041–3046. https://doi.org/10.1073/pnas.0711741105.

(134) Souers, A. J.; Leverson, J. D.; Boghaert, E. R.; Ackler, S. L.; Catron, N. D.; Chen, J.; Dayton, B. D.; Ding, H.; Enschede, S. H.; Fairbrother, W. J.; Huang, D. C. S.; Hymowitz, S. G.; Jin, S.; Khaw, S. L.; Kovar, P. J.; Lam, L. T.; Lee, J.; Maecker, H. L.; Marsh, K. C.; Mason, K. D.; Mitten, M. J.; Nimmer, P. M.; Oleksijew, A.; Park, C. H.; Park, C. M.; Phillips, D. C.; Roberts, A. W.; Sampath, D.; Seymour, J. F.; Smith, M. L.; Sullivan, G. M.; Tahir, S. K.; Tse, C.; Wendt, M. D.; Xiao, Y.; Xue, J. C.; Zhang, H.; Humerickhouse, R. A.; Rosenberg, S. H.; Elmore, S. W. ABT-199, a Potent and Selective BCL-2 Inhibitor, Achieves Antitumor Activity While Sparing Platelets. *Nat. Med.* **2013**, *19* (2), 202–208. https://doi.org/10.1038/nm.3048.

(135) Murray, C. W.; Newell, D. R.; Angibaud, P. A Successful Collaboration between Academia, Biotech and Pharma Led to Discovery of Erdafitinib, a Selective FGFR Inhibitor Recently Approved by the FDA. *MedChemComm* **2019**, *10* (9), 1509–1511. https://doi.org/10.1039/c9md90044f.

(136) Tap, W. D.; Wainberg, Z. A.; Anthony, S. P.; Ibrahim, P. N.; Zhang, C.; Healey, J. H.; Chmielowski, B.; Staddon, A. P.; Cohn, A. L.; Shapiro, G. I.; Keedy, V. L.; Singh, A. S.; Puzanov, I.; Kwak, E. L.; Wagner, A. J.; Von Hoff, D. D.; Weiss, G. J.; Ramanathan, R. K.; Zhang, J.; Habets, G.; Zhang, Y.; Burton, E. A.; Visor, G.; Sanftner, L.; Severson, P.; Nguyen, H.; Kim, M. J.; Marimuthu, A.; Tsang, G.; Shellooe, R.; Gee, C.; West, B. L.; Hirth, P.; Nolop, K.; van de Rijn, M.; Hsu, H. H.; Peterfy, C.; Lin, P. S.; Tong-Starksen, S.; Bollag, G. Structure-Guided Blockade of CSF1R Kinase in Tenosynovial Giant-Cell

Tumor. *N. Engl. J. Med.* **2015**, *373* (5), 428–437. https://doi.org/10.1056/nejmoa1411366.

(137) Bohacek, R. S.; McMartin, C.; Guida, W. C. The Art and Practice of Structure-Based Drug Design: A Molecular Modeling Perspective. *Med. Res. Rev.* **1996**, *16* (1), 3–50. https://doi.org/10.1002/(SICI)1098-1128(199601)16:1<3::AID-MED1>3.0.CO;2-6.

(138) Kitevski-LeBlanc, J. L.; Prosser, R. S. Current Applications of 19F NMR to Studies of Protein Structure and Dynamics. *Prog. Nucl. Magn. Reson. Spectrosc.* **2012**, *62*, 1–33. https://doi.org/10.1016/j.pnmrs.2011.06.003.

(139) Marsh, E. N. G.; Suzuki, Y. Using 19F NMR to Probe Biological Interactions of Proteins and Peptides. *ACS Chem. Biol.* **2014**, *9* (6), 1242–1250. https://doi.org/10.1021/cb500111u.

(140) Jordan, J. B.; Poppe, L.; Xia, X.; Cheng, A. C.; Sun, Y.; Michelsen, K.; Eastwood, H.; Schnier, P. D.; Nixey, T.; Zhong, W. Fragment Based Drug Discovery: Practical Implementation Based on 19F NMR Spectroscopy. *J. Med. Chem.* **2012**, *55* (2), 678–687. https://doi.org/10.1021/jm201441k.

(141) Troelsen, N. S.; Shanina, E.; Gonzalez-Romero, D.; Danková, D.; Jensen, I. S. A.; Śniady, K. J.; Nami, F.; Zhang, H.; Rademacher, C.; Cuenda, A.; Gotfredsen, C. H.; Clausen, M. H. The 3F Library: Fluorinated Fsp ^{3} -Rich Fragments for Expeditious ^{19} F NMR Based Screening. *Angew. Chem. Int. Ed.* **2020**, *59* (6), 2204–2210. https://doi.org/10.1002/anie.201913125.

(142) Lingel, A.; Vulpetti, A.; Reinsperger, T.; Proudfoot, A.; Denay, R.; Frommlet, A.; Henry, C.; Hommel, U.; Gossert, A. D.; Luy, B.; Frank, A. O. Comprehensive and High-Throughput Exploration of Chemical Space Using Broadband 19F NMR-Based Screening. *Angew. Chem.* **2020**, *132* (35), 14919–14927. https://doi.org/10.1002/ange.202002463.

(143) Rüdisser, S. H.; Goldberg, N.; Ebert, M. O.; Kovacs, H.; Gossert, A. D. Efficient Affinity Ranking of Fluorinated Ligands by 19F NMR: CSAR and FastCSAR. *J. Biomol. NMR* **2020**, *74*, 579–594. https://doi.org/10.1007/s10858-020-00325-x.

(144) Dalvit, C.; Parent, A.; Vallée, F.; Mathieu, M.; Rak, A. Fast NMR Methods for Measuring in the Direct and/or Competition Mode the Dissociation Constants of Chemical Fragments Interacting with a Receptor. *ChemMedChem* **2019**, *14* (11), 1115–1127. https://doi.org/10.1002/cmdc.201900152.

(145) Dalvit, C.; Vulpetti, A. Technical and Practical Aspects of 19F NMR-based Screening: Toward Sensitive High-throughput Screening with Rapid Deconvolution. *Magn. Reson. Chem.* **2012**, *50* (9), 592–597. https://doi.org/10.1002/MRC.3842.

(146) Veronesi, M.; Giacomina, F.; Romeo, E.; Castellani, B.; Ottonello, G.; Lambruschini, C.; Garau, G.; Scarpelli, R.; Bandiera, T.; Piomelli, D.; Dalvit, C. Fluorine Nuclear Magnetic

Resonance-Based Assay in Living Mammalian Cells. *Anal. Biochem.* **2016**, *495*, 52–59. https://doi.org/10.1016/j.ab.2015.11.015.

(147) Veronesi, M.; Romeo, E.; Lambruschini, C.; Piomelli, D.; Bandiera, T.; Scarpelli, R.; Garau, G.; Dalvit, C. Fluorine NMR-Based Screening on Cell Membrane Extracts. *ChemMedChem* **2014**, *9* (2), 286–289. https://doi.org/10.1002/cmdc.201300438.

(148) Carr, H. Y.; Purcell, E. M. Effects of Diffusion on Free Precession in Nuclear Magnetic Resonance Experiments. *Phys. Rev.* **1954**, *94* (3), 630–638. https://doi.org/10.1103/PhysRev.94.630.

(149) Meiboom, S.; Gill, D. Modified Spin-Echo Method for Measuring Nuclear Relaxation Times. *Rev. Sci. Instrum.* **1958**, *29* (8), 688–691. https://doi.org/10.1063/1.1716296.

(150) Gerig, J. T. Fluorine Nuclear Magnetic Resonance of Fluorinated Ligands. *Methods Enzymol.* **1989**, *177*, 3–23. https://doi.org/10.1016/0076-6879(89)77003-8.

(151) De Castro, G. V.; Ciulli, A. Spy: Vs. Spy: Selecting the Best Reporter for 19F NMR Competition Experiments. *Chem. Commun.* **2019**, *55* (10), 1482–1485. https://doi.org/10.1039/c8cc09790a.

(152) Alen, J.; Schade, M.; Wagener, M.; Christian, F.; Nordhoff, S.; Merla, B.; Dunkern, T. R.; Bahrenberg, G.; Ratcliffe, P. Fragment-Based Discovery of Novel Potent Sepiapterin Reductase Inhibitors. *J. Med. Chem.* **2019**, *62* (13), 6391–6397. https://doi.org/10.1021/acs.jmedchem.9b00218.

(153) Dalvit, C.; Vulpetti, A. Fluorine-Protein Interactions and 19F NMR Isotropic Chemical Shifts: An Empirical Correlation with Implications for Drug Design. *ChemMedChem* **2011**, *6* (1), 104–114. https://doi.org/10.1002/cmdc.201000412.

(154) Garavís, M.; López-Méndez, B.; Somoza, A.; Oyarzabal, J.; Dalvit, C.; Villasante, A.; Campos-Olivas, R.; González, C. Discovery of Selective Ligands for Telomeric RNA G-Quadruplexes (TERRA) through 19F-NMR Based Fragment Screening. *ACS Chem. Biol.* **2014**, *9* (7), 1559–1566. https://doi.org/10.1021/cb500100z.

(155) Binas, O.; Jesus, V.; Landgraf, T.; Völklein, A. E.; Martins, J.; Hymon, D.; Kaur Bains, J.; Berg, H.; Biedenbänder, T.; Fürtig, B.; Lakshmi Gande, S.; Niesteruk, A.; Oxenfarth, A.; Shahin Qureshi, N.; Schamber, T.; Schnieders, R.; Tröster, A.; Wacker, A.; Wirmer-Bartoschek, J.; Wirtz Martin, M. A.; Stirnal, E.; Azzaoui, K.; Richter, C.; Sreeramulu, S.; José Blommers, M. J.; Schwalbe, H. 19 F NMR-Based Fragment Screening for 14 Different Biologically Active RNAs and 10 DNA and Protein Counter-Screens. *ChemBioChem* **2020**, *21* (2), 423–433. https://doi.org/10.1002/cbic.202000476.

(156) Dalvit, C.; Papeo, G.; Mongelli, N.; Giordano, P.; Saccardo, B.; Costa, A.; Veronesi, M.; Ko, S. Y. Rapid NMR-Based Functional Screening and IC50 Measurements Performed at Unprecedentedly Low Enzyme Concentration. *Drug Dev. Res.* **2005**, *64* (2), 105–113. https://doi.org/10.1002/ddr.10430.

(157) Shea, T. A.; Burburan, P. J.; Matubia, V. N.; Ramcharan, S. S.; Rosario, I.; Parkin, D. W.; Stockman, B. J. Identification of Proton-Pump Inhibitor Drugs That Inhibit Trichomonas Vaginalis Uridine Nucleoside Ribohydrolase. *Bioorg. Med. Chem. Lett.* **2014**, *24* (4), 1080–1084. https://doi.org/10.1016/j.bmcl.2014.01.014.

(158) Auletta, S.; Caravan, W.; Persaud, J. K.; Thuilot, S. F.; Brown, D. G.; Parkin, D. W.; Stockman, B. J. Discovery of Ligand-Efficient Scaffolds for the Design of Novel Trichomonas Vaginalis Uridine Nucleoside Ribohydrolase Inhibitors Using Fragment Screening. *ACS Omega* **2019**, *4* (14), 16226–16232. https://doi.org/10.1021/acsomega.9b02472.

(159) Hopkins, A. L.; Groom, C. R.; Alex, A. Ligand Efficiency: A Useful Metric for Lead Selection. *Drug Discov. Today* **2004**, *9* (10), 430–431. https://doi.org/10.1016/S1359-6446(04)03069-7.

(160) Tressler, C. M.; Zondlo, N. J. Perfluoro- Tert-Butyl Hydroxyprolines as Sensitive, Conformationally Responsive Molecular Probes: Detection of Protein Kinase Activity by 19F NMR. *ACS Chem. Biol.* **2020**, *15* (4), 1096–1103. https://doi.org/10.1021/acschembio.0c00131.

(161) Tressler, C. M.; Zondlo, N. J. Synthesis of Perfluoro-Tert-Butyl Tyrosine, for Application in 19F NMR, via a Diazonium-Coupling Reaction. *Org. Lett.* **2016**, *18* (24), 6240–6243. https://doi.org/10.1021/acs.orglett.6b02858.

(162) Tressler, C. M.; Zondlo, N. J. Perfluoro-Tert-Butyl Homoserine Is a Helix-Promoting, Highly Fluorinated, NMR-Sensitive Aliphatic Amino Acid: Detection of the Estrogen Receptor·Coactivator Protein-Protein Interaction by 19F NMR. *Biochemistry* **2017**, *56* (8), 1062–1074. https://doi.org/10.1021/acs.biochem.6b01020.

(163) Tressler, C. M.; Zondlo, N. J. (2 S,4 R)- and (2 S,4 S)-Perfluoro- Tert -Butyl 4-Hydroxyproline: Two Conformationally Distinct Proline Amino Acids for Sensitive Application in 19F NMR. *J. Org. Chem.* **2014**, *79* (12), 5880–5886. https://doi.org/10.1021/jo5008674.

(164) Fuller, N.; Spadola, L.; Cowen, S.; Patel, J.; Schönherr, H.; Cao, Q.; McKenzie, A.; Edfeldt, F.; Rabow, A.; Goodnow, R. An Improved Model for Fragment-Based Lead Generation at AstraZeneca. *Drug Discov. Today* **2016**, *21* (8), 1272–1283. https://doi.org/10.1016/j.drudis.2016.04.023.

(165) Prescher, H.; Koch, G.; Schuhmann, T.; Ertl, P.; Bussenault, A.; Glick, M.; Dix, I.; Petersen, F.; Lizos, D. E. Construction of a 3D-Shaped, Natural Product like Fragment Library by Fragmentation and Diversification of Natural Products. *Bioorg. Med. Chem.* **2017**, *25* (3), 921–925. https://doi.org/10.1016/j.bmc.2016.12.005.

(166) Lingel, A.; Vulpetti, A.; Reinsperger, T.; Proudfoot, A.; Denay, R.; Frommlet, A.; Henry, C.; Hommel, U.; Gossert, A. D.; Luy, B.; Frank, A. O. Comprehensive and High-Throughput Exploration of Chemical Space Using Broadband ^{19} F NMR-Based

Screening. *Angew. Chem.* **2020**, *132* (35), ange.202002463. https://doi.org/10.1002/ange.202002463.

(167) Aretz, J.; Rademacher, C. Ranking Hits from Saturation Transfer Difference Nuclear Magnetic Resonance-Based Fragment Screening. *Front. Chem.* **2019**, *7* (215), 1–8. https://doi.org/10.3389/fchem.2019.00215.

(168) Murray, C. W.; Callaghan, O.; Chessari, G.; Cleasby, A.; Congreve, M.; Frederickson, M.; Hartshorn, M. J.; McMenamin, R.; Patel, S.; Wallis, N. Application of Fragment Screening by X-Ray Crystallography to β-Secretase. *J. Med. Chem.* **2007**, *50* (6), 1116–1123. https://doi.org/10.1021/jm0611962.

(169) Geschwindner, S.; Olsson, L.-L.; Albert, J. S.; Deinum, J.; Edwards, P. D.; de Beer, T.; Folmer, R. H. A. Discovery of a Novel Warhead against β-Secretase through Fragment-Based Lead Generation §. *J. Med. Chem.* **2007**, *50* (24), 5903–5911. https://doi.org/10.1021/jm070825k.

(170) Cheng, Y.; Judd, T. C.; Bartberger, M. D.; Brown, J.; Chen, K.; Fremeau, R. T.; Hickman, D.; Hitchcock, S. A.; Jordan, B.; Li, V.; Lopez, P.; Louie, S. W.; Luo, Y.; Michelsen, K.; Nixey, T.; Powers, T. S.; Rattan, C.; Sickmier, E. A.; St. Jean, D. J.; Wahl, R. C.; Wen, P. H.; Wood, S. From Fragment Screening to in Vivo Efficacy: Optimization of a Series of 2-Aminoquinolines as Potent Inhibitors of Beta-Site Amyloid Precursor Protein Cleaving Enzyme 1 (Bace1). *J. Med. Chem.* **2011**, *54* (16), 5836–5857. https://doi.org/10.1021/jm200544q.

(171) Jordan, J. B.; Whittington, D. A.; Bartberger, M. D.; Sickmier, E. A.; Chen, K.; Cheng, Y.; Judd, T. Fragment-Linking Approach Using 19F NMR Spectroscopy to Obtain Highly Potent and Selective Inhibitors of β-Secretase. *J. Med. Chem.* **2016**, *59* (8), 3732–3749. https://doi.org/10.1021/acs.jmedchem.5b01917.

(172) Lambruschini, C.; Veronesi, M.; Romeo, E.; Garau, G.; Bandiera, T.; Piomelli, D.; Scarpelli, R.; Dalvit, C. Development of Fragment-Based *n* -FABS NMR Screening Applied to the Membrane Enzyme FAAH. *ChemBioChem* **2013**, *14* (13), 1611–1619. https://doi.org/10.1002/cbic.201300347.

(173) Frieden, C.; Hoeltzli, S. D.; Bann, J. G. The Preparation of 19F-Labeled Proteins for NMR Studies. *Methods Enzymol.* **2004**, *380*, 400–415. https://doi.org/10.1016/S0076-6879(04)80018-1.

(174) Sharaf, N. G.; Gronenborn, A. M. 19F-Modified Proteins and 19F-Containing Ligands as Tools in Solution NMR Studies of Protein Interactions. In *Methods in Enzymology*; Academic Press Inc., 2015; Vol. 565, pp 67–95. https://doi.org/10.1016/bs.mie.2015.05.014.

(175) Cellitti, S. E.; Jones, D. H.; Lagpacan, L.; Hao, X.; Zhang, Q.; Hu, H.; Brittain, S. M.; Brinker, A.; Caldwell, J.; Bursulaya, B.; Spraggon, G.; Brock, A.; Ryu, Y.; Uno, T.; Schultz, P. G.; Geierstanger, B. H. In Vivo Incorporation of Unnatural Amino Acids to Probe Structure, Dynamics, and Ligand Binding in a Large Protein by Nuclear Magnetic

Resonance Spectroscopy. *J. Am. Chem. Soc.* **2008**, *130* (29), 9268–9281. https://doi.org/10.1021/ja801602q.

(176) Jackson, J. C.; Hammill, J. T.; Mehl, R. A. Site-Specific Incorporation of a 19F-Amino Acid into Proteins as an NMR Probe for Characterizing Protein Structure and Reactivity. *J. Am. Chem. Soc.* **2007**, *129* (5), 1160–1166. https://doi.org/10.1021/ja064661t.

(177) Imiołek, M.; Karunanithy, G.; Ng, W. L.; Baldwin, A. J.; Gouverneur, V.; Davis, B. G. Selective Radical Trifluoromethylation of Native Residues in Proteins. *J. Am. Chem. Soc.* **2018**, *140* (5), 1568–1571. https://doi.org/10.1021/jacs.7b10230.

(178) Boutureira, O.; Bernardes, G. J. L.; D'Hooge, F.; Davis, B. G. Direct Radiolabelling of Proteins at Cysteine Using [18F]- Fluorosugars. *Chem. Commun.* **2011**, *47* (36), 10010–10012. https://doi.org/10.1039/c1cc13524d.

(179) Hattori, Y.; Heidenreich, D.; Ono, Y.; Sugiki, T.; Yokoyama, K. ichi; Suzuki, E. ichiro; Fujiwara, T.; Kojima, C. Protein 19F-Labeling Using Transglutaminase for the NMR Study of Intermolecular Interactions. *J. Biomol. NMR* **2017**, *68* (4), 271–279. https://doi.org/10.1007/s10858-017-0125-6.

(180) Gee, C. T.; Arntson, K. E.; Urick, A. K.; Mishra, N. K.; Hawk, L. M. L.; Wisniewski, A. J.; Pomerantz, W. C. K. Protein-Observed 19F-NMR for Fragment Screening, Affinity Quantification and Druggability Assessment. *Nat. Protoc.* **2016**, *11* (8), 1414–1427. https://doi.org/10.1038/nprot.2016.079.

(181) Shanina, E.; Siebs, E.; Zhang, H.; Varón Silva, D.; Joachim, I.; Titz, A.; Rademacher, C. Protein-Observed 19F NMR of LecA from Pseudomonas Aeruginosa. *Glycobiology* **2021**, *31* (2), 159–165. https://doi.org/10.1093/glycob/cwaa057.

(182) Kim, T. H.; Chung, K. Y.; Manglik, A.; Hansen, A. L.; Dror, R. O.; Mildorf, T. J.; Shaw, D. E.; Kobilka, B. K.; Prosser, R. S. The Role of Ligands on the Equilibria between Functional States of a G Protein-Coupled Receptor. *J. Am. Chem. Soc.* **2013**, *135* (25), 9465–9474. https://doi.org/10.1021/ja404305k.

(183) Frei, J. N.; Broadhurst, R. W.; Bostock, M. J.; Solt, A.; Jones, A. J. Y.; Gabriel, F.; Tandale, A.; Shrestha, B.; Nietlispach, D. Conformational Plasticity of Ligand-Bound and Ternary GPCR Complexes Studied by 19F NMR of the Β1-Adrenergic Receptor. *Nat. Commun.* **2020**, *11* (669), 1–14. https://doi.org/10.1038/s41467-020-14526-3.

(184) Manglik, A.; Kim, T. H.; Masureel, M.; Altenbach, C.; Yang, Z.; Hilger, D.; Lerch, M. T.; Kobilka, T. S.; Thian, F. S.; Hubbell, W. L.; Prosser, R. S.; Kobilka, B. K. Structural Insights into the Dynamic Process of Β2-Adrenergic Receptor Signaling. *Cell* **2015**, *161* (5), 1101–1111. https://doi.org/10.1016/j.cell.2015.04.043.

(185) Ye, L.; Van Eps, N.; Zimmer, M.; Ernst, O. P.; Scott Prosser, R. Activation of the A 2A Adenosine G-Protein-Coupled Receptor by Conformational Selection. *Nature* **2016**, *533* (7602), 265–268. https://doi.org/10.1038/nature17668.

(186) Ye, L.; Neale, C.; Sljoka, A.; Lyda, B.; Pichugin, D.; Tsuchimura, N.; Larda, S. T.; Pomès, R.; García, A. E.; Ernst, O. P.; Sunahara, R. K.; Prosser, R. S. Mechanistic Insights into Allosteric Regulation of the A2A Adenosine G Protein-Coupled Receptor by Physiological Cations. *Nat. Commun.* **2018**, *9* (1372), 1–13. https://doi.org/10.1038/s41467-018-03314-9.

(187) Huang, S. K.; Pandey, A.; Tran, D. P.; Villanueva, N. L.; Kitao, A.; Sunahara, R. K.; Sljoka, A.; Prosser, R. S. Delineating the Conformational Landscape of the Adenosine A2A Receptor during G Protein Coupling. *Cell* **2021**, *184* (7), 1884–1894. https://doi.org/10.1016/j.cell.2021.02.041.

(188) Abboud, M. I.; Hinchliffe, P.; Brem, J.; Macsics, R.; Pfeffer, I.; Makena, A.; Umland, K. D.; Rydzik, A. M.; Li, G. B.; Spencer, J.; Claridge, T. D. W.; Schofield, C. J. 19F-NMR Reveals the Role of Mobile Loops in Product and Inhibitor Binding by the São Paulo Metallo-β-Lactamase. *Angew. Chem. - Int. Ed.* **2017**, *56* (14), 3862–3866. https://doi.org/10.1002/anie.201612185.

(189) Chrisman, I. M.; Nemetchek, M. D.; De Vera, I. M. S.; Shang, J.; Heidari, Z.; Long, Y.; Reyes-Caballero, H.; Galindo-Murillo, R.; Cheatham, T. E.; Blayo, A. L.; Shin, Y.; Fuhrmann, J.; Griffin, P. R.; Kamenecka, T. M.; Kojetin, D. J.; Hughes, T. S. Defining a Conformational Ensemble That Directs Activation of PPARγ. *Nat. Commun.* **2018**, *9* (1), 1–16. https://doi.org/10.1038/s41467-018-04176-x.

(190) Zor, T.; De Guzman, R. N.; Dyson, H. J.; Wright, P. E. Solution Structure of the KIX Domain of CBP Bound to the Transactivation Domain of C-Myb. *J. Mol. Biol.* **2004**, *337* (3), 521–534. https://doi.org/10.1016/j.jmb.2004.01.038.

(191) Goto, N. K.; Zor, T.; Martinez-Yamout, M.; Dyson, H. J.; Wright, P. E. Cooperativity in Transcription Factor Binding to the Coactivator CREB-Binding Protein (CBP): The Mixed Lineage Leukemia Protein (MLL) Activation Domain Binds to an Allosteric Site on the KIX Domain. *J. Biol. Chem.* **2002**, *277* (45), 43168–43174. https://doi.org/10.1074/jbc.M207660200.

(192) Bogan, A. A.; Thorn, K. S. Anatomy of Hot Spots in Protein Interfaces. *J. Mol. Biol.* **1998**, *280* (1), 1–9. https://doi.org/10.1006/jmbi.1998.1843.

(193) Bullock, B. N.; Jochim, A. L.; Arora, P. S. Assessing Helical Protein Interfaces for Inhibitor Design. *J. Am. Chem. Soc.* **2011**, *133* (36), 14220–14223. https://doi.org/10.1021/ja206074j.

(194) Best, J. L.; Amezcua, C. A.; Mayr, B.; Flechner, L.; Murawsky, C. M.; Emerson, B.; Zor, T.; Gardner, K. H.; Montminy, M. Identification of Small-Molecule Antagonist That Inhibit an Activator:Coactivator Interaction. *Proc. Natl. Acad. Sci. U. S. A.* **2004**, *101* (51), 17622–17627. https://doi.org/10.1073/pnas.0406374101.

(195) Wang, N.; Majmudar, C. Y.; Pomerantz, W. C.; Gagnon, J. K.; Sadowsky, J. D.; Meagher, J. L.; Johnson, T. K.; Stuckey, J. A.; Brooks, C. L.; Wells, J. A.; Mapp, A. K.

Ordering a Dynamic Protein Via a Small-Molecule Stabilizer. *J. Am. Chem. Soc.* **2013**, *135* (9), 3363–3366. https://doi.org/10.1021/ja3122334.

(196) Gee, C. T.; Koleski, E. J.; Pomerantz, W. C. K. Fragment Screening and Druggability Assessment for the CBP/P300 KIX Domain through Protein-Observed ^{19}F NMR Spectroscopy. *Angew. Chem. Int. Ed.* **2015**, *54* (12), 3735–3739. https://doi.org/10.1002/anie.201411658.

(197) Gee, C. T.; Arntson, K. E.; Koleski, E. J.; Staebell, R. L.; Pomerantz, W. C. K. Dual Labeling of the CBP/P300 KIX Domain for ^{19}F NMR Leads to Identification of a New Small-Molecule Binding Site. *ChemBioChem* **2018**, *19* (9), 963–969. https://doi.org/10.1002/cbic.201700686.

(198) Leung, E. W. W.; Yagi, H.; Harjani, J. R.; Mulcair, M. D.; Scanlon, M. J.; Baell, J. B.; Norton, R. S. ^{19}F NMR as a Probe of Ligand Interactions with the INOS Binding Site of SPRY Domain-Containing SOCS Box Protein 2. *Chem. Biol. Drug Des.* **2014**, *84* (5), 616–625. https://doi.org/10.1111/cbdd.12355.

(199) Yap, B. K.; Leung, E. W. W.; Yagi, H.; Galea, C. A.; Chhabra, S.; Chalmers, D. K.; Nicholson, S. E.; Thompson, P. E.; Norton, R. S. A Potent Cyclic Peptide Targeting SPSB2 Protein as a Potential Anti-Infective Agent. *J. Med. Chem.* **2014**, *57* (16), 7006–7015. https://doi.org/10.1021/jm500596j.

(200) Yap, B. K.; Harjani, J. R.; Leung, E. W. W.; Nicholson, S. E.; Scanlon, M. J.; Chalmers, D. K.; Thompson, P. E.; Baell, J. B.; Norton, R. S. Redox-Stable Cyclic Peptide Inhibitors of the SPSB2-INOS Interaction. *FEBS Lett.* **2016**, *590* (6), 696–704. https://doi.org/10.1002/1873-3468.12115.

(201) Devine, S. M.; MacRaild, C. A.; Norton, R. S.; Scammells, P. J. Antimalarial Drug Discovery Targeting Apical Membrane Antigen 1. *MedChemComm* **2017**, *8* (1), 13–20. https://doi.org/10.1039/c6md00495d.

(202) Harjani, J. R.; Yap, B. K.; Leung, E. W. W.; Lucke, A.; Nicholson, S. E.; Scanlon, M. J.; Chalmers, D. K.; Thompson, P. E.; Norton, R. S.; Baell, J. B. Design, Synthesis, and Characterization of Cyclic Peptidomimetics of the Inducible Nitric Oxide Synthase Binding Epitope That Disrupt the Protein-Protein Interaction Involving SPRY Domain-Containing Suppressor of Cytokine Signaling Box Protein (SPSB) 2 and Inducible Nitric Oxide Synthase. *J. Med. Chem.* **2016**, *59* (12), 5799–5809. https://doi.org/10.1021/acs.jmedchem.6b00386.

(203) Sadek, M. M.; Barlow, N.; Leung, E. W. W.; Williams-Noonan, B. J.; Keat, B.; Fairolniza, M. S.; Caradoc-Davies, T. T.; Nicholson, S. E.; Chalmers, D. K.; Thompson, P. E.; Law, R. H. P.; Norton, R. S. A Cyclic Peptide Inhibitor of the INOS−SPSB Protein−Protein Interaction as a Potential Anti-Infective Agent. *ACS Chem Biol* **2018**, *13* (10), 2930–2938. https://doi.org/10.1021/acschembio.8b00561.

(204) Leung, E. W. W.; Mulcair, M. D.; Keat, B.; Nicholson, S. E.; Scanlon, M. J.; Norton, R. S. Molecular Insights into the Interaction Between the SPRY Domain-Containing SOCS

Box Protein SPSB2 and Peptides Based on the Binding Motif from INOS. *Aust. J. Chem.* **2017**, *70* (2), 191–200. https://doi.org/10.1071/CH16510.

(205) Ge, X.; Macraild, C. A.; Devine, S. M.; Debono, C. O.; Wang, G.; Scammells, P. J.; Scanlon, M. J.; Anders, R. F.; Foley, M.; Norton, R. S. Ligand-Induced Conformational Change of Plasmodium Falciparum AMA1 Detected Using 19F NMR. *J. Med. Chem.* **2014**, *57* (15), 6419–6427. https://doi.org/10.1021/jm500390g.

(206) Mishra, N. K.; Urick, A. K.; Ember, S. W. J.; Schönbrunn, E.; Pomerantz, W. C. Fluorinated Aromatic Amino Acids Are Sensitive 19F NMR Probes for Bromodomain-Ligand Interactions. *ACS Chem. Biol.* **2014**, *9* (12), 2755–2760. https://doi.org/10.1021/cb5007344.

(207) Olson, N. M.; Kroc, S.; Johnson, J. A.; Zahid, H.; Ycas, P. D.; Chan, A.; Kimbrough, J. R.; Kalra, P.; Schönbrunn, E.; Pomerantz, W. C. K. NMR Analyses of Acetylated H2A.Z Isoforms Identify Differential Binding Interactions with the Bromodomain of the NURF Nucleosome Remodeling Complex. *Biochemistry* **2020**, *59* (20), 1871–1880. https://doi.org/10.1021/acs.biochem.0c00159.

(208) Kalra, P.; McGraw, L.; Kimbrough, J. R.; Pandey, A. K.; Solberg, J.; Cui, H.; Divakaran, A.; John, K.; Hawkinson, J. E.; Pomerantz, W. C. K. Quantifying the Selectivity of Protein-Protein and Small Molecule Interactions with Fluorinated Tandem Bromodomain Reader Proteins. *ACS Chem. Biol.* **2020**, *15* (11), 3038–3049. https://doi.org/10.1021/acschembio.0c00720.

(209) Johnson, J. A.; Olson, N. M.; Tooker, M. J.; Bur, S. K.; Pomerantz, W. C. K. Combined Protein- and Ligand-Observed NMR Workflow to Screen Fragment Cocktails against Multiple Proteins: A Case Study Using Bromodomains. *Molecules* **2020**, *25* (17), 3949. https://doi.org/10.3390/molecules25173949.

(210) Brand, M.; Clayton, J.; Moroglu, M.; Schiedel, M.; Picaud, S.; Bluck, J. P.; Skwarska, A.; Chan, A. K. N.; Laurin, C. M. C.; Scorah, A. R.; Larissa See, K. F.; Rooney, T. P. C.; Fedorov, O.; Perell, G.; Kalra, P.; Cortopassi, W. A.; Christensen, K. E.; Cooper, R. I.; Paton, R. S.; Pomerantz, W. C. K.; Biggin, P. C.; Hammond, E. M.; Filippakopoulos, P.; Conway, S. J. Controlling Intramolecular Interactions in the Design of Selective, High-Affinity, Ligands for the CREBBP Bromodomain. *ChemRxiv* **2020**. https://doi.org/10.26434/chemrxiv.12081999.v1.

(211) Divakaran, A.; Talluri, S. K.; Ayoub, A. M.; Mishra, N. K.; Cui, H.; Widen, J. C.; Berndt, N.; Zhu, J. Y.; Carlson, A. S.; Topczewski, J. J.; Schonbrunn, E. K.; Harki, D. A.; Pomerantz, W. C. K. Molecular Basis for the N-Terminal Bromodomain-and-Extra-Terminal-Family Selectivity of a Dual Kinase-Bromodomain Inhibitor. *J. Med. Chem.* **2018**, *61* (20), 9316–9334. https://doi.org/10.1021/acs.jmedchem.8b01248.

(212) Cui, H.; Divakaran, A.; Pandey, A. K.; Johnson, J. A.; Zahid, H.; Hoell, Z. J.; Ellingson, M. O.; Shi, K.; Aihara, H.; Harki, D. A.; Pomerantz, W. C. K. Selective N-Terminal BET Bromodomain Inhibitors by Targeting Non-Conserved Residues and Structured Water

Displacement. *Angew. Chem. Int. Ed.* **2021**, *60* (3), 1220–1226. https://doi.org/10.1002/anie.202008625.

(213) Curtis-Marof, R.; Doko, D.; Rowe, M. L.; Richards, K. L.; Williamson, R. A.; Howard, M. J. 19F NMR Spectroscopy Monitors Ligand Binding to Recombinantly Fluorine-Labelled b ′ x from Human Protein Disulphide Isomerase (HPDI). *Org. Biomol. Chem.* **2014**, *12* (23), 3808–3812. https://doi.org/10.1039/c4ob00699b.

(214) Stadmiller, S. S.; Aguilar, J. S.; Waudby, C. A.; Pielak, G. J. Rapid Quantification of Protein-Ligand Binding via 19F NMR Lineshape Analysis. *Biophys. J.* **2020**, *118* (10), 2537–2548. https://doi.org/10.1016/j.bpj.2020.03.031.

(215) Taroni, C.; Jones, S.; Thornton, J. M. Analysis and Prediction of Carbohydrate Binding Sites. *Protein Eng. Des. Sel.* **2000**, *13* (2), 89–98. https://doi.org/10.1093/protein/13.2.89.

(216) Yu, L.; Hajduk, P. J.; Mack, J.; Olejniczak, E. T. Structural Studies of Bcl-XL/Ligand Complexes Using 19F NMR. *J. Biomol. NMR* **2006**, *34* (4), 221–227. https://doi.org/10.1007/s10858-006-0005-y.

(217) Loewen, M. C.; Klein-Seetharaman, J.; Getmanova, E. V.; Reeves, P. J.; Schwalbe, H.; Khorana, H. G. Solution 19F Nuclear Overhauser Effects in Structural Studies of the Cytoplasmic Domain of Mammalian Rhodopsin. *Proc. Natl. Acad. Sci. U. S. A.* **2001**, *98* (9), 4888–4892. https://doi.org/10.1073/pnas.051633098.

(218) Evanics, F.; Kitevski, J. L.; Bezsonova, I.; Forman-Kay, J.; Prosser, R. S. 19F NMR Studies of Solvent Exposure and Peptide Binding to an SH3 Domain. *Biochim. Biophys. Acta - Gen. Subj.* **2007**, *1770* (2), 221–230. https://doi.org/10.1016/j.bbagen.2006.10.017.

(219) Li, H.; Frieden, C. NMR Studies of 4-19F-Phenylalanine-Labeled Intestinal Fatty Acid Binding Protein: Evidence for Conformational Heterogeneity in the Native State. *Biochemistry* **2005**, *44* (7), 2369–2377. https://doi.org/10.1021/bi047600l.

(220) Li, H.; Frieden, C. Observation of Sequential Steps in the Folding of Intestinal Fatty Acid Binding Protein Using a Slow Folding Mutant and 19F NMR. *Proc. Natl. Acad. Sci. U. S. A.* **2007**, *104* (29), 11993–11998. https://doi.org/10.1073/pnas.0705253104.

(221) Qianzhu, H.; Welegedara, A. P.; Williamson, H.; McGrath, A. E.; Mahawaththa, M. C.; Dixon, N. E.; Otting, G.; Huber, T. Genetic Encoding of Para-Pentafluorosulfanyl Phenylalanine: A Highly Hydrophobic and Strongly Electronegative Group for Stable Protein Interactions. *J. Am. Chem. Soc.* **2020**, *142* (41), 17277–17281. https://doi.org/10.1021/jacs.0c07976.

(222) Matei, E.; Gronenborn, A. M. 19F Paramagnetic Relaxation Enhancement: A Valuable Tool for Distance Measurements in Proteins. *Angew. Chem. - Int. Ed.* **2016**, *55* (1), 150–154. https://doi.org/10.1002/anie.201508464.

(223) Somlyay, M.; Ledolter, K.; Kitzler, M.; Sandford, G.; Cobb, S. L.; Konrat, R. ^{19}F NMR Spectroscopy Tagging and Paramagnetic Relaxation Enhancement-Based Conformation

Analysis of Intrinsically Disordered Protein Complexes. *ChemBioChem* **2020**, *21* (5), 696–701. https://doi.org/10.1002/cbic.201900453.

(224) Brindle, K.; Williams, S.-P.; Boulton, M. ^{19} F NMR Detection of a Fluorine-Labelled Enzyme in Vivo. *FEBS Lett.* **1989**, *255* (1), 121–124. https://doi.org/10.1016/0014-5793(89)81073-7.

(225) Williams, S. P.; Haggie, P. M.; Brindle, K. M. NMR Measurements of the Rotational Mobility of Proteins in Vivo. *Biophys. J.* **1997**, *72* (1), 490–498. https://doi.org/10.1016/S0006-3495(97)78690-9.

(226) Williams, S. P.; Fulton, A. M.; Brindle, K. M. Estimation of the Intracellular Free ADP Concentration by 19F NMR Studies of Fluorine-Labeled Yeast Phosphoglycerate Kinase in Vivo. *Biochemistry* **1993**, *32* (18), 4895–4902. https://doi.org/10.1021/bi00069a026.

(227) Haggie, P. M.; Brindle, K. M. Mitochondrial Citrate Synthase Is Immobilized in Vivo. *J. Biol. Chem.* **1999**, *274* (7), 3941–3945. https://doi.org/10.1074/jbc.274.7.3941.

(228) Li, C.; Charlton, L. M.; Lakkavaram, A.; Seagle, C.; Wang, G.; Young, G. B.; Macdonald, J. M.; Pielak, G. J. Differential Dynamical Effects of Macromolecular Crowding on an Intrinsically Disordered Protein and a Globular Protein: Implications for in-Cell NMR Spectroscopy. *J. Am. Chem. Soc.* **2008**, *130* (20), 6310–6311. https://doi.org/10.1021/ja801020z.

(229) Xu, G.; Ye, Y.; Liu, X.; Cao, S.; Wu, Q.; Cheng, K.; Liu, M.; Pielak, G. J.; Li, C. Strategies for Protein NMR in Escherichia Coli. *Biochemistry* **2014**, *53* (12), 1971–1981. https://doi.org/10.1021/bi500079u.

(230) Cheng, K.; Wu, Q.; Jiang, L.; Liu, M.; Li, C. Protein Stability Analysis in Ionic Liquids by 19F NMR. *Anal. Bioanal. Chem.* **2019**, *411* (19), 4929–4935. https://doi.org/10.1007/s00216-019-01804-3.

(231) Ye, Y.; Wu, Q.; Zheng, W.; Jiang, B.; Pielak, G. J.; Liu, M.; Li, C. Positively Charged Tags Impede Protein Mobility in Cells as Quantified by 19F NMR. *J. Phys. Chem. B* **2019**, *123* (21), 4527–4533. https://doi.org/10.1021/acs.jpcb.9b02162.

(232) Smith, A. E.; Zhou, L. Z.; Gorensek, A. H.; Senske, M.; Pielak, G. J. In-Cell Thermodynamics and a New Role for Protein Surfaces. *Proc. Natl. Acad. Sci. U. S. A.* **2016**, *113* (7), 1725–1730. https://doi.org/10.1073/pnas.1518620113.

(233) Thole, J. F.; Stadmiller, S. S.; Pielak, G. J. Zebrafish Oocytes as a Tool for Eukaryotic In-Cell NMR. *Biophys. J.* **2020**, *118* (3), 196a. https://doi.org/10.1016/j.bpj.2019.11.1184.

(234) Kim, Y.; Hilty, C. Affinity Screening Using Competitive Binding with Fluorine-19 Hyperpolarized Ligands. *Angew. Chem. - Int. Ed.* **2015**, *54* (16), 4941–4944. https://doi.org/10.1002/anie.201411424.

(235) Hoang, J.; Prosser, R. S. Conformational Selection and Functional Dynamics of Calmodulin: A 19 F Nuclear Magnetic Resonance Study. *Biochemistry* **2014**, *53* (36), 5727–5736. https://doi.org/10.1021/bi500679c.

(236) Overbeck, J. H.; Kremer, W.; Sprangers, R. A Suite of 19F Based Relaxation Dispersion Experiments to Assess Biomolecular Motions. *J. Biomol. NMR* **2020**, *74* (12), 753–766. https://doi.org/10.1007/s10858-020-00348-4.

(237) Heidari, Z.; Chrisman, I. M.; Nemetchek, M. D.; Novick, S. J.; Blayo, A.-L.; Patton, T.; Mendes, D. E.; Diaz, P.; Kamenecka, T. M.; Griffin, P. R.; Hughes, T. S. Definition of Functionally and Structurally Distinct Repressive States in the Nuclear Receptor PPARγ. *Nat. Commun.* **2019**, *10* (5825), 1–14. https://doi.org/10.1038/s41467-019-13768-0.

(238) Goldberg, A. D.; Allis, C. D.; Bernstein, E. Epigenetics: A Landscape Takes Shape. *Cell* **2007**, *128* (4), 635–638. https://doi.org/10.1016/j.cell.2007.02.006.

(239) Allis, C. D.; Jenuwein, T. The Molecular Hallmarks of Epigenetic Control. *Nat. Rev. Genet.* **2016**, *17* (8), 487–500. https://doi.org/10.1038/nrg.2016.59.

(240) Clapier, C. R.; Iwasa, J.; Cairns, B. R.; Peterson, C. L. Mechanisms of Action and Regulation of ATP-Dependent Chromatin-Remodelling Complexes. *Nat. Rev. Mol. Cell Biol.* **2017**, *18* (7), 407–422. https://doi.org/10.1038/nrm.2017.26.

(241) Hohmann, A. F.; Vakoc, C. R. A Rationale to Target the SWI/SNF Complex for Cancer Therapy. *Trends Genet.* **2014**, *30* (8), 356–363. https://doi.org/10.1016/j.tig.2014.05.001.

(242) St. Pierre, R.; Kadoch, C. Mammalian SWI/SNF Complexes in Cancer: Emerging Therapeutic Opportunities. *Curr. Opin. Genet. Dev.* **2017**, *42*, 56–67. https://doi.org/10.1016/j.gde.2017.02.004.

(243) Zoppi, V.; Hughes, S. J.; Maniaci, C.; Testa, A.; Gmaschitz, T.; Wieshofer, C.; Koegl, M.; Riching, K. M.; Daniels, D. L.; Spallarossa, A.; Ciulli, A. Iterative Design and Optimization of Initially Inactive Proteolysis Targeting Chimeras (PROTACs) Identify VZ185 as a Potent, Fast, and Selective von Hippel–Lindau (VHL) Based Dual Degrader Probe of BRD9 and BRD7. *J. Med. Chem.* **2019**, *62* (2), 699–726.

(244) Barak, O.; Lazzaro, M. A.; Lane, W. S.; Speicher, D. W.; Picketts, D. J.; Shiekhattar, R. Isolation of Human NURF: A Regulator of Engrailed Gene Expression. *EMBO J.* **2003**, *22* (22), 6089–6100. https://doi.org/10.1093/emboj/cdg582.

(245) Zahid, H.; Olson, N. M.; Pomerantz, W. C. K. Opportunity Knocks for Uncovering the New Function of an Understudied Nucleosome Remodeling Complex Member, the Bromodomain PHD Finger Transcription Factor, BPTF. *Curr. Opin. Chem. Biol.* **2021**, *63*, 57–67. https://doi.org/10.1016/j.cbpa.2021.02.003.

(246) Pomerantz, W. C. K.; Johnson, J. A.; Ycas, P. D. Applied Biophysics for Bromodomain Drug Discovery; 2019; pp 287–337. https://doi.org/10.1007/7355_2019_79.

(247) Xiao, H.; Sandaltzopoulos, R.; Wang, H.-M.; Hamiche, A.; Ranallo, R.; Lee, K.-M.; Fu, D.; Wu, C. Dual Functions of Largest NURF Subunit NURF301 in Nucleosome Sliding and Transcription Factor Interactions. *Mol. Cell* **2001**, *8* (3), 531–543. https://doi.org/10.1016/S1097-2765(01)00345-8.

(248) Jones, M. H.; Hamana, N.; Shimane, M. Identification and Characterization of BPTF, a Novel Bromodomain Transcription Factor. *Genomics* **2000**, *63* (1), 35–39. https://doi.org/10.1006/geno.1999.6070.

(249) Ruthenburg, A. J.; Li, H.; Milne, T. A.; Dewell, S.; McGinty, R. K.; Yuen, M.; Ueberheide, B.; Dou, Y.; Muir, T. W.; Patel, D. J.; Allis, C. D. Recognition of a Mononucleosomal Histone Modification Pattern by BPTF via Multivalent Interactions. *Cell* **2011**, *145* (5), 692–706. https://doi.org/10.1016/j.cell.2011.03.053.

(250) Landry, J.; Sharov, A. A.; Piao, Y.; Sharova, L. V.; Xiao, H.; Southon, E.; Matta, J.; Tessarollo, L.; Zhang, Y. E.; Ko, M. S. H.; Kuehn, M. R.; Yamaguchi, T. P.; Wu, C. Essential Role of Chromatin Remodeling Protein Bptf in Early Mouse Embryos and Embryonic Stem Cells. *PLoS Genet.* **2008**, *4* (10), e1000241. https://doi.org/10.1371/journal.pgen.1000241.

(251) Wu, B.; Wang, Y.; Wang, C.; Wang, G. G.; Wu, J.; Wan, Y. Y. BPTF Is Essential for T Cell Homeostasis and Function. *J. Immunol.* **2016**, *197* (11), 4325–4333. https://doi.org/10.4049/jimmunol.1600642.

(252) Frey, W. D.; Chaudhry, A.; Slepicka, P. F.; Ouellette, A. M.; Kirberger, S. E.; Pomerantz, W. C. K.; Hannon, G. J.; dos Santos, C. O. BPTF Maintains Chromatin Accessibility and the Self-Renewal Capacity of Mammary Gland Stem Cells. *Stem Cell Rep.* **2017**, *9* (1), 23–31. https://doi.org/10.1016/j.stemcr.2017.04.031.

(253) Dar, A. A.; Nosrati, M.; Bezrookove, V.; de Semir, D.; Majid, S.; Thummala, S.; Sun, V.; Tong, S.; Leong, S. P. L.; Minor, D.; Billings, P. R.; Soroceanu, L.; Debs, R.; Miller III, J. R.; Sagebiel, R. W.; Kashani-Sabet, M. The Role of BPTF in Melanoma Progression and in Response to BRAF-Targeted Therapy. *JNCI J. Natl. Cancer Inst.* **2015**, *107* (5). https://doi.org/10.1093/jnci/djv034.

(254) Koludrovic, D.; Laurette, P.; Strub, T.; Keime, C.; Le Coz, M.; Coassolo, S.; Mengus, G.; Larue, L.; Davidson, I. Chromatin-Remodelling Complex NURF Is Essential for Differentiation of Adult Melanocyte Stem Cells. *PLOS Genet.* **2015**, *11* (10), e1005555. https://doi.org/10.1371/journal.pgen.1005555.

(255) Richart, L.; Carrillo-de Santa Pau, E.; Río-Machín, A.; de Andrés, M. P.; Cigudosa, J. C.; Lobo, V. J. S. S.-A.; Real, F. X. BPTF Is Required for C-MYC Transcriptional Activity and in Vivo Tumorigenesis. *Nat. Commun.* **2016**, *7* (1), 10153. https://doi.org/10.1038/ncomms10153.

(256) Richart, L.; Real, F. X.; Sanchez-Arevalo Lobo, V. J. C-MYC Partners with BPTF in Human Cancer. *Mol. Cell. Oncol.* **2016**, *3* (3), e1152346. https://doi.org/10.1080/23723556.2016.1152346.

(257) Lee, J. H.; Kim, M. S.; Yoo, N. J.; Lee, S. H. BPTF, a Chromatin Remodeling-Related Gene, Exhibits Frameshift Mutations in Gastric and Colorectal Cancers. *Apmis* **2016**, *124* (5), 425–427. https://doi.org/10.1111/apm.12512.

(258) Zhao, X.; Zheng, F.; Li, Y.; Hao, J.; Tang, Z.; Tian, C.; Yang, Q.; Zhu, T.; Diao, C.; Zhang, C.; Chen, M.; Hu, S.; Guo, P.; Zhang, L.; Liao, Y.; Yu, W.; Chen, M.; Zou, L.; Guo, W.; Deng, W. BPTF Promotes Hepatocellular Carcinoma Growth by Modulating HTERT Signaling and Cancer Stem Cell Traits. *Redox Biol.* **2019**, *20* (October 2018), 427–441. https://doi.org/10.1016/j.redox.2018.10.018.

(259) Vidler, L. R.; Brown, N.; Knapp, S.; Hoelder, S. Druggability Analysis and Structural Classification of Bromodomain Acetyl-Lysine Binding Sites. *J. Med. Chem.* **2012**, *55* (17), 7346–7359. https://doi.org/10.1021/jm300346w.

(260) Petretich, M.; Demont, E. H.; Grandi, P. Domain-Selective Targeting of BET Proteins in Cancer and Immunological Diseases. *Curr. Opin. Chem. Biol.* **2020**, *57*, 184–193. https://doi.org/10.1016/j.cbpa.2020.02.003.

(261) Clegg, M. A.; Tomkinson, N. C. O.; Prinjha, R. K.; Humphreys, P. G. Advancements in the Development of Non-BET Bromodomain Chemical Probes. *ChemMedChem* **2019**, *14* (4), 362–385. https://doi.org/10.1002/cmdc.201800738.

(262) Urick, A. K.; Hawk, L. M. L.; Cassel, M. K.; Mishra, N. K.; Liu, S.; Adhikari, N.; Zhang, W.; Dos Santos, C. O.; Hall, J. L.; Pomerantz, W. C. K. Dual Screening of BPTF and Brd4 Using Protein-Observed Fluorine NMR Uncovers New Bromodomain Probe Molecules. *ACS Chem. Biol.* **2015**, *10* (10), 2246–2256. https://doi.org/10.1021/acschembio.5b00483.

(263) Belkina, A. C.; Denis, G. V. BET Domain Co-Regulators in Obesity, Inflammation and Cancer. *Nat. Rev. Cancer* **2012**, *12* (7), 465–477. https://doi.org/10.1038/nrc3256.

(264) Kirberger, S. E.; Ycas, P. D.; Johnson, J. A.; Chen, C.; Ciccone, M. F.; Woo, R. W. L.; Urick, A. K.; Zahid, H.; Shi, K.; Aihara, H.; McAllister, S. D.; Kashani-Sabet, M.; Shi, J.; Dickson, A.; dos Santos, C. O.; Pomerantz, W. C. K. Selectivity, Ligand Deconstruction, and Cellular Activity Analysis of a BPTF Bromodomain Inhibitor. *Org. Biomol. Chem.* **2019**, *17* (7), 2020–2027. https://doi.org/10.1039/C8OB02599A.

(265) Tyutyunyk-Massey, L.; Sun, Y.; Dao, N.; Ngo, H.; Dammalapati, M.; Vaidyanathan, A.; Singh, M.; Haqqani, S.; Haueis, J.; Finnegan, R.; Deng, X.; Kirberger, S. E.; Bos, P. D.; Bandyopadhyay, D.; Pomerantz, W. C. K.; Pommier, Y.; Gewirtz, D. A.; Landry, J. W. Autophagy-Dependent Sensitization of Triple-Negative Breast Cancer Models to Topoisomerase II Poisons by Inhibition of The Nucleosome Remodeling Factor. *Mol. Cancer Res.* **2021**. https://doi.org/10.1158/1541-7786.MCR-20-0743.

(266) *Structural Genomics Consortium. TP-238 A chemical probe for CECR2/BPTF bromodomains*. https://www.thesgc.org/chemical-probes/TP-238. https://www.thesgc.org/chemical-probes/TP-238.

(267) *Structural Genomics Consortium. NVS-BPTF-1 A chemical probe for BPTF*. https://www.thesgc.org/chemical-probes/NVS-BPTF-1.

(268) Mélin, L.; Calosing, C.; Kharenko, O. A.; Hansen, H. C.; Gagnon, A. Synthesis of NVS-BPTF-1 and Evaluation of Its Biological Activity. *Bioorg. Med. Chem. Lett.* **2021**, *47* (June), 128208. https://doi.org/10.1016/j.bmcl.2021.128208.

(269) Humphreys, P. G.; Bamborough, P.; Chung, C. W.; Craggs, P. D.; Gordon, L.; Grandi, P.; Hayhow, T. G.; Hussain, J.; Jones, K. L.; Lindon, M.; Michon, A. M.; Renaux, J. F.; Suckling, C. J.; Tough, D. F.; Prinjha, R. K. Discovery of a Potent, Cell Penetrant, and Selective P300/CBP-Associated Factor (PCAF)/General Control Nonderepressible 5 (GCN5) Bromodomain Chemical Probe. *J. Med. Chem.* **2017**, *60* (2), 695–709. https://doi.org/10.1021/acs.jmedchem.6b01566.

(270) Ycas, P. D.; Zahid, H.; Chan, A.; Olson, N. M.; Johnson, J. A.; Talluri, S. K.; Schonbrunn, E.; Pomerantz, W. C. K. New Inhibitors for the BPTF Bromodomain Enabled by Structural Biology and Biophysical Assay Development. *Org. Biomol. Chem.* **2020**, *18* (27), 5174–5182. https://doi.org/10.1039/D0OB00506A.

(271) Humphreys, P. G.; Bamborough, P.; Chung, C. W.; Craggs, P. D.; Gordon, L.; Grandi, P.; Hayhow, T. G.; Hussain, J.; Jones, K. L.; Lindon, M.; Michon, A. M.; Renaux, J. F.; Suckling, C. J.; Tough, D. F.; Prinjha, R. K. Discovery of a Potent, Cell Penetrant, and Selective P300/CBP-Associated Factor (PCAF)/General Control Nonderepressible 5 (GCN5) Bromodomain Chemical Probe. *J. Med. Chem.* **2017**, *60* (2), 695–709. https://doi.org/10.1021/acs.jmedchem.6b01566.

(272) Mishra, N. K.; Urick, A. K.; Ember, S. W. J.; Schönbrunn, E.; Pomerantz, W. C. Fluorinated Aromatic Amino Acids Are Sensitive 19 F NMR Probes for Bromodomain-Ligand Interactions. *ACS Chem. Biol.* **2014**, *9* (12), 2755–2760. https://doi.org/10.1021/cb5007344.

(273) Hopkins, A. L.; Keserü, G. M.; Leeson, P. D.; Rees, D. C.; Reynolds, C. H. The Role of Ligand Efficiency Metrics in Drug Discovery. *Nat. Rev. Drug Discov.* **2014**, *13* (2), 105–121. https://doi.org/10.1038/nrd4163.

(274) *pKa Table (Evans and Ripin)*. https://organicchemistrydata.org/hansreich/resources/pka/#pka_water_compilation_evans.

(275) Humphreys, P. G.; Bamborough, P.; Chung, C. W.; Craggs, P. D.; Gordon, L.; Grandi, P.; Hayhow, T. G.; Hussain, J.; Jones, K. L.; Lindon, M.; Michon, A. M.; Renaux, J. F.; Suckling, C. J.; Tough, D. F.; Prinjha, R. K. Discovery of a Potent, Cell Penetrant, and Selective P300/CBP-Associated Factor (PCAF)/General Control Nonderepressible 5 (GCN5) Bromodomain Chemical Probe. *J. Med. Chem.* **2017**, *60* (2), 695–709. https://doi.org/10.1021/acs.jmedchem.6b01566.

(276) Clegg, M. A.; Bamborough, P.; Chung, C.; Craggs, P. D.; Gordon, L.; Grandi, P.; Leveridge, M.; Lindon, M.; Liwicki, G. M.; Michon, A.-M.; Molnar, J.; Rioja, I.; Soden,

P. E.; Theodoulou, N. H.; Werner, T.; Tomkinson, N. C. O.; Prinjha, R. K.; Humphreys, P. G. Application of Atypical Acetyl-Lysine Methyl Mimetics in the Development of Selective Inhibitors of the Bromodomain-Containing Protein 7 (BRD7)/Bromodomain-Containing Protein 9 (BRD9) Bromodomains. *J. Med. Chem.* **2020**, *63* (11), 5816–5840. https://doi.org/10.1021/acs.jmedchem.0c00075.

(277) Matsson, P.; Doak, B. C.; Over, B.; Kihlberg, J. Cell Permeability beyond the Rule of 5. *Adv. Drug Deliv. Rev.* **2016**, *101*, 42–61. https://doi.org/10.1016/j.addr.2016.03.013.

(278) Cui, H.; Divakaran, A.; Pandey, A. K.; Johnson, J. A.; Zahid, H.; Hoell, Z. J.; Ellingson, M. O.; Shi, K.; Aihara, H.; Harki, D. A.; Pomerantz, W. C. K. Selective N-Terminal BET Bromodomain Inhibitors by Targeting Non-Conserved Residues and Structured Water Displacement. *Angew. Chem. Int. Ed.* **2021**, *60* (3), 1220–1226. https://doi.org/10.1002/anie.202008625.

(279) Xiong, L.; Mao, X.; Guo, Y.; Zhou, Y.; Chen, M.; Chen, P.; Yang, S.; Li, L. Discovery of Selective BPTF Bromodomain Inhibitors by Screening and Structure-Based Optimization. *Biochem. Biophys. Res. Commun.* **2021**, *545*, 125–131. https://doi.org/10.1016/j.bbrc.2021.01.067.

(280) Aslakson, C. J.; Miller, F. R. Selective Events in the Metastatic Process Defined by Analysis of the Sequential Dissemination of Subpopulations of a Mouse Mammary Tumor. *Cancer Res.* **1992**, *52* (6), 1399–1405.

(281) Mayes, K.; Alkhatib, S. G.; Peterson, K.; Alhazmi, A.; Song, C.; Chan, V.; Blevins, T.; Roberts, M.; Dumur, C. I.; Wang, X.-Y.; Landry, J. W. BPTF Depletion Enhances T-Cell–Mediated Antitumor Immunity. *Cancer Res.* **2016**, *76* (21), 6183–6192. https://doi.org/10.1158/0008-5472.CAN-15-3125.

(282) Lin, A.; Giuliano, C. J.; Palladino, A.; John, K. M.; Abramowicz, C.; Yuan, M. Lou; Sausville, E. L.; Lukow, D. A.; Liu, L.; Chait, A. R.; Galluzzo, Z. C.; Tucker, C.; Sheltzer, J. M. Off-Target Toxicity Is a Common Mechanism of Action of Cancer Drugs Undergoing Clinical Trials. *Sci. Transl. Med.* **2019**, *11* (509), eaaw8412. https://doi.org/10.1126/scitranslmed.aaw8412.

(283) Xu, R.; Nelson, C. M.; Muschler, J. L.; Veiseh, M.; Vonderhaar, B. K.; Bissell, M. J. Sustained Activation of STAT5 Is Essential for Chromatin Remodeling and Maintenance of Mammary-Specific Function. *J. Cell Biol.* **2009**, *184* (1), 57–66. https://doi.org/10.1083/jcb.200807021.

(284) Geletu, M.; Hoskin, V.; Starova, B.; Niit, M.; Adan, H.; Elliot, B.; Gunning, P.; Raptis, L. Differentiation of Mouse Breast Epithelial HC11 and EpH4 Cells. *J. Vis. Exp.* **2020**, No. 156. https://doi.org/10.3791/60147.

(285) Carlson, A. S.; Cui, H.; Divakaran, A.; Johnson, J. A.; Brunner, R. M.; Pomerantz, W. C. K.; Topczewski, J. J. Systematically Mitigating the P38α Activity of Triazole-Based BET Inhibitors. *ACS Med. Chem. Lett.* **2019**, *10* (9), 1296–1301. https://doi.org/10.1021/acsmedchemlett.9b00227.

(286) Humphreys, P. G.; Bamborough, P.; Chung, C. W.; Craggs, P. D.; Gordon, L.; Grandi, P.; Hayhow, T. G.; Hussain, J.; Jones, K. L.; Lindon, M.; Michon, A. M.; Renaux, J. F.; Suckling, C. J.; Tough, D. F.; Prinjha, R. K. Discovery of a Potent, Cell Penetrant, and Selective P300/CBP-Associated Factor (PCAF)/General Control Nonderepressible 5 (GCN5) Bromodomain Chemical Probe. *J. Med. Chem.* **2017**, *60* (2), 695–709. https://doi.org/10.1021/acs.jmedchem.6b01566.

(287) Kabsch, W. XDS. *Acta Crystallogr. D Biol. Crystallogr.* **2010**, *66* (2), 125–132. https://doi.org/10.1107/S0907444909047337.

(288) Adams, P. D.; Afonine, P. V.; Bunkóczi, G.; Chen, V. B.; Davis, I. W.; Echols, N.; Headd, J. J.; Hung, L.-W.; Kapral, G. J.; Grosse-Kunstleve, R. W.; McCoy, A. J.; Moriarty, N. W.; Oeffner, R.; Read, R. J.; Richardson, D. C.; Richardson, J. S.; Terwilliger, T. C.; Zwart, P. H. PHENIX : A Comprehensive Python-Based System for Macromolecular Structure Solution. *Acta Crystallogr. D Biol. Crystallogr.* **2010**, *66* (2), 213–221. https://doi.org/10.1107/S0907444909052925.

(289) Emsley, P.; Lohkamp, B.; Scott, W. G.; Cowtan, K. Features and Development of Coot. *Acta Crystallogr. D Biol. Crystallogr.* **2010**, *66* (4), 486–501. https://doi.org/10.1107/S0907444910007493.

(290) Filippakopoulos, P.; Picaud, S.; Mangos, M.; Keates, T.; Lambert, J. P.; Barsyte-Lovejoy, D.; Felletar, I.; Volkmer, R.; Müller, S.; Pawson, T.; Gingras, A. C.; Arrowsmith, C. H.; Knapp, S. Histone Recognition and Large-Scale Structural Analysis of the Human Bromodomain Family. *Cell* **2012**, *149* (1), 214–231. https://doi.org/10.1016/j.cell.2012.02.013.

(291) Noel, B. M.; Ouellette, S. B.; Marholz, L.; Dickey, D.; Navis, C.; Yang, T.-Y.; Nguyen, V.; Parker, S. J.; Bernlohr, D.; Sachs, Z.; Parker, L. L. Multiomic Profiling of Tyrosine Kinase Inhibitor-Resistant K562 Cells Suggests Metabolic Reprogramming To Promote Cell Survival. *J. Proteome Res.* **2019**, *18* (4), 1842–1856. https://doi.org/10.1021/acs.jproteome.9b00028.

(292) Rampersad, S. N. Multiple Applications of Alamar Blue as an Indicator of Metabolic Function and Cellular Health in Cell Viability Bioassays. *Sensors* **2012**, *12* (9), 12347–12360. https://doi.org/10.3390/s120912347.

(293) Ouellette, S. B.; Noel, B. M.; Parker, L. L. A Cell-Based Assay for Measuring Endogenous BcrAbl Kinase Activity and Inhibitor Resistance. *PLOS ONE* **2016**, *11* (9), e0161748. https://doi.org/10.1371/journal.pone.0161748.

(294) Shoemaker, R. H. The NCI60 Human Tumour Cell Line Anticancer Drug Screen. *Nat. Rev. Cancer* **2006**, *6* (10), 813–823. https://doi.org/10.1038/nrc1951.

(295) Gao, S.; Zhang, W.; Ma, J.; Ni, X. PHF6 Recruits BPTF to Promote HIF-Dependent Pathway and Progression in YAP-High Breast Cancer. *J. Transl. Med.* **2023**, *21* (1), 220. https://doi.org/10.1186/s12967-023-04031-8.

(296) Zahid, H.; Costello, J.; Kimbrough, J.; Actis, M.; Rankovic, Z.; Pomerantz, W. Design of Class I/IV Bromodomain-Targeting Degraders for Chromatin Remodeling Complexes. ChemRxiv October 5, 2022. https://doi.org/10.26434/chemrxiv-2022-41npn.

(297) Heiderscheit, E. A.; Eguchi, A.; Spurgat, M. C.; Ansari, A. Z. Reprogramming Cell Fate with Artificial Transcription Factors. *FEBS Lett.* **2018**, *592* (6), 888–900. https://doi.org/10.1002/1873-3468.12993.

(298) Erwin, G. S.; Grieshop, M. P.; Ali, A.; Jun, Q.; Lawlor, M.; Kumar, D.; Ahmad, I.; McNally, A.; Teider, N.; Worringer, K.; Sivasankaran, R.; Syed, D. N.; Eguchi, A.; Ashraf, Md.; Jeffery, J.; Mousheng, X.; Park, P. M. C.; Mukhtar, H.; Srivastava, A. K.; Faruq, M.; Bradner, J. E.; Ansari, A. Z. Synthetic Transcription Elongation Factors License Transcription across Repressive Chromatin. *Science* **2017**, *358* (6370), 1617–1622. https://doi.org/10.1126/science.aan6414.

(299) Brenke, R.; Kozakov, D.; Chuang, G.-Y.; Beglov, D.; Hall, D.; Landon, M. R.; Mattos, C.; Vajda, S. Fragment-Based Identification of Druggable “hot Spots” of Proteins Using Fourier Domain Correlation Techniques. *Bioinforma. Oxf. Engl.* **2009**, *25* (5), 621–627. https://doi.org/10.1093/bioinformatics/btp036.

(300) Kozakov, D.; Hall, D. R.; Chuang, G.-Y.; Cencic, R.; Brenke, R.; Grove, L. E.; Beglov, D.; Pelletier, J.; Whitty, A.; Vajda, S. Structural Conservation of Druggable Hot Spots in Protein-Protein Interfaces. *Proc. Natl. Acad. Sci. U. S. A.* **2011**, *108* (33), 13528–13533. https://doi.org/10.1073/pnas.1101835108.

(301) Baell, J. B.; Holloway, G. A. New Substructure Filters for Removal of Pan Assay Interference Compounds (PAINS) from Screening Libraries and for Their Exclusion in Bioassays. *J. Med. Chem.* **2010**, *53* (7), 2719–2740. https://doi.org/10.1021/jm901137j.

(302) Bröker, J.; Waterson, A. G.; Smethurst, C.; Kessler, D.; Böttcher, J.; Mayer, M.; Gmaschitz, G.; Phan, J.; Little, A.; Abbott, J. R.; Sun, Q.; Gmachl, M.; Rudolph, D.; Arnhof, H.; Rumpel, K.; Savarese, F.; Gerstberger, T.; Mischerikow, N.; Treu, M.; Herdeis, L.; Wunberg, T.; Gollner, A.; Weinstabl, H.; Mantoulidis, A.; Krämer, O.; McConnell, D. B.; W. Fesik, S. Fragment Optimization of Reversible Binding to the Switch II Pocket on KRAS Leads to a Potent, In Vivo Active KRASG12C Inhibitor. *J. Med. Chem.* **2022**, *65* (21), 14614–14629. https://doi.org/10.1021/acs.jmedchem.2c01120.

(303) Pandey, A. K.; Buchholz, C. R.; Nathan Kochen, N.; Pomerantz, W. C. K.; Braun, A. R.; Sachs, J. N. PH Effects Can Dominate Chemical Shift Perturbations in 1H,15N-HSQC NMR Spectroscopy for Studies of Small Molecule/α-Synuclein Interactions. *ACS Chem. Neurosci.* **2023**, *14* (4), 800–808. https://doi.org/10.1021/acschemneuro.2c00782.

(304) Azatian, S. B.; Kaur, N.; Latham, M. P. Increasing the Buffering Capacity of Minimal Media Leads to Higher Protein Yield. *J. Biomol. NMR* **2019**, *73* (1), 11–17. https://doi.org/10.1007/s10858-018-00222-4.

(305) Williamson, M. P. Using Chemical Shift Perturbation to Characterise Ligand Binding. *Prog. Nucl. Magn. Reson. Spectrosc.* **2013**, *73*, 1–16. https://doi.org/10.1016/j.pnmrs.2013.02.001.

(306) *Site Directed Mutagenesis Kits*. Agilent. https://www.agilent.com/en/product/mutagenesis-cloning/mutagenesis-kits/site-directed-mutagenesis-kits/quikchange-233116#literature (accessed 2023-05-03).

(307) Wang, G. G.; Song, J.; Wang, Z.; Dormann, H. L.; Casadio, F.; Li, H.; Luo, J.-L.; Patel, D. J.; Allis, C. D. Haematopoietic Malignancies Caused by Dysregulation of a Chromatin-Binding PHD Finger. *Nature* **2009**, *459* (7248), 847–851. https://doi.org/10.1038/nature08036.

6) Appendix A: Crystallography for BET Bromodomain, BRD4

Portions of this appendix reprinted with permission from Cui, H.; Carlson, A.C.; Schleiff, M.A.; Divakaran, A.; Johnson, J.A.; Buchholz, C.R.; Zahid, H.; Vail, N.R.; Shi, K.; Aihara, H.; Harki, D.A.; Miller, G.P.; Topczewski, J.J.; Pomerantz, W.C.K. 4-Methyl-1,2,3-Triazoles as N-Acetyl-Lysine Mimics Afford Potent BET Bromodomain Inhibitors with Improved Selectivity. *J. Med. Chem.*, **2021**, *64*, 14, 10497–10511.

Contribution of Authors: H.C. and A.C.C. synthesized the compounds; J.A.J., C.R.B., H.Z., N.R.V., K.S. performed crystallography. H.A., D.A.H., G.P.M., J.T.P., W.C.K.P directed research.

Motivation: The goal of the work described in this Appendix chapter is to use X-ray crystallography as a structural biology tool to guide bromodomain inhibitor development, by obtaining co-crystal structures with small molecules. My contribution to this work has been solving a crystal structure for BRD4 D1, co-crystallized with one of the BET bromodomain inhibitors designed in the Pomerantz lab.

6.1 Introduction

To improve our understanding of the role of individual bromodomains, selective inhibitors for specific BET bromodomains have been developed. We recently reported on UMN627, featuring an imidazole ring as the acetylated histone mimetic (**Figure 6.1A**), as a selective BRD4 D1 inhibitor.[1,2] UMN627 engaged BRD4 at submicromolar concentrations, but, unexpectedly, it did not inhibit c-Myc expression at these concentrations.[1] However, UMN627 effectively suppressed chemokine expression resulting from inflammation in the liver in vitro and in vivo.[2] Given the sometimes unanticipated biological effects of BET inhibitors, new design strategies are needed to develop selective bromodomain inhibitors. More selective inhibitors could be used to illuminate the biological mechanisms of specific bromodomains and potentially be used as therapeutic agents. However, the long synthetic route needed to synthesize UMN627 precluded rapid assessment of the structure–activity relationships (SARs) to improve affinity and selectivity. To address this challenge, Pomerantz and Topczewski lab members developed a similar inhibitor based on a triazole scaffold using a click reaction.[1,3] Starting from our previously reported inhibitor, **1**,[3] this report described a systematic SAR study using the triazole scaffold that led to compounds with improved BRD4 D1 affinity, D1 vs D2 selectivity, and metabolic stability (**Figure 6.1B**).

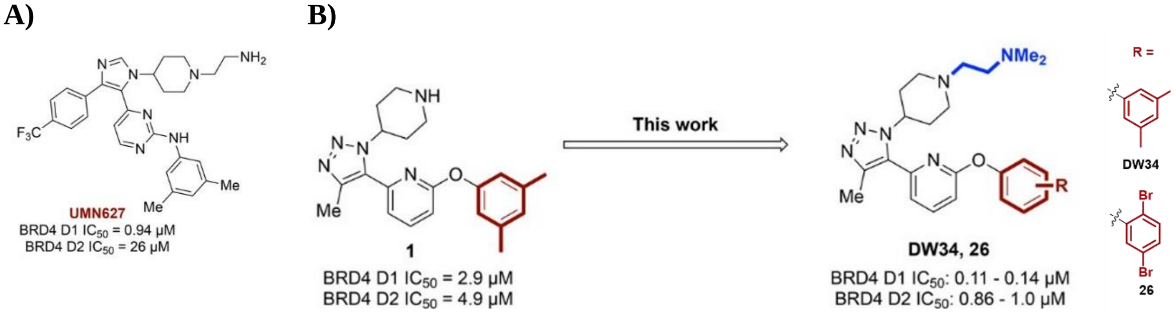

Figure 6.1: BET Bromodomain Inhibitors.

(A) BRD4 D1 inhibitor UMN627. (B) Exploiting D2/D1 differences to improve selectivity.

6.2 Co-Crystal Structure of BRD4 D1 with Compound 23

Insights into the triazole scaffold inhibitor binding were gleaned through crystallography. Previously, an ethylamino group was used in UMN627 to target a nonconserved amino acid residue, Asp144, in BRD4 D1. In this case, a 2.1-fold affinity increase was observed; however, inspection of the resulting cocrystal structure indicated the basic amino group was oriented in an unfavorable direction, positioned 10.4 Å (N to O═C) away.[1] To compare the triazole scaffold, a cocrystal structure of inhibitor **23 (Figure 6.2A**) with BRD4 D1 was obtained. A structural analysis indicated a more favorable orientation of the piperidyl ring pointing toward Asp 144 (**Figure 6.2B**). This interaction indicated that attaching a basic group might be particularly advantageous. The distance between the piperidyl nitrogen atom on inhibitor **23** was 6.3 Å away from a carboxylate oxygen in Asp144. With this information, an *N*,*N*-dimethylethylamino group was installed on inhibitors **1** and **23** to yield two new inhibitors **25**, now referred to as **DW34**, and **26** (**Figure 6.1B**).

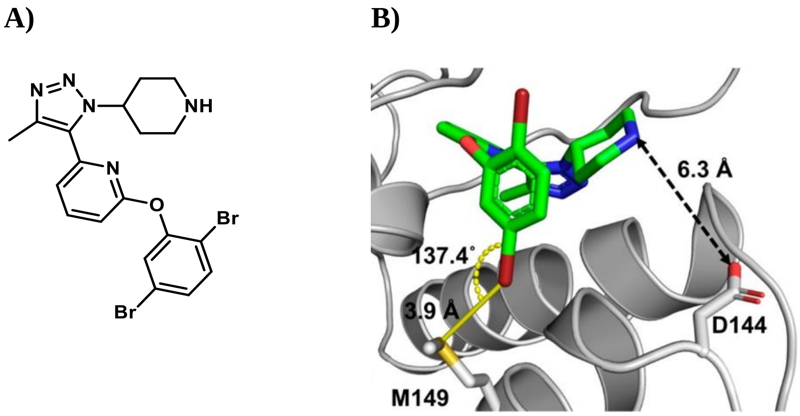

Figure 6.2: Co-crystal structure of BRD4 D1 with Compound 23.

(A) Compound **23** (B) Co-crystal structure of **23** (green) with BRD4 D1 (gray). The distance between the piperidyl group of **23** and Asp144 is indicated. The distance and bond angle between bromide on the aryl group and M149 are shown, which are inconsistent with halogen bonding. PDB ID: 7MLS.

6.3 Experimental Section

Crystallization Conditions and X-ray Data Collection Methods. Compound **23** (500 μM) was cocrystallized with BRD4 D1 (300 μM, in 10 mM HEPES, 100 mM NaCl, pH 7.4) in 100 mM Bis-Tris propane, 20% (v/v) PEG 3350, 10% (v/v) ethylene glycol at pH 8.5 using the hanging drop method. Harvestable crystals grew in 1–2 days at ambient temperature. Crystals were harvested, cryoprotected in ethylene glycol, and flash frozen. Data were collected at Advanced Photon Source with the NE-CAT 24-ID-C and E beamlines. Phaser was used to solve the structure via molecular replacement using PDB ID 3MXF as a search model.[4] Phenix[5] and Coot[6] were used for structure refinement (data collection and refinement statistics in **Table 6.1**).

Table 6.1. Data collection and refinement statistics for compound 23.

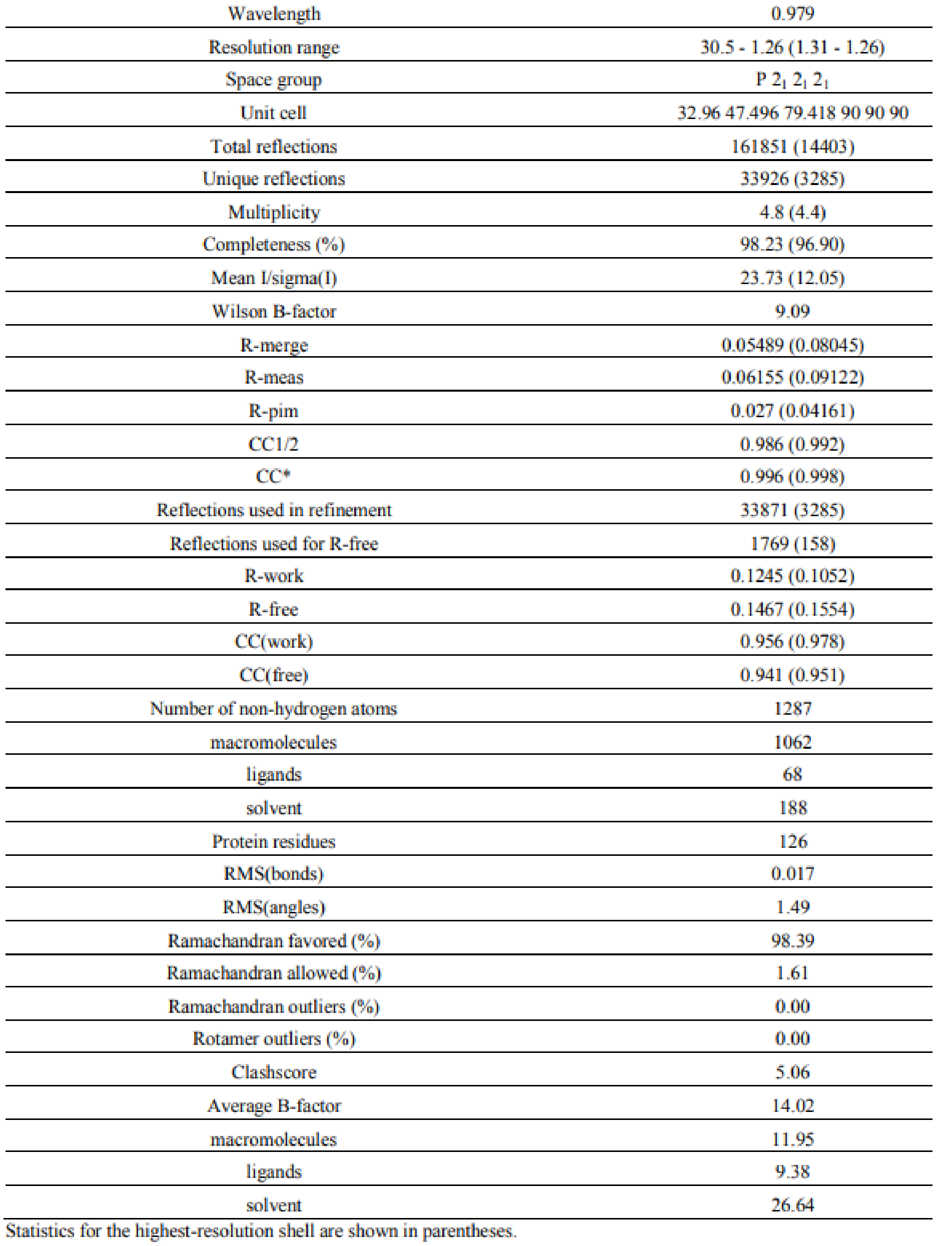

Wavelength	0.979
Resolution range	30.5 - 1.26 (1.31 - 1.26)
Space group	P 2_1 2_1 2_1
Unit cell	32.96 47.496 79.418 90 90 90
Total reflections	161851 (14403)
Unique reflections	33926 (3285)
Multiplicity	4.8 (4.4)
Completeness (%)	98.23 (96.90)
Mean I/sigma(I)	23.73 (12.05)
Wilson B-factor	9.09
R-merge	0.05489 (0.08045)
R-meas	0.06155 (0.09122)
R-pim	0.027 (0.04161)
CC1/2	0.986 (0.992)
CC*	0.996 (0.998)
Reflections used in refinement	33871 (3285)
Reflections used for R-free	1769 (158)
R-work	0.1245 (0.1052)
R-free	0.1467 (0.1554)
CC(work)	0.956 (0.978)
CC(free)	0.941 (0.951)
Number of non-hydrogen atoms	1287
macromolecules	1062
ligands	68
solvent	188
Protein residues	126
RMS(bonds)	0.017
RMS(angles)	1.49
Ramachandran favored (%)	98.39
Ramachandran allowed (%)	1.61
Ramachandran outliers (%)	0.00
Rotamer outliers (%)	0.00
Clashscore	5.06
Average B-factor	14.02
macromolecules	11.95
ligands	9.38
solvent	26.64

Statistics for the highest-resolution shell are shown in parentheses.

6.4 References

(1) Cui, H.; Divakaran, A.; Pandey, A. K.; Johnson, J. A.; Zahid, H.; Hoell, Z. J.; Ellingson, M. O.; Shi, K.; Aihara, H.; Harki, D. A.; et al. Selective N-Terminal BET Bromodomain Inhibitors

by Targeting Non-Conserved Residues and Structured Water Displacement**. Angew. Chem., Int. Ed. 2021, 60, 1220−1226.

(2) Gao, J.; Wei, B.; Liu, M.; Hirsova, P.; Sehrawat, T. S.; Cao, S.; Hu, X.; Xue, F.; Yaqoob, U.; Kang, N.; et al. Endothelial P300 Promotes Portal Hypertension and Hepatic Fibrosis through C-C Motif Chemokine Ligand 2-mediated Angiocrine Signaling. Hepatology 2021, 73 (6), 2468−2483.

(3) Carlson, A. S.; Cui, H.; Divakaran, A.; Johnson, J. A.; Brunner, R. M.; Pomerantz, W. C. K.; Topczewski, J. J. Systematically Mitigating the P38α Activity of Triazole-Based BET Inhibitors. ACS Med. Chem. Lett. 2019, 10 (9), 1296−1301.

(4) Mccoy, A. J.; Grosse-kunstleve, R. W.; Adams, P. D.; Winn, M. D.; Storoni, L. C.; Read, R. J. Research Papers Phaser Crystallographic Software Research Papers. J. Appl. Crystallogr. 2007, 40, 658−674.

(5) Adams, P. D.; Afonine, P. V.; Bunkóczi, G.; Chen, V. B.; Davis, I. W.; Echols, N.; Headd, J. J.; Hung, L. W.; Kapral, G. J.; GrosseKunstleve, R. W.; et al. PHENIX: A Comprehensive Python-Based System for Macromolecular Structure Solution. Acta Crystallogr., Sect. D: Biol. Crystallogr. 2010, 66 (2), 213−221.

(6) Emsley, P.; Lohkamp, B.; Scott, W. G.; Cowtan, K. Features and Development of Coot. Acta Crystallogr., Sect. D: Biol. Crystallogr. 2010, 66 (4), 486−501.

7) Appendix B: ^{1}H,^{15}N-HSQC NMR Analysis of Alpha Synuclein/Small Molecule Interactions at Varying pH

Portions of this appendix reprinted with permission from Pandey, A.K.; Buchholz, C.R.; Kochen, N.N.; Pomerantz, W.C.K.; Braun, A.R.; Sachs, J. pH Effects Can Dominate Chemical Shift Perturbations in ^{1}H,^{15}N-HSQC NMR Spectroscopy of Small Molecule/alpha-Synuclein Interactions. *ACS Chem. Neurosci.* **2023**, *14*, 800-808.

Author Contributions: A.K.P. and A.R.B. contributed equally to this work. A.P., A.R.B., and J.N.S. conceived of and directed the study. A.P. and N.N.K. produced and purified recombinant protein; A.P. performed all HSQC NMR experiments; N.N.K. performed all aggregation experiments; A.P. and C.R.B. performed resonance assignment. W.C.K.P. provided consultation on HSQC experiment interpretation and data analysis. A.P., A.R.B., and J.N.S. wrote and edited the manuscript.

Motivation: The goal of the work described in this chapter is to use ^{1}H,^{15}N-HSQC NMR spectroscopy as a structural biology tool to explore small molecule/α-synuclein interactions. My contribution to this work has been performing resonance analysis on HSQC NMR spectra obtained in the Sachs lab to calculate chemical shift perturbations.

7.1 Introduction

α-synuclein (aSyn) is an intrinsically disordered protein whose misfolding and aggregation into toxic oligomers and fibrils (e.g., Lewy bodies) are implicated in numerous α-synucleinopathies, including Parkinson's disease. Small molecule inhibitors that arrest this intrinsically disordered protein transformation are highly desired.[1-5] We recently published a series of small molecules that reduce aSyn toxicity in multiple cell lines with high potency.[6] In this study, we employ ^{1}H,^{15}N-HSQC NMR and chemical shift perturbation (CSP) to examine direct target engagement for these hit compounds. In preliminary experiments, it quickly became apparent that small-molecule formulations (specifically those complexed with acidic salts) can significantly influence the pH of the NMR sample, confounding interpretation of the HSQC spectrum and CSP profile. To decouple compound binding from small-molecule-induced effects on solution pH, we undertook a detailed investigation of the pH effects on aSyn HSQC NMR spectra, confirming the importance of stringent pH control when exploring small molecule binders of monomeric aSyn.

7.2 Changes in pH Induce Large-Scale Perturbation of aSyn HSQC Spectra

Taking advantage of the residue-specific sensitivity of ^{1}H,^{15}N-HSQC NMR, we examined pH-induced changes on the intrinsically disordered monomeric form of aSyn. **Figure 7.1B** illustrates the HSQC NMR spectra and residue assignments for aSyn at pH 7.4, recapitulating spectra in previous studies.[7-9] CSP of the amide resonances corresponding to basic and acidic residues are known to be sensitive to pH changes in HSQC NMR. **Figure 7.1B-G** demonstrate the significant structural changes that occur to aSyn throughout the pH titration range (4.5, 5, 5.5, 6, 6.5, 7, and 7.4; ±0.1). Large-scale pH-induced structural perturbations are observed at all acidic pH values relative to pH 7.4. Throughout the pH titration, we observe the most significant ΔCSP for the H50 resonance (**Figure 7.1B,C**), where most of the change occurs between pH 7.4 and pH 6.0. Across the full pH titration, the histidine amide resonance moved from 8.30 to 8.53 ppm ($\Delta\delta = 0.23$ ppm) along ^{1}H axis and 124.7–123.1 ppm ($\Delta\delta = 1.6$ ppm) along the ^{15}N axis. Indeed, when we look at the overall CSP profile (**Figure 7.1G**), it is dominated by the H50 perturbation, although additional, nonionizable residues near H50 also display significant perturbation at pH 6 (**Figure 7.1G**; T44, E46, V48, and V52), suggesting that the ionization of H50 induces a sufficient change in the local chemical environment to result in a structural change capable of increasing aSyn’s aggregation propensity.

aSyn's acidic residues also undergo dramatic ΔCSP across the pH titration, with the greatest perturbations occurring near aSyn's pI, between pH 5.0 and 4.5 (in particular residues E20, E83, D119, D121, E126, E137). Interestingly, this effect is predominantly observed with the C-terminal acidic residues more so than those located in the N-terminal domain and was previously described at a more acidic pH of 3.0.[9] The pH transition with the largest ΔCSP for these acidic residues coincides with the second increase in fibrillization rate. This suggests that the degree of ionization required to induce an aggregation-prone aSyn monomer conformation is closer to aSyn's pI, and the corresponding structural changes are localized to C-terminal residues.

Multiple nonacidic residues (both polar and nonpolar) were also significantly impacted by pH changes. These include V3, G7, V52, G84, N103, Q109, L113, S129, and A140. All of these residues, except G7, are adjacent to at least one acidic residue, whereas N103, L113, and S129 (**Figure 7.1D**) precede 2 acidic residues. These shifts could be attributed to the electronic effects caused by changes in the ionization states of these acidic residues or due to changes in the local environment or structure. Threonine residues displayed a modest pH-dependent CSP. Among the aromatic residues, Y125 and Y136 showed appreciable movement (**Figure 7.1E**) of the amide resonance—which was not surprising as these residues are within the acidic C-terminal tail—whereas both phenylalanine residues displayed no resolvable ΔCSP.

These large pH-driven effects in the aSyn HSQC spectrum highlight the need for caution while investigating small-molecule interactions. Many small molecules are formulated with acidic salts that could overwhelm the buffering capacity of samples at the concentrations typically used in HSQC NMR experiments. Evaluation of small molecules–protein interactions should control for these effects to minimize the potential for interpreting false-positive CSP. Below, we evaluate a series of known small-molecule binders to aSyn as well as novel compounds recently published by our group.[6]

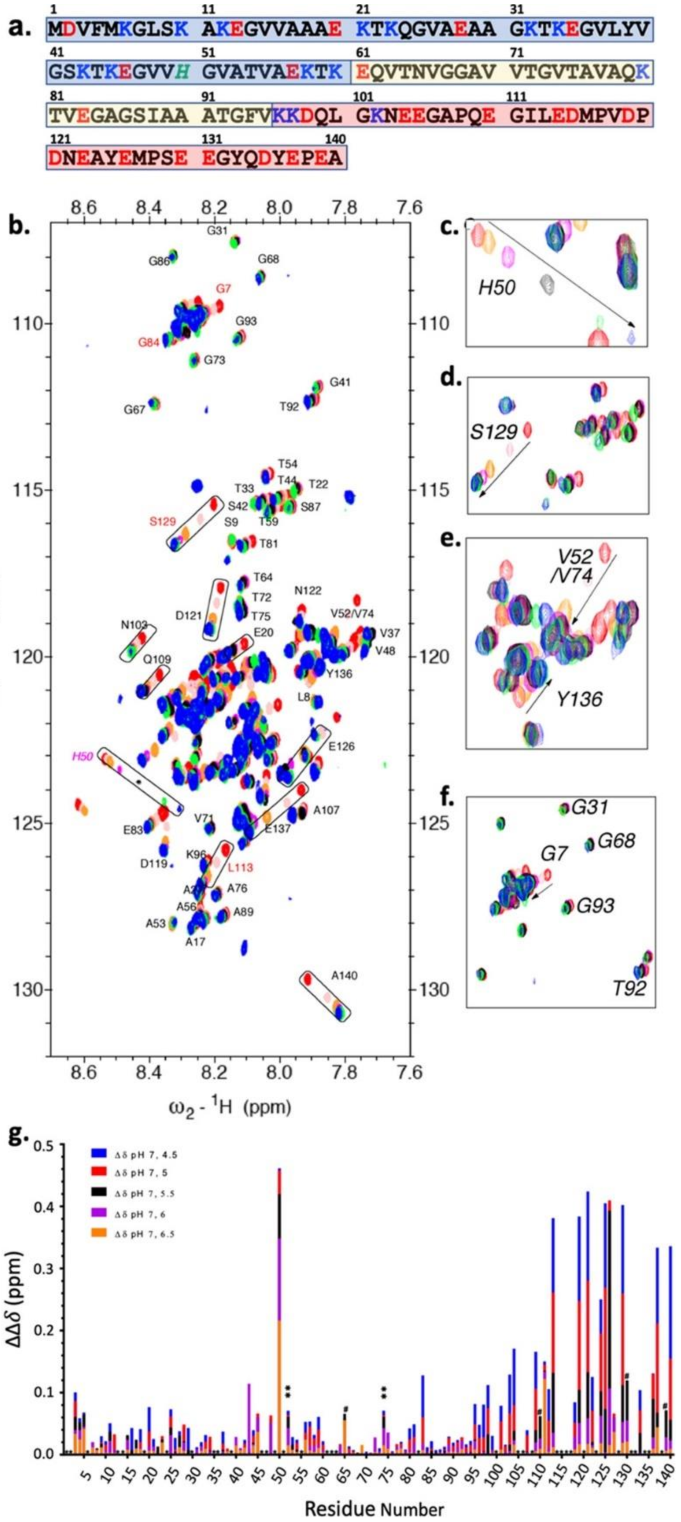

Figure 7.1: pH effects on aSyn.

(a) Sequence of aSyn. N-terminal segment (1–60) is shaded in light blue, NAC region (61–95) in light yellow, and C-terminal segment (96–140) in pink. Basic residues, lysine residues are colored blue, and aspartic and glutamic acids are colored red; (b) pH titration of aSyn at pH 4.5 (red), 5.0 (pink), 5.5 (orange), 6.0 (magenta), 6.5 (black), 7.0 (green), and 7.4 (blue). Residues adjacent to acidic amino acids are colored red; (c–f) pH effects on residues His50, Ser129, Val52, Tyr136, and Gly7. (g) Summary of ΔCSP due to pH changes. * indicates an unresolved resonance at all pH; # indicates an unresolved resonance at pH 4.5, 5; ** resonance 52/74 are indistinguishable.

7.3 Small-Molecule Binding with Monomeric α Synuclein Using HSQC NMR Spectroscopy

Using rigorously controlled pH experimental conditions in HSQC NMR spectroscopy─including micro-pH electrode monitoring of NMR sample pH and H50’s resonance as an internal pH calibration point─we tested a series of compounds previously investigated as aSyn binders (EGCG, Baicalin, and DOPA).

EGCG has been extensively reported in the literature to bind the monomeric or low-molecular-weight aSyn species using various analytical approaches, including HSQC NMR. We did not observe any significant shift at H50 with the addition of 5 molar equivalents (eqv) of EGCG at pH 7.0, indicating a consistent pH between apo and with added EGCG samples However, there was significant CSP for numerous other residues (**Figure 7.2A**). These shifts across the protein indicate a nonspecific binding pattern with EGCG, as was previously described.[7] Baicalin is another small molecule that is a known modulator of aSyn aggregation.[10-14] We observed modest changes in the amide chemical shifts, along with signal attenuation of several residues without perturbation of H50 (**Figure 7.2B**), indicating small-molecule binding with no pH effect.

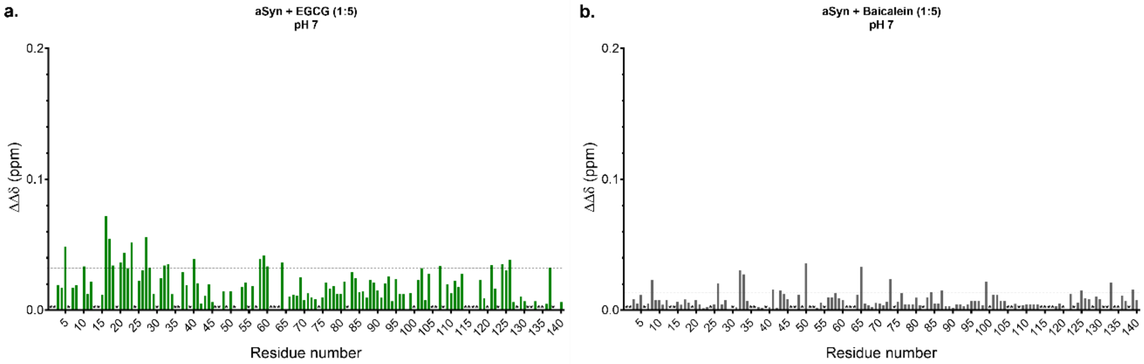

Figure 7.2: Small molecule effects on aSyn.

Chemical shift perturbation (CSP) of aSyn (pH 7) in the presence of (a) EGCG (5 eq.); (b) Baicalin (5 eq.). A dashed line represents perturbation greater than the average plus one standard deviation. pH of the samples was measured prior to NMR acquisition. * indicates an unresolved resonance.

7.4 pH-Driven Artifacts in HSQC NMR Spectroscopy Result in False-Positive Interpretation of Small-Molecule Binding

We next evaluated DOPA-induced effects on aSyn's HSQC NMR spectra. When we applied rigorous control for the pH of our samples, we did not observe any significant changes in CSP at physiological pH 7.0, even with 5 eqv of DOPA (**Figure 7.3A**). This is in stark contrast to results from a previous HSQC NMR study,[7] where DOPA–aSyn interactions induced a significant CSP at H50 as well as throughout the C-terminal tail. Closer inspection of that DOPA titration CSP profile[7] shows a large initial CSP at H50 (0.2 DOPA eqv), followed by increasing CSP at the C-terminal tail with increasing DOPA concentrations, a trend that mirrors the pH-induced CSP profile observed here (**Figure 7.1G**).

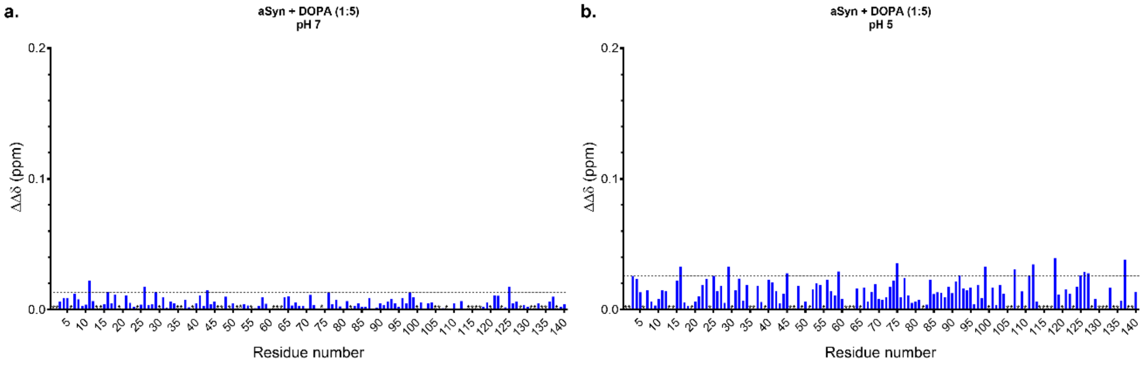

Figure 7.3: pH effects on DOPA

CSP of APO vs +DOPA ((a) pH 7.0; (b) pH 5.0). A dashed line represents perturbation greater than the average plus one standard deviation. pH of the samples was measured prior to NMR acquisition.
* indicates an unresolved resonance.

Commercially available DOPA is formulated as a hydrochloride (HCl) salt, and the acid component can significantly alter the pH of the solution. It is important to note that differences in buffering solutions would result in different magnitudes of pH change due to small molecule additions. In the previous DOPA–aSyn study, a Gly-NaOH buffer (ideal buffering range: pH 8.6–10.6) was used, whereas in this study, we employed phosphate buffer (ideal buffering range: pH 5.8–8.0). Without pH correction in our phosphate-buffered samples, the addition of 5 eqv of DOPA-HCl resulted in a significant pH change (ΔpH = −2.0, and a corresponding H50 shift of ~0.05 ppm). These large changes could easily mask or overwhelm small-molecule binding effects, highlighting that for a more accurate evaluation of ligand–aSyn interactions, a closer control of experimental conditions is essential.

When we compare apo aSyn at pH 5.0 to DOPA at pH 5.0 (**Figure 7.3B**), we observe significant DOPA-induced CSP for multiple resonances that are not due to pH effects (e.g., no discernible H50 $\Delta\delta$ ppm). Although these CSPs are significantly reduced relative to the pH effect CSP, there are perturbations not observed in the pH 7.0 Apo vs DOPA pH 7.0 spectra that suggests DOPA interacts with aSyn at pH 5.0, and the pH-controlled conditions provide an artifact-free mapping of DOPA interactions with aSyn.

These results highlight the significant challenge of potential false-positive interpretation of small-molecule binding to aSyn via HSQC NMR if pH effects are not considered, especially for compounds complexed in acidic salts.

7.5 Experimental Section

NMR Spectroscopy. $^1H,^{15}N$-HSQC NMR data were acquired on an 850 MHz Bruker Avance III equipped with a 5 mm triple resonance cryoprobe at 288 K in pH 6 phosphate buffer containing 5 mM phosphate, 25 mM NaCl, 5% D_2O, and 0.01% DSS at the Minnesota NMR (MNMR) center at the University of Minnesota. Proteins were uniformly enriched with ^{15}N, as described before.[15] DSS (4,4-dimethyl-4-silapentane-1-sulfonic acid) was used as an internal reference for spectra calibration, and assignments were made by analogy as per published reports deposited in BMRB (BMRB accession number 16543). NMR spectra were processed using Topspin 4.0.8 and analyzed with Sparky 3.115. To investigate residue-specific structural perturbations due to pH changes in the α synuclein protein, CSPs (chemical shift perturbations) were calculated using the equation CSP = $\sqrt{}(\Delta\ \delta H_N)^2 + (0.1\Delta\ \delta N_H)^2$, where $\Delta\ \delta H_N$ and δN_H are the difference in the chemical shift of proton and nitrogen, respectively.[16] HSQC spectra were collected with 100 μM uniformly ^{15}N-labeled protein samples with 256 data points and with 8 scans.

7.6 References

(1) Dyson, H. J.; Wright, P. E. Intrinsically unstructured proteins and their functions. Nat. Rev. Mol. Cell Biol. 2005, 6, 197−208.

(2) Wright, P. E.; Dyson, H. J. Intrinsically disordered proteins in cellular signalling and regulation. Nat. Rev. Mol. Cell Biol. 2015, 16, 18−29.

(3) Ayyadevara, S.; Ganne, A.; Balasubramaniam, M.; Reis, R. J. S. Intrinsically disordered proteins identified in the aggregate proteome serve as biomarkers of neurodegeneration. Metab. Brain Dis. 2022, 37, 147−152.

(4) Morris, O. M.; Torpey, J. H.; Isaacson, R. L. Intrinsically disordered proteins: modes of binding with emphasis on disordered domains. Open Biol. 2021, 11, No. 210222.

(5) Cuchillo, R.; Michel, J. Mechanisms of small-molecule binding to intrinsically disordered proteins. Biochem. Soc. Trans. 2012, 40, 1004− 1008.

(6) Braun, A. R.; Liao, E. E.; Horvath, M.; Kalra, P.; Acosta, K.; Young, M. C.; Kochen, N. N.; Lo, C. H.; Brown, R.; Evans, M. D.; et al. Potent inhibitors of toxic alpha-synuclein identified via cellular time-resolved FRET biosensors. npj Parkinson's Dis. 2021, 7, No. 52.

(7) Jha, N. N.; Rakesh, K.; Rajlaxmi, P.; Ambuja, N.; Dhiman, G.; Shruti, S.; Mritunjoy, M.; Ashutosh, K.; K, M. S. Comparison of alpha-Synuclein Fibril Inhibition by Four Different Amyloid Inhibitors. ACS Chem. Neurosci. 2017, 8, 2722−2733.

(8) Cho, M. K.; Nodet, G.; Kim, H. Y.; Jensen, M. R.; Bernado, P.; Fernandez, C. O.; Becker, S.; Blackledge, M.; Zweckstetter, M. Structural characterization of alpha-synuclein in an aggregation prone state. Protein Sci. 2009, 18, 1840−1846.

(9) McClendon, S.; Rospigliosi, C. C.; Eliezer, D. Charge neutralization and collapse of the C-terminal tail of alpha-synuclein at low pH. Protein Sci. 2009, 18, 1531−1540.

(10) Zhu, M.; Rajamani, S.; Kaylor, J.; Han, S.; Zhou, F.; Fink, A. L. The flavonoid baicalein inhibits fibrillation of alpha-synuclein and disaggregates existing fibrils. J. Biol. Chem. 2004, 279, 26846−26857.

(11) Kragh, C. L.; Lund, L. B.; Febbraro, F.; Hansen, H. D.; Gai, W. P.; El-Agnaf, O.; Richter-Landsberg, C.; Jensen, P. H. Alpha-synuclein aggregation and Ser-129 phosphorylation-dependent cell death in oligodendroglial cells. J. Biol. Chem. 2009, 284, 10211−10222.

(12) Jiang, M.; Porat-Shliom, Y.; Pei, Z.; Cheng, Y.; Xiang, L.; Sommers, K.; Li, Q.; Gillardon, F.; Hengerer, B.; Berlinicke, C.; et al. Baicalein reduces E46K α-synuclein aggregation in vitro and protects cells against E46K α-synuclein toxicity in cell models of familiar Parkinsonism. J. Neurochem. 2010, 114, 419−429.

(13) Lu, J. H.; Ardah, M. T.; Durairajan, S. S.; Liu, L. F.; Xie, L. X.; Fong, W. F.; Hasan, M. Y.; Huang, J. D.; El-Agnaf, O. M.; Li, M. Baicalein inhibits formation of α-synuclein oligomers within living cells and prevents Aβ peptide fibrillation and oligomerisation. Chembiochem 2011, 12, 615−624.

(14) Caruana, M.; Neuner, J.; Högen, T.; Schmidt, F.; Kamp, F.; Scerri, C.; Giese, A.; Vassallo, N. Polyphenolic compounds are novel protective agents against lipid membrane damage by α-synuclein aggregates in vitro. Biochim. Biophys. Acta, Biomembr. 2012, 1818, 2502−2510.

(15) Marley, J.; Lu, M.; Bracken, C. A method for efficient isotopic labeling of recombinant proteins. J. Biomol. NMR 2001, 20, 71−75.

(16) Williamson, M. P. Using chemical shift perturbation to characterise ligand binding. Prog. Nucl. Magn. Reson. Spectrosc. 2013, 73, 1– 16.

8) Appendix C: ^{1}H and ^{13}C NMR Spectra of Small Molecules from Chapters 2, 4, and 5

8.1 Chapter 2 NMR Spectra

2.4, ^{1}H NMR (400 MHz, DMSO-d_6)

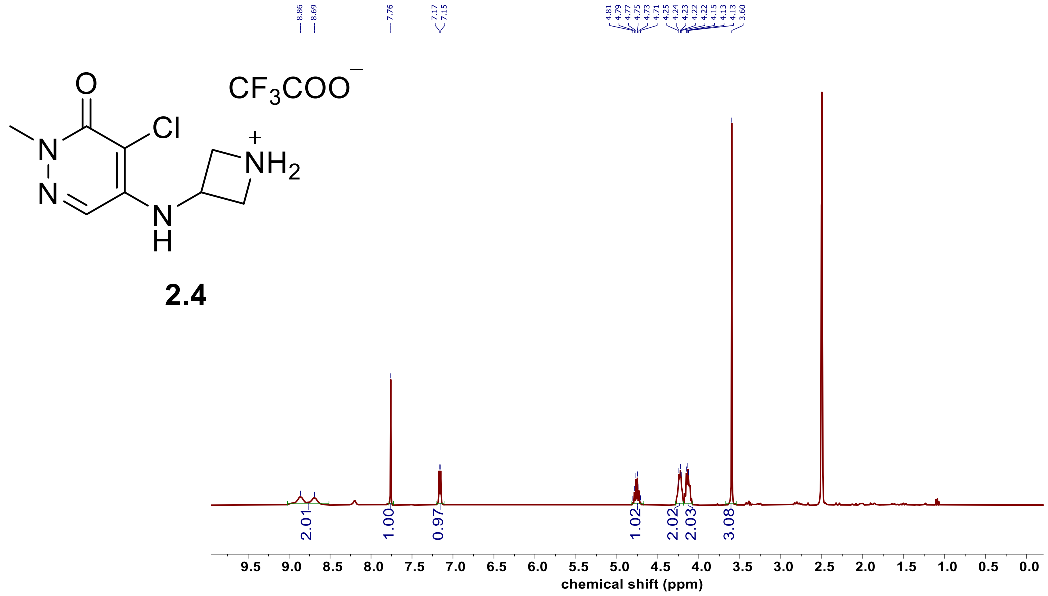

2.4, ^{13}C NMR (126 MHz, DMSO-d_6)

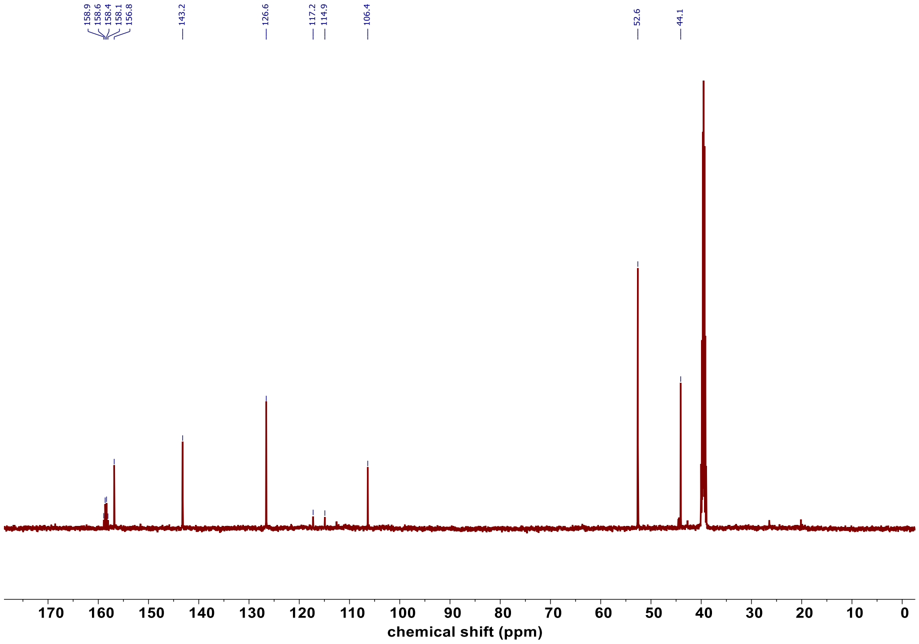

2.5, ^{1}H NMR (500 MHz, DMSO-d_6)

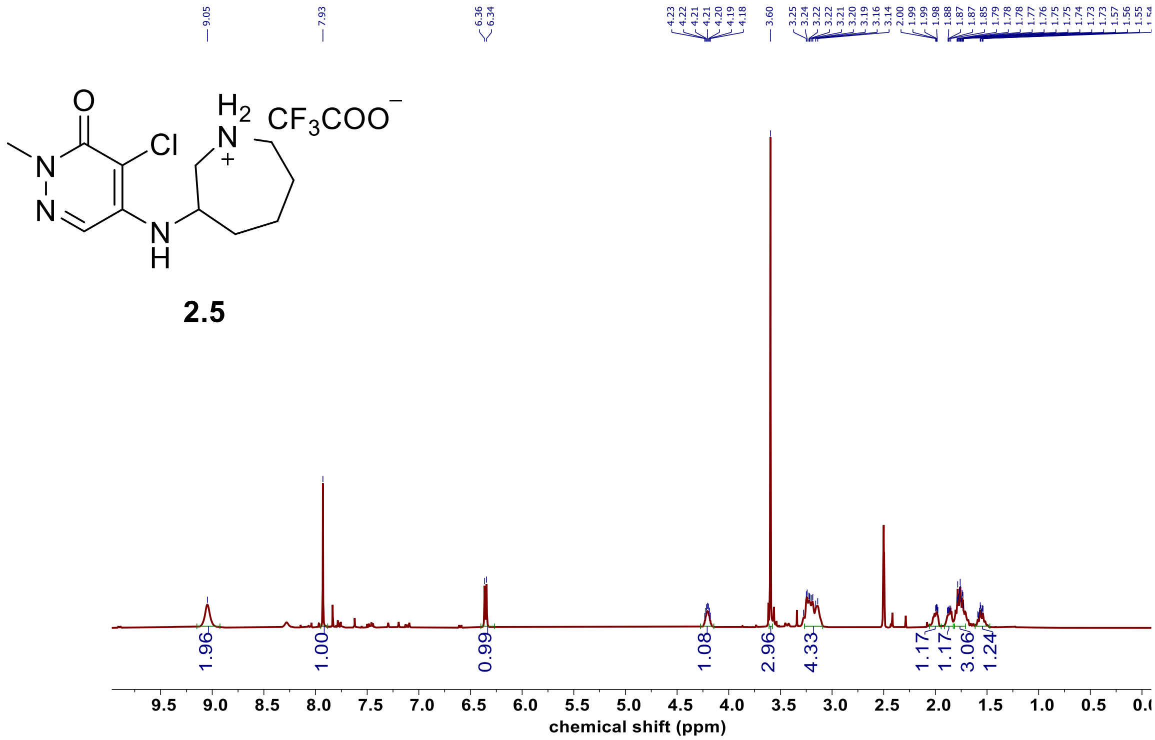

2.5, ^{13}C NMR (126 MHz, DMSO-d_6)

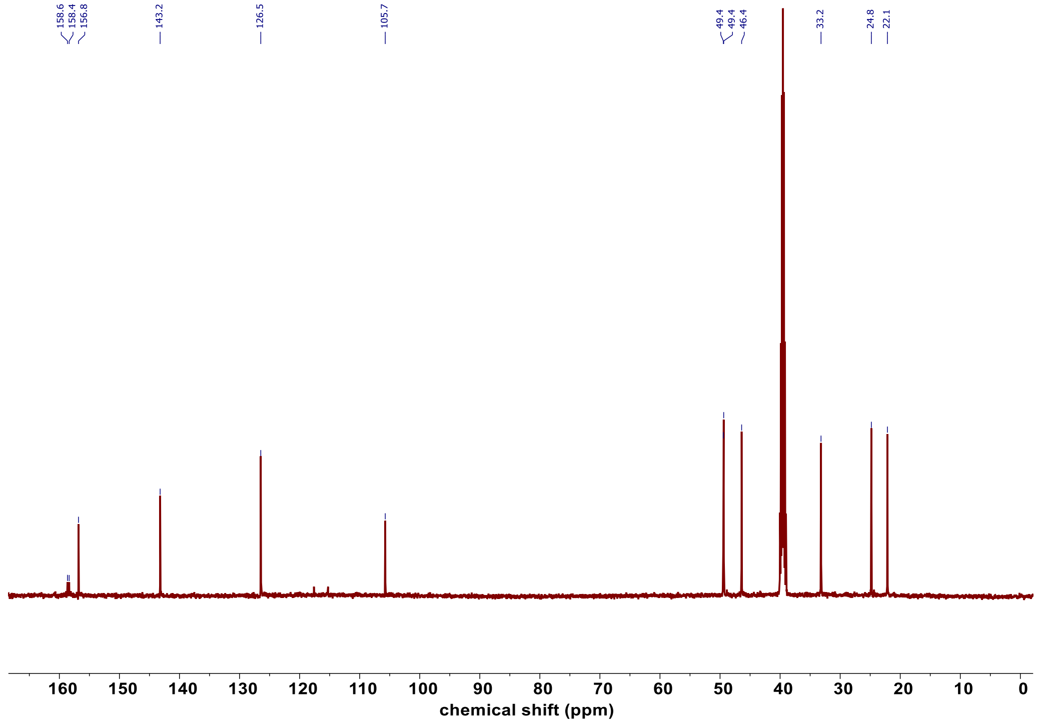

2.6, ^{1}H NMR (500 MHz, DMSO-d_6)

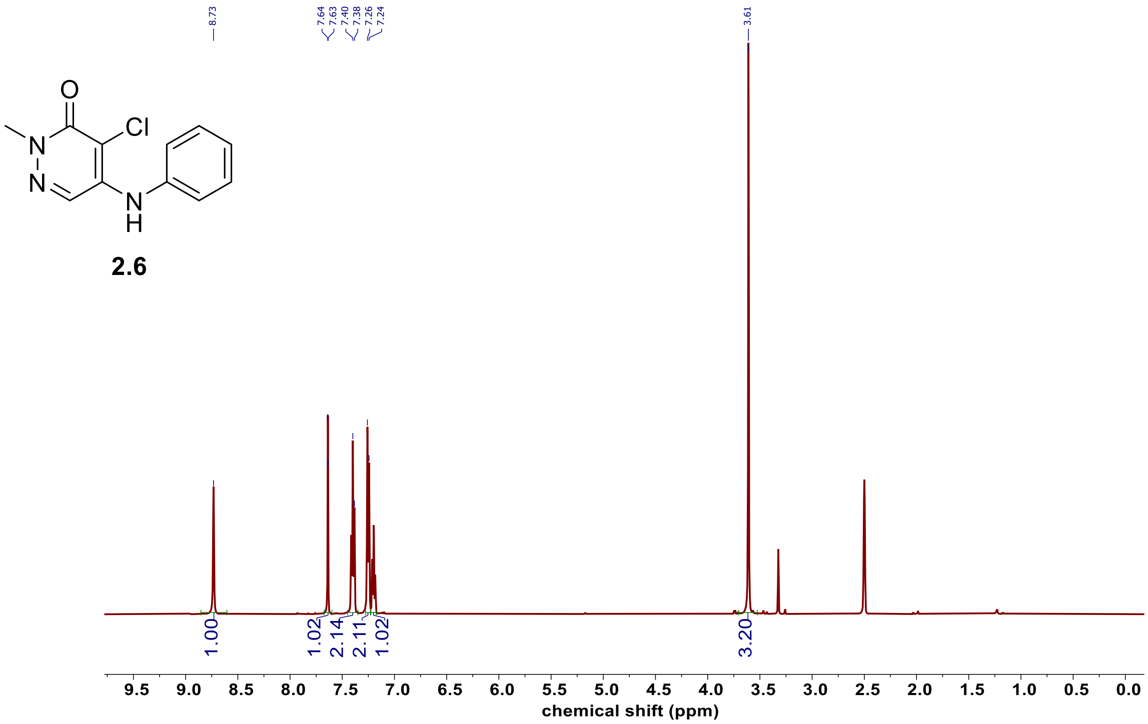

2.6

2.6, ^{13}C NMR (126 MHz, DMSO-d_6)

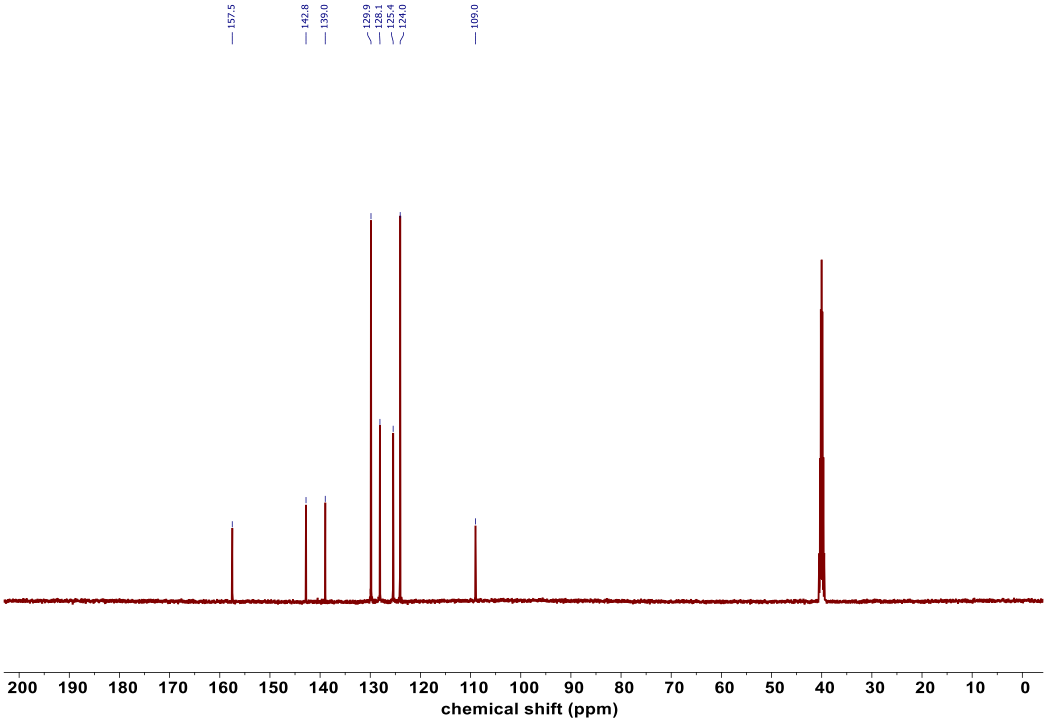

2.7, ^{1}H NMR (500 MHz, Methanol-d_4)

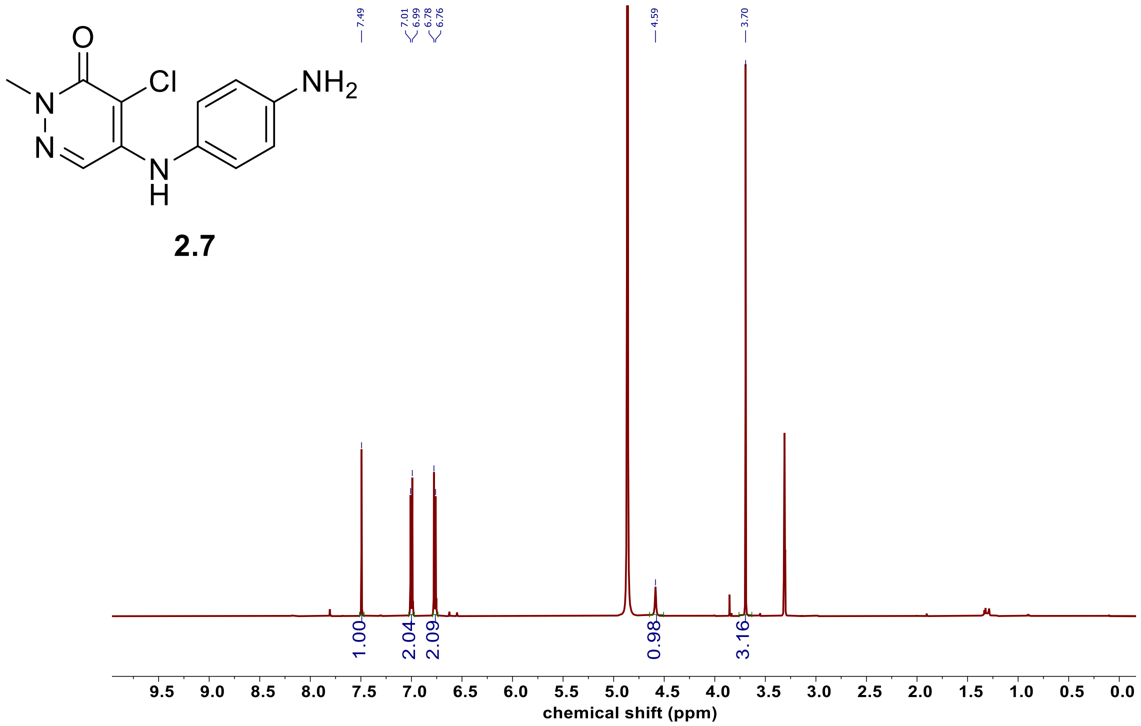

2.7, ^{13}C NMR (126 MHz, Methanol-d_4)

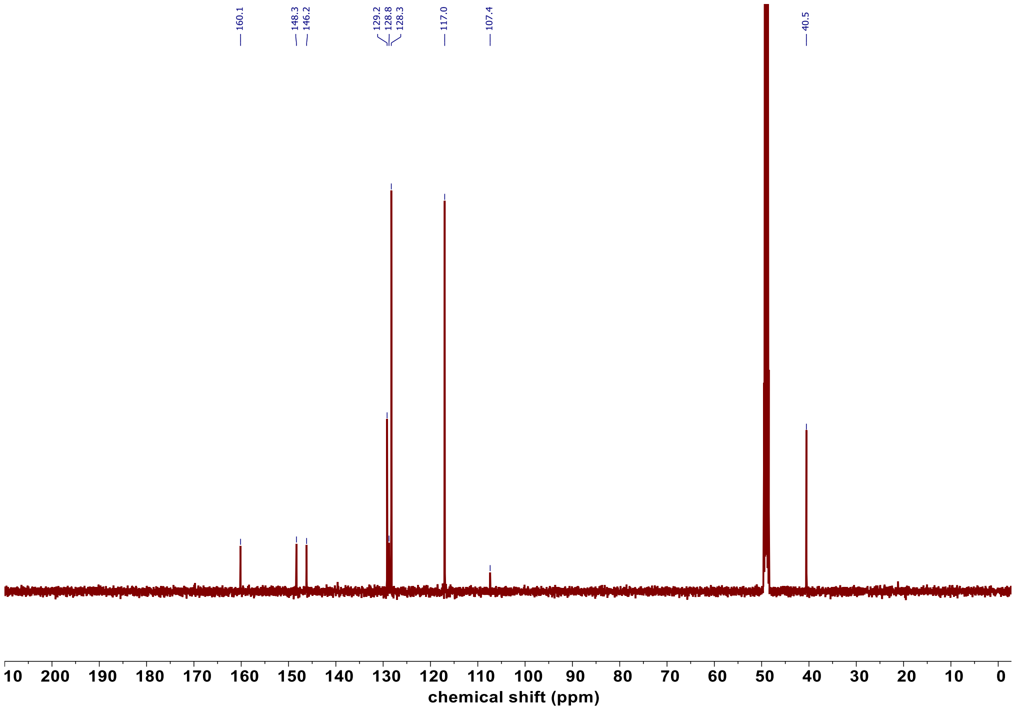

2.8, ^{1}H NMR (500 MHz, DMSO-d_6)

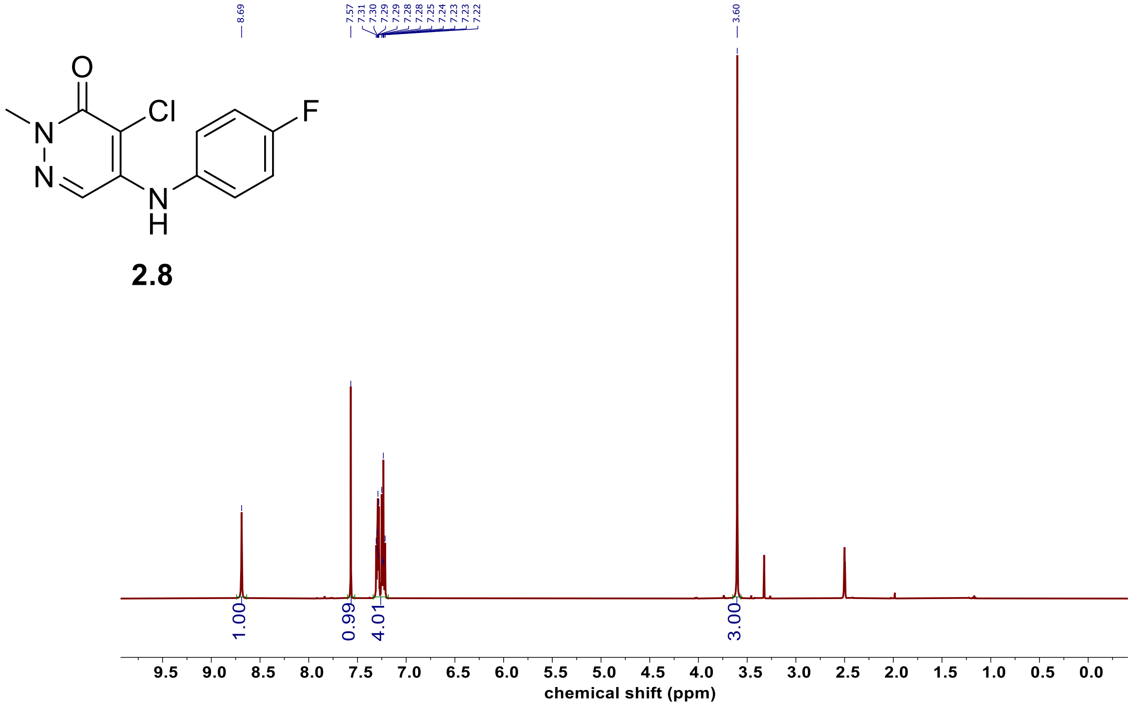

2.8, ^{13}C NMR (126 MHz, DMSO-d_6)

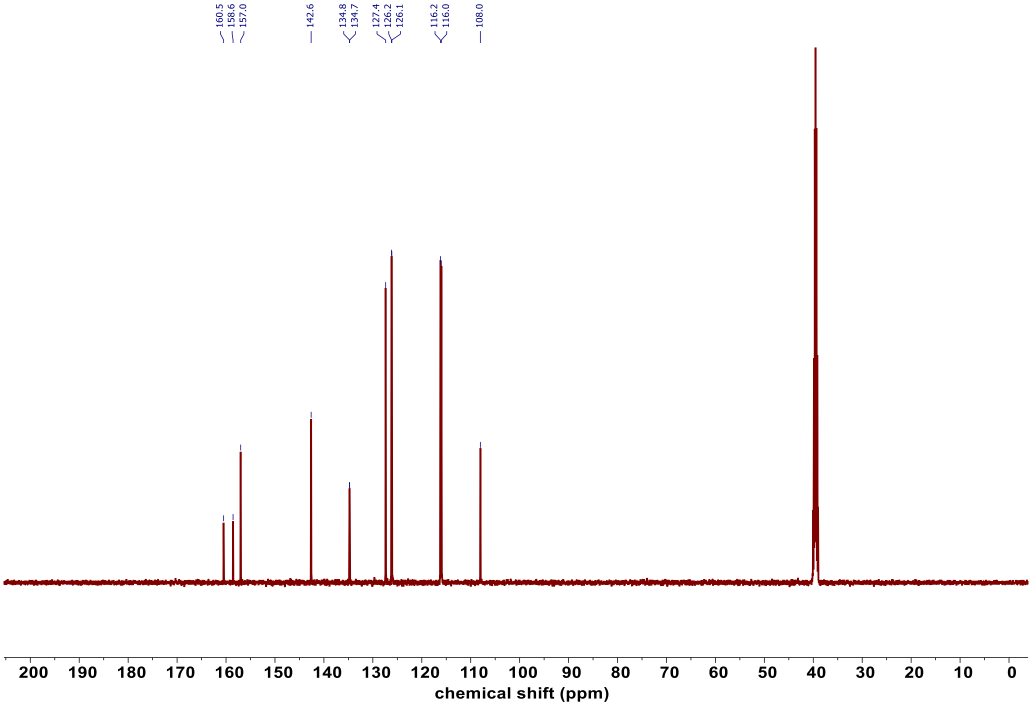

2.9, ^{1}H NMR (500 MHz, DMSO-d_6)

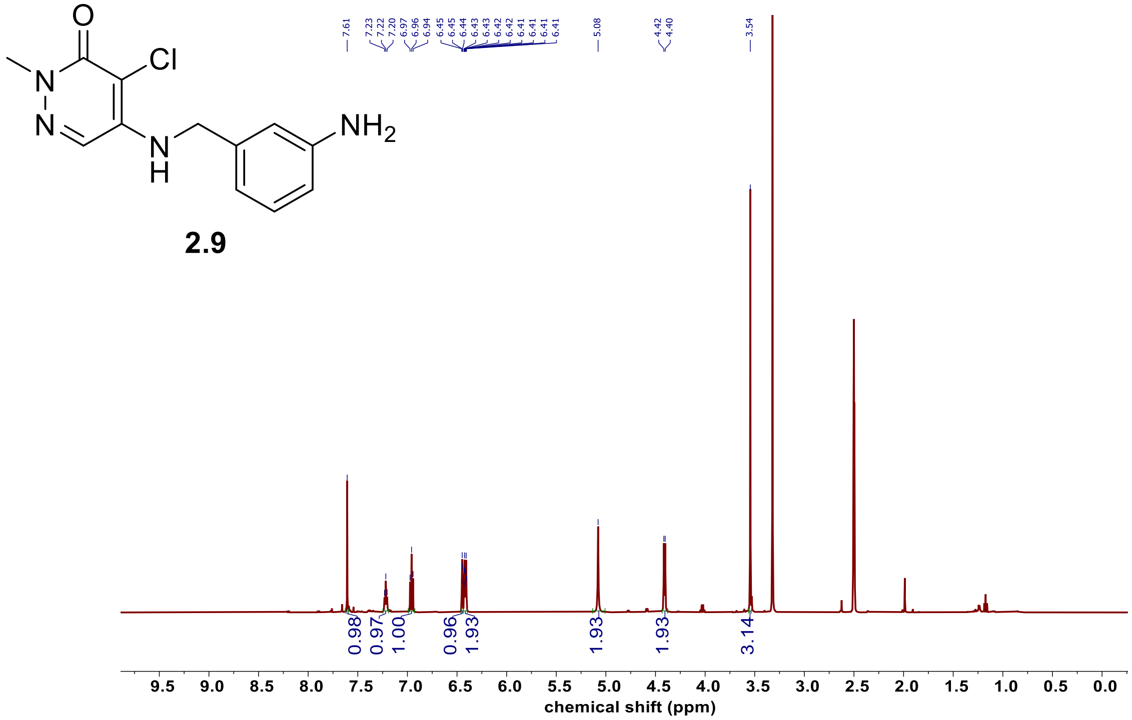

2.9, ^{13}C NMR (126 MHz, DMSO-d_6)

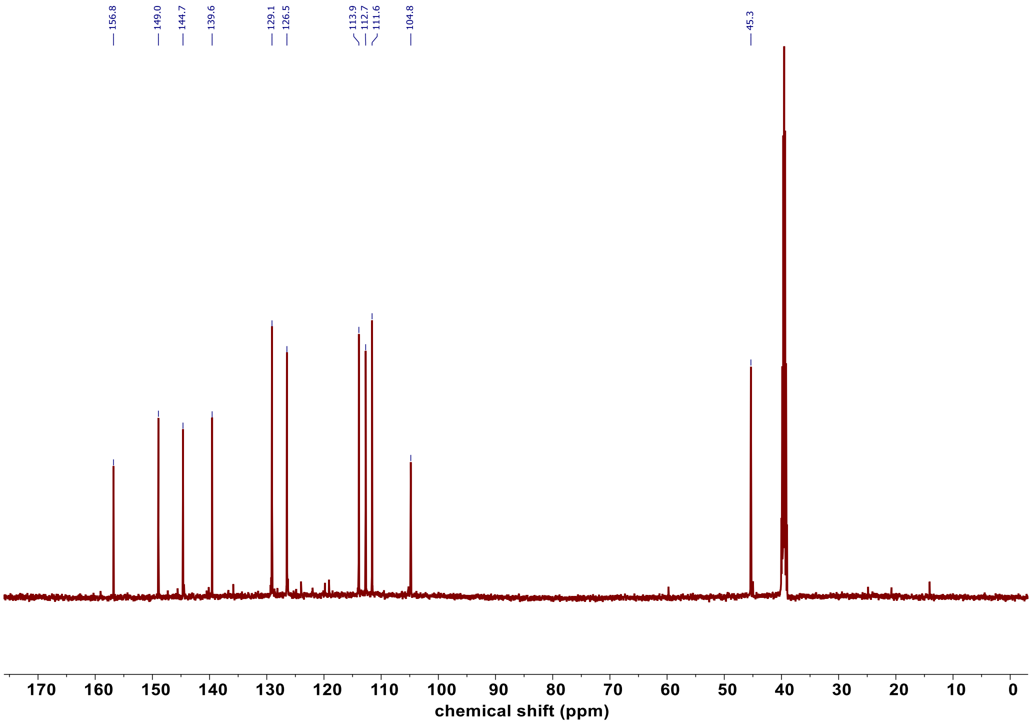

2.10, ^{1}H NMR (500 MHz, DMSO-*d*$_6$)

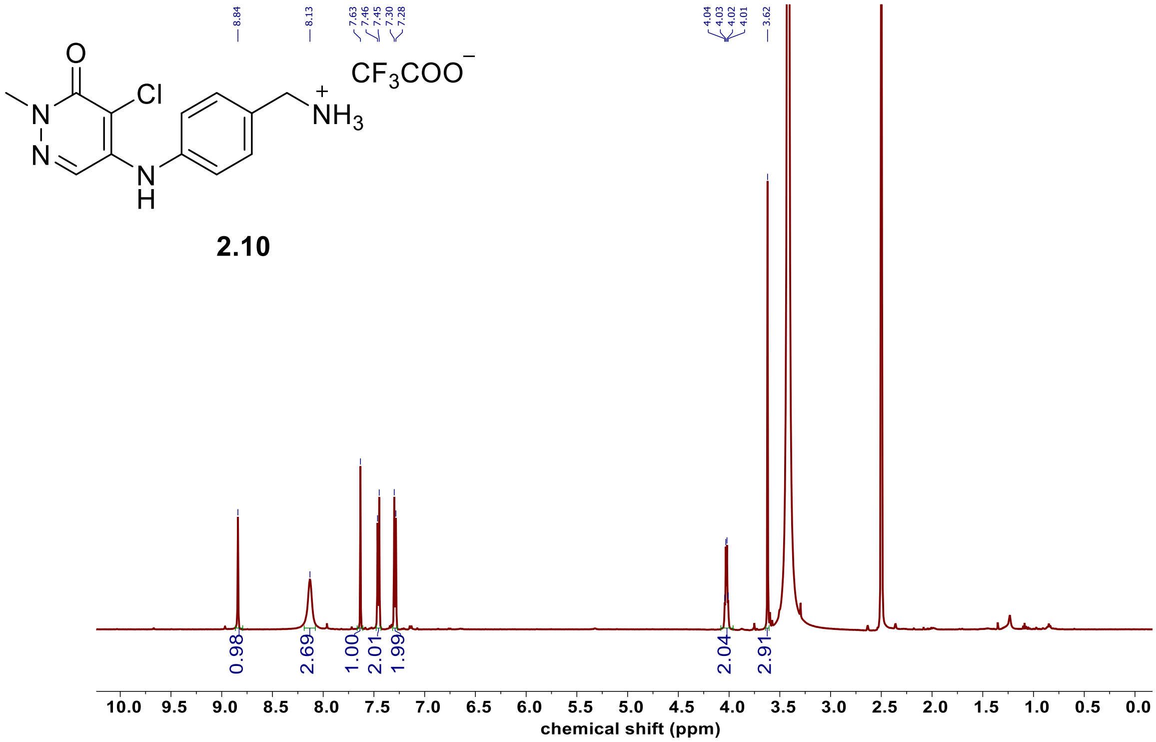

2.10, ^{13}C NMR (126 MHz, DMSO-*d*$_6$)

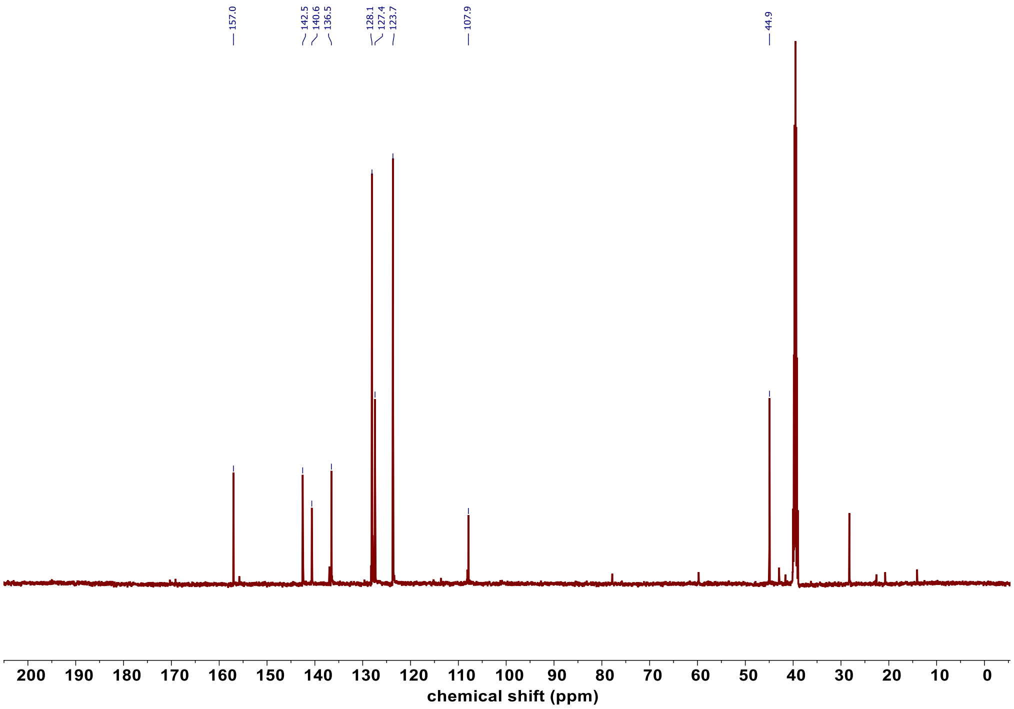

2.11, ^{1}H NMR (500 MHz, Chloroform-*d*)

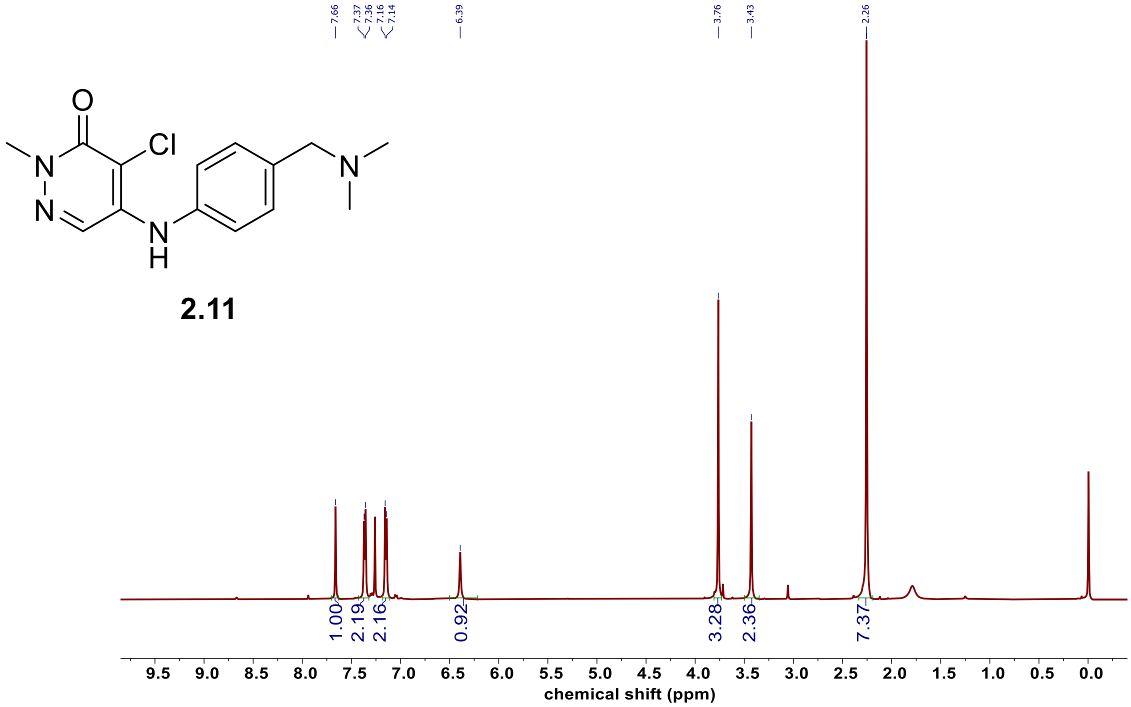

2.11

2.11, ^{13}C NMR (126 MHz, DMSO-d_6)

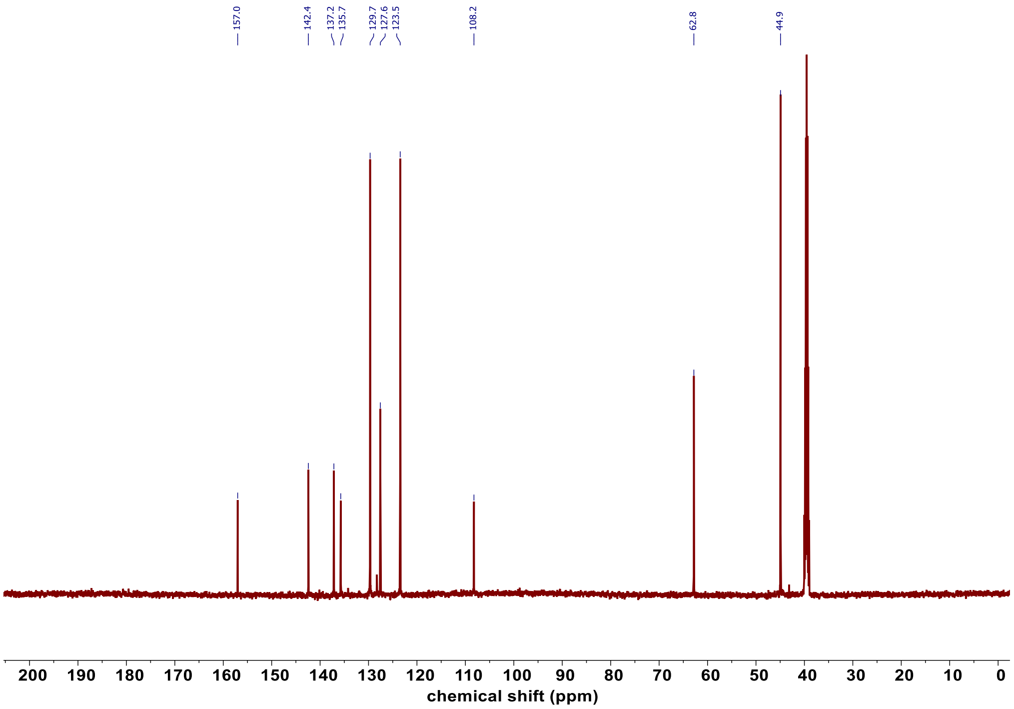

2.12, ^{1}H NMR (500 MHz, DMSO-d_6)

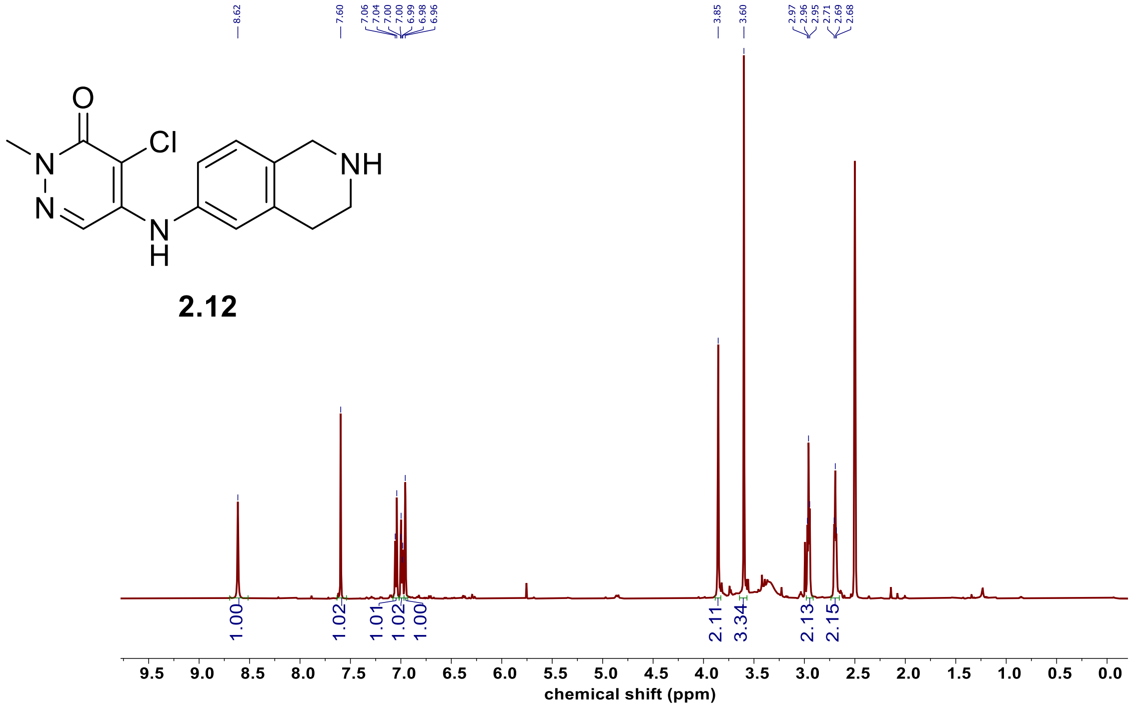

2.12, ^{13}C NMR (126 MHz, DMSO-d_6)

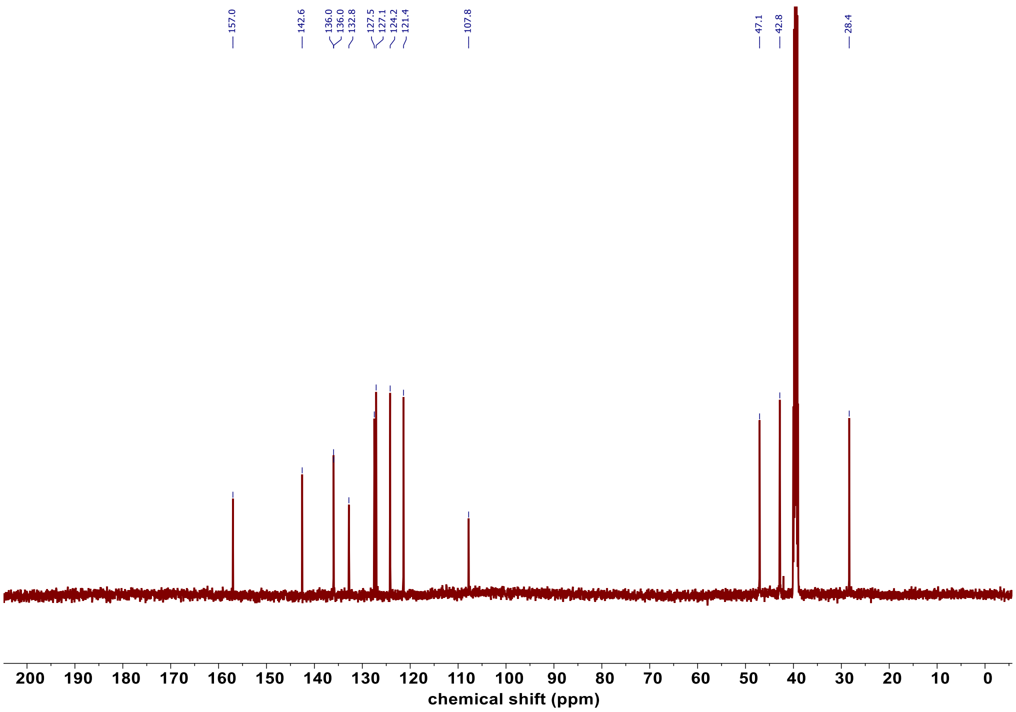

2.13, ^{1}H NMR (500 MHz, DMSO-d_6)

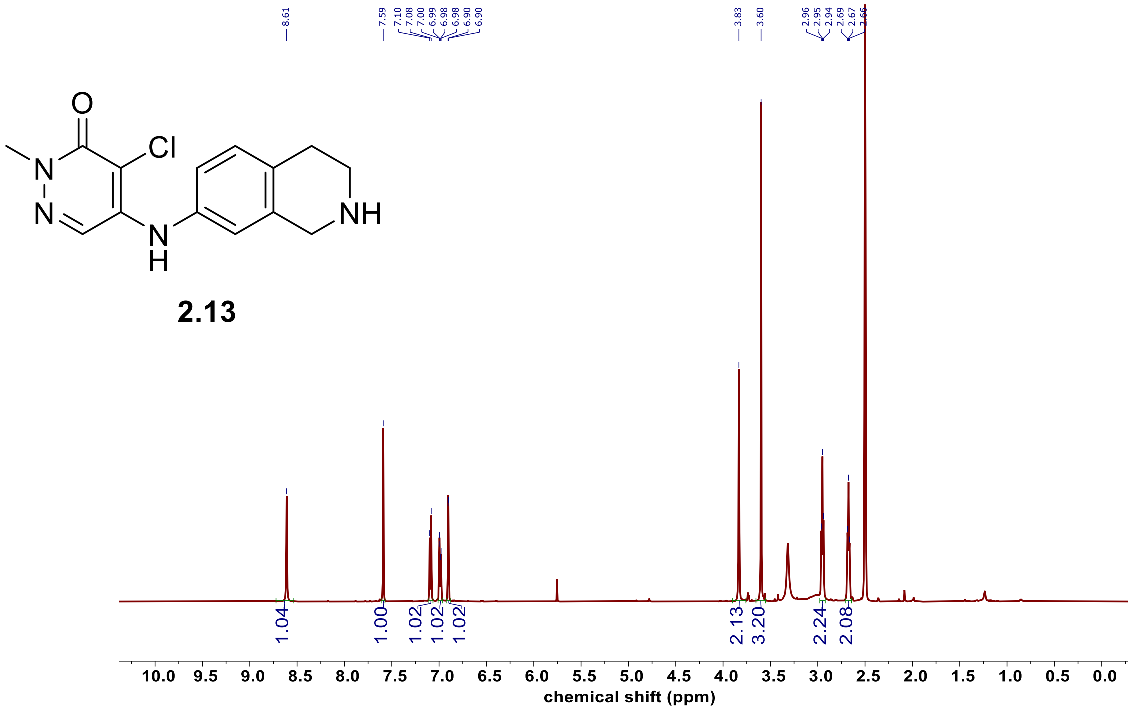

2.13, ^{13}C NMR (126 MHz, DMSO-d_6)

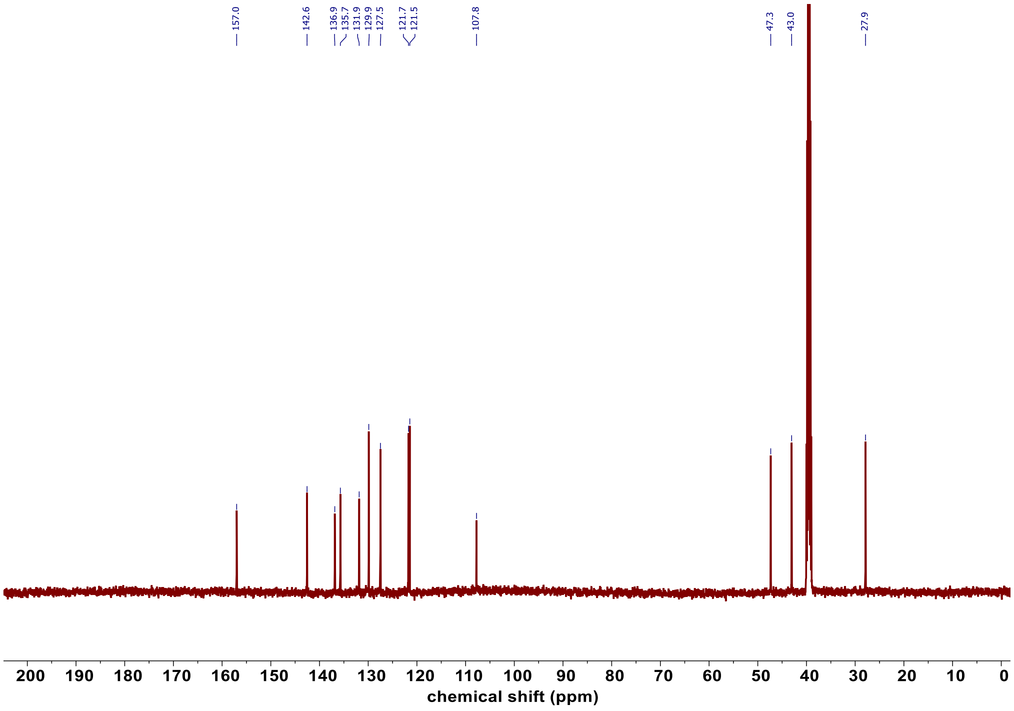

2.14, ^{1}H NMR (500 MHz, DMSO-d_6)

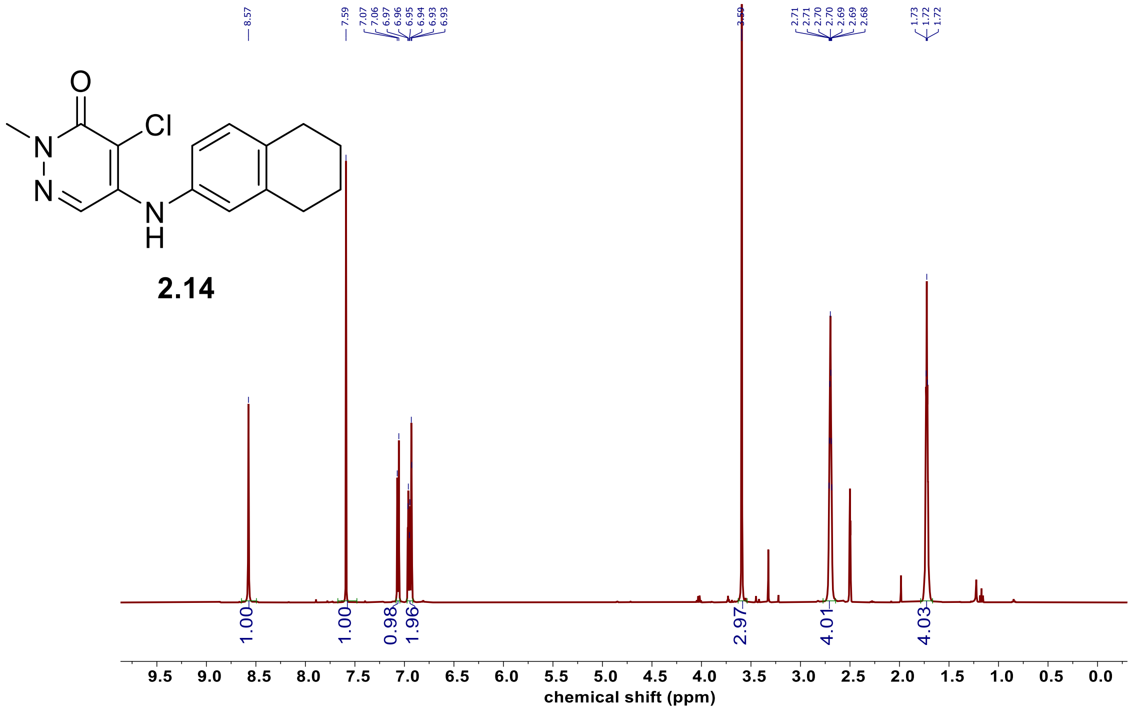

2.14, ^{13}C NMR (126 MHz, DMSO-d_6)

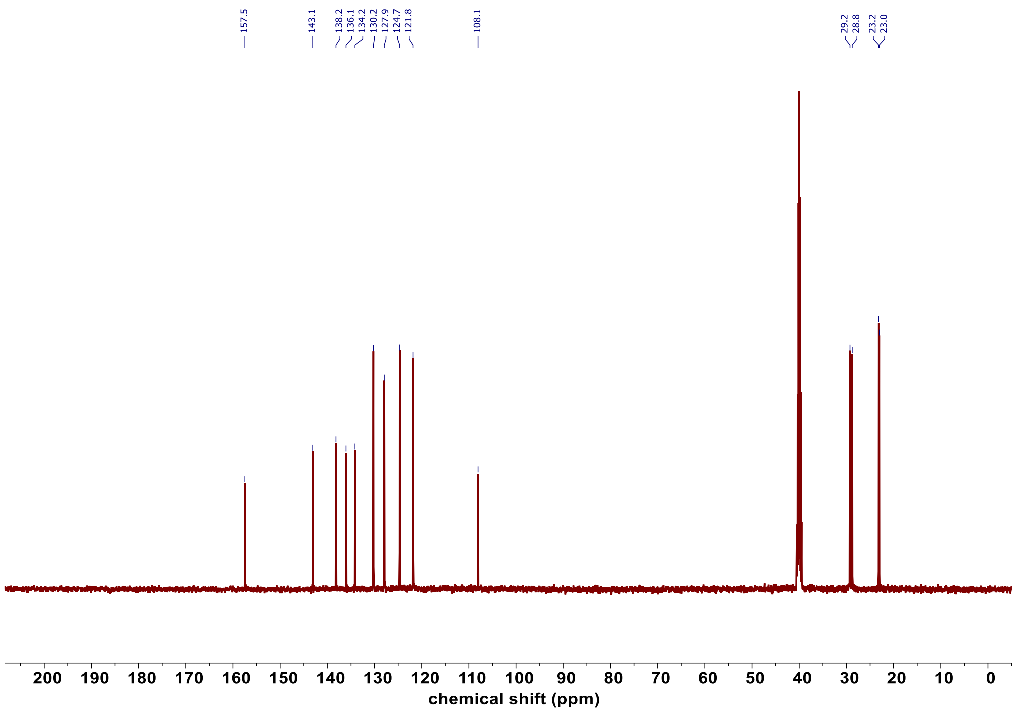

2.15, ^{1}H NMR (500 MHz, DMSO-d_6)

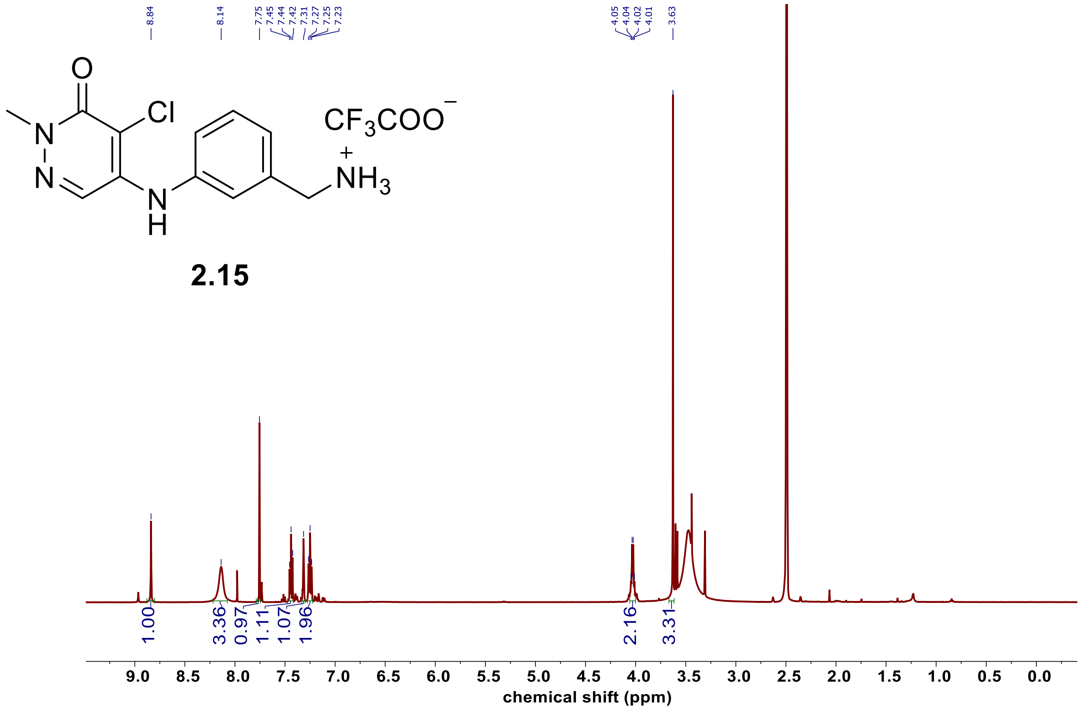

2.15

2.15, ^{13}C NMR (126 MHz, DMSO-d_6)

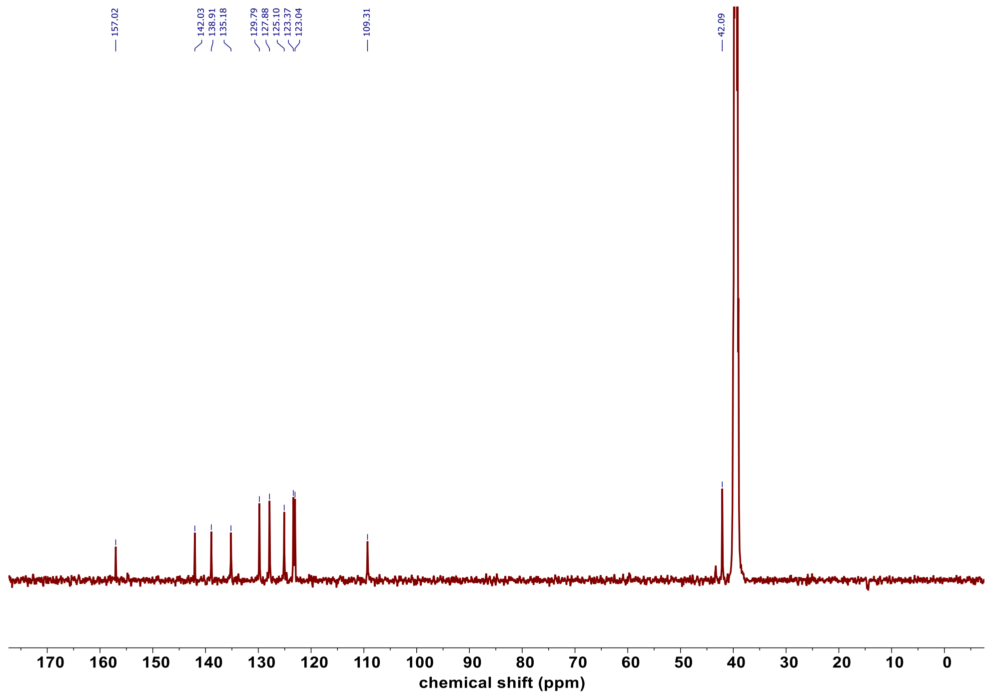

2.16, ^{1}H NMR (500 MHz, DMSO-d_6)

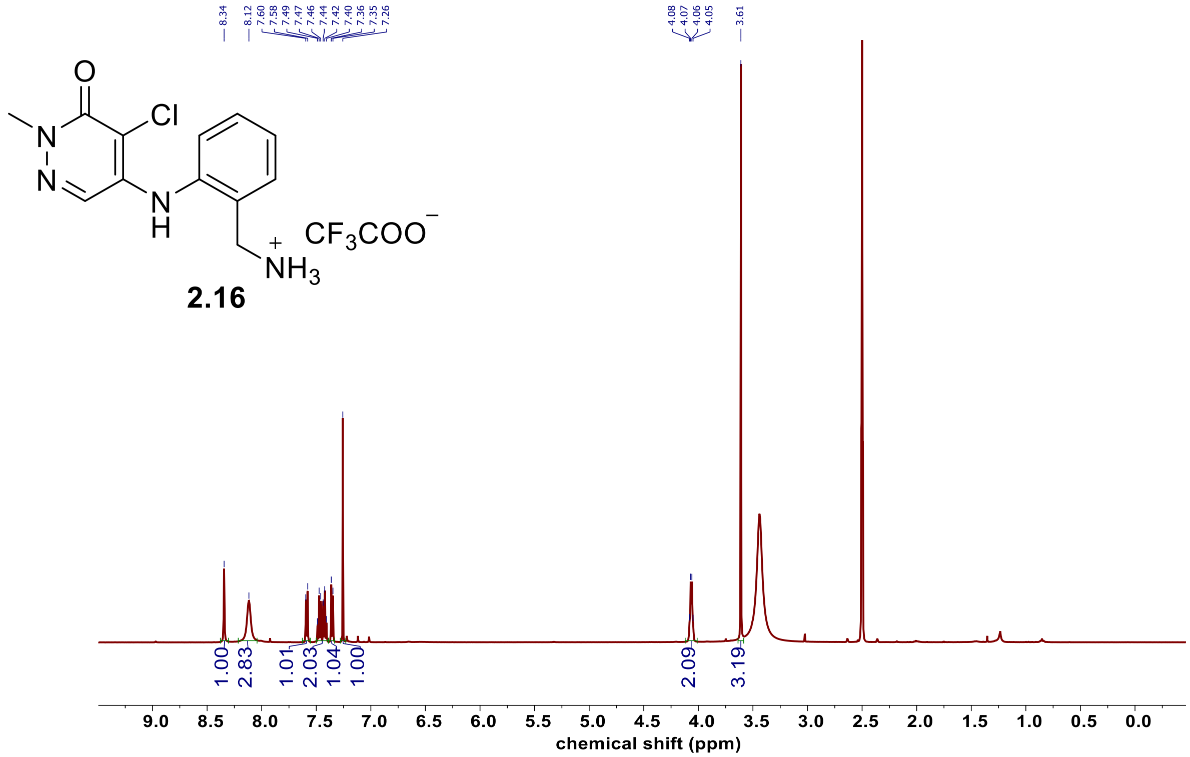
8.34
8.12
7.60
7.58
7.49
7.47
7.46
7.44
7.42
7.40
7.36
7.35
7.26
4.08
4.07
4.06
4.05
3.61
O
Cl
N
N
N
H
CF3COO−
+
NH3
2.16
1.00
2.83
1.01
2.03
1.04
1.00
2.09
3.19
9.0
8.5
8.0
7.5
7.0
6.5
6.0
5.5
5.0
4.5
4.0
3.5
3.0
2.5
2.0
1.5
1.0
0.5
0.0
chemical shift (ppm)

2.17, ^{1}H NMR (500 MHz, Chloroform-*d*)

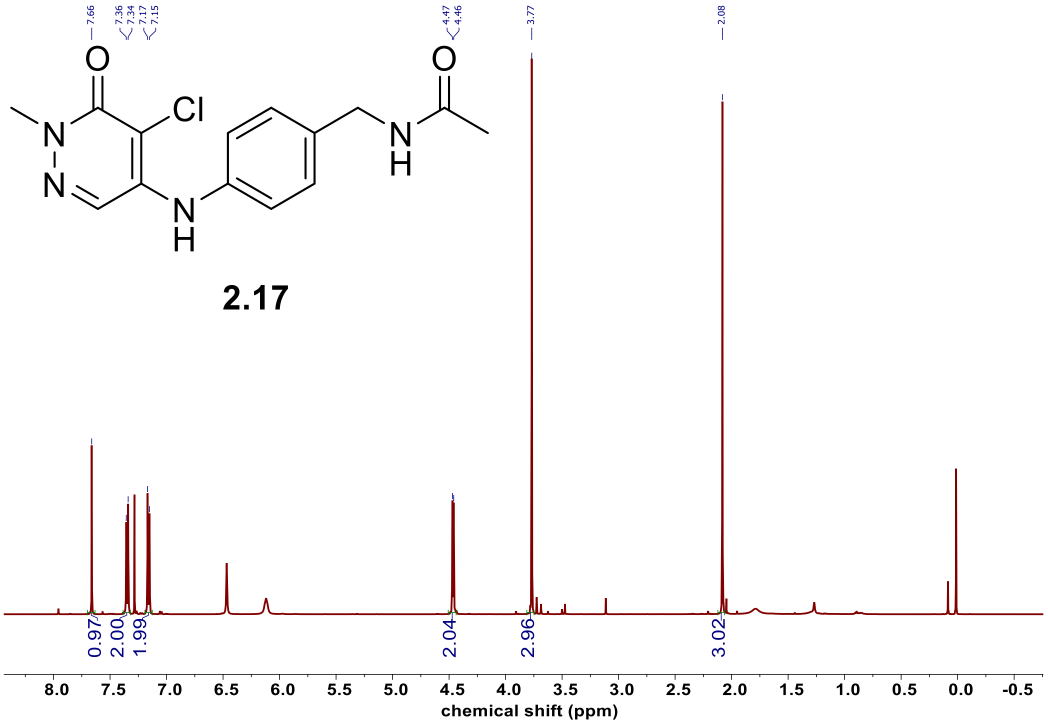

2.17, ^{13}C NMR (126 MHz, Chloroform-*d*)

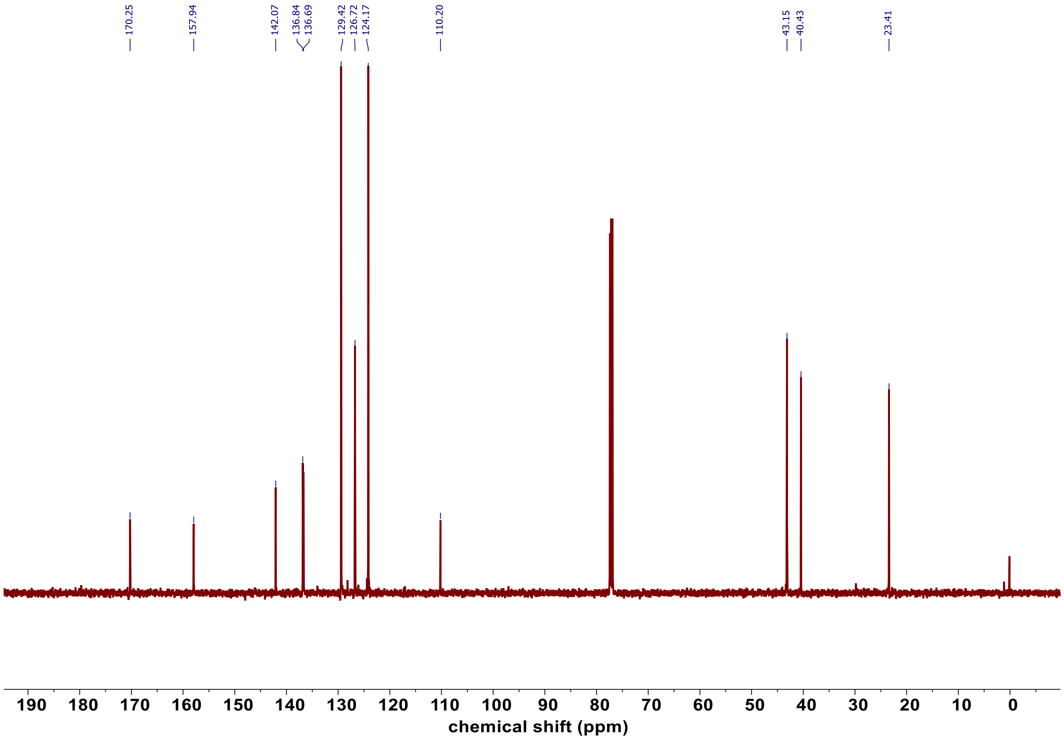

2.18, ^{1}H NMR (500 MHz, DMSO-d_6)

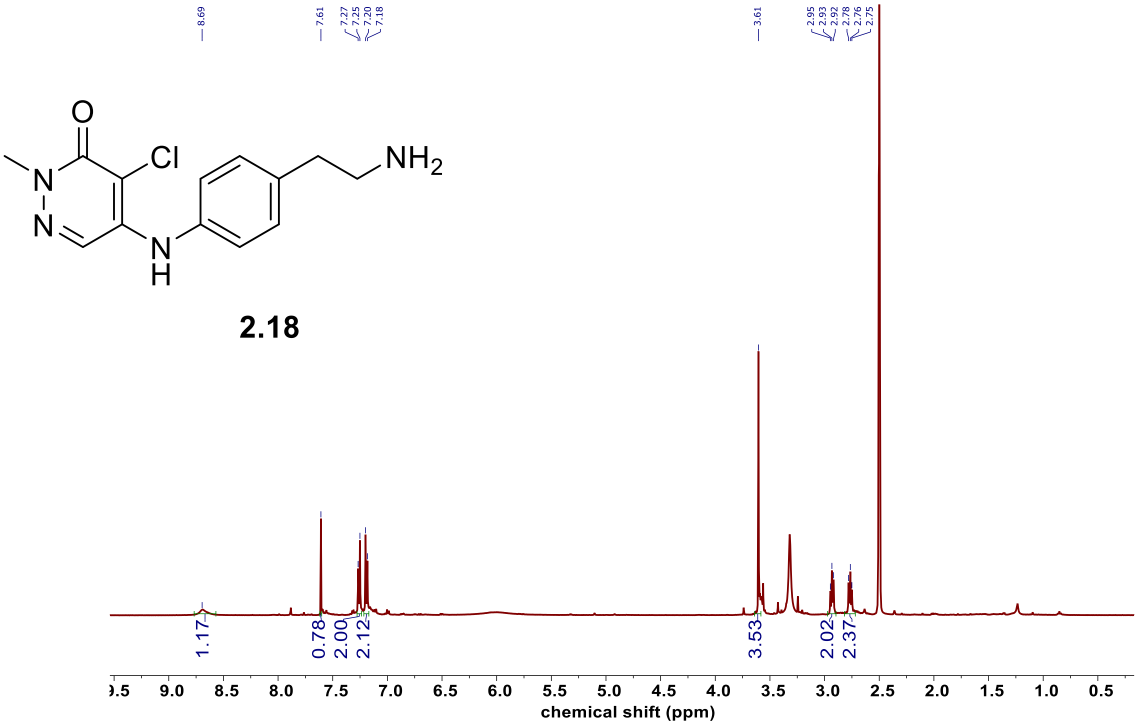

2.18, ^{13}C NMR (126 MHz, DMSO-d_6)

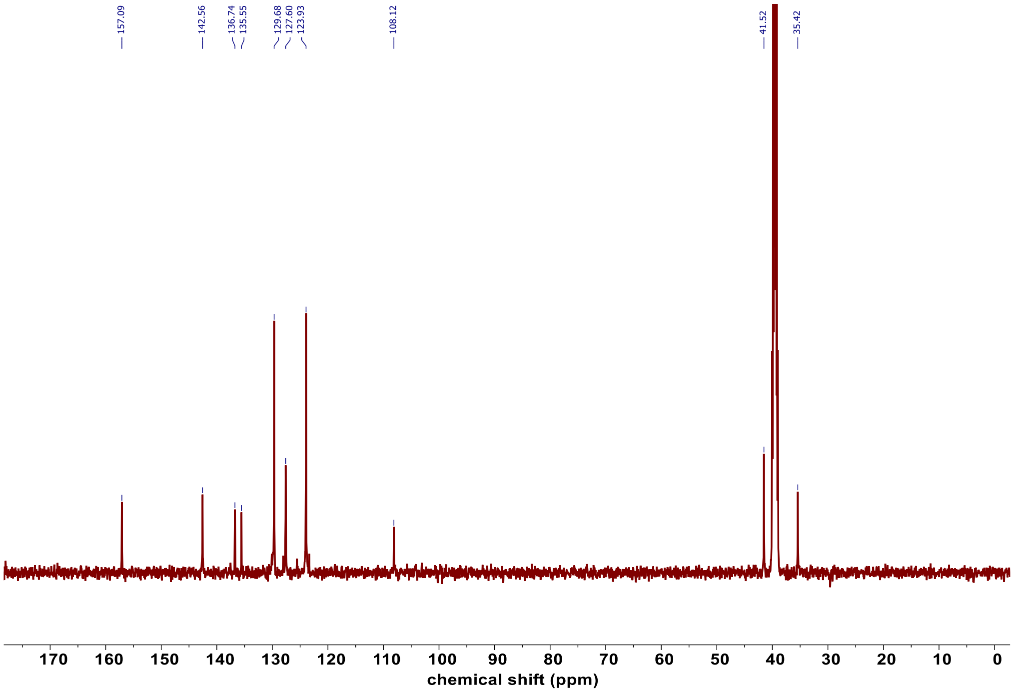

2.19, ^{1}H NMR (500 MHz, DMSO-d_6)

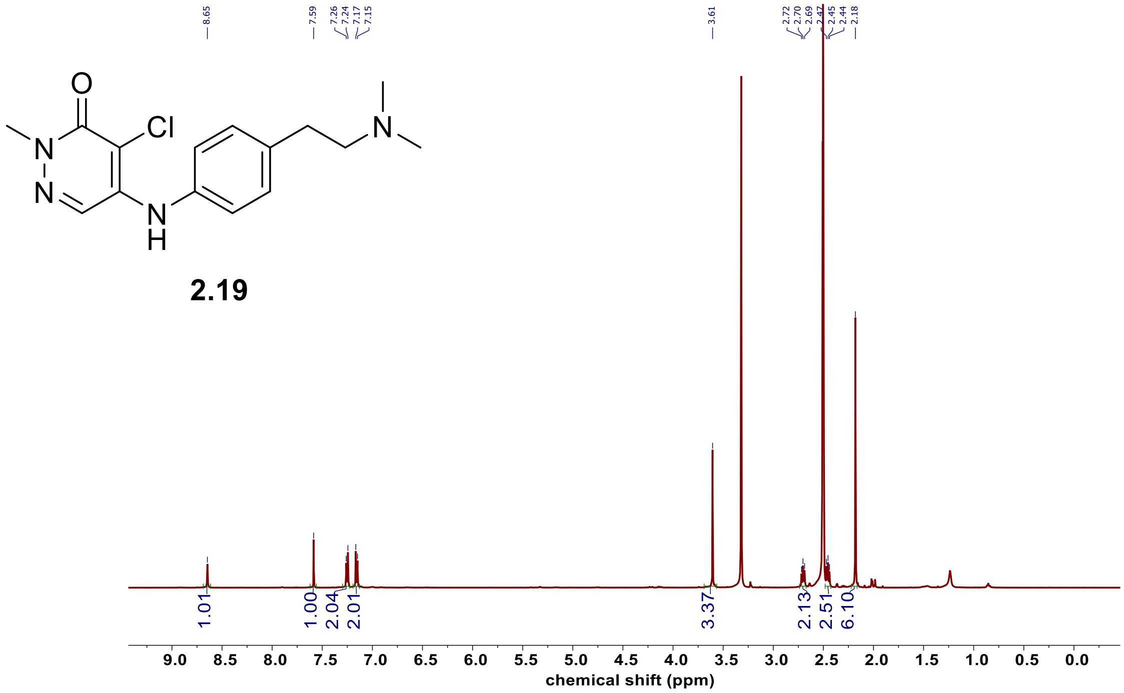

2.19

2.19, ^{13}C NMR (126 MHz, Chloroform-d)

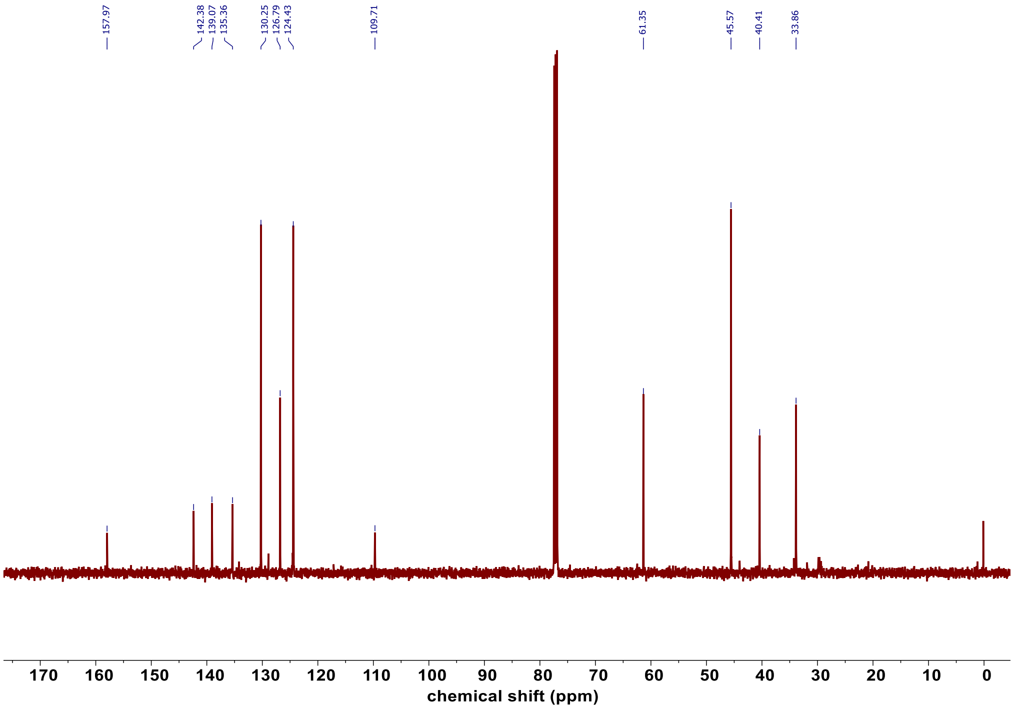

2.20, ^{1}H NMR (500 MHz, DMSO-d_6)

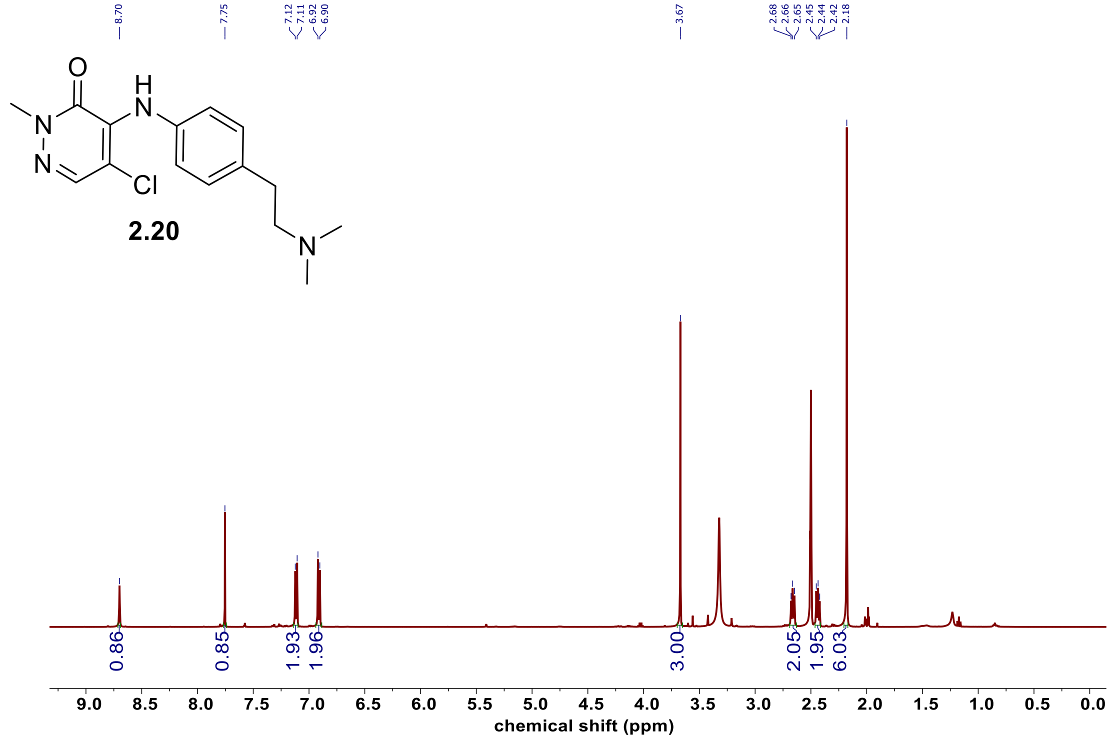

2.20, ^{13}C NMR (126 MHz, Chloroform-*d*)

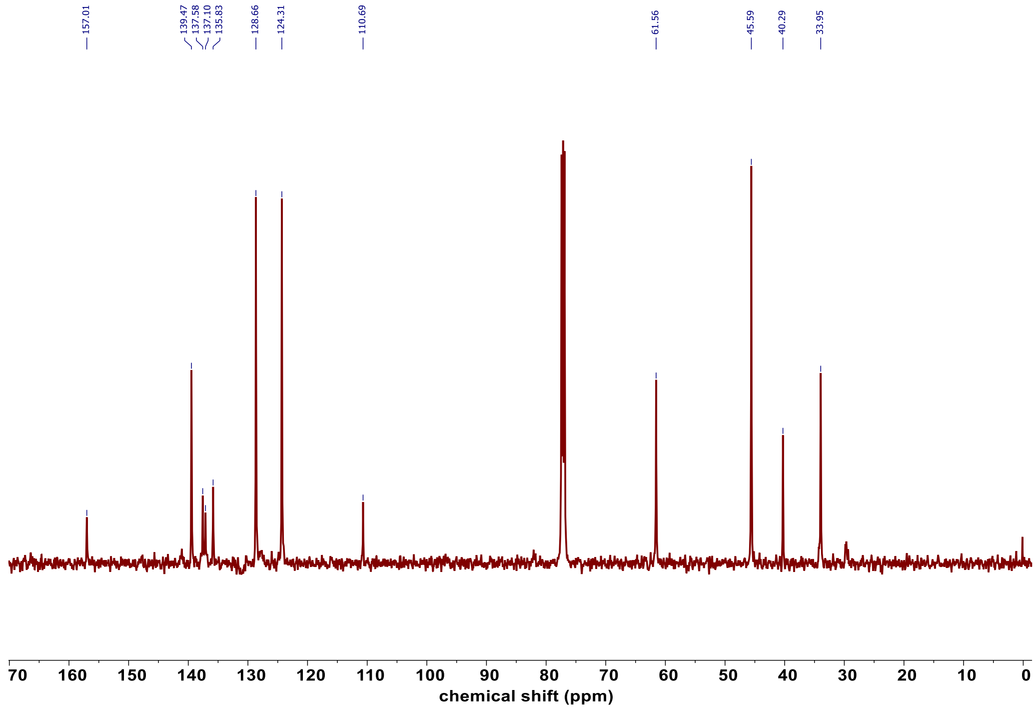

2.21, ^{1}H NMR (500 MHz, DMSO-*d*$_6$)

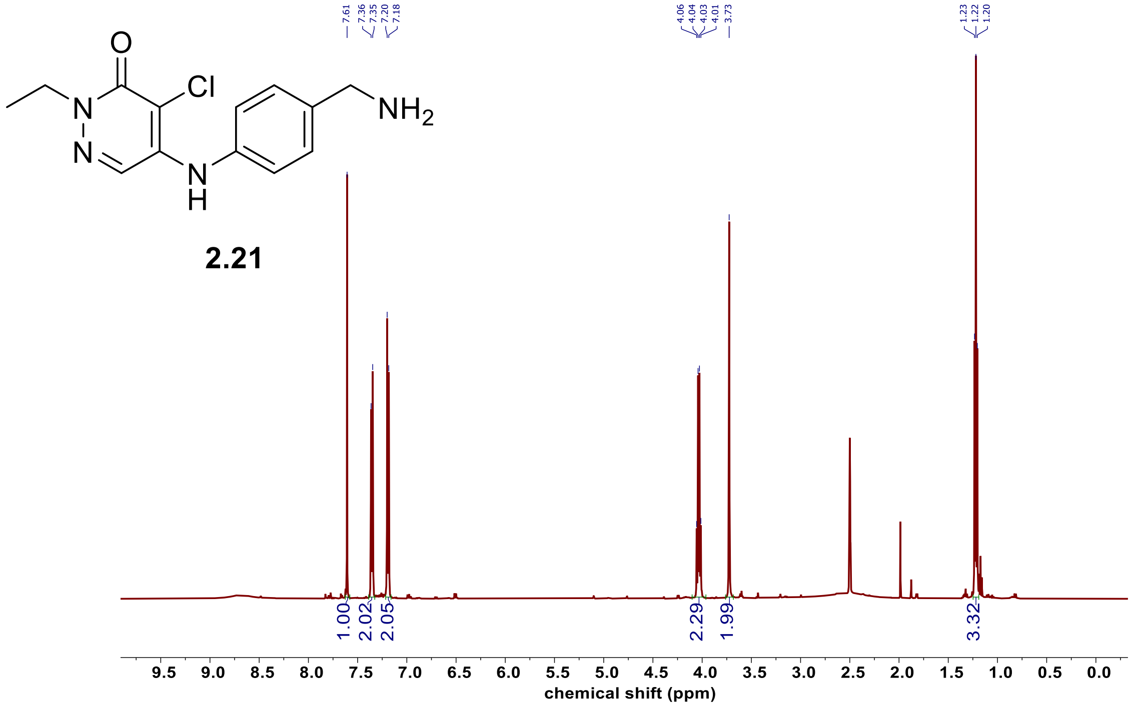

2.21, ^{13}C NMR (126 MHz, DMSO-d_6)

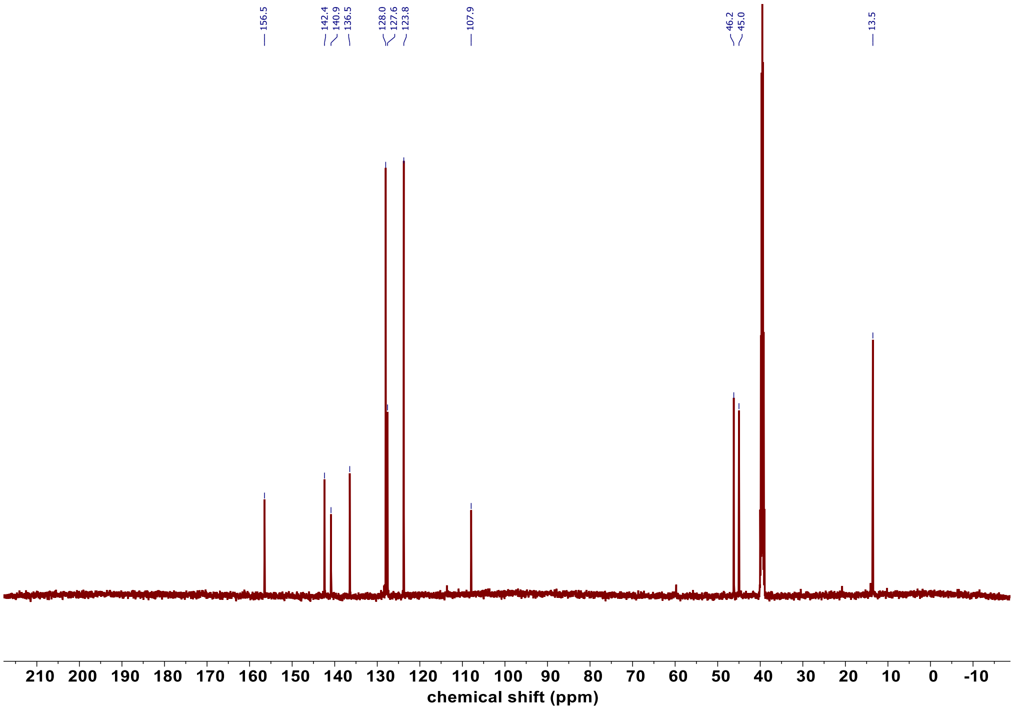

2.22, ^{1}H NMR (500 MHz, DMSO-d_6)

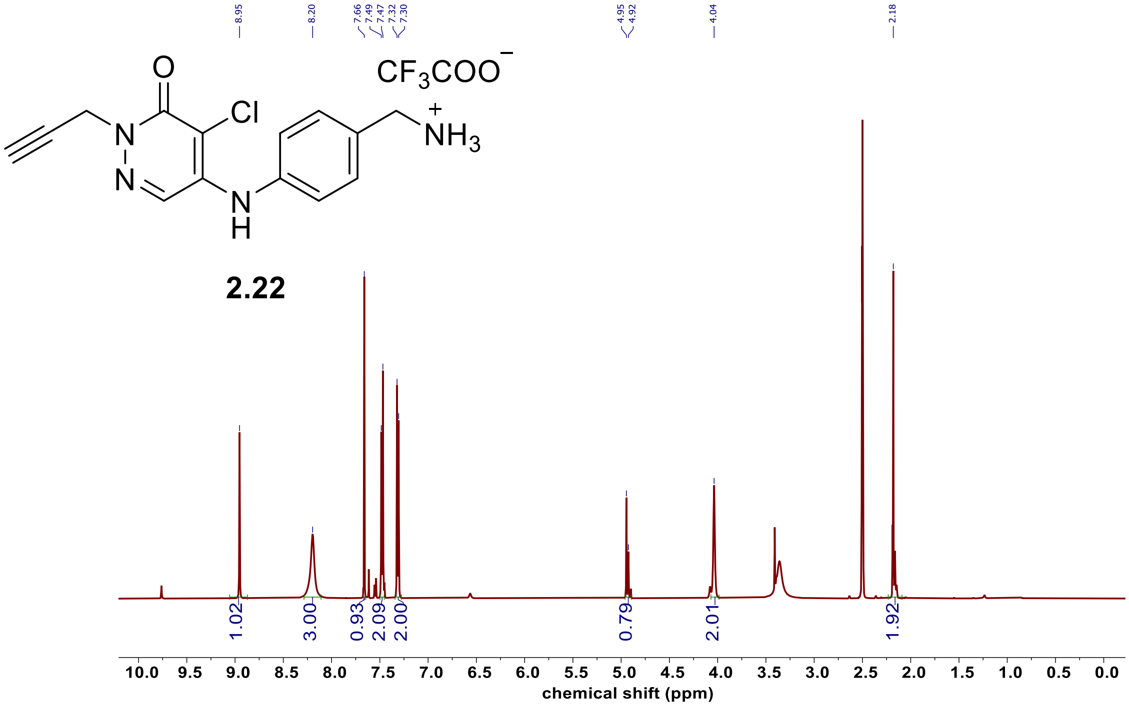

2.22, ^{13}C NMR (126 MHz, DMSO-d_6)

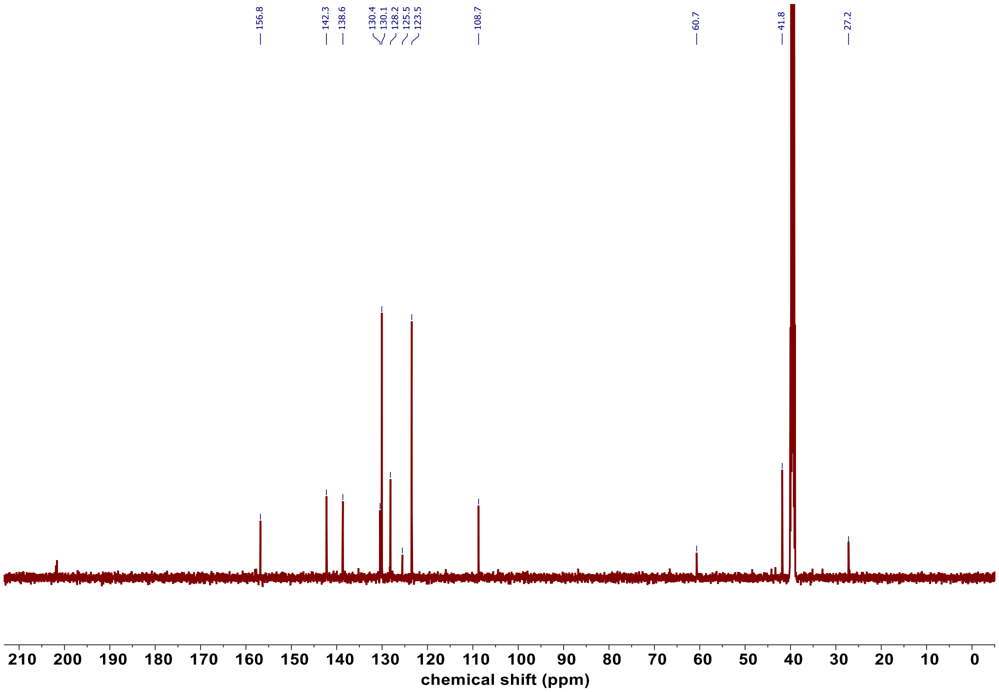

2.23, ^{1}H NMR (500 MHz, DMSO-d_6)

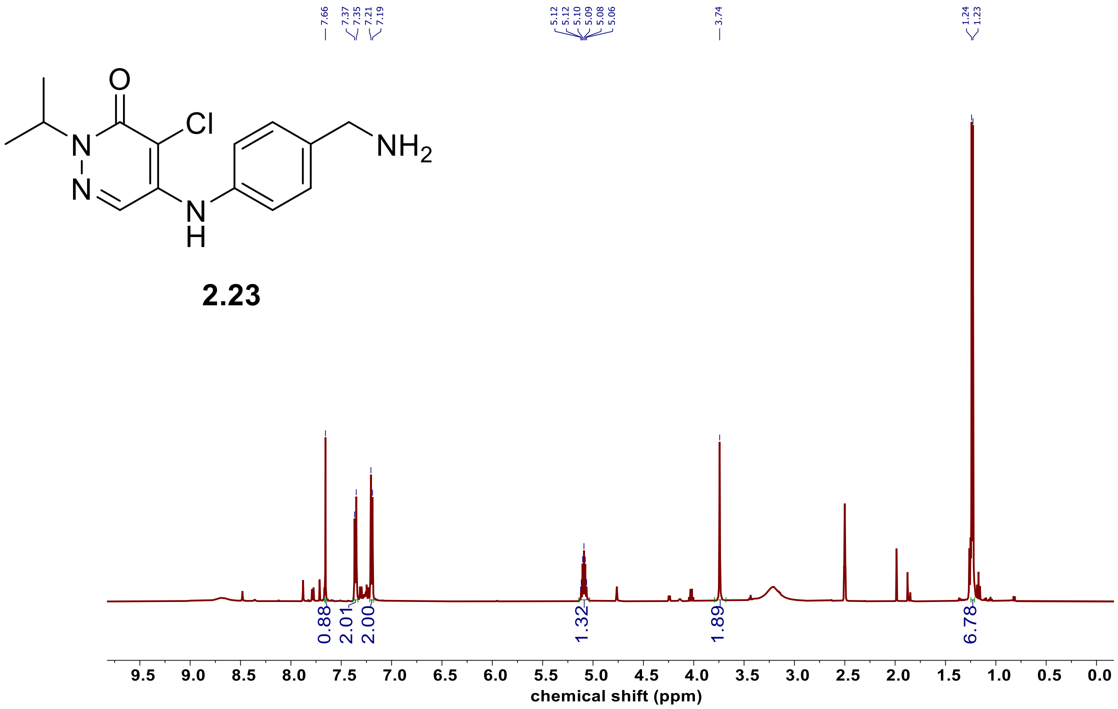

2.23, ^{13}C NMR (126 MHz, DMSO-d_6)

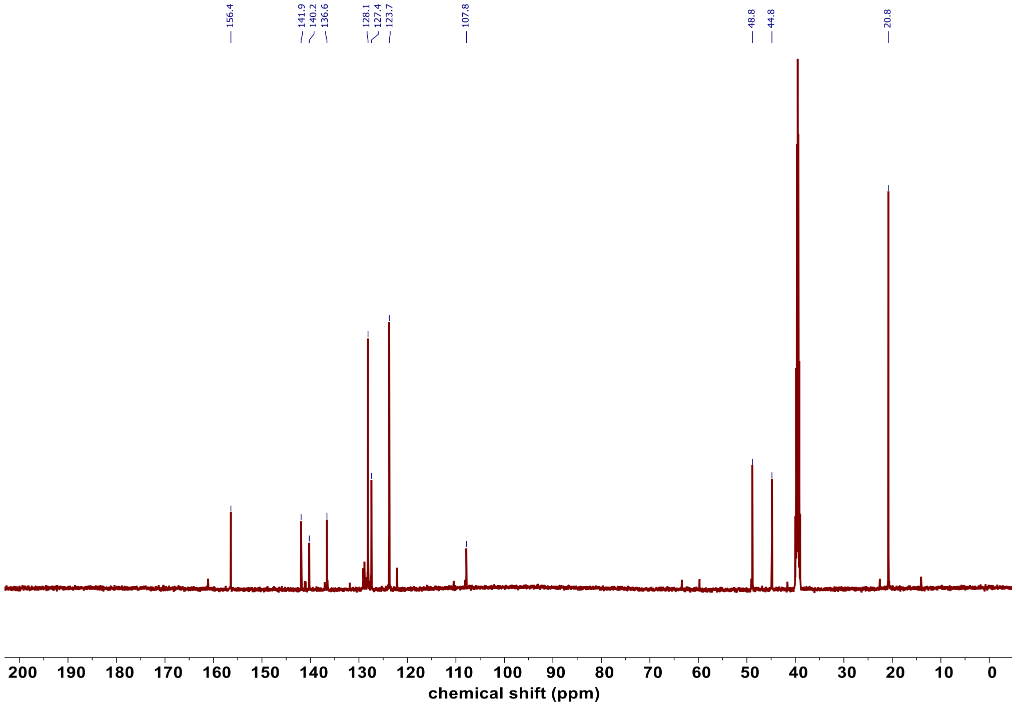

2.24, ^{1}H NMR (500 MHz, DMSO-d_6)

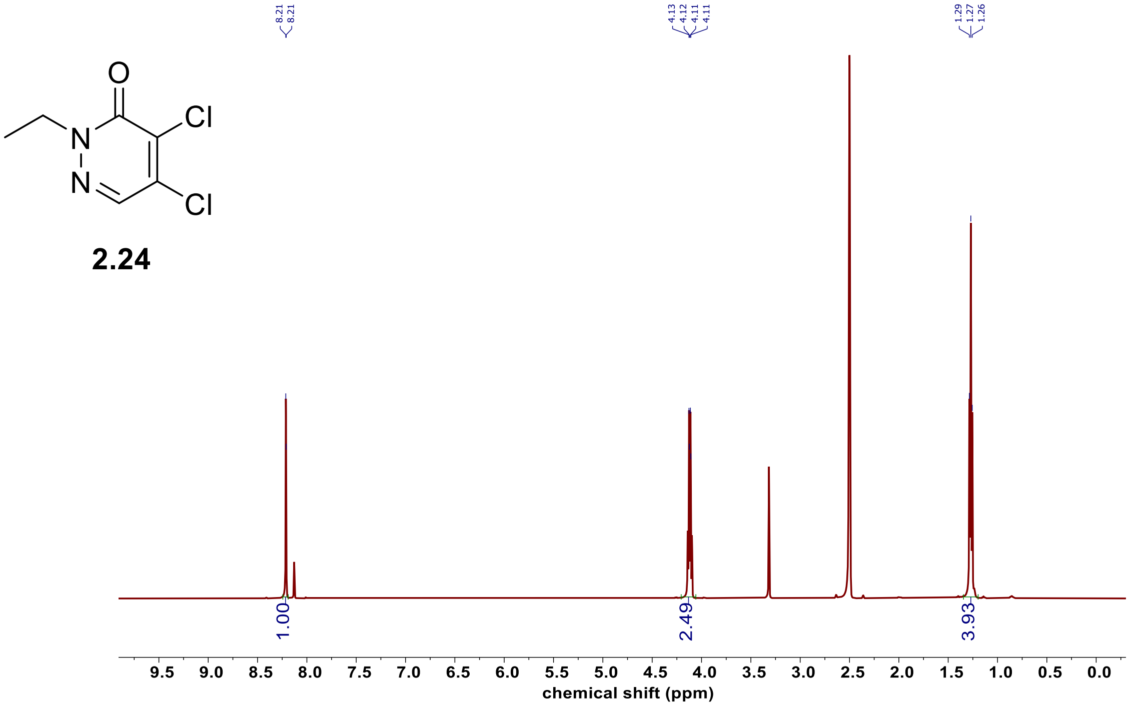

2.24

2.24, ^{13}C NMR (126 MHz, DMSO-d_6)

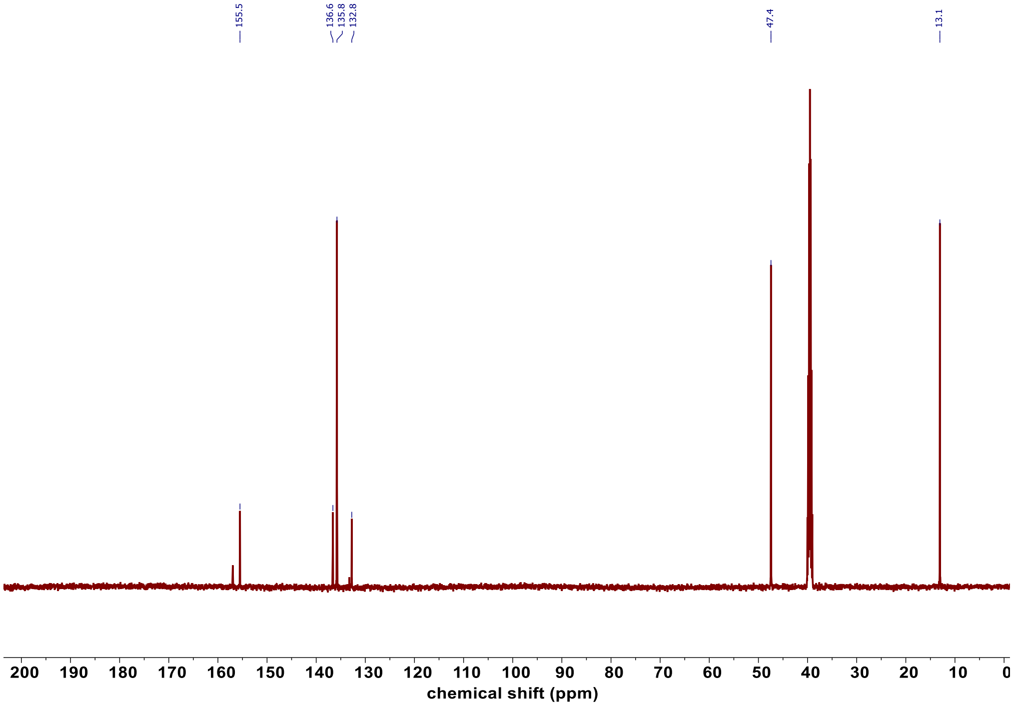

2.25, ^{1}H NMR (500 MHz, DMSO-d_6)

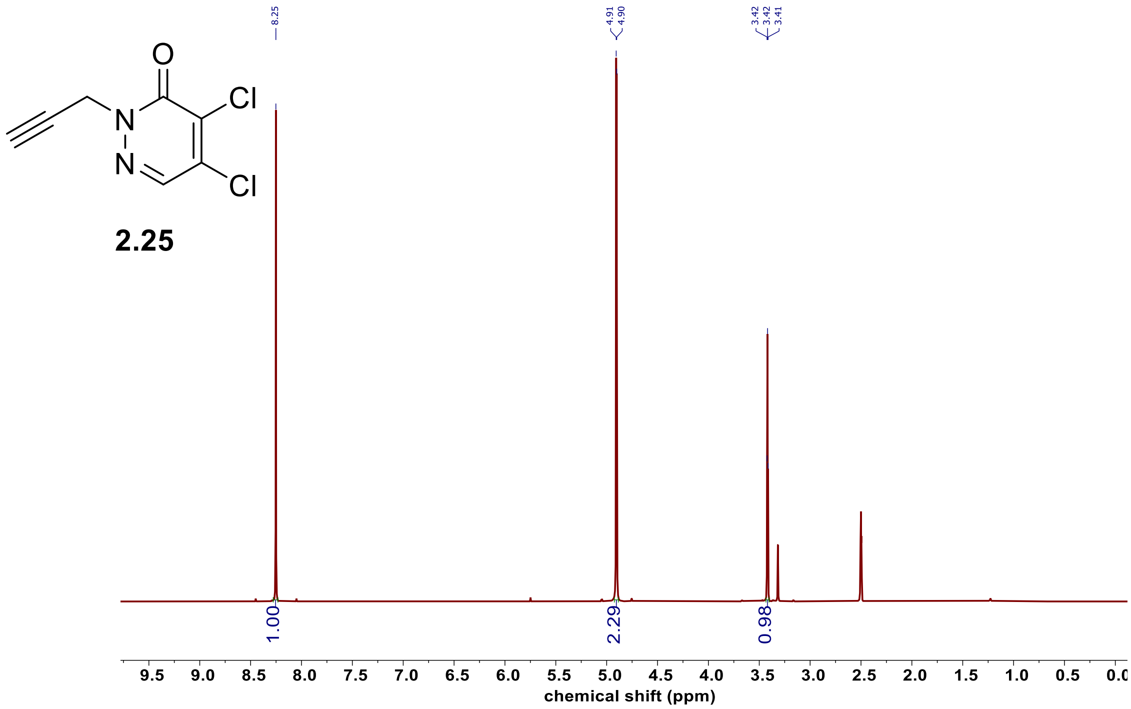

2.25, ^{13}C NMR (126 MHz, DMSO-d_6)

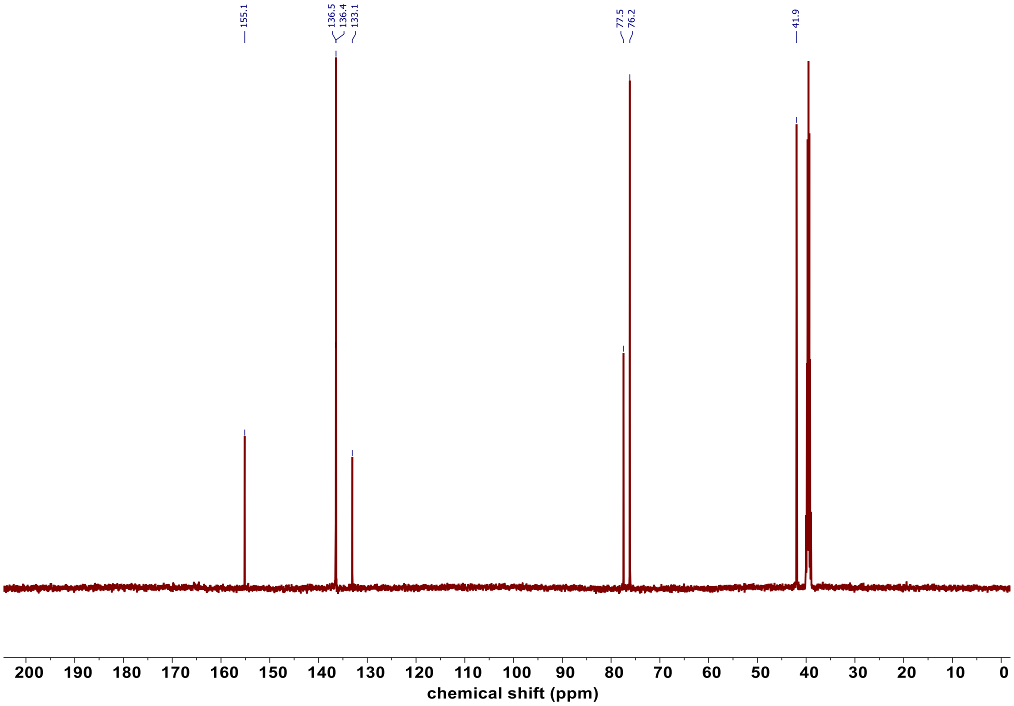

2.26, ^{1}H NMR (500 MHz, DMSO-d_6)

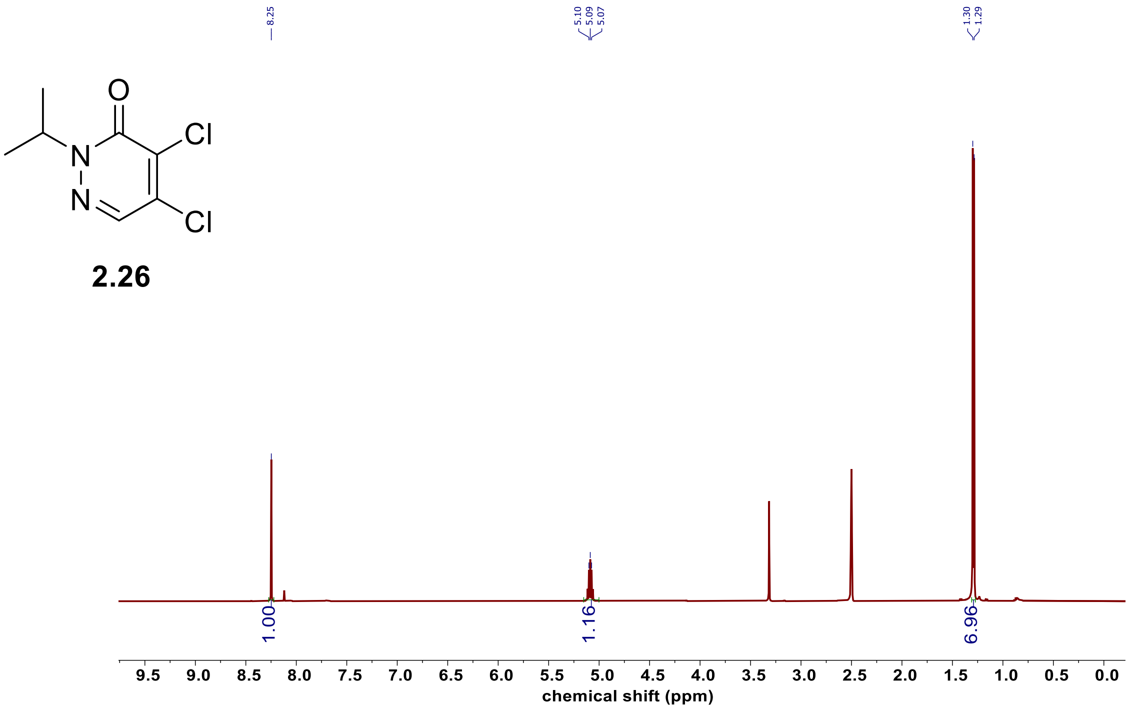

2.26

2.26, ^{13}C NMR (126 MHz, DMSO-d_6)

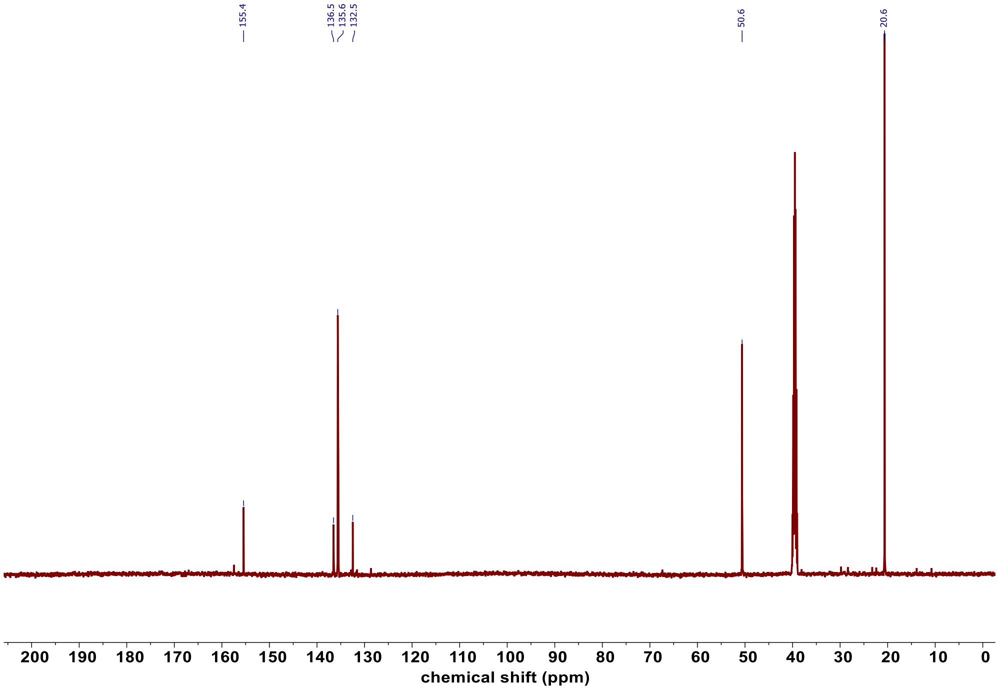

8.2 Chapter 4 NMR Spectra

F1*, ^{1}H NMR (500 MHz, $CDCl_3$)

F1*

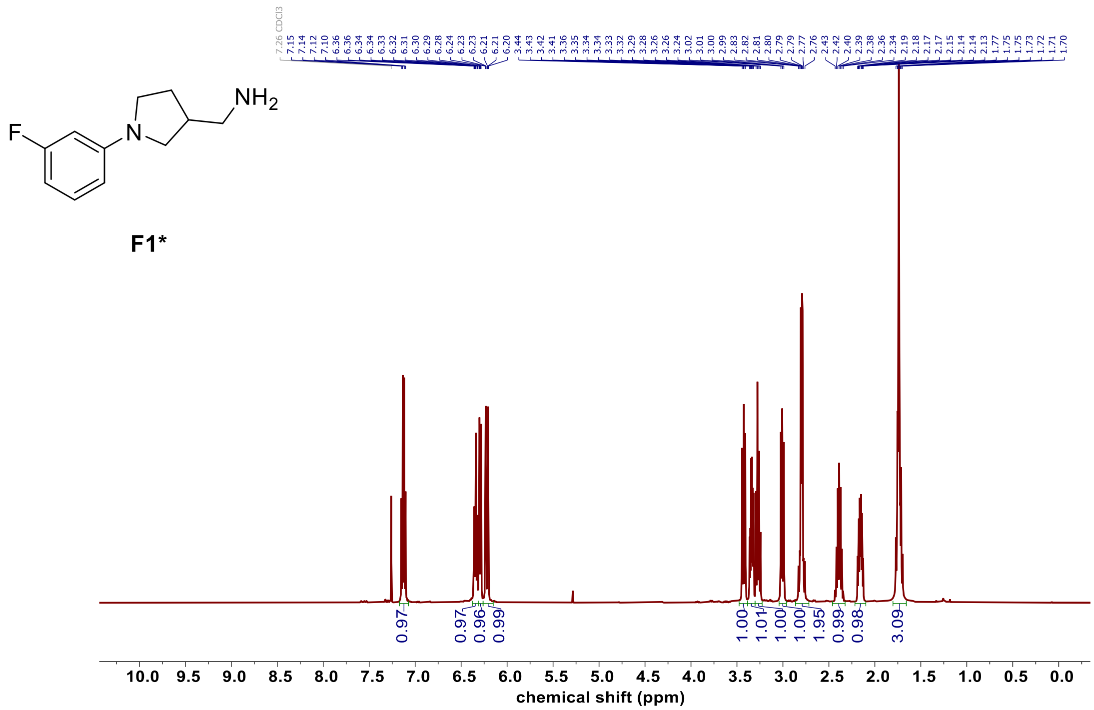

F1*, ^{13}C NMR (500 MHz, $CDCl_3$)

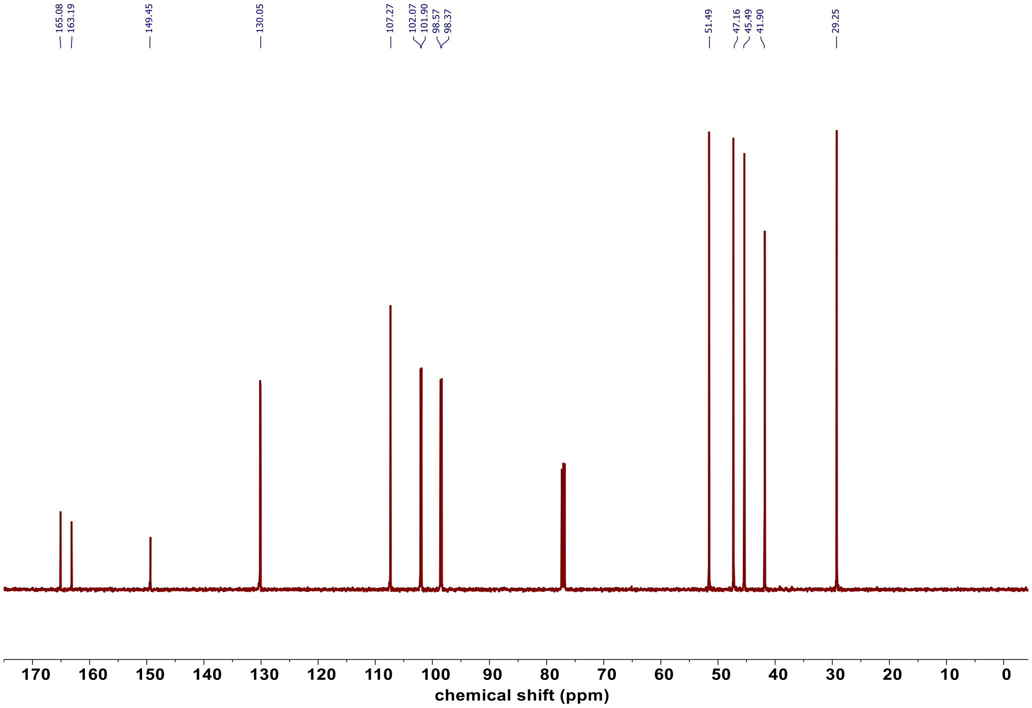

F2*, ^{1}H NMR (500 MHz, DMSO-d_6)

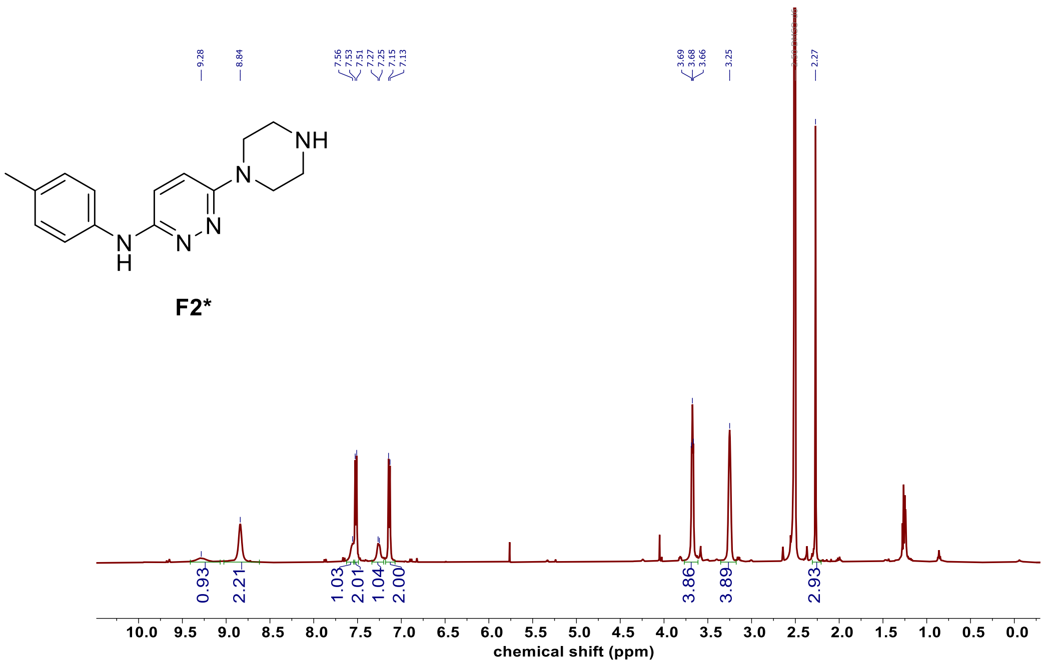

F2*

F2*, ^{13}C NMR (500 MHz, DMSO-d_6)

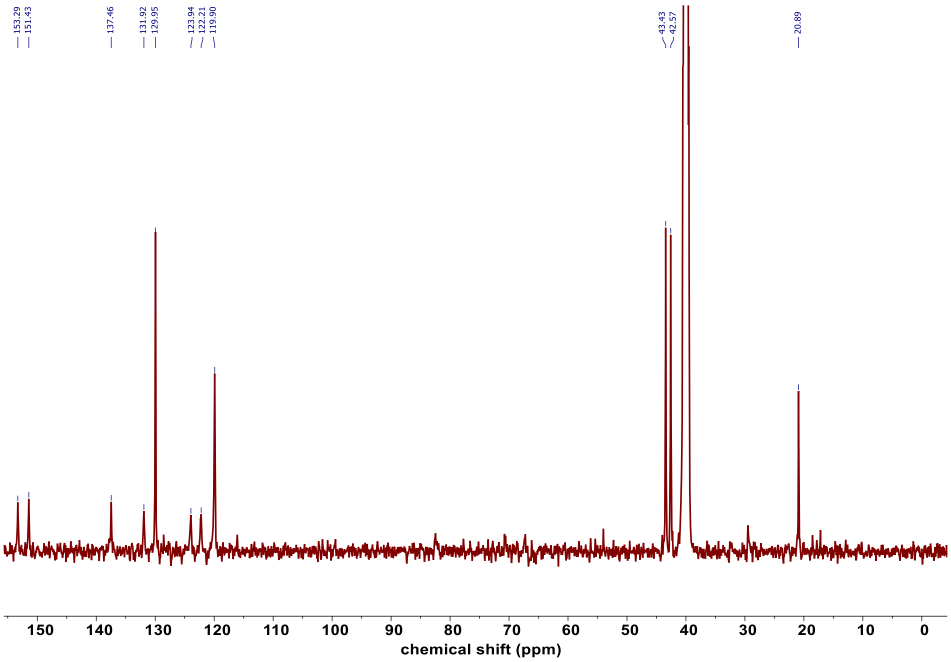

F2.5, ^{1}H NMR (500 MHz, DMSO-d_6)

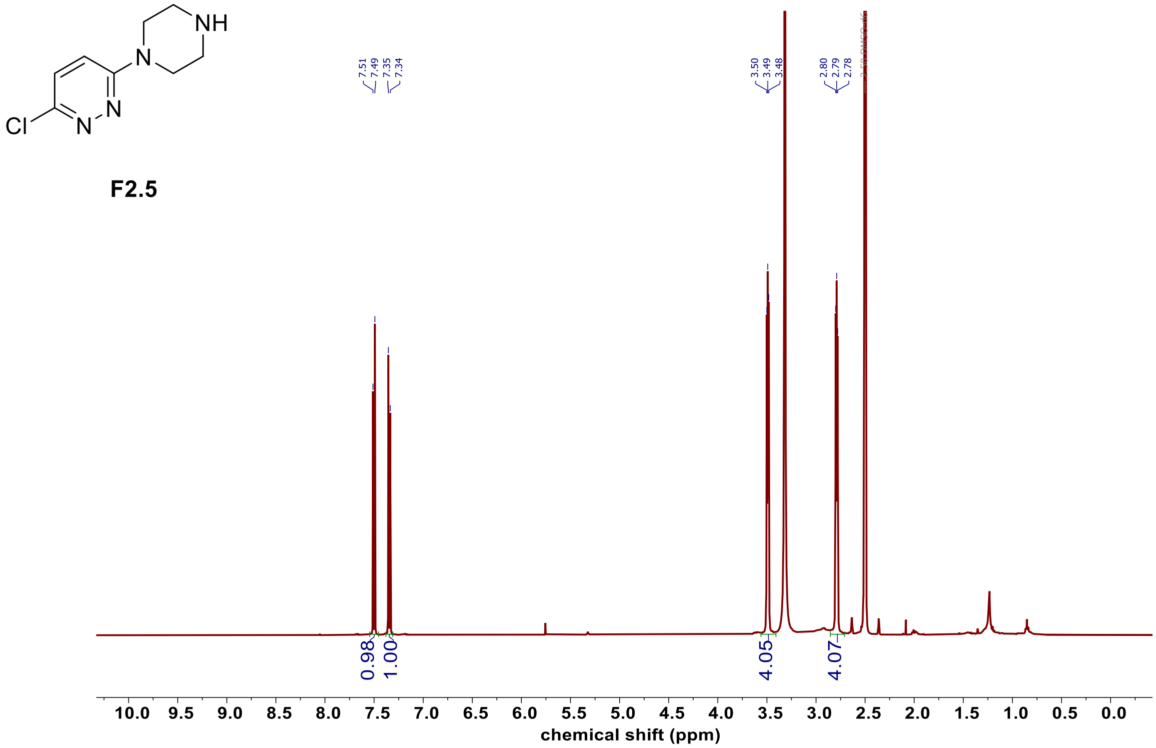

F2.6, ^{1}H NMR (500 MHz, $CDCl_3$)

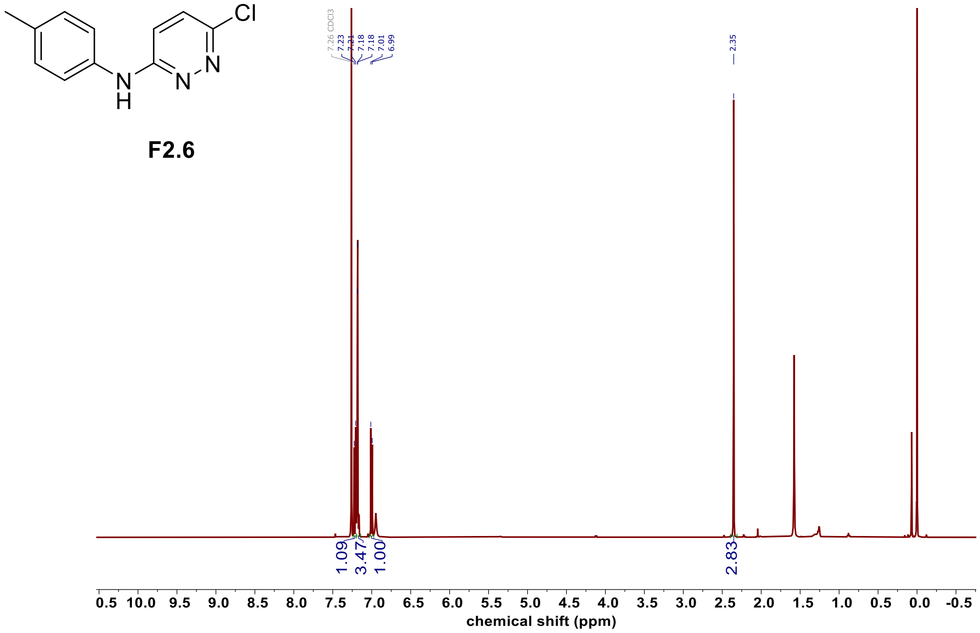

F2.6, ^{13}C NMR (500 MHz, DMSO-d_6)

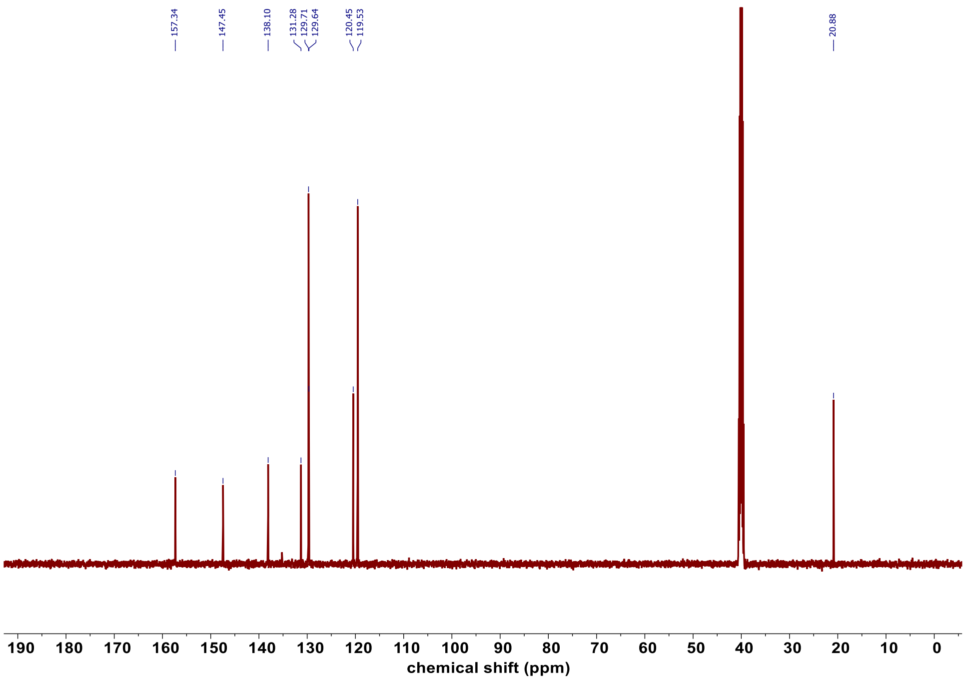

8.3 Chapter 5 NMR Spectra

F2.7, ^{1}H NMR (500 MHz, DMSO- d_6)

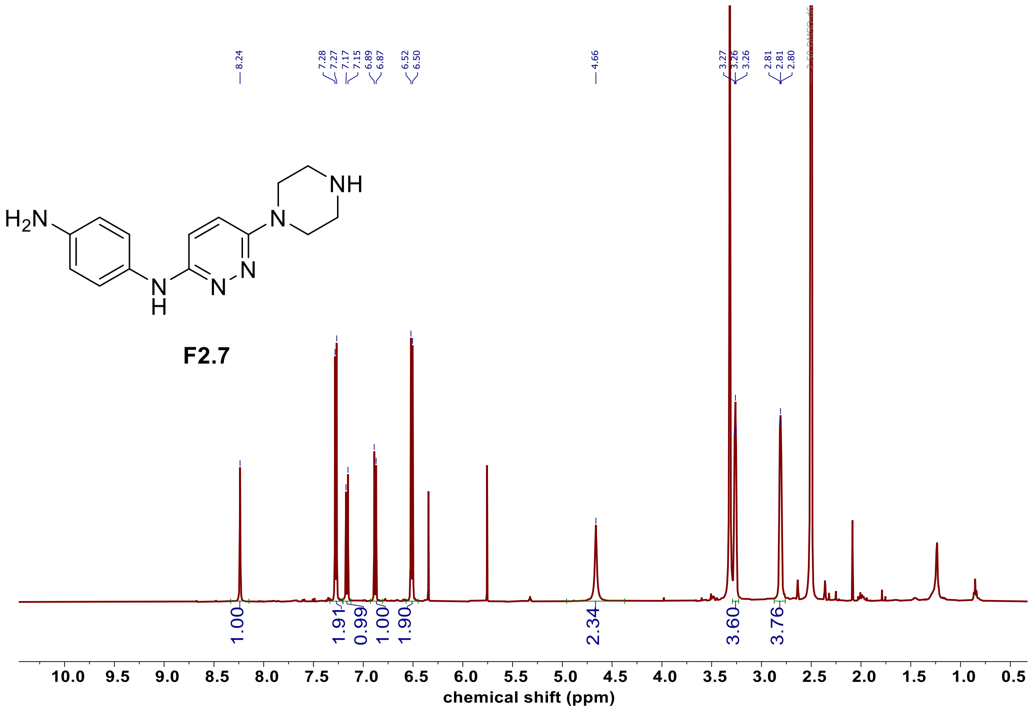

F2.8, ^{1}H NMR (500 MHz, DMSO- d_6)

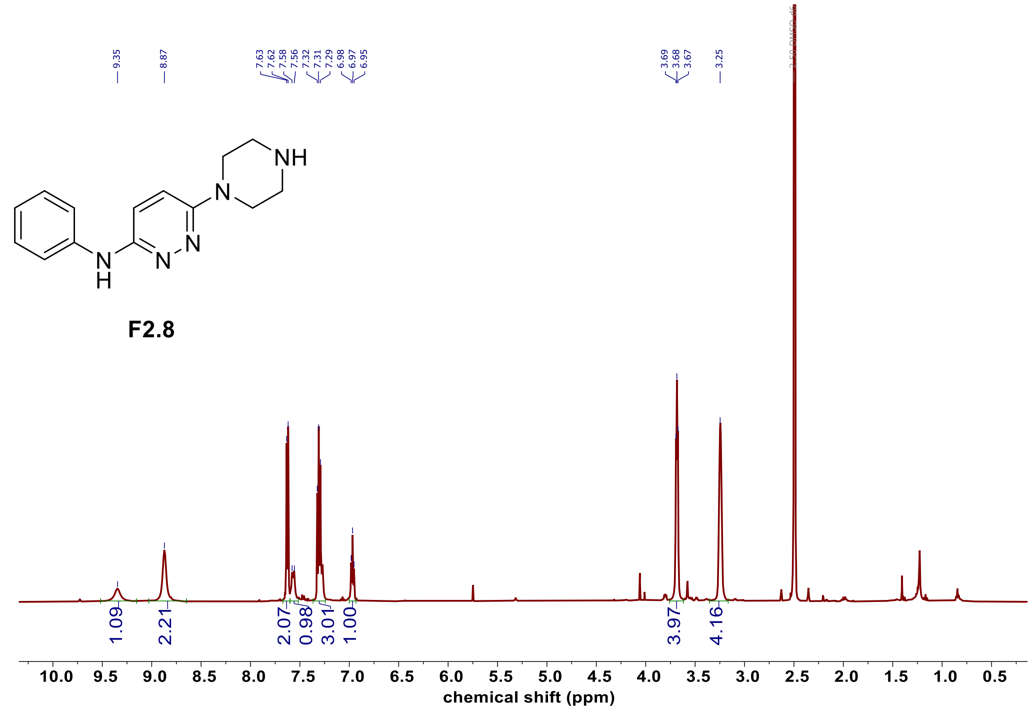

F2.9, ^{1}H NMR (500 MHz, DMSO- d_6)

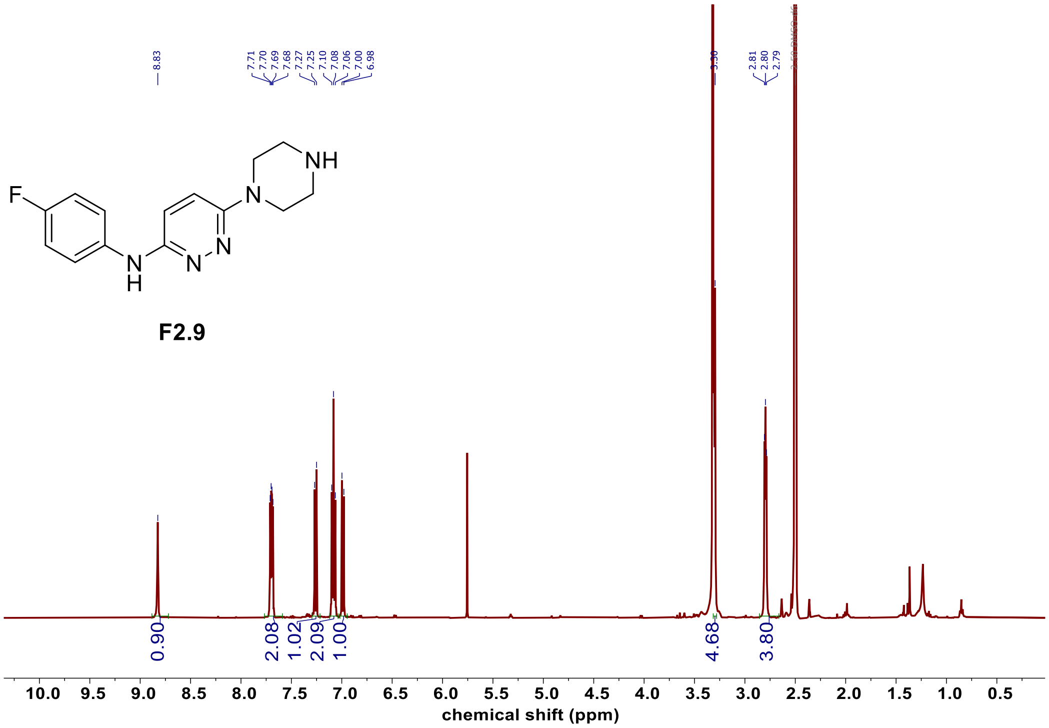

F2.10, ^{1}H NMR (500 MHz, DMSO- d_6)